Multi-materials nano-heterostructures for combined therapy and diagnosis

Sergio Fiorito

Supervisors:

Dr. Teresa Pellegrino (Italian Institute of Technology)

Prof. Fabio Canepa (University of Genova)

Declaration

This dissertation is the result of my own work and includes nothing, which is the outcome of work done in collaboration except where specifically indicated in the text. It has not been submitted, in part or completely, to any university or institution of any degree, diploma, or other qualification.

DATE: Sergio Fiorito

19th March 2020

“I am among those who think that science has great beauty. A scientist in his laboratory is not only a technician: he is also a child placed before natural phenomena, which impress him like a fairy tale.”

[M. Skłodowska-Curie]

Table of contents

Thesis abstract 1

Introduction 3

Nanoparticles for cancer therapy and diagnosis 3

Multimodal therapy through nano-heterostructures 6

References 8

1 Chapter 1: ZnS nanoparticles as vectors for radioactive ^{64}Cu 15

1.1. Introduction 15
1.1.1. Application of radioisotopes in nuclear medicine 15
1.1.2. Commonly used radionuclides in PET and in TRT 17
1.1.3. Nanoparticles as carriers for ^{64}Cu in TRT and PET 18

1.2. Results and discussion 20
1.2.1. Synthesis of ZnS nanoparticles 20
1.2.2. Water transfer of ZnS nanoparticles 21
1.2.3. Cation exchange from ZnS to $Cu_{2-x}S$ 24
1.2.4. Radiolabeling of ZnS nanoparticles with ^{64}Cu 26

1.3. Conclusions and outlook 30

1.4. Experimental procedures 31

1.5. References 34

2 Chapter 2: Synthesis of multifunctional nano-heterostructures 39

2.1. Introduction 39
2.1.1. Janus nanoparticles: properties and parameters influencing their synthesis 39
2.1.2. Synthesis procedures for JNPs having an iron oxide and a chalcogenide domain 41

2.2. Results and discussion 43
2.2.1. Synthesis of γ-Fe_2O_3@ZnS heterostructures 43
2.2.2. Synthesis of IONC@ZnS heterostructures 44
2.2.3. Synthesis of Au@FeO_y heterostructures 48
2.2.4. Synthesis of Au@$Cu_{2-x}S$ heterostructures 50
2.2.5. Synthesis of Au@ZnS heterostructures 52
2.2.6. Synthesis of FeO_y@Au@$Cu_{2-x}S$ heterostructures 55

2.3. Conclusions and outlook 69

2.4. Experimental procedures 70

2.5. References 74

3 Chapter 3: FeO_y@Au@$Cu_{2-x}S$ nano-heterostructures as probes for magnetic hyperthermia, nuclear medicine and photothermal therapy 79

3.1. Introduction 79
3.1.1. Treating cancer using heat with hyperthermia treatments 79
3.1.2. Magnetic hyperthermia cancer treatments using magnetic nanoparticles 81
3.1.3. Photothermal therapy using nanoparticles 84

3.2. Results and discussion 87
3.2.1. Water transfer of FeO_y@Au@$Cu_{2-x}S$ heterostructures 87
3.2.2. Magnetic hyperthermia performances of FeO_y@Au@$Cu_{2-x}S$ heterostructures 96
3.2.3. Radiolabeling with ^{64}Cu of FeO_y@Au@$Cu_{2-x}S$ heterostructures 99
3.2.4. Photothermal performances of FeO_y@Au@$Cu_{2-x}S$ heterostructures 105

3.3. Conclusions and outlook 109

3.4. Experimental procedures 110

3.5. References 114

Appendix 122

List of abbreviations 126

List of contributions 132

Curriculum Vitae of the candidate 133

Summary 135

Thesis abstract

The present dissertation is resulting from the work performed during the Ph.D. research activity carried out at the Italian Institute of Technology (IIT) under the supervision of Dr. Teresa Pellegrino (Nanomaterials for biomedical research line) of the Italian Institute of Technology and Fabio Canepa of the University of Genova. The thesis has been conducted in the framework of the ERC-founded project ICARO (ERC starting grant n° 678109, Principal Investigator: Dr. Teresa Pellegrino), whose main purpose is the development of novel inorganic nanostructures for radiotherapy and chemotherapy of cancer. Thus, this thesis aims to progress the field of nanomedicine. In particular, the first goal of this work is to synthesize innovative water stable chalcogenide nanoparticles, with the purpose of achieving nano-sized platforms capable of incorporating radioactive ^{64}Cu ions, which would make such systems suitable for the use in radiotherapy and for positron emission tomography. The second goal is to explore the coupling of such chalcogenide nanocrystals with magnetic nanoparticles, which are already part of the nanoparticles' portfolio available in the research group where this thesis was carried out. These nanoparticles have shown great potential for magnetic hyperthermia treatment of cancer and, in combination with radiotherapy, could result in a synergic and more effective cancer treatment. Thus, this thesis provides new ground in the rational design of multifunctional nano-heterostructures for cancer diagnosis and therapy.

The first chapter of this thesis deals with the synthesis, water transfer and radiolabeling of ZnS nanoparticles. A non-hydrolitycal thermal decomposition synthesis route was exploited in order to obtain quasi-spherical nanoparticles. Such nanoparticles have hydrophobic ligands on their surface and thus are stable in organic solvents. In order to successfully transfer them to water phase, the ligands were exchanged through a procedure that employs a multi-dentate amphiphilic polymer (cysteamine-poly(isobutylene-alt-maleic anhydride)-polyethylene glycol, CYS-PIMA-PEG), which resulted in inorganic colloids with perfect stability in aqueous phase. On this system, cation exchange reactions with both radioactive and non-radioactive copper were carried out. The optimized protocol for the radiolabeling of ZnS nanocrystals with ^{64}Cu permitted to obtain high values of radiochemical yield (93%), defined as the percentage of the total activity used that is incorporated in the crystals, without losing colloidal stability during radiolabeling reaction or subsequent concentration and purification process. The results obtained indicate ZnS nanoparticles as an efficient nano-platform for the use in radiotherapy and positron emission tomography, given the fast, reproducible and easily clinical-translatable radiolabeling procedure resulting in quantitative incorporation of ^{64}Cu ions.

In the second chapter we report the research activity carried out to couple in a single nano-heterostructure, the ZnS nanoparticles or copper-deficient copper sulfide nanoparticles (previously reported to be exploitable as radioisotopes carriers) with highly performing magnetic nanoparticles (iron oxide nanocubes, IONCs) or nano-heterostructures (gold-iron oxide dimers, $Au@FeO_y$). Although the direct growth of ZnS domains on IONCs, through colloidal two-pot seeded-growth synthesis procedures, was not possible, this thesis succeeds on merging the different nanoparticles in a single nano-platform by exploiting the use of gold NPs as "linkers" between magnetic iron oxide domains and copper deficient $Cu_{2-x}S$ domains, using $Au@FeO_y$ dimers as seeds for the growth of copper sulfide domains. Thus, this procedure resulted in the production of $FeO_y@Au@Cu_{2-x}S$

trimers, with the additional possibility to tune the size of the $Cu_{2-x}S$ domain by changing precursors' concentration. These trimers were thoroughly characterized through diverse structural and magnetic analysis techniques (transition electron microscopy, X-ray diffraction, SQUID magnetometry and UV-VIS-NIR spectroscopy). In particular, magnetic properties measurements, allowed to conclude that the magnetic properties of the FeO_y@Au@$Cu_{2-x}S$ trimers are comparable to the ones of the Au@FeO_y dimers (used as seeds for the subsequent reaction of growth of $Cu_{2-x}S$ domain). In addition, the trimers display two localized surface plasmon resonance absorption bands, one assigned to the gold domain and the other assignable to the copper deficient copper sulfide domain, respectively localized in the first and second NIR biological windows and, consequently, exploitable in photothermal therapy.

In the third chapter, the newly synthesized trimers were transferred to water phase and tested for the application as carriers for ^{64}Cu and as heating probes in magnetic hyperthermia and photothermal therapy. Different strategies were explored in order to develop a reproducible and high-yield water transfer protocol. Among them, a two-step ligand exchange procedure employing methoxy-poly(ethylene glycol)-thiol and poly(catechol)-poly(ethylene glycol) as amphiphilic ligands resulted in aqueous phase stable trimers with high water transfer procedure yield (> 80 %). FeO_y@Au@$Cu_{2-x}S$ trimers were also successfully transferred to water, although with lower yields if compared to previous procedure, using a polymer coating procedure and employing commercially available and cost-effective poly-(maleic anhydride-alt-1-octadecene). Lastly, the developed nano-platform showed great relevance in the field of nanomedicine. Indeed, when employed in magnetic hyperthermia, trimers resulted in high SAR values, preserving the excellent hyperthermia performances of the Au@FeO_y used as seeds for their synthesis and thus in line with the best magnetic nano-heterostructures reported so far. Radiolabeling reactions were performed on trimers, resulting in a radiochemical yield of 97 %, higher than any value reported so far for ^{64}Cu incorporation in water stable nanocrystals. Furthermore, the stability of the trimers during the radiolabeling and subsequent purification procedures was likewise ensured by the use of CYS-PIMA-PEG as stabilizing agent, permitting to recover quantitatively the nanocrystals and the associated radioactivity. The performances of FeO_y@Au@$Cu_{2-x}S$ trimers when used in photothermal heating were also tested under the exposure to 808 nm laser irradiation. Although when using high power density (4.67 W/cm^2), a temperature increase of 33°C in five minutes was registered, the performances obtained with lower laser's power density were limited. However, the possibility to tune the absorption wavelengths by means of changing gold and copper sulfide domain's properties, gives space to further improvements for these multifunctional nano-heterostructures. To the best of our knowledge, the here described FeO_y@Au@$Cu_{2-x}S$ trimers are the first ever reported nano-heterostructures able to combine in one single nano-object the possibility to perform magnetic hyperthermia, photothermal therapy and radiotherapy/positron emission tomography, thus allowing the possible development of more efficient cancer treatments.

Introduction

Nanoparticles for cancer therapy and diagnosis

Cancer is one of the leading causes of death worldwide accounting for 9.6 million of deaths (almost 17 % of all deaths globally, 20 % of all deaths in Europe) in 2018[1]. Beside surgery, the most commonly used therapies for the tumor treatment, are chemotherapy and radiotherapy. However, together with the large heterogeneity of cancers, many factors, such as, for example, multidrug resistance (MDR) in the case of chemotherapy and, for what regards radiotherapy treatments, the low sensitivity of hypoxic cancers to the ionizing radiations, can reduce the effectiveness of these treatments.[2] This calls for the development of new innovative cancer treatments, with higher specificity and consequently causing less damage to surroundings healthy tissues. Among the different strategies investigated, the use of nanoparticles as remote probes for cancer diagnosis and treatment (nanomedicine) has widely attracted the attention of the research community in last two decades.[3,4] An advantage of the use of nanoparticles is their tunable size (from few to hundred nanometers) that place them in the range of dimensions of biological targets such as cells (10 – 100 µm), viruses (20 – 450 nm), proteins (5 – 50 nm) or genes (2 nm wide and 10 – 100 nm long).[5] Moreover, thanks to their small size, the surface to volume ratio of nanoparticles is orders of magnitude higher than the one of bulk materials, this increasing the number of surface atoms with respect to the one of atoms composing the core. This large surface/volume ratio increases the importance of interface and surface phenomena and gives, for example, the possibility to increase the number of molecules of anti-cancer drugs that can be loaded on a single nanoparticle used as carrier.[6] For these reasons, in last two decades, nanoparticles were widely studied to improve the efficacy of chemotherapeutic[7–9] and radiotherapeutic[10,11] treatments and the number of FDA approved nanomedicines has increased drastically.[12]

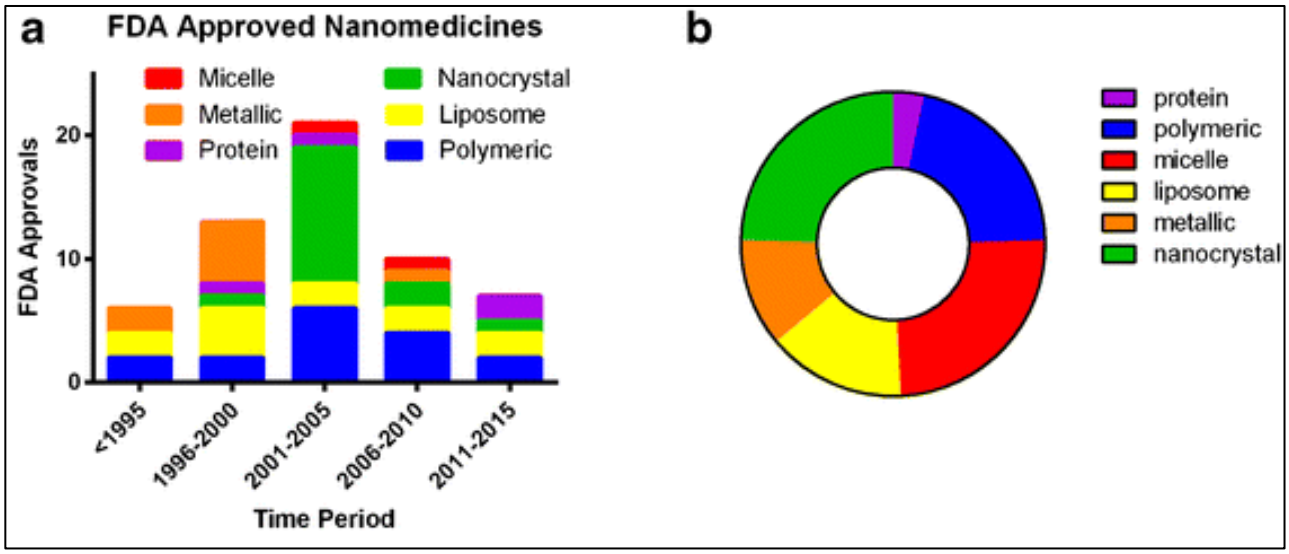

Figure 1: Trends in the development of nanomedicines. (a) FDA approved nanomedicines per time period, stratified by category; (b) FDA-approved nanomedicines stratified by category overall. Reprinted and adapted, with permissions, from reference 12.

Among the different classes of nanoparticles studied, inorganic nanoparticles are of particular importance for their peculiar and tunable chemical and physical properties that confer additional

therapeutic and diagnostic features to the nano-formulations.[13] Consequently, other than being functionalized and used as carriers for chemotherapeutic drug delivery,[14] inorganic nanoparticles can be exploited for a new generation of biomedical applications relying on their peculiar properties such as, for example, magnetic resonance, photoacoustic tomography and computed tomography for diagnosis or magnetic hyperthermia, photothermal therapy and photodynamic therapy for therapy. Moreover, inorganic nanoparticles can be coated with biocompatible polymers[15] in order to improve their stability,[16] increase their blood circulation time,[17] reduce their toxicity,[18] and enhance their target specificity.[19]

Among the wide range of inorganic nanoparticles having different composition studied for biomedical applications, three main classes have been of particular interest for their chemical and physical properties: noble metal nanoparticles,[20] semiconductors nanoparticles[21] and magnetic nanoparticles.[22]

Noble metal (Au, Ag, Pt) nanoparticles have been widely investigated for biomedical applications[23] because of the large portfolio of synthesis procedure reported,[24,25] the broad possibility of functionalization[26–28] and because of their biocompatibility.[29] Silver nanoparticles have been mainly studied for their antimicrobial activity[30,31] while the DNA damaging effect has been reported for platinum nanoparticles.[32] Among noble metal nanoparticles, the most studied for their possible applications in cancer treatment and diagnosis are gold-based NPs.[33] Indeed, gold nanoparticles (GNPs) of different size and shapes have been reported to be exploitable in both cancer therapy and diagnosis. For what regards diagnosis, they have been reported to be efficient when used as contrast agents in computed tomography (CT)[34,35], in photoacoustic tomography[36,37] and in surface enhanced Raman scattering (SERS) imaging[38,39]. On the other hand, GNPs have also been reported to be candidate nanomaterials for the use in cancer therapy through photothermal therapy (PTT, see Chapter 3),[40,41] in photodynamic treatments (PDT)[42,43] and as radiosensitizing agents in radiation therapy.[44,45]

Second class of nanoparticles employed in biomedical applications is provided by semiconductor nanocrystals. Although they have lower biocompatibility than gold-based materials,[46] numerous studies investigated the possibility of the use of semiconductor nanocrystals in biomedical applications.[47–50]. Their optical adsorption and emission properties, tunable in the visible and infrared range, have made them optimal as imaging probe. In particular, less cytotoxic copper-based chalcogenides nanocrystals have been reported as probes for cancer cells imaging through photoacoustic tomography[51] and as effective when used in PDT[52,53] and in PTT.[54,55] Recently, copper sulfide nanocrystals have been also reported as effective for the incorporation of ^{64}Cu [56] and, consequently, to be exploitable in the development of radiopharmaceutical nano-formulations for positron emission tomography (PET) and targeted radionuclide therapy (TRT). A new ^{64}Cu radiolabeling procedure for chalcogenide nanocrystals, allowing to incorporate ^{64}Cu on water stable CuS crystal exploiting a fast and easily clinical-translatable protocol has been recently developed in the research group where this thesis work was carried out.[57]

Magnetic nanoparticles (MNPs) are the third class of widely used nanoparticles of particular interest in the field of nanomedicine for the possibility of being remotely manipulated by the application of a static or an alternated magnetic field that can permeate human body.[58–60] Other than for magnetic drug targeting [61–63] MNPs have been reported to be exploitable for cancer therapy through magnetic

hyperthermia treatments (MHT, see Chapter 3)[64,65]. Another possibility related to the use of magnetic nanoparticle in cancer nanomedicine is the possibility to exploit them in cancer diagnosis as contrast agents in magnetic resonance imaging (MRI)[66,67] or as tracers in magnetic particles imaging (MPI).[68,69] Among all the MNPs with different composition reported in literature (such as, for example Fe(0)[70], FePt[71] FeC and mixed ferrite nanoparticles, obtained from iron oxide by partial replacement of the Fe^{2+} ions in the inverse spinel structure with other transition metal ions [72–74]), FDA approved iron oxide nanoparticles (IONPs) are the most studied[75,76] for biological applications given the large portfolio of reported procedures for their synthesis and surface functionalization[77] and their proven biocompatibility.[78] The group where this thesis work was carried out has developed, over the last decade, a wide knowhow on the synthesis and functionalization of magnetic nanoparticles with high hyperthermia performances.[79–82].

Multimodal therapy through nano-heterostructures

Some of the nanoparticles reported for biomedical applications have intrinsic multimodal diagnosis and therapy features.[83] Some examples include a single composition nanomaterial like gold nanorods, that have been reported to be exploitable both in cancer cell imaging and photothermal therapy[84], or copper sulfide nanocrystals that have been exploited for dual PDT and PTT treatment[85] or for photoacoustic imaging-guided photothermal therapy.[86] Iron oxide nanoparticles are also commonly studied for theragnostic, exploiting MRI (or MPI) as imaging technique and MHT for therapy[87] and have recently been reported to be exploitable in dual MHT and PTT treatments.[88]

The possibility to obtain through one single nano-object multiple treatment and diagnosis modalities is of key interest for the future development of nanomedicine. Indeed, the development of multimodal treatment and diagnosis nano-platform, would permit to increase the efficiency of the treatments, this scaling down the amount, and related cytotoxicity,[89] of the nanoparticles used.[90] In order to further enhance this possibility, researchers working on nanoparticles for biomedical applications started putting efforts on the development of nano-heterostructures (NHs) composed of different nano-domains with different properties.[91] Different strategies to fulfill this aim were developed, such as coupling the two domains though a silica matrix [92–94] or embedding nanoparticles with different composition in a polymeric shell.[95] This work was focused on the study of nano-heterostructures having different domains joint through a solid interface (Janus nanoparticles, see Chapter 2), this allowing to obtain multifunctional nano-objects with reduced size and to tune properties arising from the formation of the solid heterojunction.[96] Moreover, particular interest was directed towards nano-heterostructures developed in order to combine multiple therapeutic modality overcoming the intrinsic limitations of each single therapy, with a special focus on the ones having a magnetic domain with good efficiency when used in magnetic hyperthermia.

Nano-heterostructures coupling magnetic nanoparticles with noble metals have been widely reported to be exploitable in biomedical applications.[97–99] However, in most of them the therapy is performed exploiting photothermal [100,101] or photodynamic[102] therapies since only few have magnetic properties suitable to be used in magnetic hyperthermia with good efficiencies.[103–105] Similarly, among the reported NHs including a magnetic and a semiconductor domain,[106–108] most of them have been reported for magnetically guided (through MRI) photothermal therapy[109,110] and only recently, Curcio et al. reported rattle-type iron oxide@CuS hybrids able to combine PTT and PDT with magnetic hyperthermia.[111] Knowing the lack of reports on tri-functional nano-systems able to merge in one single NHs magnetic hyperthermia, photothermal therapy and radiotherapy (through the possibility to incorporate ^{64}Cu in the nanocrystals, without the addition of further functionalization) we have been working on the development and proof of principle of application of such NHs.

The results obtained from the research activity carried out during my PhD, focused on the development of multifunctional nano-heterostructures for cancer therapy and diagnosis, are here described and are organized in three chapters:

In Chapter 1 I will report on the development new chalcogenide nanomaterials (ZnS nanoparticles) and on their radiolabeling with ^{64}Cu in order to develop new nano-carriers for radioactive ions.

In Chapter 2 I will focus on the development of non-hydrolitycal colloidal synthesis approaches in order to couple chalcogenide nanocrystals (demonstrated to be able to carry ^{64}Cu ions) with magnetic nanoparticles having excellent performances in magnetic hyperthermia.

In chapter 3 I will describe the results obtained by the applications of newly developed FeO_y@Au@$Cu_{2-x}S$ trimers in magnetic and photothermal hyperthermia as well as the results obtained by the radiolabeling of the trimers using ^{64}Cu.

References

1. World Health Organization (WHO). Available at: https://www.who.int/news-room/fact-sheets/detail/cancer.

2. Fan, W., Yung, B., Huang, P. & Chen, X. Nanotechnology for Multimodal Synergistic Cancer Therapy. *Chem. Rev.* **117**, 13566–13638 (2017).

3. Mi, Y., Shao, Z., Vang, J., Kaidar-Person, O. & Wang, A. Z. Application of nanotechnology to cancer radiotherapy. *Cancer Nanotechnol.* **7**, (2016).

4. Zhao, C. Y., Cheng, R., Yang, Z. & Tian, Z. M. Nanotechnology for cancer therapy based on chemotherapy. *Molecules* **23**, (2018).

5. Pankhurst, Q. A., Connolly, J., Jones, S. K. & Dobson, J. J. Applications of magnetic nanoparticles in biomedicine. *J. Phys. D. Appl. Phys.* **36**, R167 (2003).

6. Doane, T. L. & Burda, C. The unique role of nanoparticles in nanomedicine: Imaging, drug delivery and therapy. *Chem. Soc. Rev.* **41**, 2885–2911 (2012).

7. Wong, H. L., Bendayan, R., Rauth, A. M., Li, Y. & Wu, X. Y. Chemotherapy with anticancer drugs encapsulated in solid lipid nanoparticles. *Advanced Drug Delivery Reviews* **59**, 491–504 (2007).

8. Parhi, P., Mohanty, C. & Sahoo, S. K. Nanotechnology-based combinational drug delivery: An emerging approach for cancer therapy. *Drug Discovery Today* **17**, 1044–1052 (2012).

9. Steiniger, S. C. J. *et al.* Chemotherapy of glioblastoma in rats using doxorubicin-loaded nanoparticles. *Int. J. Cancer* **109**, 759–767 (2004).

10. Yi, X. *et al.* Core–shell Au@MnO2 nanoparticles for enhanced radiotherapy via improving the tumor oxygenation. *Nano Res.* **9**, 3267–3278 (2016).

11. Kim, M. S. *et al.* Gold nanoparticles enhance anti-tumor effect of radiotherapy to hypoxic tumor. *Radiat. Oncol. J.* **34**, 230–238 (2016).

12. Bobo, D., Robinson, K. J., Islam, J., Thurecht, K. J. & Corrie, S. R. Nanoparticle-Based Medicines: A Review of FDA-Approved Materials and Clinical Trials to Date. *Pharm. Res.* **33**, 2373–2387 (2016).

13. Anselmo, A. C. & Mitragotri, S. A Review of Clinical Translation of Inorganic Nanoparticles. *AAPS J.* **17**, 1041–54 (2015).

14. Jurgons, R. *et al.* Drug loaded magnetic nanoparticles for cancer therapy. *J. Phys. Condens. Matter* **18**, (2006).

15. Mout, R., Moyano, D. F., Rana, S. & Rotello, V. M. Surface functionalization of nanoparticles for nanomedicine. *Chemical Society Reviews* **41**, 2539–2544 (2012).

16. Soliman, M. G., Pelaz, B., Parak, W. J. & Del Pino, P. Phase transfer and polymer coating methods toward improving the stability of metallic nanoparticles for biological applications. *Chem. Mater.* **27**, 990–997 (2015).

17. Xiao, W. *et al.* Prolonged in vivo circulation time by zwitterionic modification of magnetite

nanoparticles for blood pool contrast agents. *Contrast Media Mol. Imaging* **7**, 320–327 (2012).

18. Shukla, S. *et al.* In vitro toxicity assessment of chitosan oligosaccharide coated iron oxide nanoparticles. *Toxicol. Reports* **2**, 27–39 (2015).

19. Tian, X. H. *et al.* Enhanced brain targeting of temozolomide in polysorbate-80 coated polybutylcyanoacrylate nanoparticles. *Int. J. Nanomedicine* **6**, 445–452 (2011).

20. Jain, P. K., Huang, X., El-Sayed, I. H. & El-Sayed, M. A. Noble metals on the nanoscale: Optical and photothermal properties and some applications in imaging, sensing, biology, and medicine. *Acc. Chem. Res.* **41**, 1578–1586 (2008).

21. Abbasi, E. *et al.* Biomedical and biological applications of quantum dots. *Artif. Cells, Nanomedicine Biotechnol.* **44**, 885–891 (2016).

22. Reddy, L. H., Arias, J. L., Nicolas, J. & Couvreur, P. Magnetic nanoparticles: Design and characterization, toxicity and biocompatibility, pharmaceutical and biomedical applications. *Chem. Rev.* **112**, 5818–5878 (2012).

23. Rai, M., Ingle, A. P., Birla, S., Yadav, A. & Santos, C. A. Dos. Strategic role of selected noble metal nanoparticles in medicine. *Crit. Rev. Microbiol.* **42**, 696–719 (2016).

24. Sau, T. K. & Rogach, A. L. Nonspherical noble metal nanoparticles: Colloid-chemical synthesis and morphology control. *Adv. Mater.* **22**, 1781–1804 (2010).

25. Zheng, N., Fan, J. & Stucky, G. D. One-step one-phase synthesis of monodisperse noble-metallic nanoparticles and their colloidal crystals. *J. Am. Chem. Soc.* **128**, 6550–6551 (2006).

26. Thierry, B., Ng, J., Krieg, T. & Griesser, H. J. A robust procedure for the functionalization of gold nanorods and noble metal nanoparticles. *Chem. Commun.* **1**, 1724–1726 (2009).

27. Burt, J. L., Gutiérrez-Wing, C., Miki-Yoshida, M. & José-Yacamán, M. Noble-metal nanoparticles directly conjugated to globular proteins. *Langmuir* **20**, 11778–11783 (2004).

28. Zhang, Y. J., Huang, R., Zhu, X. F., Wang, L. Z. & Wu, C. X. Synthesis, properties, and optical applications of noble metal nanoparticle-biomolecule conjugates. *Chinese Sci. Bull.* **57**, 238–246 (2012).

29. Connor, E. E., Mwamuka, J., Gole, A., Murphy, C. J. & Wyatt, M. D. Gold nanoparticles are taken up by human cells but do not cause acute cytotoxicity. *Small* **1**, 325–327 (2005).

30. Kim, J. S. *et al.* Antimicrobial effects of silver nanoparticles. *Nanomedicine Nanotechnology, Biol. Med.* **3**, 95–101 (2007).

31. Shrivastava, S. *et al.* Characterization of enhanced antibacterial effects of novel silver nanoparticles. *Nanotechnology* **18**, (2007).

32. Pelka, J. *et al.* Cellular uptake of platinum nanoparticles in human colon carcinoma cells and their impact on cellular redox systems and DNA integrity. *Chem. Res. Toxicol.* **22**, 649–659 (2009).

33. Sperling, R. A., Rivera Gil, P., Zhang, F., Zanella, M. & Parak, W. J. Biological applications of gold nanoparticles. *Chem. Soc. Rev.* **37**, 1896–1908 (2008).

34. Hainfeld, J. F., Slatkin, D. N., Focella, T. M. & Smilowitz, H. M. Gold nanoparticles: a new X-ray contrast agent. *Br. J. Radiol.* **79**, 248–253 (2006).

35. Popovtzer, R. *et al.* Targeted gold nanoparticles enable molecular CT imaging of cancer. *Nano Lett.* **8**, 4593–4596 (2008).

36. Li, W. & Chen, X. Gold nanoparticles for photoacoustic imaging. *Nanomedicine* **10**, 299–320 (2015).

37. Zhang, Q. *et al.* Gold nanoparticles as a contrast agent for invivo tumor imaging with photoacoustic tomography. *Nanotechnology* **20**, (2009).

38. Yigit, M. V & Medarova, Z. In vivo and ex vivo applications of gold nanoparticles for biomedical SERS imagingi. *Am. J. Nucl. Med. Mol. Imaging* **2**, 232–41 (2012).

39. Xie, J., Zhang, Q., Lee, J. Y. & Wang, D. I. C. The synthesis of SERS-active gold nanoflower tags for in vivo applications. *ACS Nano* **2**, 2473–2480 (2008).

40. Dickerson, E. B. *et al.* Gold nanorod assisted near-infrared plasmonic photothermal therapy (PPTT) of squamous cell carcinoma in mice. *Cancer Lett.* **269**, 57–66 (2008).

41. Choi, W. Il *et al.* Tumor regression in vivo by photothermal therapy based on gold-nanorod-loaded, functional nanocarriers. *ACS Nano* **5**, 1995–2003 (2011).

42. Hone, D. C. *et al.* Generation of cytotoxic singlet oxygen via phthalocyaninel-stabilized gold nanoparticles: A potential delivery vehicle for photodynamic therapy. *Langmuir* **18**, 2985–2987 (2002).

43. Stuchinskaya, T., Moreno, M., Cook, M. J., Edwards, D. R. & Russell, D. A. Targeted photodynamic therapy of breast cancer cells using antibody-phthalocyanine-gold nanoparticle conjugates. *Photochem. Photobiol. Sci.* **10**, 822–831 (2011).

44. Butterworth, K. T., McMahon, S. J., Currell, F. J. & Prise, K. M. Physical basis and biological mechanisms of gold nanoparticle radiosensitization. *Nanoscale* **4**, 4830–4838 (2012).

45. Joh, D. Y. *et al.* Selective Targeting of Brain Tumors with Gold Nanoparticle-Induced Radiosensitization. *PLoS One* **8**, (2013).

46. Derfus, A. M., Chan, W. C. W. & Bhatia, S. N. Probing the Cytotoxicity of Semiconductor Quantum Dots. *Nano Lett.* **4**, 11–18 (2004).

47. Fu, A., Gu, W., Larabell, C. & Alivisatos, A. P. Semiconductor nanocrystals for biological imaging. *Current Opinion in Neurobiology* **15**, 568–575 (2005).

48. Gao, X., Cui, Y., Levenson, R. M., Chung, L. W. K. & Nie, S. In vivo cancer targeting and imaging with semiconductor quantum dots. *Nat. Biotechnol.* **22**, 969–976 (2004).

49. Qi, L. & Gao, X. Emerging application of quantum dots for drug delivery and therapy. *Expert Opinion on Drug Delivery* **5**, 263–267 (2008).

50. Samia, A. C. S., Chen, X. & Burda, C. Semiconductor Quantum Dots for Photodynamic Therapy. *J. Am. Chem. Soc.* **125**, 15736–15737 (2003).

51. Ku, G. *et al.* Copper Sulfide Nanoparticles As a New Class of Photoacoustic Contrast Agent for Deep Tissue Imaging at 1064 nm. *ACS Nano* **6**, 7489–7496 (2012).

52. Liu, Z., Liu, X., Du, Y., Ren, J. & Qu, X. Using Plasmonic Copper Sulfide Nanocrystals as Smart Light-Driven Sterilants. *ACS Nano* **9**, 10335–10346 (2015).

53. Wang, S. *et al.* Plasmonic Copper Sulfide Nanocrystals Exhibiting Near-Infrared Photothermal and Photodynamic Therapeutic Effects. *ACS Nano* **9**, 1788–1800 (2015).

54. Guo, L. *et al.* Combinatorial Photothermal and Immuno Cancer Therapy Using Chitosan-Coated Hollow Copper Sulfide Nanoparticles. *ACS Nano* **8**, 5670–5681 (2014).

55. Li, Y., Lu, W., Huang, Q., Li, C. & Chen, W. Copper sulfide nanoparticles for photothermal ablation of tumor cells. *Nanomedicine* **5**, 1161–1171 (2010).

56. Zhou, M. *et al.* A chelator-free multifunctional [64Cu]CuS nanoparticle platform for simultaneous micro-PET/CT imaging and photothermal ablation therapy. *J. Am. Chem. Soc.* **132**, 15351–15358 (2010).

57. Riedinger, A. *et al.* Post-Synthesis Incorporation of 64Cu in CuS Nanocrystals to Radiolabel Photothermal Probes: A Feasible Approach for Clinics. *J. Am. Chem. Soc.* **137**, 15145–15151 (2015).

58. Giri, S., Trewyn, B. G., Stellmaker, M. P. & Lin, V. S.-Y. Stimuli-Responsive Controlled-Release Delivery System Based on Mesoporous Silica Nanorods Capped with Magnetic Nanoparticles. *Angew. Chemie Int. Ed.* **44**, 5038–5044 (2005).

59. Adams, J. D., Kim, U. & Soh, H. T. Multitarget magnetic activated cell sorter. *Proc. Natl. Acad. Sci. U. S. A.* **105**, 18165–18170 (2008).

60. Arruebo, M., Fernández-Pacheco, R., Ibarra, M. R. & Santamaría, J. Magnetic nanoparticles for drug delivery. *Nano Today* **2**, 22–32 (2007).

61. Lübbe, A. S., Alexiou, C. & Bergemann, C. Clinical applications of magnetic drug targeting. *J. Surg. Res.* **95**, 200–206 (2001).

62. Lübbe, A. S. *et al.* Clinical experiences with magnetic drug targeting: A phase I study with 4'-epidoxorubicin in 14 patients with advanced solid tumors. *Cancer Res.* **56**, 4686–4693 (1996).

63. Gang, J. *et al.* Magnetic poly ε-caprolactone nanoparticles containing Fe3 O4 and gemcitabine enhance anti-tumor effect in pancreatic cancer xenograft mouse model. *J. Drug Target.* **15**, 445–453 (2007).

64. Mahmoudi, K., Bouras, A., Bozec, D., Ivkov, R. & Hadjipanayis, C. Magnetic hyperthermia therapy for the treatment of glioblastoma: a review of the therapy's history, efficacy and application in humans. *Int. J. Hyperth.* **34**, 1316–1328 (2018).

65. Cotin, G. *et al. Design of Anisotropic Iron-Oxide-Based Nanoparticles for Magnetic Hyperthermia*. *Nanomaterials for Magnetic and Optical Hyperthermia Applications* (2019). doi:10.1016/b978-0-12-813928-8.00002-8

66. Na, H. Bin, Song, I. C. & Hyeon, T. Inorganic Nanoparticles for MRI Contrast Agents. *Adv. Mater.* **21**, 2133–2148 (2009).

67. Ni, D., Bu, W., Ehlerding, E. B., Cai, W. & Shi, J. Engineering of inorganic nanoparticles as magnetic resonance imaging contrast agents. *Chemical Society Reviews* **46**, 7438–7468 (2017).

68. Gleich, B. & Weizenecker, J. Tomographic imaging using the nonlinear response of magnetic particles. *Nature* **435**, 1214–1217 (2005).

69. Bauer, L. M., Situ, S. F., Griswold, M. A. & Samia, A. C. S. Magnetic Particle Imaging Tracers: State-of-the-Art and Future Directions. *J. Phys. Chem. Lett.* **6**, 2509–2517 (2015).

70. Mehdaoui, B. *et al.* Large specific absorption rates in the magnetic hyperthermia properties of metallic iron nanocubes. *J. Magn. Magn. Mater.* **322**, (2010).

71. Seehra, M. S. *et al.* Size-dependent magnetic parameters of fcc FePt nanoparticles: Applications to magnetic hyperthermia. *J. Phys. D. Appl. Phys.* **43**, (2010).

72. Sathya, A. *et al.* Co x Fe 3– x O 4 Nanocubes for Theranostic Applications: Effect of Cobalt Content and Particle Size. *Chem. Mater.* **28**, 1769–1780 (2016).

73. Pilati, V. *et al.* Core/Shell Nanoparticles of Non-Stoichiometric Zn–Mn and Zn–Co Ferrites as Thermosensitive Heat Sources for Magnetic Fluid Hyperthermia. *J. Phys. Chem. C* **122**, 3028–3038 (2018).

74. Jang, J. *et al.* Critical Enhancements of MRI Contrast and Hyperthermic Effects by Dopant-Controlled Magnetic Nanoparticles. *Angew. Chemie* **121**, 1260–1264 (2009).

75. Cabrera, D. *et al.* Unraveling viscosity effects on the hysteresis losses of magnetic nanocubes. *Nanoscale* **9**, 5094–5101 (2017).

76. Lak, A. *et al.* Fe2+ Deficiencies, FeO Subdomains, and Structural Defects Favor Magnetic Hyperthermia Performance of Iron Oxide Nanocubes into Intracellular Environment. *Nano Lett.* **18**, 6856–6866 (2018).

77. Wu, W., He, Q. & Jiang, C. Magnetic iron oxide nanoparticles: Synthesis and surface functionalization strategies. *Nanoscale Res. Lett.* **3**, 397–415 (2008).

78. Jain, T. K., Reddy, M. K., Morales, M. A., Leslie-Pelecky, D. L. & Labhasetwar, V. Biodistribution, Clearance, and Biocompatibility of Iron Oxide Magnetic Nanoparticles in Rats. *Mol. Pharm.* **5**, 316–327 (2008).

79. Guardia, P. *et al.* Gold–iron oxide dimers for magnetic hyperthermia: the key role of chloride ions in the synthesis to boost the heating efficiency. *J. Mater. Chem. B* **5**, 4587–4594 (2017).

80. Guardia, P. *et al.* One pot synthesis of monodisperse water soluble iron oxide nanocrystals with high values of the specific absorption rate. *J. Mater. Chem. B* **2**, 4426 (2014).

81. Guardia, P. *et al.* Water-Soluble Iron Oxide Nanocubes with High Values of Specific Absorption Rate for Cancer Cell Hyperthermia Treatment. *ACS Nano* **6**, 3080–3091 (2012).

82. Mai, B. T. *et al.* Thermoresponsive Iron Oxide Nanocubes for an Effective Clinical Translation of Magnetic Hyperthermia and Heat-Mediated Chemotherapy. *ACS Appl. Mater. Interfaces* (2019). doi:10.1021/acsami.8b16226

83. Lee, D. E. *et al.* Multifunctional nanoparticles for multimodal imaging and theragnosis. *Chem. Soc. Rev.* **41**, 2656–2672 (2012).

84. Huang, X., El-Sayed, I. H., Qian, W. & El-Sayed, M. A. Cancer Cell Imaging and Photothermal Therapy in the Near-Infrared Region by Using Gold Nanorods. *J. Am. Chem. Soc.* **128**, 2115–2120 (2006).

85. Li, L. *et al.* CuS nanoagents for photodynamic and photothermal therapies: Phenomena and possible mechanisms. *Photodiagnosis Photodyn. Ther.* **19**, 5–14 (2017).

86. Mou, J. *et al.* Ultrasmall Cu2-xS nanodots for highly efficient photoacoustic imaging-guided photothermal therapy. *Small* **11**, 2275–2283 (2015).

87. Ereath Beeran, A., Fernandez, F. B. & Varma, P. R. H. Self-Controlled Hyperthermia & MRI Contrast Enhancement via Iron Oxide Embedded Hydroxyapatite Superparamagnetic particles for Theranostic Application. *ACS Biomater. Sci. Eng.* **5**, 106–113 (2019).

88. Espinosa, A. *et al.* Duality of Iron Oxide Nanoparticles in Cancer Therapy: Amplification of Heating Efficiency by Magnetic Hyperthermia and Photothermal Bimodal Treatment. *ACS Nano* **10**, 2436–2446 (2016).

89. Lewinski, N., Colvin, V. & Drezek, R. Cytotoxicity of nanopartides. *Small* **4**, 26–49 (2008).

90. Mura, S. & Couvreur, P. Nanotheranostics for personalized medicine. *Advanced Drug Delivery Reviews* **64**, 1394–1416 (2012).

91. Quarta, A., Piccirillo, C., Mandriota, G. & Di Corato, R. Nanoheterostructures (NHS) and their applications in nanomedicine: Focusing on in vivo studies. *Materials (Basel).* **12**, 1–37 (2019).

92. Salgueiriño-Maceira, V., Correa-Duarte, M. A., Spasova, M., Liz-Marzán, L. M. & Farle, M. Composite silica spheres with magnetic and luminescent functionalities. *Adv. Funct. Mater.* **16**, 509–514 (2006).

93. Sánchez, A. *et al.* Hybrid Decorated Core@Shell Janus Nanoparticles as a Flexible Platform for Targeted Multimodal Molecular Bioimaging of Cancer. *ACS Appl. Mater. Interfaces* **10**, 31032–31043 (2018).

94. Yi, D. K. *et al.* Silica-Coated Nanocomposites of Magnetic Nanoparticles and Quantum Dots. *J. Am. Chem. Soc.* **127**, 4990–4991 (2005).

95. Lu, S. *et al.* Dendrimer-Stabilized Gold Nanoflowers Embedded with Ultrasmall Iron Oxide Nanoparticles for Multimode Imaging–Guided Combination Therapy of Tumors. *Adv. Sci.* **5**, (2018).

96. Wang, C., Yin, H., Dai, S. & Sun, S. A general approach to noble metal-metal oxide dumbbell nanoparticles and their catalytic application for CO oxidation. *Chem. Mater.* **22**, 3277–3282 (2010).

97. Xu, C. *et al.* Au–Fe3O4 Dumbbell Nanoparticles as Dual-Functional Probes. *Angew. Chemie Int. Ed.* **47**, 173–176 (2008).

98. Choi, J. S. *et al.* Biocompatible heterostructured nanoparticles for multimodal biological detection. *J. Am. Chem. Soc.* **128**, 15982–15983 (2006).

99. Bao, J. *et al.* Bifunctional Au-Fe3O4 nanoparticles for protein separation. *ACS Nano* **1**, 293–298 (2007).

100. Fan, Z. *et al.* Multifunctional plasmonic shell-magnetic core nanoparticles for targeted diagnostics, isolation, and photothermal destruction of tumor cells. *ACS Nano* **6**, 1065–1073 (2012).

101. Ji, X. *et al.* Bifunctional Gold Nanoshells with a Superparamagnetic Iron Oxide-Silica Core

Suitable for Both MR Imaging and Photothermal Therapy. *J. Phys. Chem. C* **111**, 6245–6251 (2007).

102. Bhana, S. *et al.* Near-infrared-absorbing gold nanopopcorns with iron oxide cluster core for magnetically amplified photothermal and photodynamic cancer therapy. *ACS Appl. Mater. Interfaces* **7**, 11637–11647 (2015).

103. Lu, Q. *et al.* Fe 3 O 4 @Au composite magnetic nanoparticles modified with cetuximab for targeted magneto-photothermal therapy of glioma cells. *Int. J. Nanomedicine* **13**, 2491–2505 (2018).

104. Das, R. *et al.* Boosted Hyperthermia Therapy by Combined AC Magnetic and Photothermal Exposures in Ag/Fe3O4 Nanoflowers. *ACS Appl. Mater. Interfaces* **8**, 25162–25169 (2016).

105. Espinosa, A. *et al.* Can magneto-plasmonic nanohybrids efficiently combine photothermia with magnetic hyperthermia? *Nanoscale* **7**, 18872–18877 (2015).

106. Selvan, S. T., Patra, P. K., Ang, C. Y. & Ying, J. Y. Synthesis of silica-coated semiconductor and magnetic quantum dots and their use in the imaging of live cells. *Angew. Chemie - Int. Ed.* **46**, 2448–2452 (2007).

107. Lin, A. W. H. *et al.* Seed-mediated synthesis, properties and application of γ-Fe 2O3-CdSe magnetic quantum dots. *J. Solid State Chem.* **184**, 2150–2158 (2011).

108. Zhan, F. & Zhang, C. Y. Bifunctional nanoparticles with superparamagnetic and luminescence properties. *J. Mater. Chem.* **21**, 4765–4767 (2011).

109. Wu, Z. C., Li, W. P., Luo, C. H., Su, C. H. & Yeh, C. S. Rattle-Type Fe3O4@CuS Developed to Conduct Magnetically Guided Photoinduced Hyperthermia at First and Second NIR Biological Windows. *Adv. Funct. Mater.* **25**, 6527–6537 (2015).

110. Tian, Q. *et al.* Sub-10 nm Fe3O4@Cu2-xS core-shell nanoparticles for dual-modal imaging and photothermal therapy. *J. Am. Chem. Soc.* **135**, 8571–8577 (2013).

111. Curcio, A. *et al.* Iron oxide nanoflowers @ cus hybrids for cancer tri-therapy: Interplay of photothermal therapy, magnetic hyperthermia and photodynamic therapy. *Theranostics* **9**, 1288–1302 (2019).

Chapter 1: ZnS nanoparticles as vectors for radioactive ^{64}Cu

1.1. Introduction

1.1.1. Application of radioisotopes in nuclear medicine

In the medical practice, radioisotopes can be used for two main applications: nuclear imaging and targeted radionuclide therapy (TRT). In both cases, an appropriate radioisotope is bound to a carrier that has the role to specifically bring the radioisotope to the tissue selected as target of the treatment or as area of interest for diagnosis. These pharmaceutical radiolabeled drugs are commonly referred to as radiopharmaceuticals.

Nuclear imaging techniques[1] rely on the fact that biomolecules inside the body are essentially not radioactive, consequently, any tissue in which radioactive atoms (i.e. radioisotopes) are present can have nearly infinite contrast with respect to neighboring tissues. This is a clear advantage if compared to other imaging techniques (e.g. CT) where the contrast is arising from the difference between the intensities of the signals that the tissues are providing[2]. One of the most common nuclear imaging techniques is positron emission tomography (PET)[3]. Positron emission tomography is performed using radioisotopes that are decaying through the emission of positrons (i.e. positive electrons, β^+). After being emitted (see Figure 1.1), these β^+ particles lose their energy while traveling through tissues (the range varies depending on the tissue and on the positron energy[4]). Once positrons have lost most or all of their kinetic energy, they are mutually annihilating with electrons and two γ-rays with energy of 0.511 MeV[5] are emitted.

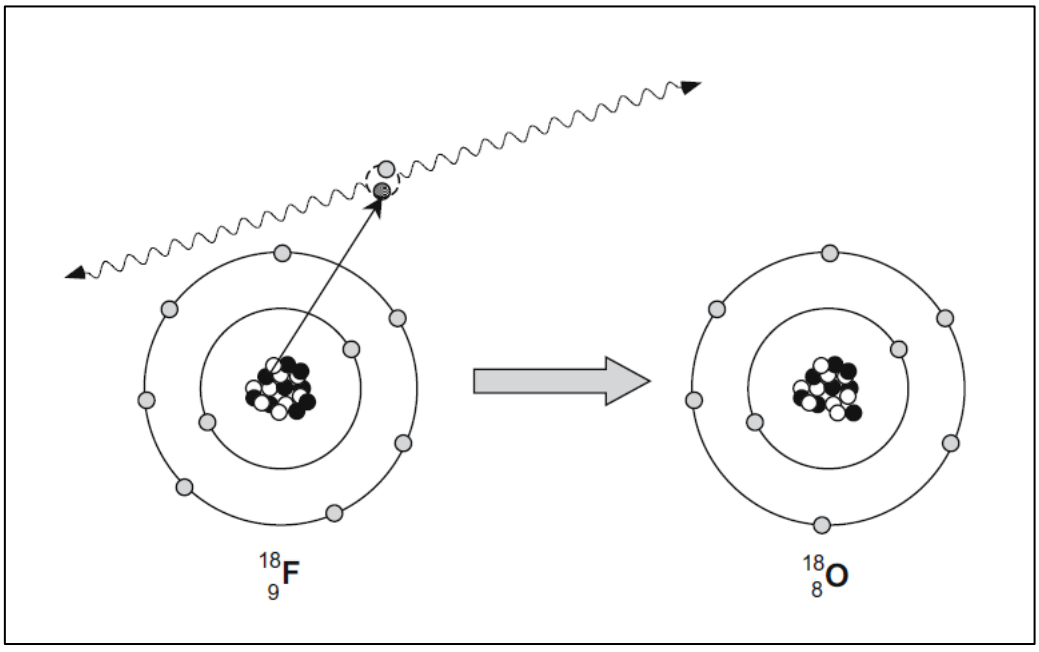

Figure 1.1: Scheme of Fluorine-18 (18F) positron emission and consequent annihilation. Reprinted with permission from reference 5.

These γ-rays couples, that are emitted in opposite direction (approximately with a 180° angle), are then detected through a ring of detectors placed around the patient, the signals are then processed and the PET image generated (see, as reference, PET imaging study performed on brains of patients with different neurodegenerative diseases shown in figure 1.2)[6]

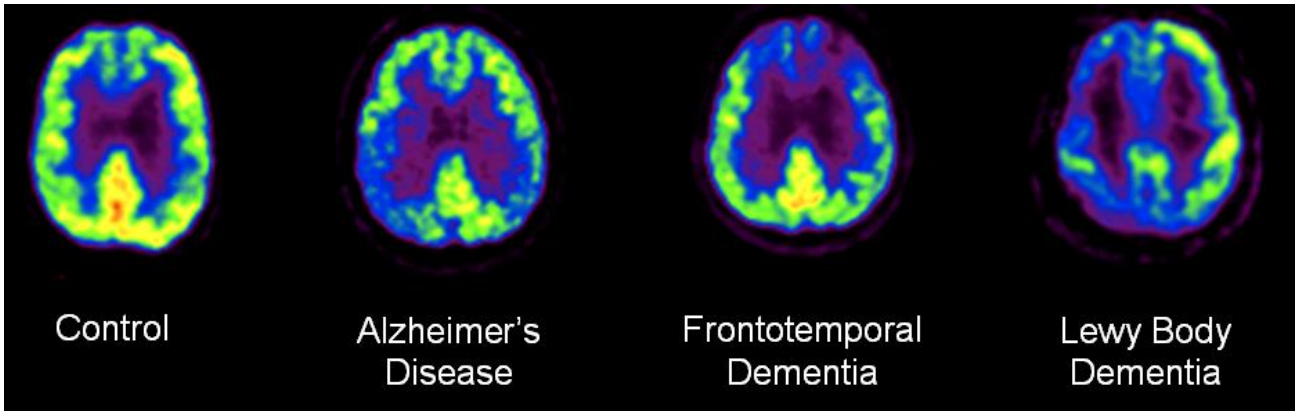

Figure 1.2: ^{18}F-Fluorodeoxyglucose PET detecting common neurodegenerative diseases. These axial images were obtained from the Austin Hospital Nuclear Medicine Department, Australia. Reprinted, with permission, from reference 6.

External beam radiation therapy, is widely used in clinical practice: approximately 50% of cancer patient undergo radiation therapy treatments and 40 % of the curative treatments are involving its use[7]. The working principle of radiation therapy[8] is the emission of a ionizing radiation. This radiation is then damaging DNA triggering cell death. The damage to DNA could be obtained following two different pathways (see Figure 1.3). In the first case, the so-called "direct damage", the ionizing radiation is directly hitting DNA helix causing breaks. In the second case, DNA breaks are caused by free radicals or reactive oxygen species (ROS) that are generated by the interaction between the ionizing radiation and water molecules.

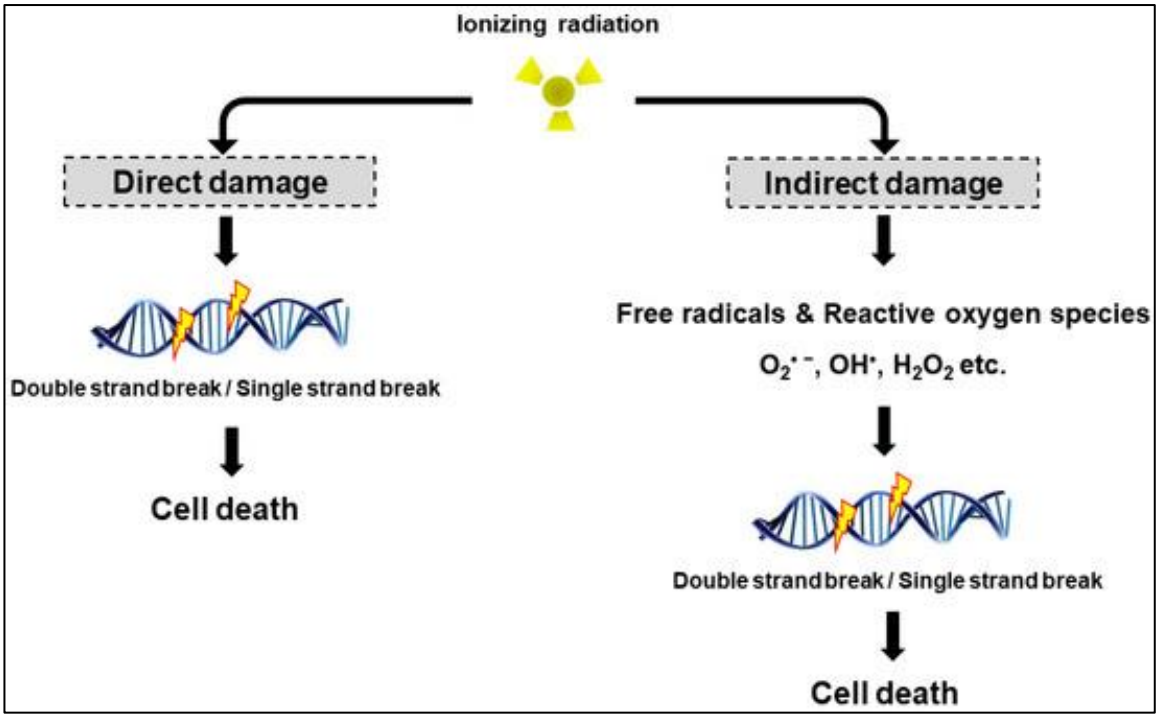

Figure 1.3: Direct and indirect DNA damage caused by an ionizing radiation. Reprinted with permission from reference 8.

Targeted radionuclide therapy[9–12] is a radiation therapy treatment performed using radiopharmaceuticals to deliver therapeutic radiation to targets inside the body. Main important advantage of targeted radionuclide therapy, when compared to standardly used external beam therapy, is its selectivity, allowing to ideally affect mainly cancer cells, reducing the unspecific damage to healthy tissues.[13]

1.1.2. Commonly used radionuclides in PET and in TRT

In order to be used as tracer in positron emission tomography, a radionuclide has to decay through the emission of β^+ with low energy, this permitting to achieve good spatial resolution. Indeed, a low energy of the positron guarantee a short path of the particle before annihilating with an electron and emitting the two 0.511 MeV γ-rays. Another important parameter, that has to be considered when developing a radiopharmaceutical as tracer for PET, is the possibility to have a radioisotope half-life matching with the blood circulation time of the targeting unit used. Consequently, the clearance of the radiopharmaceutical is important too, since it has to be slow enough for the radiopharmaceutical to be able to reach the target but should also be fast enough in order to avoid long and unspecific exposure of healthy tissues to radiation. All of these parameters have to be considered, depending on the target tissue and on the radionuclide carrier, when choosing a radioisotope for the use as tracer in PET. ^{18}F is ubiquitously used with this intention[14–16] for its low energy (0.6 MeV) positron emitted with high branching ratio (97 %, $t_{1/2}$ =110 min). Other non-metallic radioisotopes, used due their ease of being incorporated in biomolecules, are ^{11}C (99.8 %, 1 MeV, $t_{1/2}$ = 20.4 min)[17], ^{15}O (mainly used as water, 100 %, 1,7 MeV, $t_{1/2}$ = 2 min)[18] and ^{13}N(used as ammonia, 100 %, 1.2 MeV, $t_{1/2}$ = 10 min).[19] However, all of these radionuclides have short half-life that require the presence of an on-site radioisotope production and radiolabeling facility. This limit their usage to the monitoring of short length biochemical processes. In order to be able to overcome these limitations, radiometals, having longer half-lives than non-metals, were extensively studied[20,21] in last decades. Different radioactive metals such as ^{89}Zr (22.7 %, 0.396 MeV, $t_{1/2}$ = 78.4 hours)[22], ^{68}Ga (87.7 %, 0.84 MeV, $t_{1/2}$=1.03 hours)[23], ^{86}Y (11.9 %, 0.53 MeV, $t_{1/2}$ = 14.7 hours)[24] and ^{64}Cu (17.4 %, 0.655 MeV, $t_{1/2}$ = 12.7 hours)[25] are commonly used with this purpose.

A large variety of radioisotopes, with different type of emission and half-lives, is used in targeted radionuclide therapy. Three different kinds of emission are of interest for radioisotopes used in therapy: α emission, β^- emission and Auger or conversion electron emission. These particles differ for their different linear energy transfer value (LET, keV/µm). This value indicates the energy transferred by the particles in ionization events per unit of path length. LET values for α particles, β^- particles and Auger or conversion electron emission are of ≈ 80 keV/ µm, 0.2-2 keV/µm and 4 - 26 keV/µm respectively. Another important parameter that have to be considered is the penetration length of the radiation in the target tissue: while β^- particles can travel for few mm in tissue, the ranges of α particles and Auger electron are respectively reduced to 40-100 µm and below 5 µm. Consequently, the type and the extension of the tumoral mass that have to be treated dictate the choice of a radionuclide for therapy. One of the most used β^- emitters in targeted radiotherapy is ^{131}I, proposed already in 1942[26] for the treatment of hyperthyroidism with the advantage of being naturally incorporated in thyroid without the use of a carrier being necessary. Similarly, other radioisotopes such as α-emitter ^{223}Ra or β^- emitting ^{89}Sr are spontaneously accumulated in bone tissue and used for the radio treatment of bone metastases.[27,28] Two other β^- emitters commonly

employed in targeted radionuclide therapy are ^{90}Y and ^{177}Lu, respectively used for hepatocellular carcinoma[29] and prostate cancer.[30]

Among all the radiometals used in PET imaging and TRT of particular interest is ^{64}Cu for its desirable relatively long half-life (12.7 h) and for the possibility to be used in theragnostic applications. Indeed, together with positron emission (17 % 0.655 MeV) suitable for PET imaging, ^{64}Cu is decaying also through β^- emission (39 %, 0.573 MeV) and electron capture (44 %) that can be exploited in targeted radionuclide therapy. Another important advantage of ^{64}Cu is that it is currently produced in many cyclotron facilities on a routine basis,[31–33] making it an ideal candidate for the production of radio-therapeutic agents.[34–36]

1.1.3. Nanoparticles as carriers for ^{64}Cu in TRT and PET

Most common carriers used in order to deliver ^{64}Cu to the target tissues are peptides[37,38] or immunoglobulins and antibodies.[39] Recently, great interest was shown[40–42] towards the use of functionalized nanoparticles as radionuclide carriers. The use of nanoparticles as carriers for the radioisotopes in radiopharmaceuticals has many advantages such as the possibility to tune clearance length and pathways by changing their composition and size and the possibility to increase target specificity by nanoparticle's surface functionalization. Another important advantage of using nanoparticles as carriers for radioisotopes, is the possibility to attach chemotherapeutic drugs to the particle's surface (in order to combine TRT and PET with chemotherapy)[43] and to exploit the physical and chemical properties of the nanoparticle for other cancer treatments such as magnetic hyperthermia (MHT), photothermal therapy (PTT) or photodynamic therapy (PTT) and diagnosis techniques such as computer tomography (CT) or magnetic resonance imaging (MRI)[44,45]. Most used strategy in order to radiolabel with ^{64}Cu different nanocrystals is the use of suitable metal chelators anchored to the surface of the nanoparticles. Following this path, metal[46], quantum dots[47] and magnetic nanoparticles[48] were successfully radiolabelled with ^{64}Cu. However, issues related to the leakage of the radioisotopes from the nanoparticle associated chelators were initially reported.[49,50] To overcome this issue, new generation chelators, with improved stability, have been developed[51]. Recently, new approaches for the incorporation of radioactive ions in nanocrystals were reported. Zhou et al[52] in 2010 reported the synthesis of ^{64}CuS nanocrystals using a mixture of "hot" (radioactive) and "cold" (non-radioactive) $CuCl_2$ while Sun et al[53] in 2014 reported the feasibility of a cation exchange reaction performed at 60°C in organic solvent in order to introduce radioactive ^{64}Cu in pre-synthesized CdSe/ZnS quantum dots. Main limitation of these procedures is the fact that the radioactive nuclide is introduced at an early stage of the material preparation pathway. This causes two drawbacks: first, the presence of complicated chemistry facilities as well as specialist radiochemists inside the hospitals are required and second, the exposure of operators to radiations can be high in case further functionalization, such as attachment of target biomolecules or phase transfer, in the case of ^{64}Cu added in organic phase, is needed. For this reason the possibility of radiolabelling nanocrystals with ^{64}Cu as last step of the material production and functionalization pipeline with simple and fast water phase intercalation reaction was investigated by researchers from the group in which this research activity was carried out.[54] By means of intercalation reactions in aqueous solution it has been possible to successfully radiolabel CuS covellite nanocrystals with excellent results. Following this previous study, new chalcogenides nanomaterials for the quantitative radiolabelling with ^{64}Cu were synthesized and water transferred and, finally,

radiolabelling trials were performed on their stable aqueous dispersion. Results related to synthesis, water transfer and radiolabelling of zinc sulfide nanoparticles are reported in this chapter. Radiolabeling experiments were carried out in collaboration with Dr. Tommaso Avellini.

1.2. Results and discussion

1.2.1. Synthesis of ZnS nanoparticles

Zinc sulfide nanoparticles were synthesized following the procedure reported by Joo et al.[55] with minor modifications. Briefly, $ZnCl_2$ was dissolved in oleyl amine (OA) with tri octyl phosphine oxide (TOPO) and degassed at 120°C. Then, a previously degassed solution of sulfur powder (with sulfur content tuned in order to have Zn:S ratio = 1 : 3) was injected, and the temperature increased to 290°C. After 60 minutes of annealing, the reaction mixture was cooled to room temperature and the formed nanoparticles separated from reaction mixture by means of centrifuge washings. Particles' dispersion is extremely stable (up to years) after addition of a minor amount of oleyl amine (usually 1 mL of OA is added to 20 mL of particles' dispersion in hexane). TEM analyses (see Figure 1.4), indicated that particles obtained following this route have a quasi-spherical shape with typical average diameter of 9 nm ± 1 nm and a narrow size distribution.

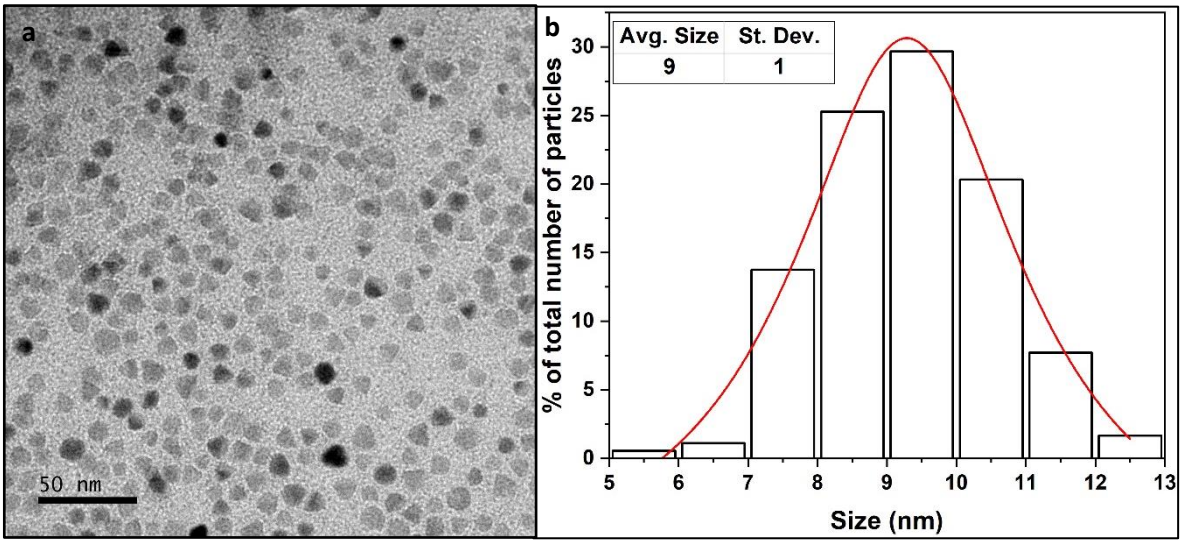

Figure 1.4: a) Representative TEM picture of as synthesized Sulfide NPS b) related size dispersion graph.

Crystalline phase of the as synthesized ZnS nanoparticles was also investigated through XRD analyses (Figure 1.5).

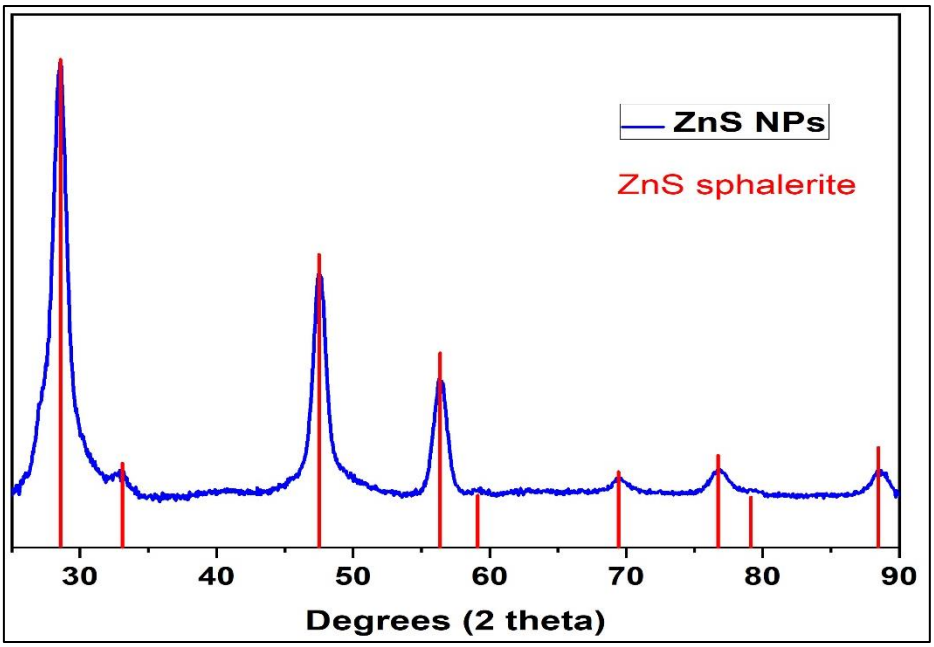

Figure 1.5: Experimental XRD pattern obtained from as synthesized ZnS nanoparticles compared with expected reflections for cubic Sphalerite ZnS (ICSD card n° 77082).

All the Bragg peaks found in the Experimental X-Ray diffraction pattern obtained from the ZnS NPs are perfectly matching the expected ones for ZnS with a Sphalerite cubic structure (ICSD card n° 77082). Through ICP-OES analyses, Zn:S ratio was found to be 1:1 for all the particles synthesized, furtherly confirming the composition of the obtained particles.

1.2.2. Water transfer of ZnS nanoparticles

Any inorganic nanoparticle which purpose is to be used in biomedical applications, has to be stable in aqueous media without forming aggregates or losing its properties. Since most of the particles are synthesized by colloidal synthesis methods and have ligands stabilizing them in organic solvents (usually chloroform, hexane or toluene), procedures to reproducibly phase transfer in water nanoparticles are continuously developed. These procedures, relying on the use of amphiphilic ligands, differ depending on many parameters such as the starting dispersion solvent, the chemistry of nanoparticles' surface and the procedure used to add the new amphiphilic ligands (by substituting the previous ligands or by intercalation between amphiphilic and hydrophobic ligands). All of these parameters are determining the particles' stability in aqueous media. In the case of ZnS sulfide, a ligands exchange procedure was used, substituting the hydrophobic ligands, stabilizing the particles in organic solvent (tri octyl phosphine oxide and oleyl amine), with a water-soluble polymer. As amphiphilic ligand, a multi-dentate ligand was preferred to a mono-dentate one in order to achieve better stability[56]. The chosen ligand, cysteamine-poly-(isobutylene-*alt*-maleic anhydride)-polyethylene glycol, (CYS-PIMA-PEG2000, see Figure 1.6) is composed by a chain of poly isobutylene maleic anhydride (PIMA) coupled with cysteamine (CYS) units as anchoring groups for the NC surface and with methoxy-poly-(ethylene glycol)-amine (CH_3O-PEG2000-NH_2) molecules as water soluble units. The synthesis of this polymer was achieved adapting a reported procedure (see experimental section)[57].

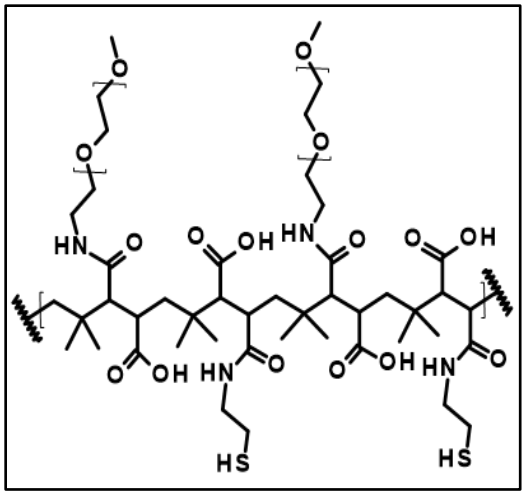

Figure 1.6: Chemical structure of CYS-PIMA-PEG2000

A key parameter in order to develop and standardize a procedure of nanocrystals water transfer is the ratio between the number of molecules of amphiphilic ligands used and the surface of particles that has to be covered with those ligands (ligands/nm^2 ratio). To obtain this data is necessary to calculate the number of ZnS nanoparticles contained in the volume of solution that has to be transferred to water (in the case of these water transfer procedures it was typically 100 µl). First step of this calculation was to determine the volume of each particle starting from the average spheres' diameter obtained from TEM analyses. Then, the calculated average volume of the particles is divided by the unit cell volume (obtained through XRD analyses) and multiplied by the number of unit formula per cell (Z =4 in ZnS ICSD n° =77082) and by the stoichiometric coefficient of the target element (ν= 1 for Zn in ZnS) in order to obtain the number of target element (Zn) atoms per particle. This number was then divided by Avogadro number (N_A) in order to obtain the number of moles of Zn (N_{Zn} in equation 1.1) per particle.

$$N_{Zn} = \frac{\frac{V_{particle}}{V_{unit\ cell}} \times (Z \times \nu)}{N_A} \left[\frac{\frac{\frac{nm^3}{particle}}{\frac{nm^3}{Unit\ cell}} \times (\frac{atoms}{unit\ cell})}{\frac{atoms}{mol}} \right] = \left[\frac{mol}{particle} \right]$$

Equation 1.1: Formula to calculate moles of target element atoms per particle.

Second step of these calculations was to multiply N_{Zn} by Zinc molecular weight (65.39 g/mol) obtaining the mass of Zinc contained in each particle. Dividing by this last value the Zinc concentration value for the sample ([Zn] in Equation 1.2), obtained through ICP analyses, the number of particles per liter ([ZnS] in Equation 1.2) was obtained.

$$[ZnS] = \frac{[Zn]}{N_{Zn} \times MW} \left[\frac{\frac{g}{l}}{\frac{mol}{particle} \times \frac{g}{mol}} \right] = \left[\frac{particle}{l} \right]$$

Equation 1.2: Formula for the calculation of the number of particles per liter.

Finally, through the volume of particles that were transferred, the sphere surface formula and the number of ligands used, the number of ligands per nanometer squared of particles' surface, ligands/nm^2 ratio can be obtained (see equation 1.3). The ratio used in the water transfer procedure for ZnS nanoparticles was calculated to be 67 ligands/nm^2.

$$Ligands/nm^2\ ratio = \frac{ligands}{V_{solution} \times S_{NPs} \times [ZnS]} \left[\frac{ligands}{l \times \frac{nm^2}{particle} \times \frac{particle}{l}} \right] = \left[\frac{ligand}{nm^2} \right]$$

Equation 1.3: Formula for the calculation of ligands/nm^2 ratio.

The procedure used for the water transfer of the particles relies on the mixing, by means of shaking at room temperature for 60 minutes, of particles' dispersion in chloroform mixed with a dimethyl sulfoxide (DMSO) solution of CYS-PIMA-PEG2000. Mixture is then precipitated using excess hexane and dispersed in Milli-Q water. Stable aqueous solution of particles is then purified from unreacted polymer through centrifuge washings in 30 kDa MWCO Amicon filter.

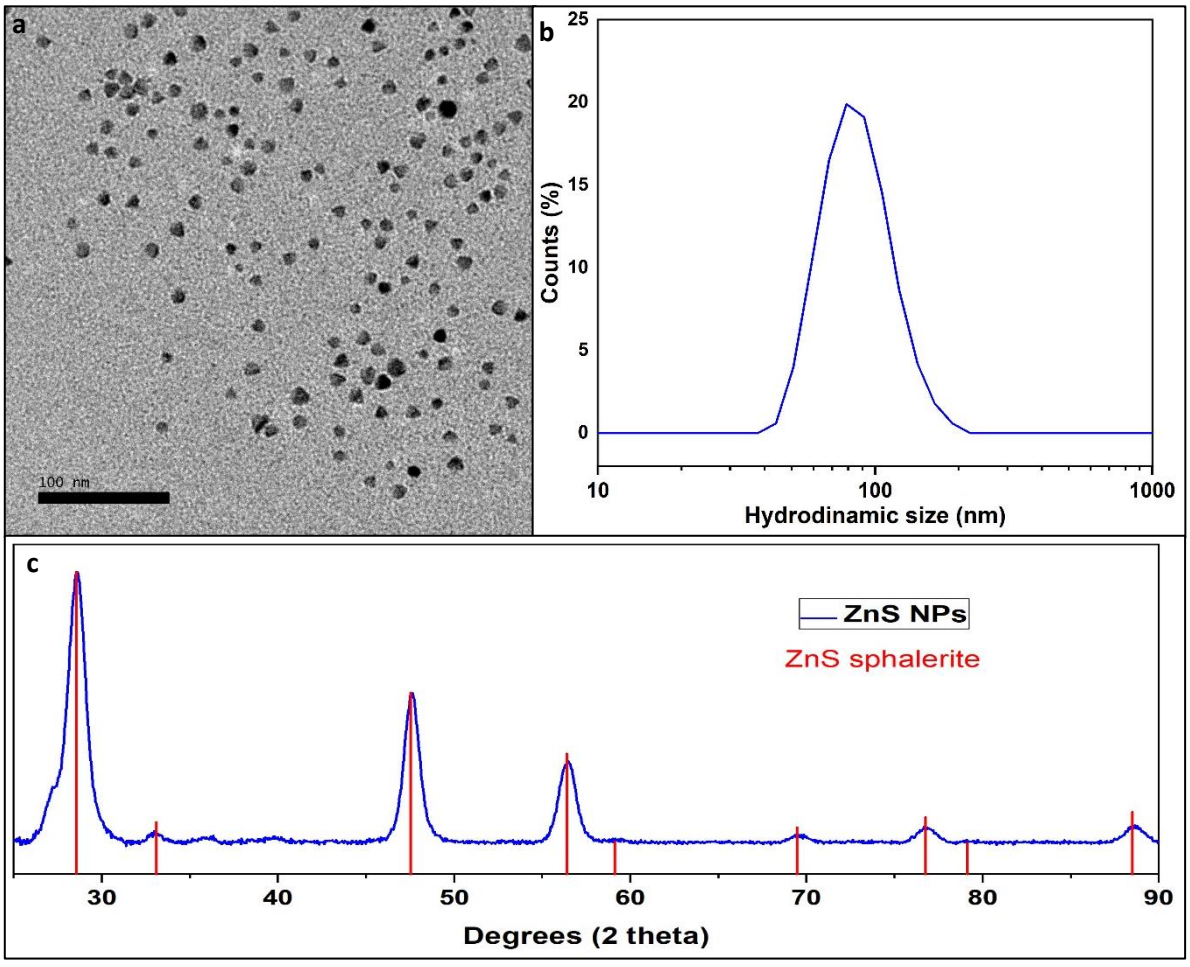

Figure 1.7: a) Representative TEM picture of the water stable CYS-PIMA-PEG2000 coated ZnS NPs; b) related DLS hydrodynamic size distribution graph by intensity; c) Experimental XRD pattern obtained from water stable ZnS nanoparticles in comparison with expected reflections for cubic Sphalerite ZnS (ICSD card n° 77082).

TEM analyses of the water stable particles (Figure 1.7a) show monodisperse particles with no appreciable change in shape or size with respect to organic-stable samples (Figure 1.4a). Hydrodynamic size distribution graph, measured though DLS (Figure 1.7b), shows a single peak,

centered at 80 nm. Although the value for hydrodynamic diameter of the particles is quite high if compared to the value of 9 nm ± 1 nm obtained by TEM, the absence of additional peaks and the representative TEM picture shown in Figure 1.7a clearly indicate the absence of particles' aggregates. XRD pattern obtained from the water stable sample shows all the expected peaks for sphalerite structure with no clear modification if compared with the one obtained from chloroform dispersed particles (Figure 1.5). All these data confirmed the excellent quality of the water transferred sample and, consequently, the possibility to use the ligand exchange procedure employing CYS-PIMA-PEG2000 for the phase transfer in water of ZnS quasi-spherical nanoparticles.

1.2.3. Cation exchange from ZnS to $Cu_{2-x}S$

In order to check the feasibility of the substitution of Zn (II) ions in ZnS nanoparticles with $^{64}Cu(I)$ ions, cation exchange experiments with non-radioactive copper ("cold" copper) were performed. Since ^{64}Cu used in the radiolabeling experiments was provided from cyclotron facility (Acom) as $^{64}Cu:CuCl_2$, also "cold" experiments were performed using $CuCl_2$ as copper source. In all the experiments, the molar ratio between $CuCl_2$ used and sulfur content in nanocrystals (S_{NCs}) was fixed in order to have $Cu_{used}:S_{NCs} = 1.8$. Reduction of Cu (II) to Cu(I) was obtained using the biocompatible mild reducing agent vitamin C (ascorbic acid, AA) in concentration equal to 5 equivalents of Cu (II) ions used in the reaction. After 60 minutes of incubation at 37°C, reaction mixture was purified, from released zinc ions and excess ascorbic acid, through centrifuge washings using a 0.5 mL 100 kDa MWCO Amicon filter, following the procedure shown in Figure 1.8. The fate of all the elements involved in the CE experiment (Cu^{2+}, Zn^{+} and S^{2-}) was traced by doing ICP-OES analyses on the final recovered solutions and on all the solutions resulting from Amicon washings.

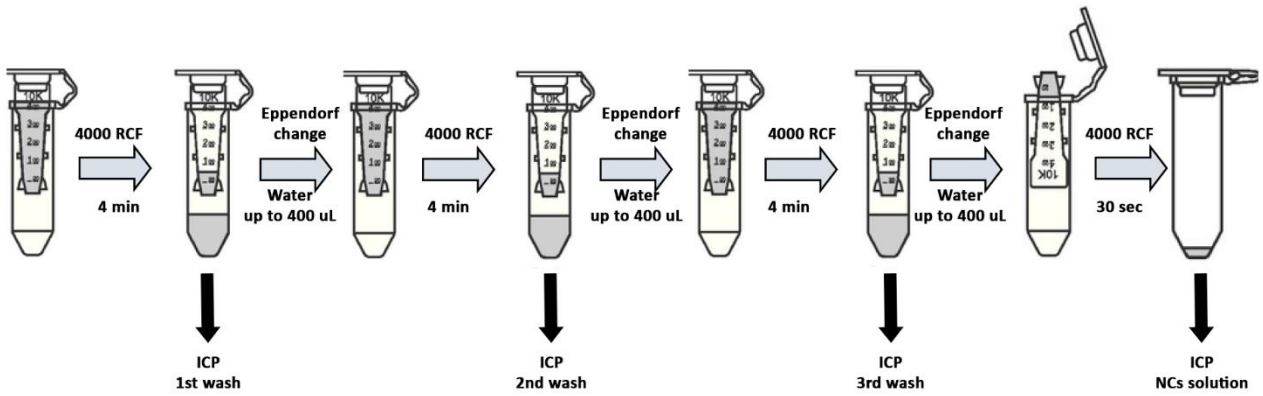

Figure 1.8: Scheme of the washing procedure used in order to purify exchanged ZnS NPs sample from released zinc ions and from excess ascorbic acid.

Results obtained from the ICP analyses performed on all the fractions are shown in Figure 1.9.

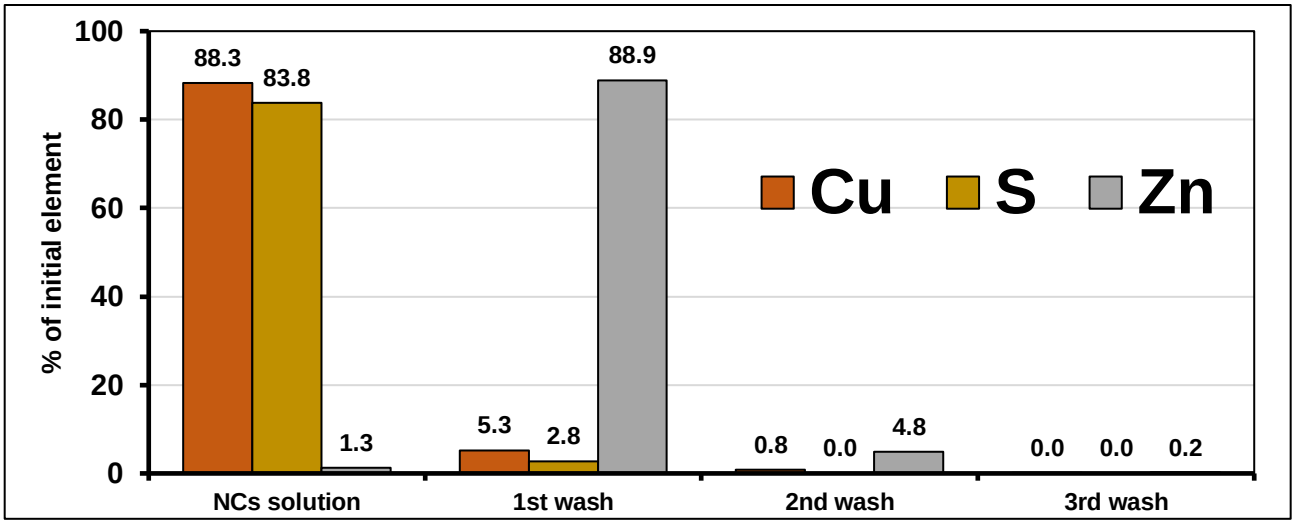

Figure 1.9: Results of ICP analyses performed on the different fractions obtained from Amicon washings of a ZnS NPs sample after 60 minutes incubation at room temperature with $CuCl_2$ (ratio $Cu_{used} : S_{NCs} = 1.8$) and ascorbic acid (ratio $AA : Cu_{used} = 5:1$). NCs solution indicates the fraction recovered at the end of the washings while 1st, 2nd and 3rd wash indicate the fraction recovered on the bottom of the Eppendorf vials after, respectively, 1st, 2nd and 3rd Amicon centrifugation.

Results shown in Figure 1.9 clearly indicate that almost 90 % of the copper is incorporated in the nanocrystals and that corresponding percentage of Zinc is eliminated from the nanocrystals solution already during the first washing. These results are showing not only the feasibility of the cation exchange reaction but also the possibility of the reaction byproduct ions (Zn^{2+}) to be almost completely washed away already with the first washing, making this reaction particularly interesting for clinical applications were a fast injection after the CE reaction and as few cleaning steps as possible would be required. Moreover, the loss of Cu^{2+} and S^{2-} ions in the nanocrystals' solution is low, and the percentages of these ions found in the washings (around 5 %) are in the range of ICP-OES analyses technique error. This last result asses the excellent stability of the ZnS particles in water, even after CE reaction and three centrifugation steps at 4000 RCF.

In order to furtherly confirm the exchange, XRD analyses were performed on exchanged sample. Experimental pattern obtained was compared with the ones obtained from fresh water transferred crystals and with reference database patterns (see Figure 1.10).

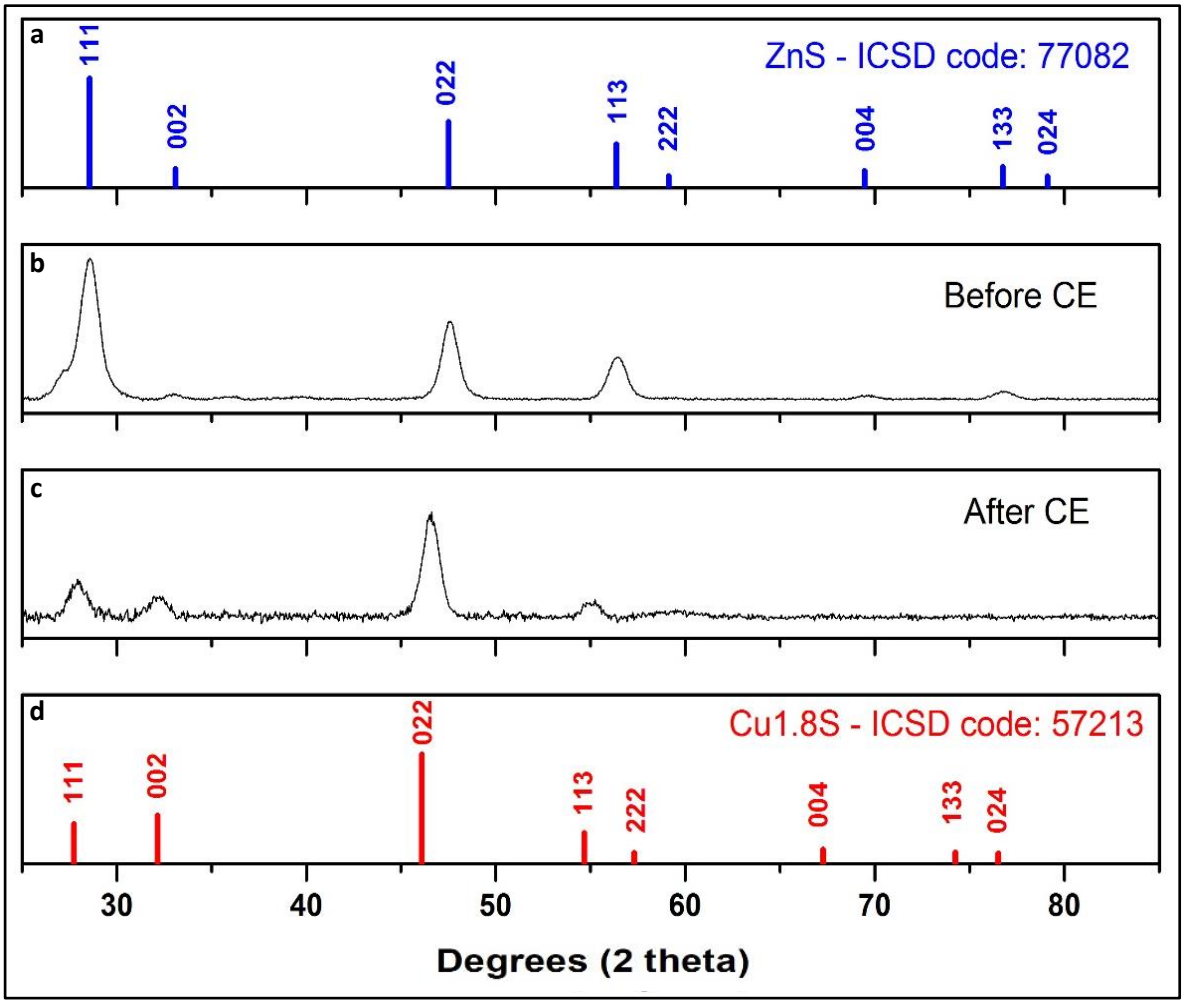

Figure 1.10: Experimental XRD pattern of a sample of ZnS nanoparticles before (b) and after (c) cation exchange reaction with Cu (Cu_{used} : S_{NCs} = 1.8), in comparison with expected reflections for cubic ZnS (a, ICSD code: 77082) and cubic $Cu_{1.8}S$ (d, ICSD code 57213).

After the cation exchange (see Figure 1.10c), main Bragg peaks that were found in the water stable sample are still present. However, all the Bragg peaks are shifted and with different relative intensities. In particular, all Bragg peaks are shifted towards lower angles (*e.g.* [022] peak moved from 47.5° to 46.1°) and, while in pattern acquired before CE reaction the peak with higher intensity was [111], after the reaction higher diffraction intensity is registered for [022]. This change in reflections position and in their relative intensity can be explained with the transformation of sphalerite ZnS structure (ICSD code 77082) into cubic $Cu_{1.8}S$ phase (ICSD code 57213). Bragg peaks in exchanged sample are broader if compared to the ones of the starting material. This could be due either to low crystallinity of the resulting particles or to the presence of few unreacted ZnS crystals.

1.2.4. Radiolabeling of ZnS nanoparticles with ^{64}Cu

In order to assess the possibility to use the produced water stable ZnS nanoparticles for the incorporation of ^{64}Cu (I) ions, the particles were tested in radiolabeling experiments similar to the ones previously used for ZnSe and $CuFeS_2$ nanoparticles (paper under submission).

The amount of activity used in any radiolabeling reaction was 18.5 MBq (0.500 mCi), in the range of the activities normally used in *in-vitro* and *in-vivo* studies[58,59]. Radioactive copper used (Acom) has

a specific activity of 140 GBq/µmol$_{Cu}$. First important value that had to be calculated was the amount of total copper corresponding to the activity used. Number of moles of total copper (Cu_{used}) employed in a radiolabeling reaction, with fixed amount of activity used and known specific activity, can be extrapolated from the formula reported in equation 1.4 where A_{MBq} is the activity used expressed in Mega Becquerel (decay×s^{-1}×10^{-6})

$$Cu_{used} = \frac{A_{MBq}}{Specific\ activity} * 10^{-9} \left[\frac{MBq}{\frac{GBq}{mol}}\right] = [mol]$$

Equation 1.4: Formula used for the calculation of total moles of copper used in radiolabeling reactions.

Another important parameter that has to be known in order to standardize radiolabeling reaction, is the number of moles of radioactive copper corresponding to the activity used (in our case 18.5 MBq). This value ($^{64}Cu_{used}$) is calculated following the formula reported in equation 1.5 where A_{Bq} is the activity used expressed in Becquerel (decay/s), N_A is Avogadro number (6.022×10^{23} mol^{-1}) and $t_{1/2}$ is the half-life of the radioisotope used ($t_{1/2}$(^{64}Cu) =12.7 h, 45720 s).

$$^{64}Cu_{used} = \frac{A_{Bq} * t_{\frac{1}{2}}}{N_A * \ln(2)} \left[\frac{s^{-1} * s}{mol^{-1}}\right] = [mol]$$

Equation 1.5: Formula used for the calculation of moles of radioactive copper (^{64}Cu) used in radiolabeling reactions.

Considering the activity used (18.5 MBq) in each experiment performed, the total amount of copper used, based on specific activity, was 1.32×10^{-10} moles, while the amount of radioactive copper used is 2.03×10^{-12} moles.

Most important parameter when evaluating the results of a radiolabeling reaction is the radiochemical yield (RCY): This is defined as the percentage of the total activity used in the reaction that is effectively incorporated in the nanocrystals. Radiochemical yield is a parameter of key importance when evaluating the results of a radiolabeling reaction for the translation to clinics. Indeed, if RCY of a radiolabeling reaction is high (≥90 %), meaning that majority of the ^{64}Cu introduced in the reaction is incorporated in nanocrystals, purification steps can be reduced or removed, decreasing the time between the labeling of the crystals and the injection to the patient and, consequently, reducing the manipulation time of the radioisotope and reducing the radioactivity in waste. RCY was evaluated through deposition of 1 µL of sample on instant Thin Layer Chromatography Silica Gel that is then run using 0.1 M EDTA (pH = 7.5) as mobile phase. Nanocrystals fraction is remaining in deposition spot while unbound copper migrates together with the eluent. In Figure 1.11 is shown the scheme of a TLC (Figure 1.11a) and the TLC obtained by a radiolabeling reaction with radiochemical yield of 25 % (Figure 1.11b) compared with the TLC obtained from a $^{64}Cu:CuCl_2$ solution (Figure 1.11c) as a reference.

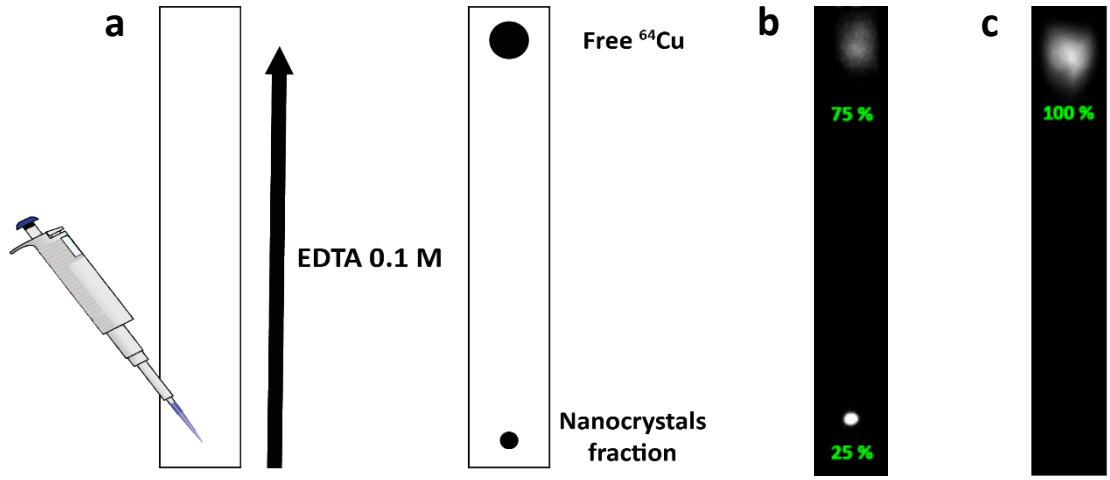

Figure 1.11: a) Schematic representation of the TLC used to calculate radiochemical yield; b) TLC obtained by a radiolabeling reaction with radiochemical yield of 25 %; c) reference TLC obtained by $^{64}Cu:CuCl_2$ solution.

The radiolabeling procedure for the ZnS NPs (see Figure 1.12 a) was performed by mixing in an Eppendorf vial an aqueous solution of $^{64}Cu:CuCl_2$ in HCl 0.1 N, corresponding to an activity of 18.5 MBq, with 150 µL of 0.3 M MES buffer. Then, if needed, pH of the solution was brought to a value around 6 by 2M NaOH addition. After obtaining the desired pH, ascorbic acid was added to reduce the ^{64}Cu (II) to ^{64}Cu (I). Finally, aqueous solution of the ZnS nanocrystals was added and the reaction mixture incubated at 37°C for 60 minutes. The amount of nanocrystal added was tuned in order to have the moles of radioactive ("hot") copper used (2.03×10^{-12}) equal to 0.2 % of the sulfur atoms in ZnS NPs.

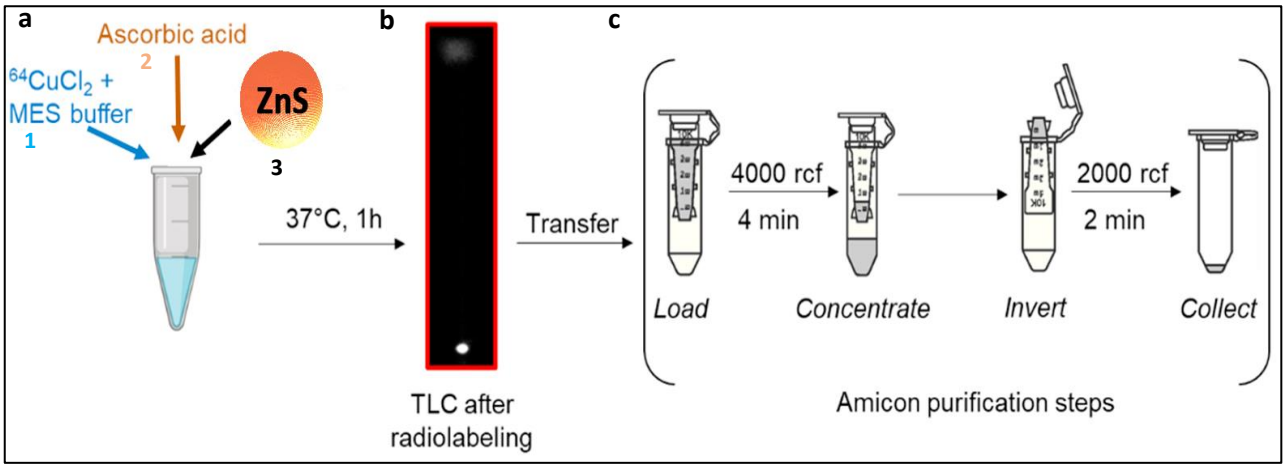

Figure 1.12: Scheme of the entire radiolabeling and purification procedure; a) addition of the reactants in the reaction vial; b) iTLC of the reaction product used to determine radiochemical yield (RCY); c) purification process by means of Amicon centrifugation.

Similarly to what was done in "cold experiments", in all the radiolabeling experiments performed, the washing and concentration of the radiolabeled nanocrystals was performed (see scheme in Figure 1.12c) through centrifugation in a 100 kDa MWCO Amicon tube at 4000 RCF for 4 minutes. Subsequently, in order to recover the nanocrystals solution, this first step was followed by nanocrystals' solution recovery obtained through inverting the Amicon tube cartridge in a new Eppendorf vial and centrifugation for 2 minutes at 2000 RCF. These conditions, needed to clean the particles from unreacted reagents and to reduce the volume of the final solution, could be quite

"stressing" for the particles and could result in their aggregation with consequent accumulation in the filter membrane. Also, if ^{64}Cu ions are not properly incorporated in the nanocrystal, the washing step could result in leakage of the radioactivity from the crystals. Consequently, the stability during the radiolabeling and the subsequent washing and concentration step was monitored by comparing the percentage of initial activity that was incorporated in the nanocrystals (RCY) to the one that was recovered at the end of the washing and concentration steps (purification yield, PY). To assess this value, activity of the samples after radiolabeling and of the recollected nanocrystals fraction were measured using a dose calibrator. Results (radiochemical yield and purification yield) obtained from the radiolabeling of ZnS nanoparticles are shown in Figure 1.13.

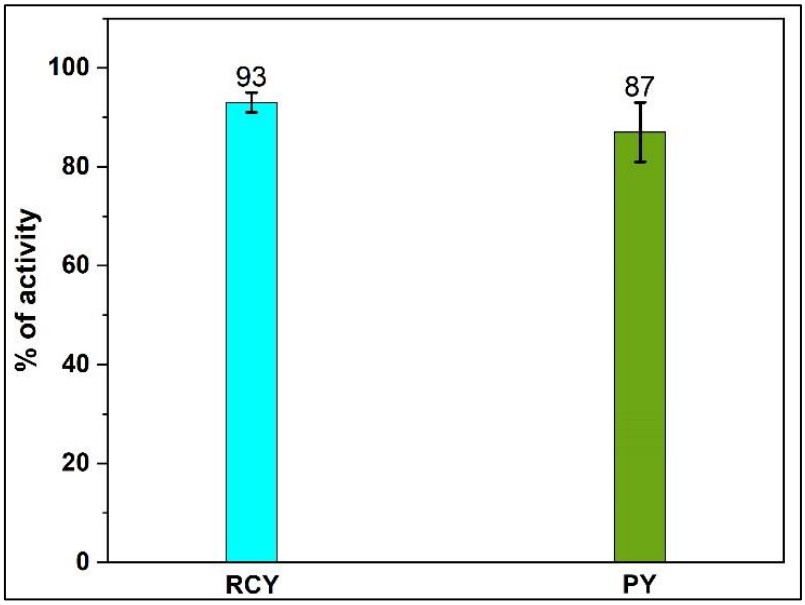

Figure 1.13: Radiochemical yield (RCY) and purification yield (PY) of radiolabeling experiments performed on ZnS NPs with ^{64}Cu:$CuCl_2$ (^{64}Cu (II) ions added in amount equivalent to 0.2 % of S atoms in nanocrystals)

Radiochemical yield of the radiolabeling reaction (light blue bar in Figure 1.13) is 93 % ± 2 meaning that only 7% of the used activity remained as free ^{64}Cu in solution. The amount of radioactive copper recovered in final nanocrystals solution after purification (PY, green bar in Figure 1.13) is 87 % ± 6 of the total activity measured after the radiolabeling reaction. This value is similar to the one obtained for the radiochemical yield, meaning that nearly all the radiolabeled nanocrystals were recovered and that only the free ^{64}Cu ions were lost during the purification, even if no additional stabilizing agents were added. These results show the possibility to use ZnS NPs as carriers for radioactive ^{64}Cu ions. The high radiochemical yield obtained demonstrate the possibility to use this water stable nanoparticles directly after radiolabeling since the amount of free ^{64}Cu in reaction mixture is negligible. In case a concentration and purification step is needed, ^{64}Cu:ZnS NPs can be easily washed through a fast washing procedure during which only a low amount of activity is lost.

1.3. Conclusions and outlook

ZnS nanoparticle were synthesized following a reported procedure with minor modifications. As synthesized particles have a quasi-spherical shape and a cubic sphalerite crystal structure. Average diameter of the as-synthesized particles is 9 nm ± 1 nm and upon addition of small amount of oleyl amine the hexane solution of the sample is perfectly stable.

In order to perform cation exchange experiments in aqueous media, ZnS NPs were phase transferred to water using a reproducible ligand exchange procedure. With this aim, multi-dentate cysteamine-poly-(isobutylene-*alt*-maleic anhydride)-polyethylene glycol amphiphilic ligands were used. Particles were transferred to water with no appreciable modification in properties (TEM size or crystal structure) and avoiding the formation of aggregates.

"Cold" (with non-radioactive copper) cation exchange reactions were performed on water stable ZnS NPs reproducing the conditions normally used in radiolabeling experiments. Quantitative exchange of Zn^{2+} ions to Cu^{+} ions has been achieved. Released Zn^{2+} ions are easily removed from nanoparticles' suspension already after one centrifugation step with Amicon filter.

Radiolabeling experiments, using an amount of ^{64}Cu ions equal to 0.2 % or the sulfur amount in nanocrystals were performed. Through 60 minutes incubation at 37°C of water stable ZnS nanoparticles with radioactive copper source ($^{64}CuCl_2$) and using biocompatible Vitamin C as mild reducing agent, quantitative (average radiochemical yield = 93%) radiolabeling has been achieved.

If needed, in order to remove exchanged zinc ions and excess ascorbic acid, fast (less than ten minutes) purification and concentration of the radiolabeled nanocrystals can be achieved through Amicon filter centrifugation. Only a small amount of activity is lost during this last process.

These results candidate ZnS nanoparticles, together with previously reported CuS nanocrystals,[54] as possible carrier of radioactive ^{64}Cu ions for PET and targeted radiotherapy applications. Moreover, in the case only radiotherapy is of interest as target application, also ^{67}Cu (100 % β^-, $t_{1/2}$=2.6 days, commonly used in targeted radiotherapy, especially in combination with immunotherapy,[60–62]) can be inserted in the developed ZnS nanoparticles.

In next chapter are discussed the different strategies investigated to merge these chalcogenide nanocrystals with highly performing in magnetic fluid hyperthermia iron oxide nanocubes[63] or Au@FeO_y dimers, [64] in order to fulfill the aim of this work.

1.4. Experimental procedures

Synthesis of zinc sulfide (ZnS) nanoparticles

ZnS particles were synthesized using the procedure reported by Joo et al.[55] with minor modifications 6 mmol of tri octyl phosphine oxide (TOPO) and 2 mmol of $ZnCl_2$ were mixed in 10 mL oleyl amine (OA). The reaction batch was then heated to 120°C and degassed under vacuum for 90 minutes. Meanwhile, a solution of 6 mmol S powder in 6 mL OA was degassed at 80°C for the same time. After switching both the reaction batches to inert atmosphere (N_2 gas), the sulfur powder solution was cooled to room temperature and then injected in the $ZnCl_2$ solution. The mixture was then heated to 290°C and annealed for 60 minutes before cooling. The resulting product was washed through centrifugation (2600 RCF 10 minutes) using hexane as solvent and ethanol as precipitant. At the end of the three washing steps, the sample was dispersed in 20 mL Hexane within glass vial and, after the addition of 1 ml of oleyl amine, the dispersion resulted perfectly stable.

Low-resolution Transmission Electron Miscopy (TEM) analyses

Shape and size of the produced samples were analyzed exploiting Low-resolution Transmission Electron Microscopy operating in Bright field mode. All the pictures were acquired using a JEOL JEM-1400Plus microscope operating at 120 kV and equipped with Gatan CCD camera Orius 830 (2048 x 2048 active pixels). Both chloroform stable and water stable samples were prepared for TEM analyses by drying a drop of the diluted particle suspension on 400 mesh ultra-thin carbon coated TEM copper grids. Particles' size distribution was evaluated through measurement of, when possible, at least 200 nanoparticles.

X-Ray Diffraction (XRD) analyses

Phase composition of all the samples synthesized was investigated employing X-Ray Diffraction analyses. XRD patterns were generally recorded on a PANalytical Empyrean X-ray diffractometer equipped with a 1.8kW Cu K_α ceramic X-ray tube, PIXcel3D 2x2 area detector and operated at 45 kV and 40 mA. The diffraction patterns were collected using Parallel- Beam (PB) geometry and symmetric reflection mode. On a set of selected samples, analyses were performed on a Rigaku Smart Lab diffractometer, equipped with a 9 kW Cu K_α rotating anode operating at 40 kV and 150 mA. The patterns were acquired in a Bragg-Brentano geometry over an angular range of 2θ = 25°-95°, using a D-teX Ultra 1D silicon strip detector set in X-ray fluorescence reduction mode. In both cases, samples were prepared by drop casting the concentrated NC solution onto a zero-diffraction silicon substrate. XRD patterns were elaborate and compared with reference patterns using Highscore 4.1 software by Panalytical.

CYS-PIMA-PEG synthesis

Synthesis of CYS-PIMA-PEG was performed reproducing a literature reported procedure[57] with some modifications. In a glass vial, 46 mg of poly-(isobutylene-alt-maleic anhydride) PIMA (MW 6000 g/mol, 7.7 µmol, 0.3 mmol of monomer units) were dispersed in 2.5 mL of DMSO. PIMA was dissolved under gently heating and then degassed by nitrogen bubbling for 10 min. Solution was heated up to 45 °C in an oil bath and then cysteamine hydrochloride (MW 113.61 g/mol, 17 mg,

0.15 mmol) dissolved in 1 mL of DMSO in presence of 21 µL of try-ethyl amine, was added dropwise. After 20 min a solution of CH_3O-PEG2000-NH_2 (MW 2000 g/mol, 0.15 mmol) dissolved in 1 mL of DMSO was added dropwise and mixture let react overnight. Solution was let to cool down at RT and stored at -20 °C for further use.

Phase transfer of zinc sulfide (ZnS) nanoparticles in water

For the standard phase transfer of 100 µl of ZnS NPs sample in water using CYS-PIMA-PEG2000, the procedure used was the standard one developed in our group for the transfer of chalcogenides nanocrystals with this polymer. Sample solution in chloroform was mixed with a dimethyl sulfoxide solution of polymer. The amount of polymer added was calculated in order to have a ligand/nm^2 ratio of 67. Chloroform was then added to the mixture up to a total of 4 ml. The mixture was then left at room temperature under shaking. After 60 minutes of reaction, hexane was added to the solution, and the vial was centrifuged (300 RCF, 5 minutes) in order to precipitate the particles. After centrifugation and supernatant removal, 4 ml of Milli-Q water were added to the vial that is then sonicated until complete dispersion of the particles. Filtration with a Regenerated Cellulose (RC) filter with 0.2 µm pores diameter followed. The solution was then cleaned from unreacted polymer through 3 cycles of centrifugation (450 RCF, 30 minutes) in pure Milli-Q water, using a 30 kDa MWCO 15 ml Amicon (Merck) filter. A typical final volume for the water-transferred sample was around 300 µl.

Dynamic Light Scattering (DLS) analyses of water dispersed nanoparticles

Water stable particles' aggregation state and hydrodynamic size distribution were evaluated using Dynamic Light Scattering measurements. Particles' hydrodynamic size distribution was measured using a Malvern Zeta Sizer operated in the 173° backscattered mode on a highly diluted aqueous solution. All measurements were performed at room temperature (20°C). Curves shown are resulting from averaging three curves obtained from 10 measurements each.

Cation exchange reaction with Cu^+ on zinc sulfide (ZnS) nanoparticles

Into a plastic Eppendorf vial, water suspension of ZnS nanoparticles, water solution of Cu^{2+} (containing 1.8 times the molar amount of S present in the nanocrystals) and a water solution of 0.1 M ascorbic acid (containing 5 times the moles of Cu^{2+} used), were mixed with water up to 300 µl. The mixture was reacted for 60 minutes at 37°C. The solution was then transferred into a 0.5 ml 100 kDa MWCO Amicon centrifuge filter and water was added up to 400 µl in order to dilute the sample. Three cycles of Amicon centrifugation (4000 RCF, 4 min) were performed in order to remove released zinc and the excess of ascorbic acid. All the washing fractions collected from the three centrifugation steps were measured through ICP-OES analyses. After the third washing, the filter containing radiolabeled nanocrystals was removed and inserted upside down in a new Eppendorf vial and centrifuged for 30 seconds at 4000 RCF and the collected NPS solution (30 – 35 µL) was analyzed through ICP-OES.

Elemental analyses through Inductively Coupled Plasma Optical Emission Spectrometry (ICP-OES)

Samples composition and elements ratio were evaluated through elemental analyses. Elemental analyses were performed using an Inductively Coupled Plasm- Optical Emission Spectroscopy (ICP-OES) instrument (Thermo Fisher, iCap 6000). Small volumes (5 µL - 25 µL) of particles suspension were digested in 1 mL of Aqua Regia in a volumetric flask. After one night of digestion at room temperature, flask was filled up with Milli-Q water and filtered through 0.2 µm PTFE membrane prior to the measurement.

Radiolabeling of ZnS nanoparticles

Into a plastic Eppendorf vial, a quantity of $^{64}Cu:CuCl_2$ corresponding to an activity of 18.5 MBq (0.500 mCi, 2.03×10^{-12} mol of ^{64}Cu, total copper 1.32×10^{-10} mol) and 150 µL of 0.3 M MES buffer (pH 5.6) were added. The pH of the solution was then brought to a value around 6 by 2 M NaOH addition, in amounts depending on the pH of the received $^{64}CuCl_2$ solution (typically, 6 µL of 2 M NaOH were used in order to adjust the pH of 35 µL of starting solution). Once the solution was brought to desired pH, 10 µL of ascorbic acid (0.1 M) were added as a reducing agent together with ZnS NPs aqueous solution, containing a number of sulfur moles equal to 7.7 times the moles of total Cu (II) used (1.02×10^{-9} moles of sulfur). Finally, the reaction mixture was incubated at 37°C for 60 minutes. After the incubation, 1 µL of the reaction mixture was spotted on instant Thin Layer Chromatography-Silica Gel (iTLC-SG) chromatography paper (Agilent technology) and the iTLC was developed in 0.1 M EDTA (pH = 7.5) as mobile phase. The dried ITLC plates were exposed on an Imaging Plate for 30s and the results were analyzed on an appropriate imaging system (FLA-9000, Perking Elmer) in order to measure radiochemical yields of the reactions. Each RCY average value and related error bar are resulting from at least three different experiments performed in the same experimental conditions.

Concentration and purification of the solution of radiolabeled nanocrystals

The washing and concentration of the nanocrystals after the radiolabeling procedure has been performed using 0.5 mL 100 kDa MWCO Amicon centrifugal filters (Merck). After the radiolabeling, the reaction mixture (approximatively 300 µL) was transferred to an Amicon filter inserted in an Eppendorf plastic vial and Milli-Q water added up to 500 µL. After 4 minutes of centrifugation at 4000 RCF, the filter containing radiolabeled nanocrystals was removed and inserted upside down in a new Eppendorf vial and centrifuged for 2 minutes at 2000 RCF. Through a dose calibrator (VDC-603, Comecer) the activity of the final nanocrystals' solution was measured and compared with the activity value obtained from the measurement of the reaction mixture after radiolabeling reaction in order to calculate the purification yield. Each purification yield average value and related error bar are resulting from at least three different experiments performed in the same experimental conditions.

1.5. References

1. Levi, H. George Hevesy and his concept of radioactive indicators-In retrospect. *Eur. J. Nucl. Med.* **1**, 3–10 (1976).

2. Rathmann, S. M. *et al. Radiopharmaceutical Chemistry*. *Radiopharmaceutical Chemistry* (Springer International Publishing, 2019). doi:10.1007/978-3-319-98947-1

3. Jones, T. The role of positron emission tomography within the spectrum of medical imaging. *Eur. J. Nucl. Med.* **23**, 207–211 (1996).

4. Alva-Sánchez, H., Quintana-Bautista, C., Martínez-Dávalos, A., Ávila-Rodríguez, M. A. & Rodríguez-Villafuerte, M. Positron range in tissue-equivalent materials: Experimental microPET studies. *Phys. Med. Biol.* **61**, 6307–6321 (2016).

5. Bailey, D. L., Karp, J. S. & Surti, S. Physics and Instrumentation in PET - Positron Emission Tomography: Basic Sciences. in *Positron Emission Tomography* 13–39 (Springer-Verlag, 2005). doi:10.1007/1-84628-007-9_2

6. Hughes, M. & MacEwan, T. Neuroimaging in dementia. *Psychiatr. Bull.* **29**, 233–233 (2005).

7. Baskar, R., Lee, K. A., Yeo, R. & Yeoh, K.-W. Cancer and Radiation Therapy: Current Advances and Future Directions. *Int. J. Med. Sci.* **9**, 193–199 (2012).

8. Hur, W. & Yoon, S. K. Molecular pathogenesis of radiation-induced cell toxicity in stem cells. *Int. J. Mol. Sci.* **18**, (2017).

9. Jhanwar, Y. S. & Divgi, C. Current status of therapy of solid tumors. *J. Nucl. Med.* **46**, 141–151 (2005).

10. Müller, C. *et al.* Terbium-161 for PSMA-targeted radionuclide therapy of prostate cancer. *Eur. J. Nucl. Med. Mol. Imaging* **46**, 1919–1930 (2019).

11. Kratochwil, C. *et al.* PSMA-targeted radionuclide therapy of metastatic castration-resistant prostate cancer with 177Lu-Labeled PSMA-617. *J. Nucl. Med.* **57**, 1170–1176 (2016).

12. Welsh, J. S., Kennedy, A. S. & Thomadsen, B. Selective internal radiation therapy (SIRT) for liver metastases secondary to colorectal adenocarcinoma. *Int. J. Radiat. Oncol. Biol. Phys.* **66**, 62–73 (2006).

13. Paes, F. M. Radionuclide Therapy. in *Cancer Metastasis - Biology and Treatment* **21**, 197–215 (2014).

14. Stokes, P. R. A. *et al.* Nature or nurture? determining the heritability of human striatal dopamine function: An [18F]-DOPA PET study. *Neuropsychopharmacology* **38**, 485–491 (2013).

15. Einat Even-Sapir, MD, PhD1, 2; Ur Metser, MD1, 2; Eyal Mishani, PhD3; Gennady Lievshitz, MD1; Hedva Lerman, M. & and Ilan Leibovitch, MD2, 4. The Detection of Bone Metastases in Patients with High-Risk Prostate Cancer : 99m Tc-MDP Planar. *J. Nucl. Med.* **47**, 287–297

(2006).

16. Fletcher, J. W. *et al.* Recommendations on the use of 18F-FDG PET in oncology. *J. Nucl. Med.* **49**, 480–508 (2008).

17. McCann, U. D. *et al.* Quantitative PET studies of the serotonin transporter in MDMA users and controls using [11C]McN5652 and [11C]DASB. *Neuropsychopharmacology* **30**, 1741–1750 (2005).

18. Hamdy, S. *et al.* Identification of the cerebral loci processing human swallowing with H215O PET activation. *J. Neurophysiol.* **81**, 1917–1926 (1999).

19. Fiechter, M. *et al.* Diagnostic value of 13N-ammonia myocardial perfusion PET: Added value of myocardial flow reserve. *J. Nucl. Med.* **53**, 1230–1234 (2012).

20. Ramogida, C. F. & Orvig, C. Tumour targeting with radiometals for diagnosis and therapy. *Chem. Commun.* **49**, 4720–4739 (2013).

21. Cutler, C. S., Hennkens, H. M., Sisay, N., Huclier-Markai, S. & Jurisson, S. S. Radiometals for combined imaging and therapy. *Chem. Rev.* **113**, 858–883 (2013).

22. Heskamp, S. *et al.* 89Zr-Immuno-Positron Emission Tomography in Oncology: State-of-the-Art 89Zr Radiochemistry. *Bioconjug. Chem.* **28**, 2211–2223 (2017).

23. Afshar-Oromieh, A. *et al.* Comparison of PET imaging with a 68Ga-labelled PSMA ligand and 18F-choline-based PET/CT for the diagnosis of recurrent prostate cancer. *Eur. J. Nucl. Med. Mol. Imaging* **41**, 11–20 (2014).

24. McDevitt, M. R. *et al.* PET imaging of soluble yttrium-86-labeled carbon nanotubes in mice. *PLoS One* **2**, (2007).

25. Anderson, C. J. *et al.* 64Cu-TETA-octreotide as a PET imaging agent for patients with neuroendocrine tumors. *J. Nucl. Med.* **42**, 213–221 (2001).

26. Dai, G., Levy, O. & Carrasco, N. Cloning and characterization of the thyroid iodide transporter. *Nature* **379**, 458–460 (1996).

27. Robinson, R. G., Preston, D. F., Schiefelbein, M. & Baxter, K. G. Strontium 89 Therapy for the Palliation of Pain Due to Osseous Metastases. *JAMA J. Am. Med. Assoc.* **274**, 420–424 (1995).

28. Pandit-Taskar, N., Larson, S. M. & Carrasquillo, J. A. Bone-seeking radiopharmaceuticals for treatment of osseous metastases, part 1: α therapy with 223Ra-dichloride. *J. Nucl. Med.* **55**, 268–274 (2014).

29. Kulik, L. M. *et al.* Safety and efficacy of 90Y radiotherapy for hepatocellular carcinoma with and without portal vein thrombosis. *Hepatology* **47**, 71–81 (2008).

30. Lantry, L. E. *et al.* 177Lu-AMBA: Synthesis and characterization of a selective177Lu-labeled GRP-R agonist for systemic radiotherapy of prostate cancer. *J. Nucl. Med.* **47**, 1144–1152 (2006).

31. McCarthy, D. W. *et al.* Efficient production of high specific activity 64Cu using a biomedical cyclotron. *Nucl. Med. Biol.* **24**, 35–43 (1997).

32. Monica, S. & Anderson, C. J. Molecular imaging of cancer with copper-64 radiopharmaceuticals and positron emission tomography (PET). *Acc. Chem. Res.* **42**, 832–841 (2009).

33. Matarrese, M. *et al.* Automated production of copper radioisotopes and preparation of high specific activity [64Cu]Cu-ATSM for PET studies. *Appl. Radiat. Isot.* **68**, 5–13 (2010).

34. Obata, A. *et al.* Basic characterization of 64Cu-ATSM as a radiotherapy agent. *Nucl. Med. Biol.* **32**, 21–28 (2005).

35. Yoshii, Y. *et al.* 64Cu-ATSM therapy targets regions with activated DNA repair and enrichment of CD133+ cells in an HT-29 tumor model: Sensitization with a nucleic acid antimetabolite. *Cancer Lett.* **376**, 74–82 (2016).

36. Yoshii, Y. *et al.* Multiple Administrations of 64Cu-ATSM as a Novel Therapeutic Option for Glioblastoma: a Translational Study Using Mice with Xenografts. *Transl. Oncol.* **11**, 24–30 (2018).

37. Wu, Y. *et al.* microPET imaging of glioma integrin αvβ3 expression using 64Cu-labeled tetrameric RGD peptide. *J. Nucl. Med.* **46**, 1707–1718 (2005).

38. Lewis, J. S. *et al.* Radiotherapy and dosimetry of 64Cu-TETA-Tyr3-octreotate in a somatostatin receptor-positive, tumor-bearing rat model. *Clin. Cancer Res.* **5**, 3608–16 (1999).

39. Cai, W. *et al.* Quantitative PET of EGFR expression in xenograft-bearing mice using 64Cu-labeled cetuximab, a chimeric anti-EGFR monoclonal antibody. *Eur. J. Nucl. Med. Mol. Imaging* **34**, 850–858 (2007).

40. Cho, Y. W. *et al.* In vivo tumor targeting and radionuclide imaging with self-assembled nanoparticles: Mechanisms, key factors, and their implications. *Biomaterials* **28**, 1236–1247 (2007).

41. Cao, J. *et al.* Preparation and radiolabeling of surface-modified magnetic nanoparticles with rhenium-188 for magnetic targeted radiotherapy. *J. Magn. Magn. Mater.* **277**, 165–174 (2004).

42. Ting, G., Chang, C.-H., Wang, H.-E. & Lee, T.-W. Nanotargeted Radionuclides for Cancer Nuclear Imaging and Internal Radiotherapy. *J. Biomed. Biotechnol.* **2010**, 1–17 (2010).

43. Yang, X. *et al.* CRGD-functionalized, DOX-conjugated, and 64Cu-labeled superparamagnetic iron oxide nanoparticles for targeted anticancer drug delivery and PET/MR imaging. *Biomaterials* **32**, 4151–4160 (2011).

44. Devaraj, N. K., Keliher, E. J., Thurber, G. M., Nahrendorf, M. & Weissleder, R. 18F labeled nanoparticles for in Vivo PET-CT imaging. *Bioconjug. Chem.* **20**, 397–401 (2009).

45. Yi, X. *et al.* Imaging-Guided Combined Photothermal and Radiotherapy to Treat Subcutaneous

and Metastatic Tumors Using Iodine-131-Doped Copper Sulfide Nanoparticles. *Adv. Funct. Mater.* **25**, 4689–4699 (2015).

46. Zhao, Y. *et al.* Copper-64-alloyed gold nanoparticles for cancer imaging: Improved radiolabel stability and diagnostic accuracy. *Angew. Chemie - Int. Ed.* **53**, 156–159 (2014).

47. Schipper, M. L. *et al.* MicroPET-based biodistribution of quantum dots in living mice. *J. Nucl. Med.* **48**, 1511–1518 (2007).

48. Glaus, C., Rossin, R., Welch, M. J. & Bao, G. In vivo evaluation of 64Cu-labeled magnetic nanoparticles as a dual-modality PET/MR imaging agent. *Bioconjug. Chem.* **21**, 715–722 (2010).

49. Kreyling, W. G. *et al.* In vivo integrity of polymer-coated gold nanoparticles. *Nat. Nanotechnol.* **10**, 619–23 (2015).

50. Bass, L. A., Wang, M., Welch, M. J. & Anderson, C. J. In vivo transchelation of copper-64 from TETA-octreotide to superoxide dismutase in rat liver. *Bioconjug. Chem.* **11**, 527–532 (2000).

51. Cai, Z. & Anderson, C. J. Chelators for copper radionuclides in positron emission tomography radiopharmaceuticals. *Journal of Labelled Compounds and Radiopharmaceuticals* **57**, 224–230 (2014).

52. Zhou, M. *et al.* A Chelator-Free Multifunctional [64 Cu]CuS Nanoparticle Platform for Simultaneous Micro-PET/CT Imaging and Photothermal Ablation Therapy. *J. Am. Chem. Soc.* **132**, 15351–15358 (2010).

53. Sun, X. *et al.* Self-illuminating 64Cu-Doped CdSe/ZnS nanocrystals for in vivo tumor imaging. *J. Am. Chem. Soc.* **136**, 1706–1709 (2014).

54. Riedinger, A. *et al.* Post-Synthesis Incorporation of 64Cu in CuS Nanocrystals to Radiolabel Photothermal Probes: A Feasible Approach for Clinics. *J. Am. Chem. Soc.* **137**, 15145–15151 (2015).

55. Joo, J. *et al.* Generalized and Facile Synthesis of Semiconducting Metal Sulfide Nanocrystals. *J. Am. Chem. Soc.* **125**, 11100–11105 (2003).

56. Zhang, H., Chen, J., Xiao, C., Tao, Y. & Wang, X. A Multifunctional Polypeptide via Ugi Reaction for Compact and Biocompatible Quantum Dots with Efficient Bioconjugation. *Bioconjug. Chem.* **29**, 1335–1343 (2018).

57. Wang, W., Ji, X., Kapur, A., Zhang, C. & Mattoussi, H. A Multifunctional Polymer Combining the Imidazole and Zwitterion Motifs as a Biocompatible Compact Coating for Quantum Dots. *J. Am. Chem. Soc.* **137**, 14158–14172 (2015).

58. Rossin, R., Muro, S., Welch, M. J., Muzykantov, V. R. & Schustery, D. P. In vivo imaging of 64 Cu-labeled polymer nanoparticles targeted to the lung endothelium. *J. Nucl. Med.* **49**, 103–111 (2008).

59. Lewis, J. S., McCarthy, D. W., McCarthy, T. J., Fujibayashi, Y. & Welch, M. J. Evaluation of 64Cu-

ATSM in vitro and in vivo in a hypoxic tumor model. *J. Nucl. Med.* **40**, 177–183 (1999).

60. Novak-Hofer, I. & Schubiger, P. A. Copper-67 as a therapeutic nuclide for radioimmunotherapy. *European Journal of Nuclear Medicine* **29**, 821–830 (2002).

61. Knogler, K. *et al.* Copper-67 Radioimmunotherapy and Growth Inhibition by Anti–L1-Cell Adhesion Molecule Monoclonal Antibodies in a Therapy Model of Ovarian Cancer Metastasis. *Clin. Cancer Res.* **13**, 603–611 (2007).

62. Desphande, S. V. *et al. Copper-67-labeled monoclonal antibody Lym-1, a potential radiopharmaceutical for cancer therapy: Labeling and biodistribution in RAJI tumored mice*. *Journal of Nuclear Medicine* **29**, (1988).

63. Guardia, P. *et al.* Water-Soluble Iron Oxide Nanocubes with High Values of Specific Absorption Rate for Cancer Cell Hyperthermia Treatment. *ACS Nano* **6**, 3080–3091 (2012).

64. Guardia, P. *et al.* Gold–iron oxide dimers for magnetic hyperthermia: the key role of chloride ions in the synthesis to boost the heating efficiency. *J. Mater. Chem. B* **5**, 4587–4594 (2017).

Chapter 2: Synthesis of multifunctional nano-heterostructures

2.1. Introduction

2.1.1. Janus nanoparticles: properties and parameters influencing their synthesis

Janus nanoparticles (JNPs), named after the double-faced Roman god, are compartmentalized particles with two sides having different chemical properties or polarity.[1] The great importance of such materials in merging different physical and chemical properties in one single nanostructure was already realized by Nobel laureate P. G. de Gennes in 1991.[2] From that year on, the synthesis of inorganic Janus NPs was further developed and optimized, increasing exponentially the number of reported procedures to obtain this kind of nanomaterial. [3–8] Several JPNs have been reported in literature, having shapes ranging from the spherical shape to disk, rod, hybrid or more complicated dumbbell or snowman shapes (see Figure 2.1). [8]

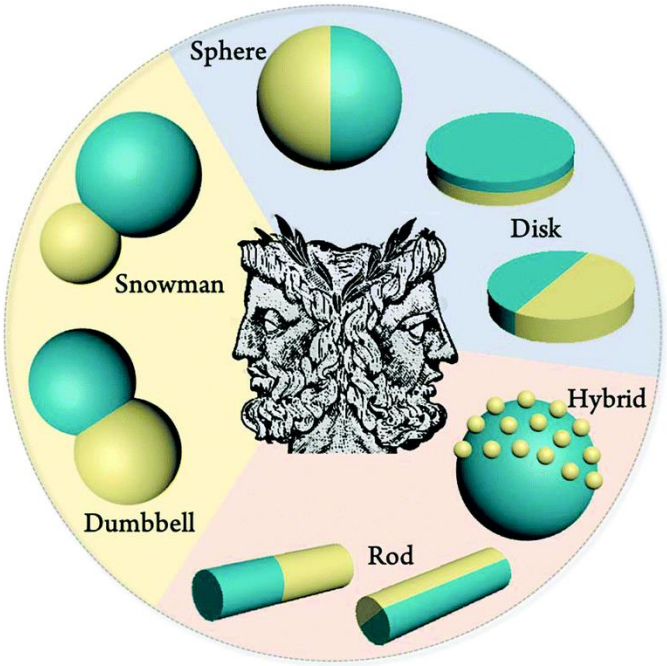

Figure 2.1: Schematic illustration of typical Janus nanostructures. Reproduced, with permission, from reference 8.

Depending on the shape and on the composition of the different heterostructures' domains, these materials have been demonstrated to be useful in many different applications, including catalysis,[9,10] micromotors,[11–13]displays[14,15] and biosensors.[16–18] Recently, the possibility to merge domains with completely different properties in one single nano-heterostructure and the opportunity to tune these properties have attracted the interest of researchers working in the development of nanomaterials for biomedical applications, who, in the last decade, have thoroughly studied the processes happening at the domains' interfaces and worked in the development of nanoparticles for cancer theragnostic.[19–21] Of particular interest for the scientific community is that these multiple-domain nano-heterostructures maintain the properties of each single domain and,

in addition, new properties can also arise from the presence of an interface between the different materials. As an example, gold nanoparticles have shown increased catalytic effect for CO after being attached to a metal oxide domain.[22] The presence of such additional properties in JNPs is commonly explained by junction effects, arising from the transfer of electrons from one domain to the other.[23] Apart from their shape, JNPs can also be categorized depending on the chemical nature of the domains composing the heterostructure: polymeric, inorganic, and polymeric-inorganic.[24] In last two decades, many efforts have been made in order to develop colloidal synthesis procedures for inorganic Janus nano-heterostructures, formed by two (or more) distinct domains permanently joint through chemical bonding interfaces (i.e., without any molecular bridges).[25] Most of those procedures rely on the growth of a second domain on the surface of a preformed nanoparticle. This mechanism is commonly referred to as "seeded growth" (or "seed mediated growth") being the starting preformed nanoparticles defined as "seeds". In order to obtain those two (or more) domains heterostructures,[26] it is critical to favor the heteronucleation of the second material on seeding NPs (against the homonucleation that is the formation of separate second material NPs surrounding the seeds).

In the classical nucleation theory,[27] thermodynamic energies that have to be taken into account for nucleation and growth are described by the excess Gibbs free energy (ΔG_r) of the system (shown in equation 2.1, where ΔG_S and ΔG_V are the free energy contributions from the surface and the bulk, respectively).

$$\Delta G_r = \Delta G_s + \Delta G_v$$

Equation 2.1: Total Gibbs free reaction energy dependence on ΔG_S (free energy contribution of the surface) and ΔG_v (free energy contribution of the bulk) during nanoparticles homogeneous nucleation.

While ΔG_V is influenced by the cubic radius of the forming nucleus, by the molar volume (V_m) of the material and by the normalized concentration of reaction species under equilibrium conditions (S), ΔG_s is influenced by the squared radius of the forming nucleus and by the surface free energy per unit area (γ). If ΔG_r is negative, nucleation is taking place. For heterogeneous nucleation on a seed, equation 2.1 becomes equation 2.2.

$$\Delta G_r = \Delta G_s + \Delta G_v + \Delta G_{inter}$$

Equation 2.2: Total Gibbs free reaction energy dependence on ΔG_S (Gibbs free energy contribution of the surface), ΔG_v (Gibbs free energy contribution of the bulk) and ΔG_{inter} (Gibbs free energy contribution of the solid/solid interface) during nanoparticles heterogeneous nucleation

The additional term (ΔG_{inter}) is related to the formation of a new solid/solid interface between the two materials, which depends on the interface's surface free energy per unit area (γ_{inter}) and on the surface of the interface (S_{inter}) (see equation 2.3).

$$\Delta G_{inter} = \gamma_{inter} * S_{inter}$$

Equation 2.3: Gibbs free energy contribution of the solid/solid interface dependence on γ_r (interface's surface free energy per unit area) and S_{inter} (surface of the interface).

Generally, heteronucleation is favored over homonucleation (heteronucleation energy barrier (ΔG_{het}) is lower than homogeneous nucleation one (ΔG_{hom})). However, depending on the interplay between many different parameters (lattice mismatch, surfactants, precursor concentration, reaction temperature, etc.) both homonucleation and heteronucleation can occur when attempting a seeded-growth nano-heterostructure synthesis.[28] A key parameter determining the morphology of the formed heterostructure is the lattice mismatch between the two materials.[29] When the lattice mismatch is low (usually within 1—3%) core-shell structures are formed (associated to high interface surface, S_{inter} in equation 2.3).[30] On the contrary, when lattice mismatch is high (associated to increased values of interface's surface free energy per unit area, γ_{inter} in equation 2.3), the surface of the interface is reduced, leading to dumbbell-like (or snowman-like) shaped heterostructures (non-centrosymmetric structures).[31] Interestingly, several studies reported that the interface strain, given by the lattice mismatch, can be reduced by the growth of amorphous domains[32] or amorphous shells, which can be then transformed into a crystalline domain by subsequent heating.[33]

2.1.2. Synthesis procedures for JNPs having an iron oxide and a chalcogenide domain

Among the wide amount of literature on JNPs, only few heterostructures composed by an iron oxide and a semiconductor domain are reported. In particular, the group of professor Moonsub Shim thoroughly studied the mechanism underlying the formation of iron oxide-chalcogenide heterostructures.[28] The synthesis they exploited was a one-pot (second domain is grown directly in the reaction mixture of the formed seeds) seeded-growth of CdS, ZnS and HgS on γ-Fe_2O_3 preformed seeds. The influence of many parameters, such as lattice mismatch and annealing time and temperature on the number of formed heterojunctions was investigated.[34] Also, they reported that, when the lattice mismatch is high, such as between iron oxide and chalcogenides NPs, a small size of the used seeds can help overcoming interfacial strain more effectively, thus helping the growth of a larger second domain.[35] This is of key importance in the case of the aimed heterostructures (comprising a magnetic domain exploitable in hyperthermia). Indeed, hyperthermia performances are strongly influenced by the size of the magnetic domain, having smaller iron oxide particles usually poor performances.[36] Few other procedures were reported in order to obtain either core-shell[37,38] or dumbbell like[39–43] γ-Fe_2O_3@MX (M = transition metal, X = chalcogen). However, when measured, their magnetic properties were not optimal and, consequently, these magnetic-chalcogenide domains JNPs were tested for MRI only.[44] In 2006, Weili Shi et. al.[45] reported another interesting approach for the synthesis of iron oxide-chalcogenide multi-domain heterostructures. Together with the synthesis of core-shell PbS@Fe_3O_4 they were also able to obtain Fe_3O_4@Au@PbS and Fe_3O_4@Au@PbSe heterostructures. These JNPs synthesis was achieved exploiting preformed Au@Fe_3O_4 dimers as seeds and growing PbS and PbSe on the surface of gold NPs. As in most of previously mentioned cases, the performances in biomedical application of these trimers were not investigated. However, the possibility of using gold NPs as "linkers" between the magnetic and the chalcogenide domains for JNPs exploitable in biomedical applications remains of high interest. Indeed, Au@Fe_3O_4 heterostructures have been widely reported in literature,[46–48] and among them, some, such as the ones developed by Pablo Guardia and other members of Teresa Pellegrino's research group, has shown outstanding efficiency when used in magnetic hyperthermia.[19,49] Also, gold nanoparticles (or other noble metal or noble metal alloys nanoparticles) have been reported to be used as seeds for the synthesis of Au@MX heterostructures,[50–54] thus making the use of gold

NPs as “linkers” between magnetic and chalcogenide domains an exploitable strategy in order to fulfill our aim.

In the following chapter, results obtained from the trials to merge in a single nano-heterostructures a magnetic nanoparticle or heterostructure, among the ones developed in this group, reported to be efficient in magnetic hyperthermia (iron oxide nanocubes[55,56] or gold-iron oxide dimers[19,49]) with a chalcogenide domain able to incorporate ^{64}Cu ions (such as previously reported CuS[57] or newly developed ZnS) are shown.

2.2. Results and discussion

2.2.1. Synthesis of γ-Fe_2O_3@ZnS heterostructures

First approach attempted in order to fulfill the aim of this project was to grow directly zinc sulfide domains on the surface of magnetic nanoparticles. A one-pot seeded growth synthesis for these heterostructures, using γ-Fe_2O_3 NPs as starting seeds, has already been reported in literature.[28] This reaction is based on the seeded growth of ZnS domains on in-situ preformed γ-Fe_2O_3 seeds. γ-Fe_2O_3 seeds are synthesized through thermal decomposition of $Fe(CO)_5$ in octyl ether (OE), in the presence of surfactant molecules (oleic acid, OLAC). ZnS domain was then grown by direct addition of precursors (zinc acetate and sulfur powder) and surfactants (tri octyl phosphine oxide, TOPO) to crude γ-Fe_2O_3 reaction mixture. The synthesis pot is then annealed at different temperatures (250°or 280°C) for different times (60 minutes or 180 minutes). Representative TEM pictures of the particles obtained reproducing this procedure are shown in Figure 2.2.

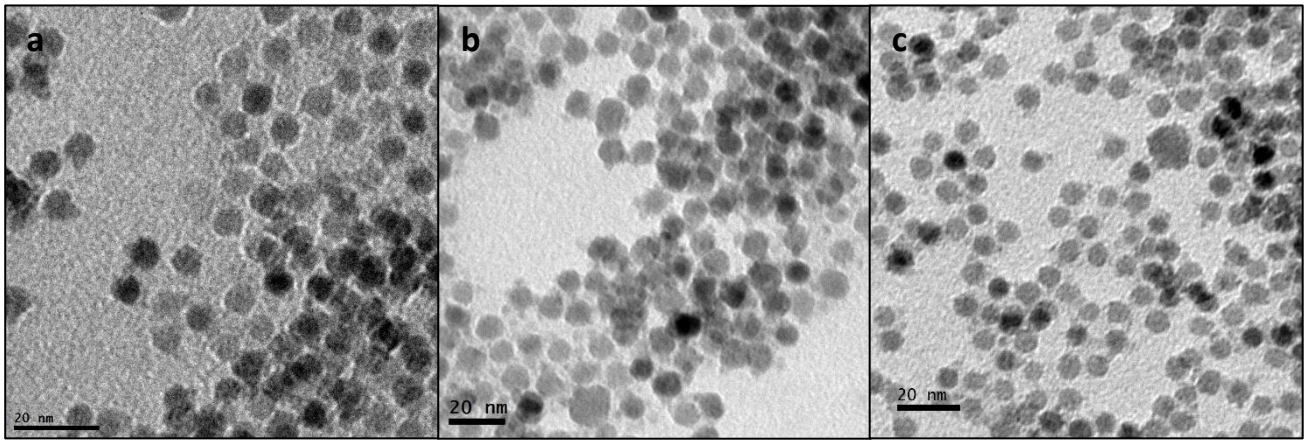

Figure 2.2: Representative TEM pictures of the obtained γ-Fe_2O_3@ZnS samples. Annealing temperature and time used in these syntheses are: a) 250°C, 60 minutes b) 280°C, 60 minutes c) 280°C, 180 minutes.

In accordance with reported data, for all the conditions tested (Figure 2.2a-c), the heterostructures obtained were composed of 6 - 8 nm average diameter size iron oxide nanoparticle cores decorated with few ZnS particles with an average diameter of about 1-2 nm. XRD analyses, shown in Figure 2.3, confirmed the precence of both low-cristallinity ZnS (only main ZnS sphalerite peak is detectable as a shoulder placed at 28° degress of the iron oxide Bragg peak at 30° degrees) and of γ-Fe_2O_3 domains (broad Bragg peaks corresponding to main γ-Fe_2O_3 reflections are present at 2θ = 30°, 35.6°, 43.4°, 57.3° and 62.8°).

Properties of the iron oxide domains exploited as seeds in this procedure were far different from the aimed ones in our research plan, having poor crystallinity and small size. This detail is of key importance since poor quality magnetic domains lead to a low heating efficiency,[36] severely compromising the final performances of γ-Fe_2O_3@ZnS heterostructures in magnetic hyperthermia.

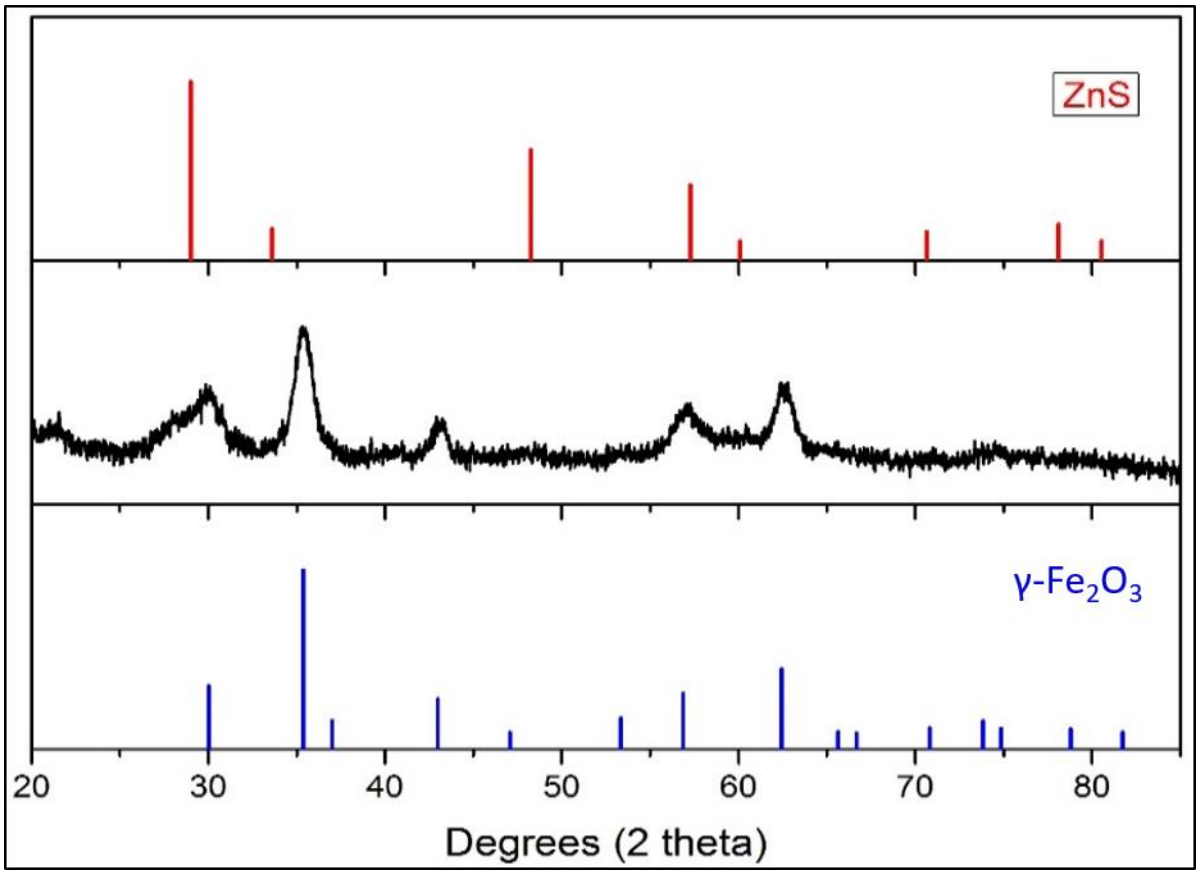

Figure 2.3: XRD pattern of the γ-Fe_2O_3@ZnS sample resulting from following literature procedure compared with expected reflection for sphalerite ZnS (ICSD code: 41985) and γ-Fe_2O_3 (ICSD code: 247035)

Consequently, this procedure to grow ZnS domains on top of iron oxide NPs had to be suitable modified in order to exploit as seeds the highly performing iron oxide nanocubes (IONCs) developed in our group.[55]

2.2.2. Synthesis of IONC@ZnS heterostructures

The procedure previously used for γ-Fe_2O_3@ZnS heterostructures was adapted to a two-steps approach, using pre-formed iron oxide nanocubes (IONCs) as seeds for the subsequent growth of ZnS domains. IONCs nanocubes of 16 ± 2 nm (see Figure 2.4a) were synthesized using standard procedure developed by our group, a thermal decomposition of iron (III) acetyl acetonate in a solvents mixture of di benzyl ether (DBE) and squalene, using decanoic acid as surfactant. Since the typical iron content of one IONCs sample produced in this synthesis is lower if compared to that of γ-Fe_2O_3 seeds synthesized in the original procedure, the mmol of iron used in the synthesis were scaled down by ten times (from 1.5 mmol used in the original synthesis to 0.15 mmol in the two-pot growth of ZnS on IONCs). Accordingly, zinc and sulfur precursors' amount was scaled down, keeping the same Fe:Zn:S ratio used in the original procedure (6:1:1:) while, initially, solvent and surfactants amount were kept the same. Figure 2.4b shows a representative TEM image of particles resulting from this first trial, using 60 minutes of annealing at 280°C.

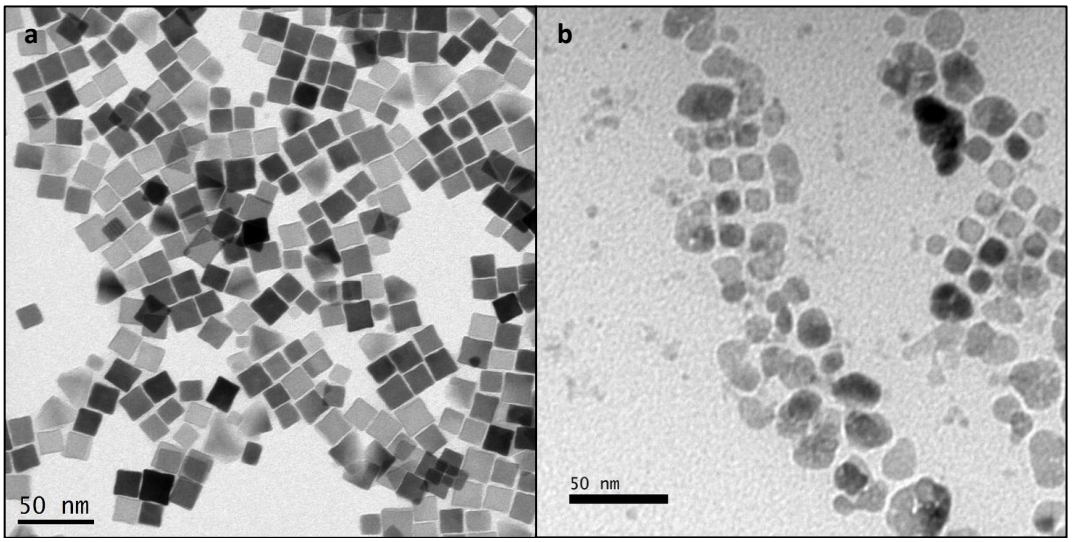

Figure 2.4: Representative TEM pictures of 16 ± 2 nm edge length IONC a) before and b) after the attempt of two-pot seeded growth of ZnS.

Figure 2.4b clearly shows that both the size and the well-defined cubic shape of the iron oxide nanocubes (see Figure 2.4a) have suffered a strong modification during the ZnS growth procedure, presenting smaller size and rounded shape, which indicated that IONCs underwent a decomposition process. In addition, it is unclear the successful nucleation of ZnS domains. To understand what was the cause of the decomposition of IONCs, a complete study on the influence of different parameters, such as the kind of solvent and the surfactant amounts was carried out. The influence of the solvent was investigated replacing OE with 1-Octadecene (ODE). The influence of the surfactants (OLAC or TOPO) was investigated removing either one or both of them in the reaction batch. All these trials were performed without adding any zinc of sulfur precursor and performing the annealing at 280°C for 60 minutes, as done in the first synthesis. For all the trials, the same batch of IONCs was used, in order to be able to separately study the influence of solvents and surfactant without any other difference in the procedures. Results obtained from these investigations are shown in Figure 2.5.

Solvent	OLAC only	TOPO only	No surfactants
OE	a	b	c
ODE	d	e	f

Figure 2.5: Representative TEM pictures obtained from investigations on different parameters causing cubes decomposition during an annealing at 280°C for 60 minutes. a) OE used as solvents and only OLAC used as surfactant, b) OE used as solvent and only TOPO used as surfactant, c) OE used as solvent and no surfactants, d) ODE used as solvents and only OLAC used as surfactant, e) ODE used as solvent and only TOPO used as surfactant, f) ODE used as solvent and no surfactants.

Solvents influence was evaluated from the trials done without adding any surfactants. Looking at pictures in Figure 2.5c (OE as solvent) and Figure 2.5f (ODE as solvent) can be seen how, although the influence is minimal, octyl ether seems to be a most suitable solvent for this procedure with respects to 1-octadecene, producing the latter one minimal aggregation of the IONCs. Regarding the surfactants, it is clear that both OLAC and TOPO are boosting cubes decomposition during the annealing. Oleic acid, in particular, is changing the shape and size of the nanocubes, producing either big cubes (up to 50 nm) surrounded by decomposed particles with OE (Figure 2.5a) or badly-shaped smaller particles with ODE (Figure 2.5d). TOPO is giving aggregation when used with OE (Figure 2.5b) while when ODE is used as solvent, it is causing also clear decomposition of the cubes. Interestingly it seemed that the effect of OLAC was amplified when OE was used as solvent (compare Figure 2.5a and 2.5d) while TOPO effect was prominent when ODE was used (compare Figure 2.5b and 2.5e). It is worth to mention that during this procedure TOPO is required, not only as surfactant for the forming ZnS NPs, but also, and most importantly, in order to allow the solubility of zinc precursor (zinc acetate) in OE. Consequently, TOPO could be scaled down with $Zn(Ac)_2$ amount but it could not be completely removed. Instead, OLAC was used to stabilize the forming γ-Fe_2O_3 seeds, so it could be removed from the procedure since the IONCs used as seeds are already covered with a surfactant, decanoic acid, and hence stable in solution after the centrifuge washings steps. Thus, in order to avoid IONCs decomposition during annealing, a new procedure was set up, scaling down the amount of TOPO used (by ten times, together with $Zn(Ac)_2$ amount) and completely removing OLAC from reaction mixture. Results of the syntheses performed with this optimized procedure are shown in Figure 2.6.

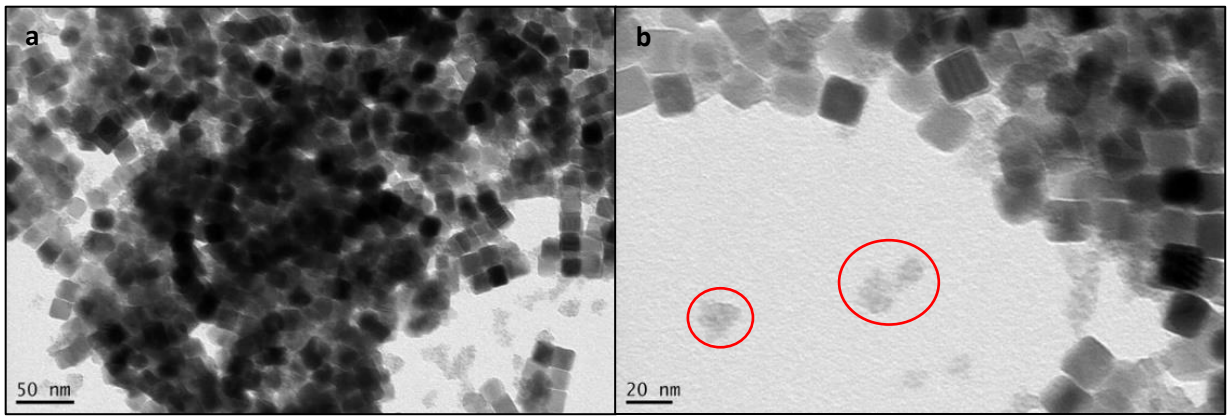

Figure 2.6: a) Representative TEM picture of a ZnS@IONCs sample synthesized with the optimized procedure, b) higher magnification particular with small particles aggregates highlighted.

As expected, although particles aggregation was observed, using the optimized parameters the IONCs are not decomposing. However, the nucleation of ZnS on the surface of IONCs and thus the formation of IONCs-ZnS heterostructures was not observed, although the presence of small (<5 nm) aggregates of nanoparticles surrounding the nanocubes (see red circles in figure 2.6b), likely due to the isolated nucleation of Zn compounds, is clear. In order to identify the composition of these small aggregates, scanning transition electron microscopy (STEM) imaging and energy dispersive X-ray spectroscopy (EDS) elemental mapping were performed on one of these samples. Results obtained from these analyses are shown in Figure 2.7.

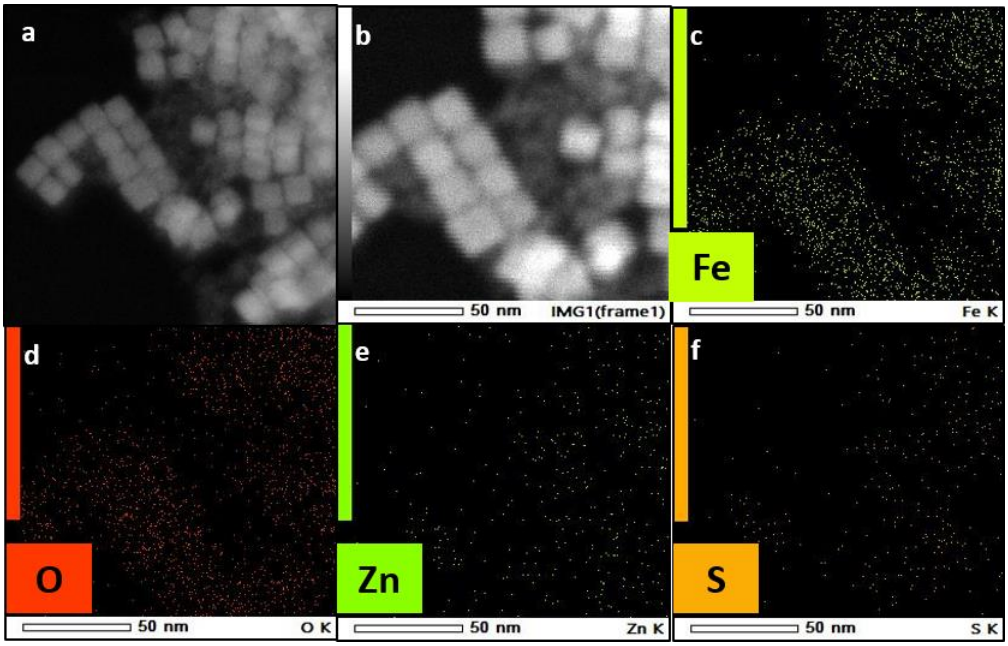

Figure 2.7: a) High Angle Annular Dark Field (HAADF) image of ZnS@IONC sample, b) HAADF image of EDS elemental mapping area c) iron distribution obtained through EDS elemental mapping, d) oxygen distribution obtained through EDS elemental mapping, e) zinc distribution obtained through EDS elemental mapping, f) sulfur distribution obtained through EDS elemental mapping.

From STEM image (Figure 2.7a) both the cubes and the small particles aggregates were clearly distinguishable. Elemental mapping for iron (Figure 2.7c) clearly indicates that this element is localized in the cubes area whereas zinc (Figure 2.7e), even though it has a low number of counts, seems to be mostly in the spaces between the cubes, where small particles' aggregates are localized. Oxygen (Figure 2.7d) seems to be allocated both on the cubes and in the interstitials between them while sulfur seems to be mainly on cubes' aggregates but the small number of counts does not allow to obtain his accurate distribution. In order to have a complete picture of the final sample composition and to clearly identify the aggregates between IONCs, XRD analyses were performed (see Figure 2.8).

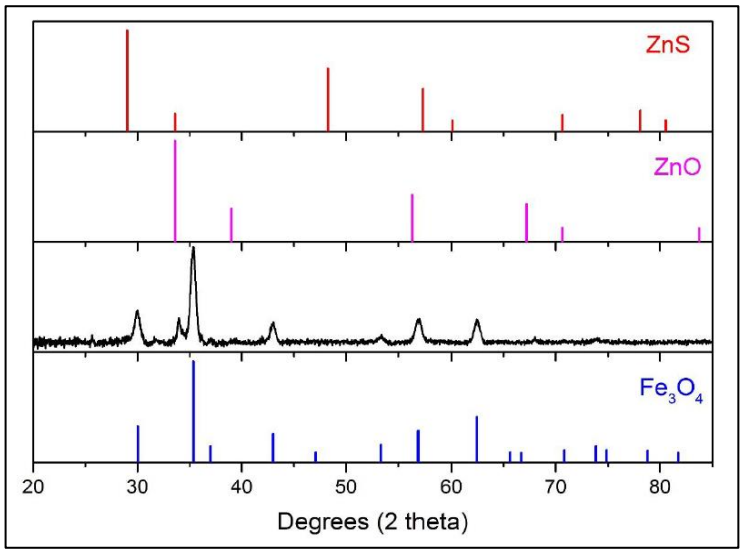

Figure 2.8: Experimental XRD pattern obtained from a ZnS@IONC sample in comparison with the expected reflection for iron oxide (ICSD code: 247035), zinc oxide (ICSD code: 38222) and zinc sulfide (ICSD code: 41985).

All the expected maximum intensity reflections for iron oxide were evident in the experimental pattern that was showing clear sharp Bragg peaks indicating optimal crystallinity. The only reflection that was not possible to attribute to iron oxide was the one at 2θ = 33.6°. This Bragg peak can be indexed with the [002] reflection of ZnS sphalerite (ICSD code: 41985) or with the [111] reflection for cubic ZnO (ICSD code:38222). For ZnS however, the [002] reflection should be much less intense of the one of the main [111] reflection at 2θ = 29°. Since the expected reflection for ZnS at 29° was not present and since the [111] reflection of ZnO at 33.6° is cubic ZnO main reflection, the particles were unambiguously identified as made of ZnO. Other reflections coming from ZnO nanoparticles are not present in the experimental XRD pattern probably because of the small quantity and low crystallinity of those particles.

2.2.3. Synthesis of Au@FeO_y heterostructures

Since the direct growth of ZnS particle directly on the surface of IONCs gave unsatisfactory results, other paths were considered in order to achieve the desired heterostructures with a magnetic domain and a chalcogenide domain. Among the highly performing magnetic materials developed in our research group, together with IONCs, also Au@FeO_y dimers were synthesized.[19] Gold-Iron oxide dimers have been reported as promising in different applications, ranging from catalysis[10,58] to biomedicine.[59] Indeed, in these heterostructures, the gold domain can be exploited for imaging technique like Surface Enhanced Raman Spectroscopy (SERS)[60], computer tomography (CT)[61] or in photothermal therapy (PTT)[62] while the iron oxide domain can be used both in Magnetic Resonance Imaging (MRI)[59] or as heat mediator in magnetic hyperthermia (MHT).[63] With respect to MHT, gold-iron oxide dimers have shown outstanding Specific Absorption Rate (SAR) values,[19] comparable to the ones of IONCs. Consequently, the possibility to merge a chalcogenide domain with Au@FeO_y heterostructures, using gold NPs as "linkers" between iron oxide and a chalcogenide domain was also investigated.

The synthesis method of those heterodimers relies on the *in-situ* growth of iron oxide domains on the surface of pre-formed gold nanoparticles through the hot injection of $Fe(CO)_5$ at 150°C in presence of OLAC and oleyl amine (OLA) (acting as surfactants) and using ODE as solvent. Iron precursor is then decomposed during an annealing step at 200°C. The size of the iron oxide domains, and therefore their magnetic properties, can be tuned (from 16 ± 2 nm to 25 ± 4 nm) by modifying the annealing time at 200°C (from 30 to 90 minutes). Key point of this synthesis is to introduce Cl^- ions, which have been found to improve the crystallinity of the iron oxide domains, with gold precursor ($HAuCl_3$), allowing thus the growth of those domains already at 200°C whereas in the absence of Cl^- ions, the growth takes place only at 300°C. Together with Au@FeO_y dimers of the mentioned size, this synthesis also produces smaller dimers and isolated gold NPs (see Figure 2.9a). In order to isolate the desired dimers from those byproducts, the as-synthesizes sample is washed with isopropanol, dispersed in chloroform and subjected to magnetic separation using a 0.4 T magnet for 180 minutes. The fraction collected was dispersed again in chloroform for subsequent experiments (see Figure 2.9b).

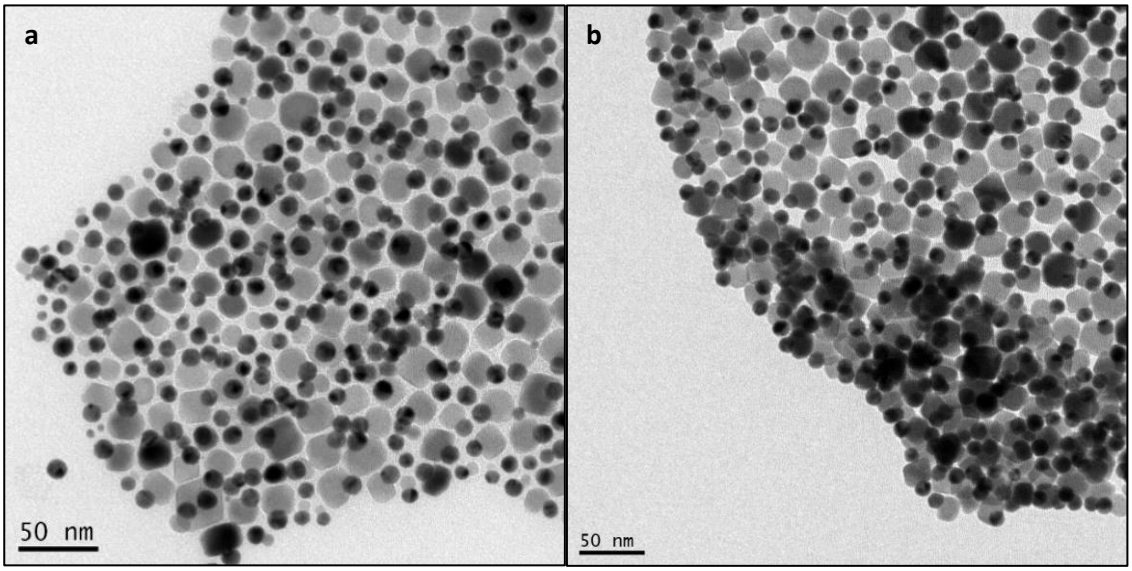

Figure 2.9: Representative TEM pictures of Au@FeO_y dimers sample with mean iron oxide size of 20 ± 2 nm before (a) and after (b) 180 minutes of magnetic separation using a 0.4 T magnet.

Phase composition of these dimers was identified through XRD analyses, whose results are shown in Figure 2.10. The reflections obtained in experimental patterns are perfectly matching the ones expected for cubic gold and iron oxide, with no possibility to discriminate accurately between γ-Fe_2O_3 and Fe_3O_4 NPs phases using XRD.

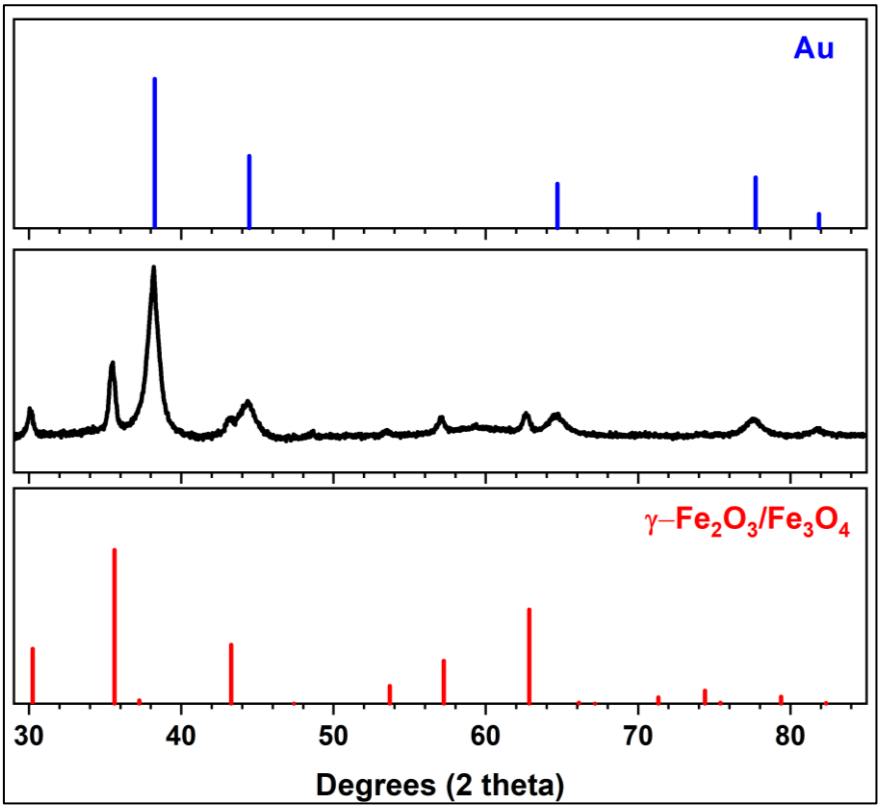

Figure 2.10: Representative XRD pattern of an Au@FeO_y dimers sample and comparison with expected reflection for gold (ICSD code 611625) and iron oxide (ICSD code 247035).

Magnetic properties of the dimers' samples were evaluated through a Superconducting Quantum Interference Device (SQUID) magnetometer. Figure 2.11 shows the field dependence of the magnetization at 10 K and 298 K (RT) (Figure 2.11a), together with Zero-Field-cooled (ZFC) heating and Field-cooled (FC) cooling magnetization vs. temperature curves (Figure 2.11b), obtained for a sample of dimers, whose iron oxide domain size was 25 ± 4 nm.

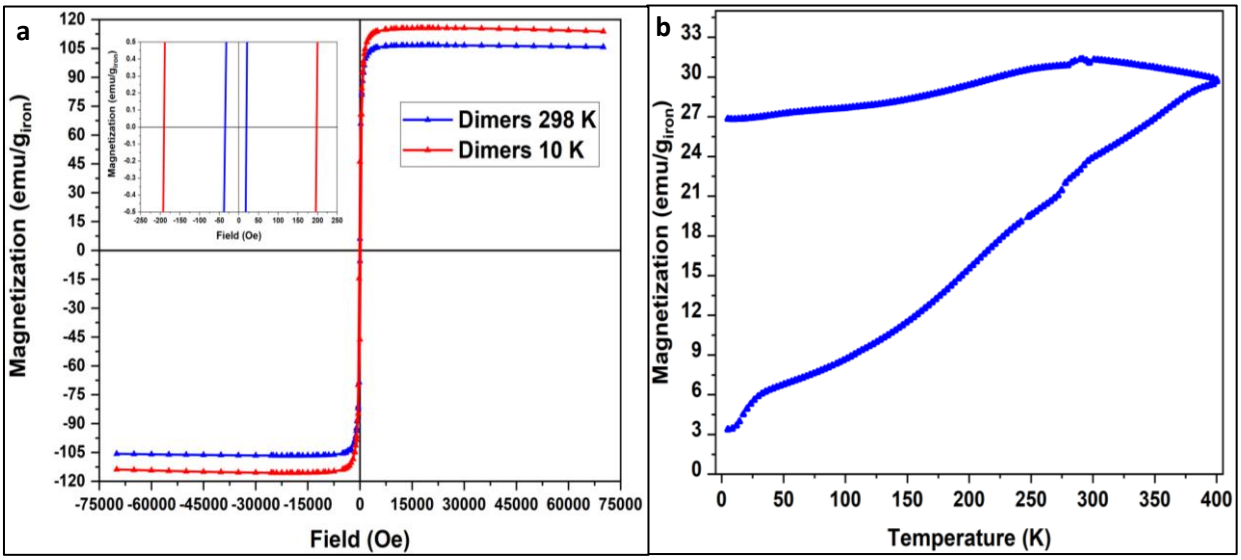

Figure 2.11: Results obtained from the magnetic characterization on a sample of Au@FeO_y dimers with 25 ± 4 nm iron oxide domain: a) zero field cooled MH curves recorded in the range ± 70 kOe at 10 K (red line) and 298 K (blue line), insert: low field region of the MH curves at 10 K and 298 K; b) ZFC heating and FC cooling curves in the range 5 K – 400 K recorded using a 50 Oe field.

Parameters determined through these measurements are reported in Table 2.1.

Table 2.1: Parameters measured through SQUID analyses on a sample of Au@FeO_y with 25 ± 4 nm iron oxide domain size.

Temperature	H_C	M_{max}
(K)	(Oe)	emu/g_{iron}
298 K	20	106
10 K	200	113

Maximum magnetization values of these particles (113 emu/g_{iron} at 10 K and 106 emu/g_{iron} at RT) are in line with the ones reported before for Au@FeO_y dimers synthesized following this procedure[19]. From ZFC-FC curves particles can be identified as blocked (and consequently ferrimagnetic) in the range of temperature tested (5K- 400K) as expected given the large size of the magnetic domains. Reduction of the magnetization in FC curves when moving from higher to lower temperature is an indication of interparticle interaction[64] as already clearly shown by TEM images in Figure 2.9. Magnetization versus temperature curves (Figure 2.11b) do not show the typical Verwey transition (expected, for magnetite nanoparticles, near 120 K)[65] associated with the presence of magnetite. However, P. Guardia et al. reported that for dimers obtained through the same synthetic route, a mixture of maghemite and magnetite is expected, as determined through Mössbauer spectroscopy, showing a proportion between maghemite (γ-Fe_2O_3) and magnetite (Fe_3O_4) of, respectively, 46 ± 2 % and 54 ± 2 %.[19]

2.2.4. Synthesis of Au@$Cu_{2-x}S$ heterostructures

Once confirmed the possibility to successfully reproduce the growth of a magnetic domain on gold NPs, different trials were carried on to couple Au NPs with a chalcogenide domain suitable for

radiolabeling such as the previously reported copper sulfide[57] or zinc sulfide (synthesis, characterization and radiolabeling reported in chapter 1).

As first step, small (≃ 4 nm) gold nanoparticles (see Figure 2.12a) were synthesized following a reported procedure[66]. Briefly, the particles were synthesized using $HAuCl_4$ as gold precursor and Tert-butyl ammine-borane complex as reducing agent in presence of Oleyl amine and using tetralin as solvent. Particles were then precipitated with isopropanol, centrifuged and dispersed in chloroform for further experiments.

In order to be able to grow a copper sulfide domain on these particles, according to the procedure reported by Wang et al.[50], they need to be dispersed in oleyl amine. Consequently, the chloroform dispersing the gold NPs was evaporated through bubbling and substituted with same amount of oleyl amine.

The synthesis of the Au@$Cu_{2-x}S$ dimers is accomplished through the growth of $Cu_{2-x}S$ domains on preformed gold NPs. First, the Au NPs oleylamine solution is mixed with the copper precursor ($CuCl_2 \times 2H_2O$) with an Au: Cu molar ratio of 1:20 in oleyl amine. Copper sulfide domains nucleation is then started by the injection at 180°C of di-tert-butyl disulfide (TBDS), with a sulfur amount equal to 20 times the equivalents of Cu precursor used. Then the reaction mixture is annealed at that temperature for 70 minutes. Resulting Au@$Cu_{2-x}S$ heterostructures are shown in Figure 2.12b.

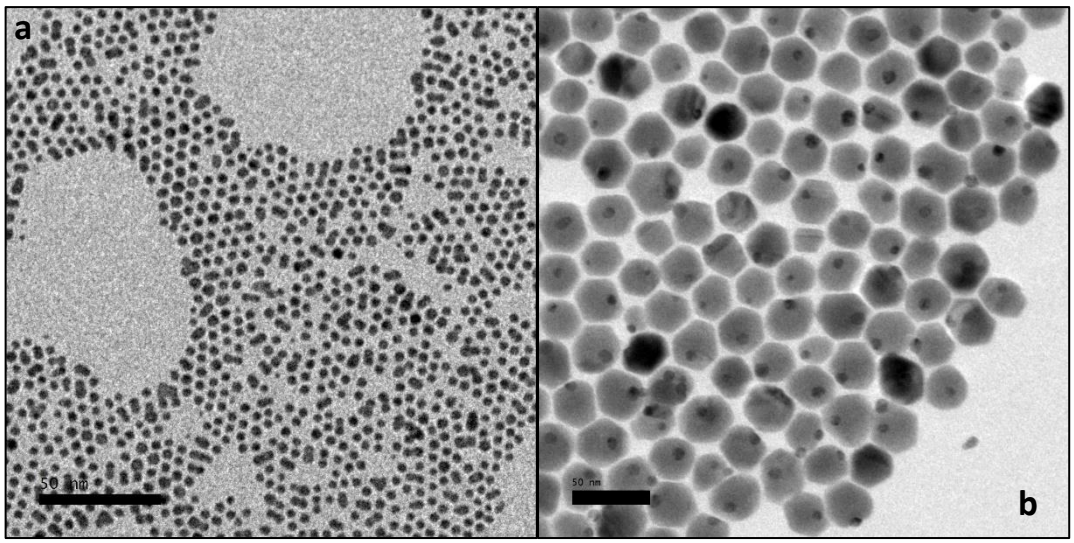

Figure 2.12: Representative TEM pictures of a) 3.7 ± 0.5 nm gold NPs used as seeds; b) Au@$Cu_{2-x}S$ dimers with gold NPs size of 7 ± 2 nm and copper sulfide size of 26 ± 2 nm.

The shape of the formed copper sulfide domains is hexagonal with a side-to-side length of 26 ± 2 nm. Interestingly, the size of gold NPs used as seeds is growing during the process, from 3.7 ± 0.5 to 7 ± 2 nm this suggesting that, other than growing the copper sulfide domains, the reaction is also affecting gold NPs. To further characterize these dimers, XRD analyses were performed (see Figure 2.13).

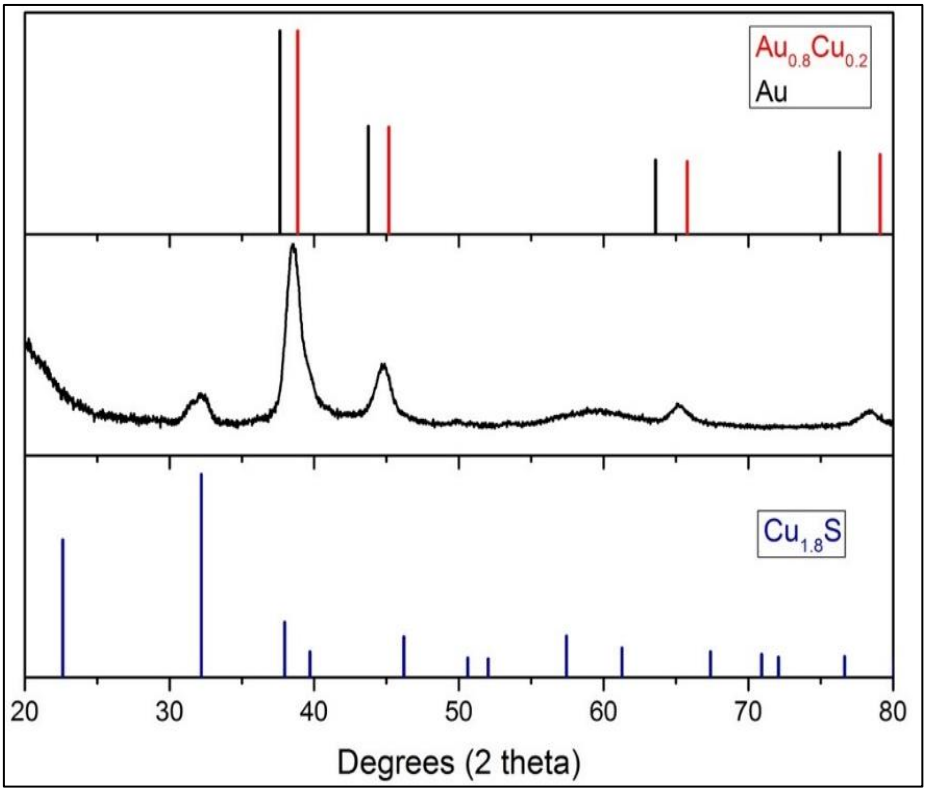

Figure 2.13: Experimental XRD pattern for a sample of Au@$Cu_{2-x}S$ in comparison with the expected reflections for hexagonal copper sulfide (ICSD code: 69756), for gold (ICSD code: 611625) and for $Au_{0.8}Cu_{0.2}$ gold copper alloy (ICSD code: 58431).

XRD analyses confirmed the presence of copper sulfide although with low crystallinity. Interestingly, these analyses also revealed the presence of a gold-copper alloy (about 20 % of copper, based on the XRD pattern) instead of pure gold phase. This means that some of the big excess of copper used in the synthesis (20 times more than gold) entered gold NPs during the annealing to give an alloy, this giving a possible explanation for the increase in gold NPs size during the synthesis.

2.2.5. Synthesis of Au@ZnS heterostructures

Before going on with the merging of the chalcogenide and the magnetic domain using gold NPs as "linkers", trials in order to grow also a ZnS domain on gold NPs were also carried on. With this purpose exactly the same seeds and procedure used for Au@$Cu_{2-x}S$ dimers (that is Au:Zn molar ratio 1:20 and annealing temperature of 180°C) replacing $CuCl_2 \times 2H_2O$ with $ZnCl_2$ as zinc precursor were employed. Using this procedure, no ZnS NPS were nucleated (see Figure 2.14a). Given the already large amount of Zinc precursor used in the procedure, ZnS domains growth was triggered increasing the temperature of TBDS injection and of annealing from 180°C to 260°C (see Figure 2.14b).

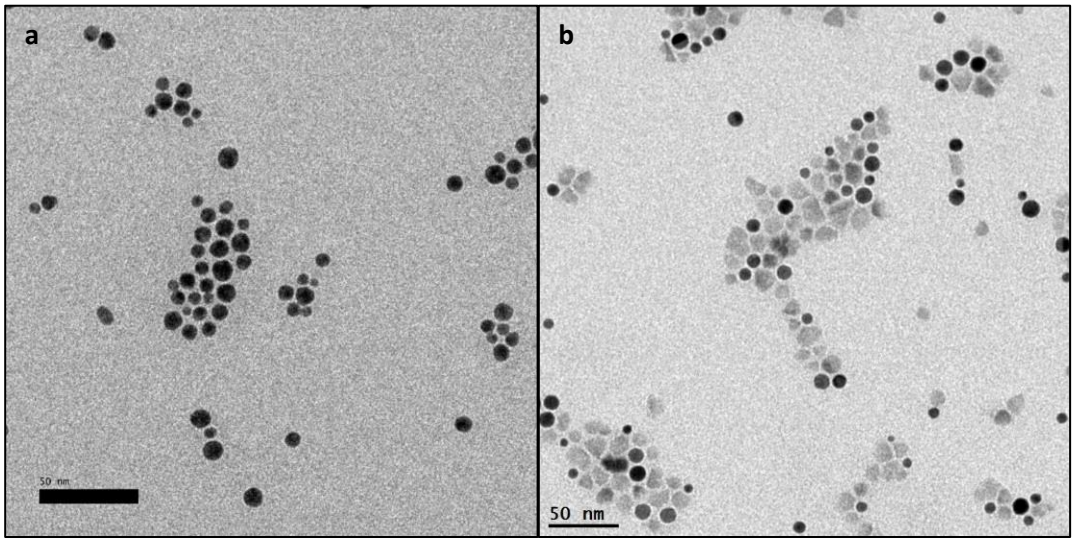

Figure 2.14: Representative TEM pictures of Au@ZnS samples synthesized using an Au:Zn molar ratio of 1:20 and an annealing temperature of 180°C (a) and 260°C (b)

While using an annealing temperature of 180°C is not sufficient for the nucleation of ZnS nanoparticles, in the sample synthesized using an annealing temperature of 260°C were found, other than increased-size gold NPs, also low-diffracting isolated domains with irregular shape. To identify those low-diffracting domains, STEM imaging and EDS quantitative analyses were carried out (See Figure 2.15).

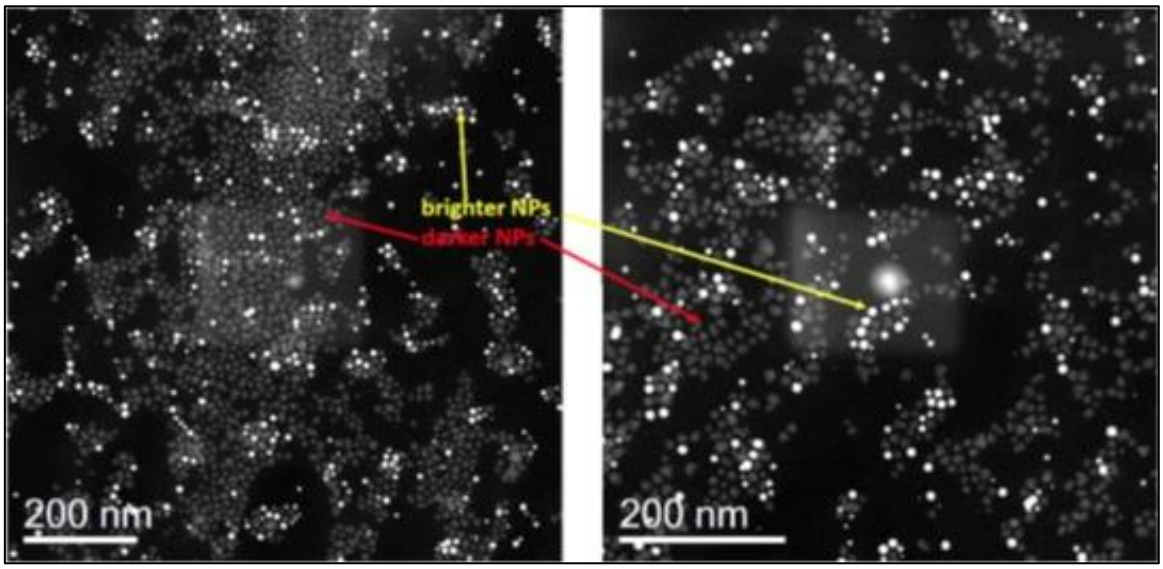

Figure 2.15: Representative HAADF images of an Au@ZnS sample synthesized using an Au:Zn ratio of 1:20 and an annealing temperature of 260°C.

Elemental analysis performed on the two population of particles in the sample gave a Zn:S ratio of 1:1 for darker particles (brighter in bright field TEM) while brighter particles in STEM images were found to be made of Au with low amount (6%) of Zinc. In order to have additional informations on this sample, XRD analyses were also performed.

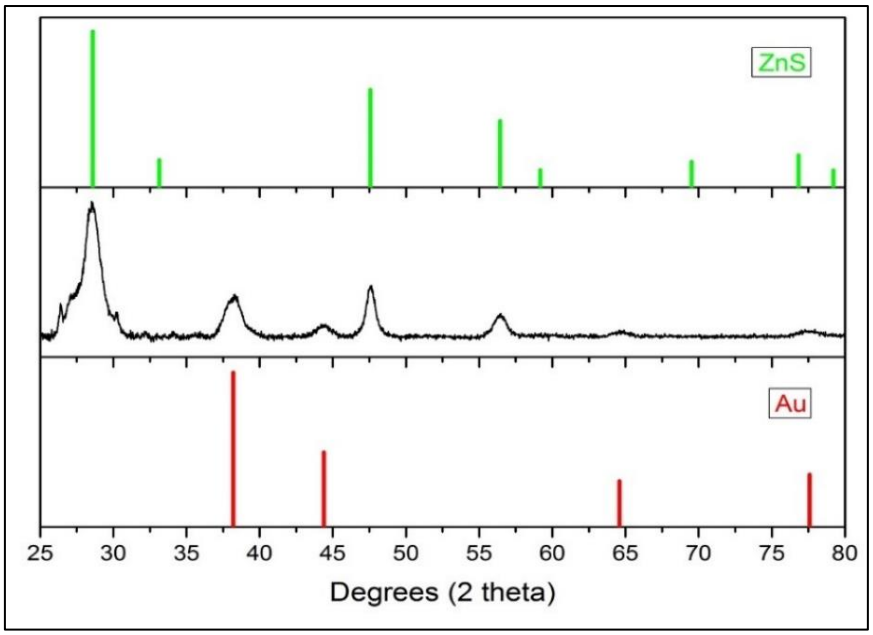

Figure 2.16: XRD experimental pattern for an Au@ZnS sample synthesized using an Au:Zn molar ratio of 1:20 and an annealing temperature of 260°C in comparison with the expected reflection for gold (ICSD code: 611625) and zinc sulfide (ICSD code: 41985).

XRD analyses (see Figure 2.16) clearly show the presence of both Au and ZnS phases as expected from the results of EDS quantitative analyses. Noteworthy, ZnS particles nucleated using this procedure have a cubic sphalerite srtucture, while copper sulfide nucleated on the top of gold NPs in Au@$Cu_{2-x}S$ dimers had a less ordered hexagonal structure. Also, in this case, only pure gold phase and no alloy was present, meaning that, even using a higher temperature (260°C instead of 180°C), zinc was not producing an alloy with gold nanoparticles as copper did during Au@$Cu_{1.8}S$ nano-heterostructures syntheses. From this first trial it was clear that, at least using a 1:20 molar ratio between gold content in Au NPs and Zn precursor, an annealing temperature of 180°C was too low to obtain ZnS nucleation while at 260°C ZnS domains were formed but the ZnS domains were homonucleating. In order to try to trigger the formation of the desired heterostructures, different annealing temperature (220°C, Figure 2.17a and 240°C, Figure 2.17b) were used. None of them allowed to obtain Au@ZnS dimers but only isolated low-diffracting domains surrounding gold NPs.

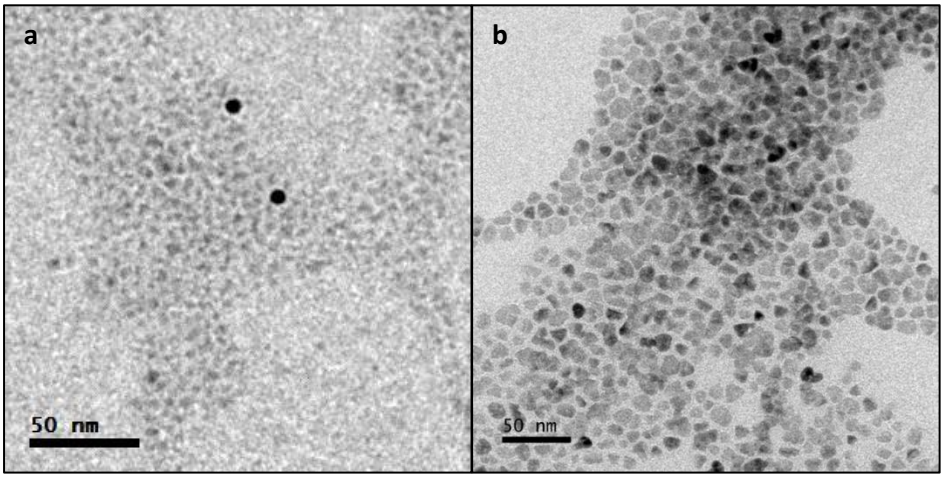

Figure 2.17: Representative TEM pictures of Au@ZnS samples synthesized using an Au:Zn ratio of 1:20 and an annealing temperature of a) 220°C, b) 240°C.

Fixing the annealing temperature to 240°C, also the influence of the Au:Zn molar ratio was tested, scaling it down to 1:10, 1;5 and 1:2.5 (see Figure 2.18) and keeping the Zn:S ratio to 1:20.

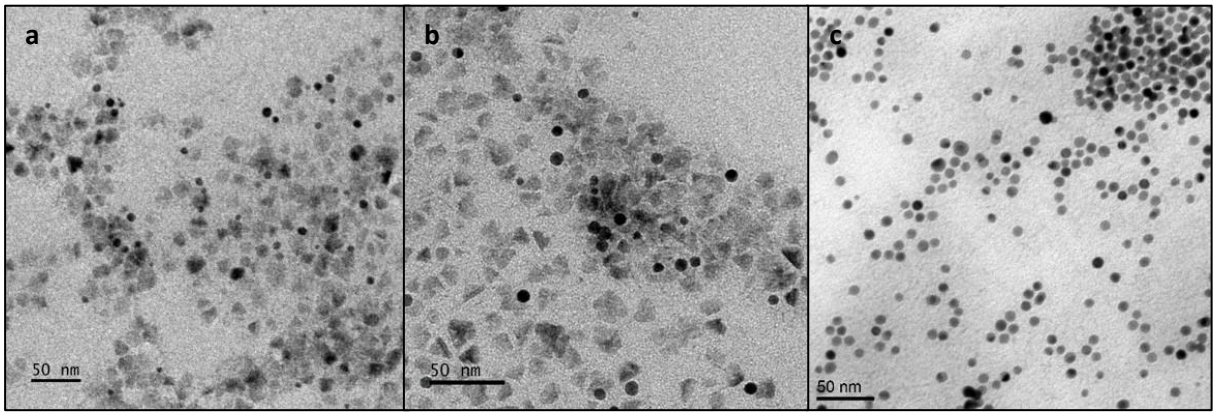

Figure 2.18: Representative TEM pictures of samples synthesized using an annealing temperature of 240°C and a) Au:Zn molar ratio of 1:10; b) Au:Zn molar ratio of 1:5; c) Au:Zn molar ratio of 1:2.5.

With none of these trials, clearly shaped Au@ZnS nano-heterostructures were formed. Indeed, only badly shaped isolated low-diffracting domains were found in samples synthesized with Au:Zn ratios of 1:10 (Figure 2.18a) or 1:5 (Figure 2.18b) while only the gold NPs used as seeds were found in the sample synthesized employing a 1:2.5 Au:Zn ratio. This behavior is suggesting a different growth mechanism with respect to the one of Au@$Cu_{2-x}S$ dimers and this difference could depend on the structure of the sulfide phase formed during the reaction. Indeed, the copper sulfide phase growing on cubic phase gold (ICSD code: 611625) or gold-copper alloy (ICSD code: 58431), has a less symmetric hexagonal crystal lattice (ICSD code: 69756) while ZnS is nucleating with a cubic crystal lattice (ICSD code: 41985). Based on these observations, it can be hypothesized that its less ordered crystal lattice, and the formation of an AuCu alloy, promotes the growth of $Cu_{2-x}S$ on gold NPs while the growth is not possible in the case of more ordered cubic ZnS crystals.

2.2.6. Synthesis of FeO_y@Au@$Cu_{2-x}S$ heterostructures

In order to grow a copper sulfide domain on Au@FeO_y dimers, different trials were carried out in order to check the influence of different parameters on the particles obtained. First, a synthesis was performed using exactly the same parameters used in Au@$Cu_{2-x}S$ synthesis. In this synthesis, the starting seeds were Au@FeO_y dimers dispersed in chloroform, which were mixed with the copper precursor ($CuCl_2 \times 2H_2O$) in oleyl amine. Later on, the seeds' solvent (chloroform) was evaporated through a 10 minutes annealing step at 100°C under N_2 gas flux, before performing TBDS injection and Au@$Cu_{2-x}S$ growth at 180°C for 70 minutes. Representative TEM pictures of the particles obtained are shown in Figure 2.19.

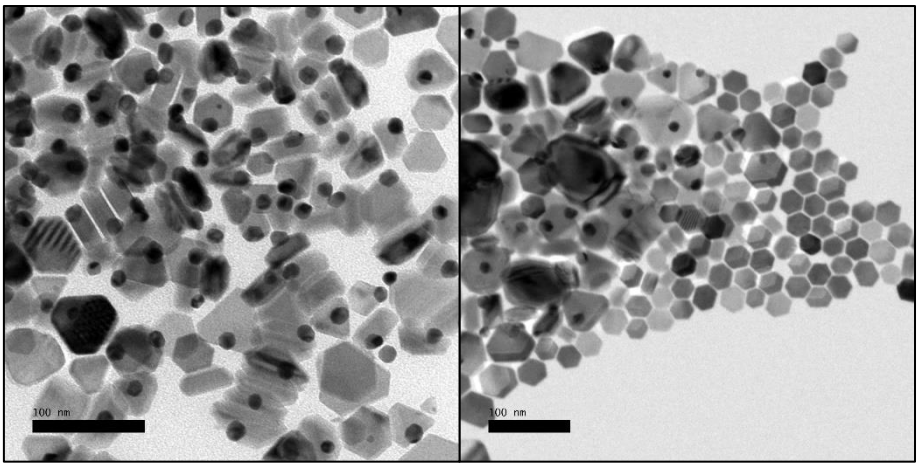

Figure 2.19: Representative TEM pictures of the particles obtained adapting the Au@$Cu_{2-x}S$ heterostructures synthesis to the use of Au@FeO_y dimers as seeds.

The product of this synthesis was a mixture of isolated hexagonal particles (presumably copper sulfide) together with heterostructures made of gold and of differently shaped (triangular o platelet-like) low diffracting domains. No trace of the starting Au@FeO_y seeds was found. These results probably indicated a ripening process of iron oxide domains, related to reaction environment and temperature.[67]

In order to avoid Au@FeO_y seeds ripening, the reaction was repeated using a lower annealing temperature (160°C). The sample resulting from this synthesis (see Figure 2.20a) is mainly made of Au@FeO_y dimers with a third domain attached on the surface of the gold NPs. Together with the three domains heterostructures (trimers from now on), also few unreacted Au@FeO_y and many isolated low diffracting particles (presumably copper sulfide domains) were present. In order to remove these non-magnetic particles, magnetic separation was done on the synthesis products using a 0.4 T magnet for 180 minutes. Particles collected with the magnetic separation and the resulting supernatant are respectively shown in Figure 2.20b and 2.20c.

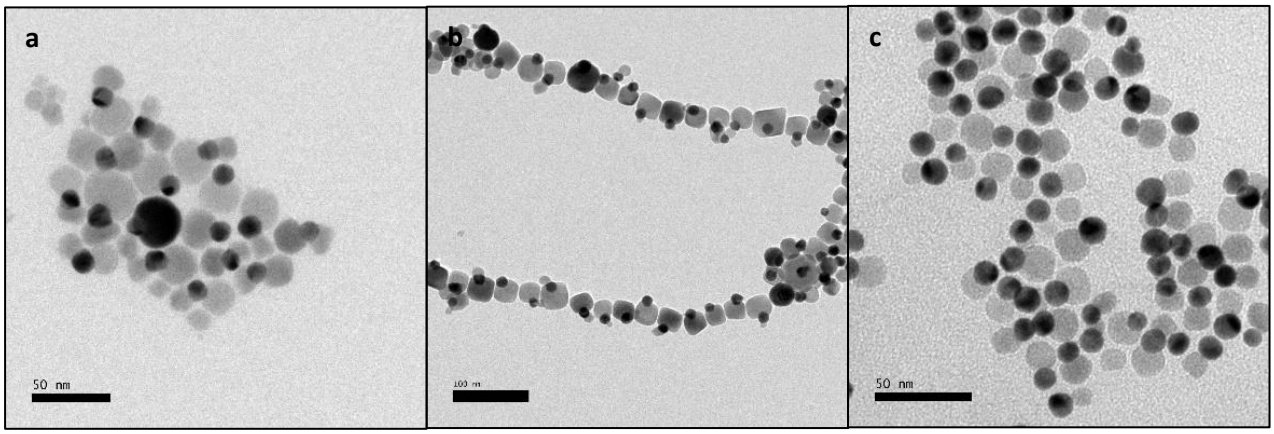

Figure 2.20: Representative TEM pictures of a) as-synthesized trimers, b) magnetic fraction recollected through 180 minutes magnetic separation with a 0.4 T permanent magnet, c) non-recollected fraction (surnatant).

While in the recollected magnetic fraction (see Figure 2.20b) mainly trimers or Au@Fe_3O_4 dimers are present, the non-recollected fraction (Figure 2.20c) is a mixture of Au@Fe_3O_4 dimers with small iron oxide domains and isolated $Cu_{2-x}S$ particles. Interestingly, the shape of the iron oxide domains in the two fractions is different: quasi-spherical domains are found in the fraction that did not move to the magnet while well-faceted iron oxide domains moved to the magnet, this suggesting their

improved magnetic properties. The collected fraction of the sample was dispersed in 10 mL of 5% OLAC solution in chloroform, in order to improve stability.

In order to check the influence of the chloroform (dispersing Au@FeO_Y dimers) in the reaction batch, a new synthesis was set up, substituting the annealing at 100°C under N_2 flux with a 60 minutes vacuum degassing step at 40°C. TEM picture of the sample synthesized evaporating the chloroform at 100°C under N_2 flux (a) and picture of the sample synthesized evaporating the chloroform at 40°C under vacuum (b) are compared in Figure 2.21.

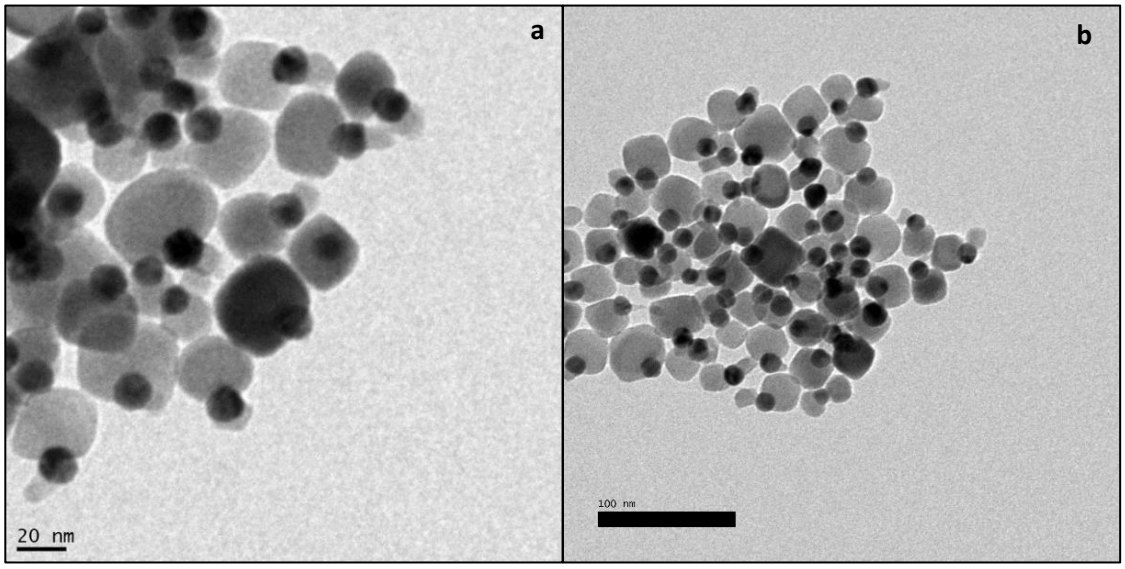

Figure 2.21. Representative TEM pictures of trimers' samples synthesized removing chloroform from reaction batch through (a) 10 minutes annealing at 100°C under N_2 flux and (b) 60 minutes degassing under vacuum at 40°C.

From TEM pictures, the samples seemed similar with no clear difference in trimers yield or third domain shape. XRD analyses (see Figure 2.22) were performed in order to acquire additional data to see if the chloroform evaporation procedure had an influence in final sample properties.

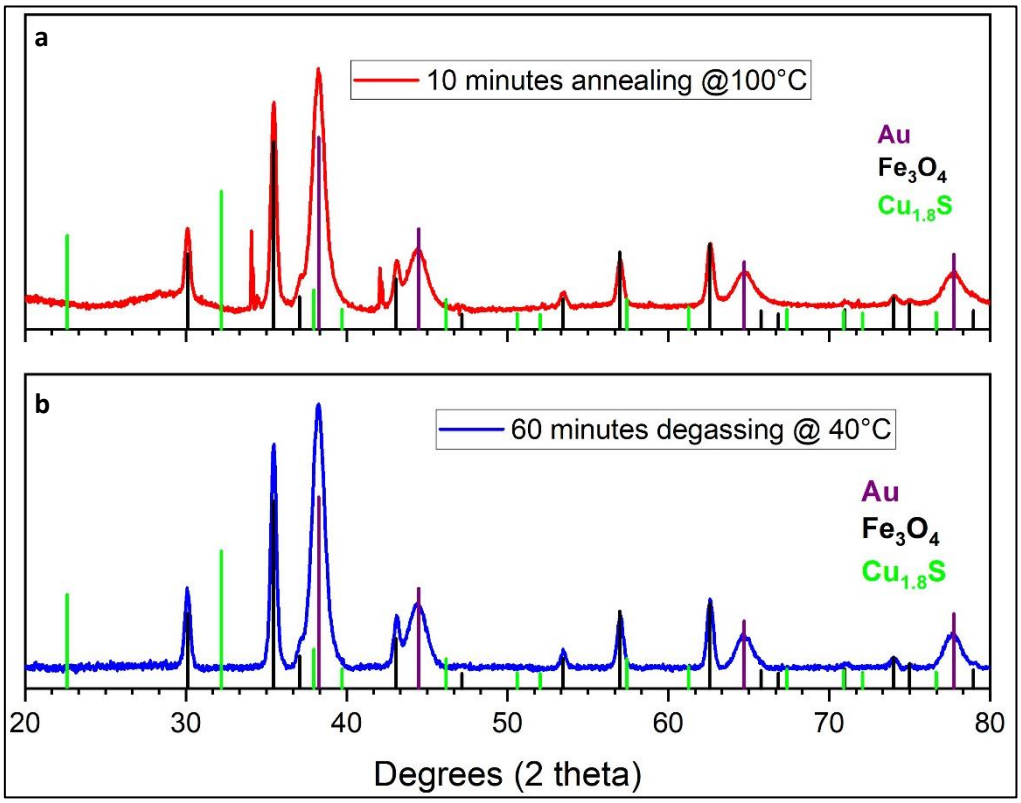

Figure 2.22: Experimental XRD diffraction patterns of trimers' samples synthesized removing chloroform from reaction batch through (a) 10 minutes annealing at 100°C under N_2 flux and (b) 60 minutes degassing under vacuum at 40°C. Both the experimental patterns are compared with the expected reflections for gold (ICSD code 611625), iron oxide (ICSD code 247035) and hexagonal copper sulfide (ICSD code 69756).

In both cases, reflection for Au and FeO_y coming from starting seeds are clearly present. In the sample obtained with the procedure in which the chloroform was evaporated under N_2 flux at 100°C (Figure 2.21a), also additional Bragg peaks at 2θ =34° and 2 θ =42° and a broad band around 2θ =30° are present. These Bragg peaks are too narrow to be associated with a nanostructure[68,69] and were impossible to index with any phase that could be resulting from the reaction mixture. Indeed, in the sample synthesized removing chloroform from reaction batch using vacuum degassing (Figure 2.22b) these additional features of the diffraction pattern are not present, suggesting the hypothesis ascribing them to the presence of impurities in the reaction mixture degassed through N_2 bubbling at 100°C. None of the samples presented Bragg peaks that confirmed the presence of any of the many possible (e.g. chalcocite, digenite) crystalline phases for copper sulfide (in Figure 2.22 is shown as reference the hexagonal $Cu_{1.8}S$ phase (ICSD code 69756) that was formed during Au@$Cu_{2-x}S$ dimers synthesis).

In all the syntheses, before the magnetic separation of the samples, together with the trimers also few unreacted Au@FeO_y and isolated $Cu_{2-x}S$ NPs were formed. In order to reduce this byproducts formation, the influence on particles obtained of the feed ratio between Au content in gold NPs and Cu precursor amount was tested. Keeping the ratio between the moles of Cu precursor and moles of sulfur provided by TBDS fixed to 1:20 as in the original synthesis, different trials with Au:Cu molar ratios of 1:40, 1:20, and 1.13.3 were performed. Results are shown in Figure 2.23.

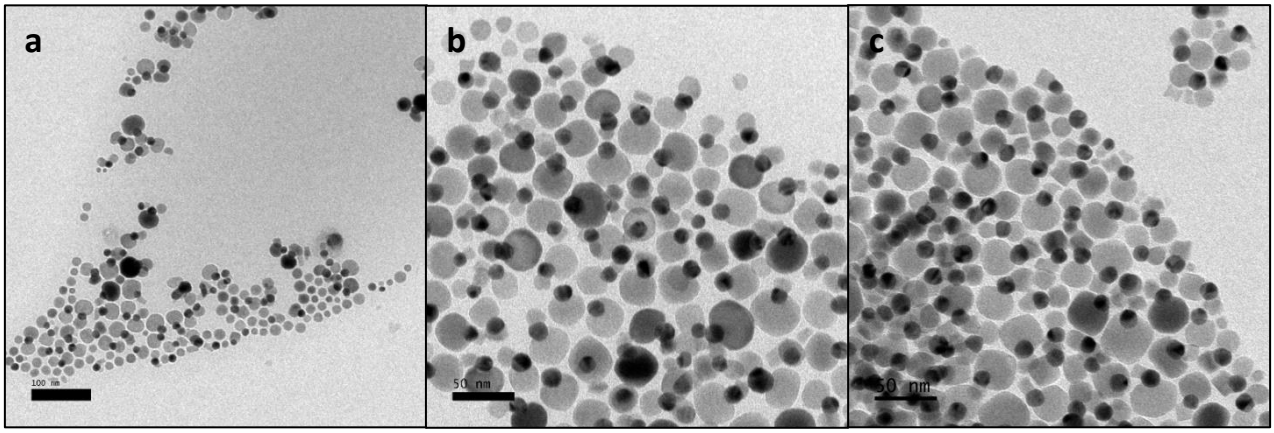

Figure 2.23: Representative TEM pictures of trimers synthesized using and Au:Cu ratio of (a) 1:40, (b) 1:20 and (c) 1:13.3.

When an Au:Cu feed ratio of 1:40 is used (Figure 2.23a) many isolated $Cu_{2-x}S$ NPs were formed. On the other hand, both in the sample synthesized using 1:20 ratio and in the sample with Au:Cu ratio of 1:13.3 less isolated domains are present. In particular, in the as synthesized sample produced using a Au:Cu molar ratio of 1:13.3, three domain heterostructures are the main part (≃85%, based on statistic performed on at least 200 particles) of the particles found in TEM analyses and only few isolated low diffracting domains and Au@FeOy dimers are present, this demonstrating the importance to select an appropriate Au:Cu molar ratio in order to achieve optimal heterostructures' yield.

Another parameter that had an influence on synthesis products was the length of the annealing performed at 160°C. Increasing times for the annealing step (120 and 240 minutes) were tested in order to check the influence of this parameter on the size, shape and crystallinity of the third domain growing on Au@FeO_y dimers. Figure 24 shows representative TEM pictures of samples synthesized using the standard annealing time (70 min, Figure 2.24a), and 120 and 240 minutes (Figure 2.24b, 2.24c).

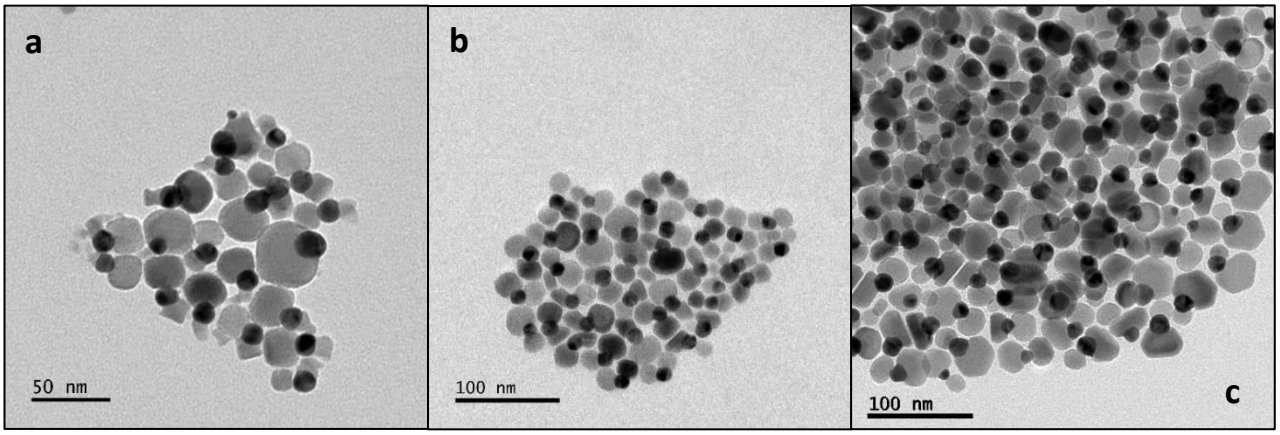

Figure 2.24: Representative TEM pictures of trimers synthesized using annealing time of (a) 70 minutes, (b) 120 minutes and (c) 240 minutes.

Although trimers were formed in all the three samples, there is a clear difference between the shapes of the forming third domain. With short annealing (70 minutes) the additional domain growing on Au@FeO_y dimers is badly shaped, with concavities and irregular boundaries. When the annealing is increased to 120 minutes, third domain becomes more defined with a mixture of shapes (either badminton-like or platelet-like). Finally, with 240 minutes annealing, third domain is definitely larger, with the same shape distribution (badminton-like + platelet-like) as in previous case. These results demonstrate the effect of the longer annealing time on the third domain' growth: being the annealing temperature relatively low (160°C) more time is needed for the third domains' growth in order to achieve larger sizes and definite shape.

In order to check if these differences in third domains' shape were having an effect also on diffraction patterns, XRD analyses were performed (see Figure 2.25).

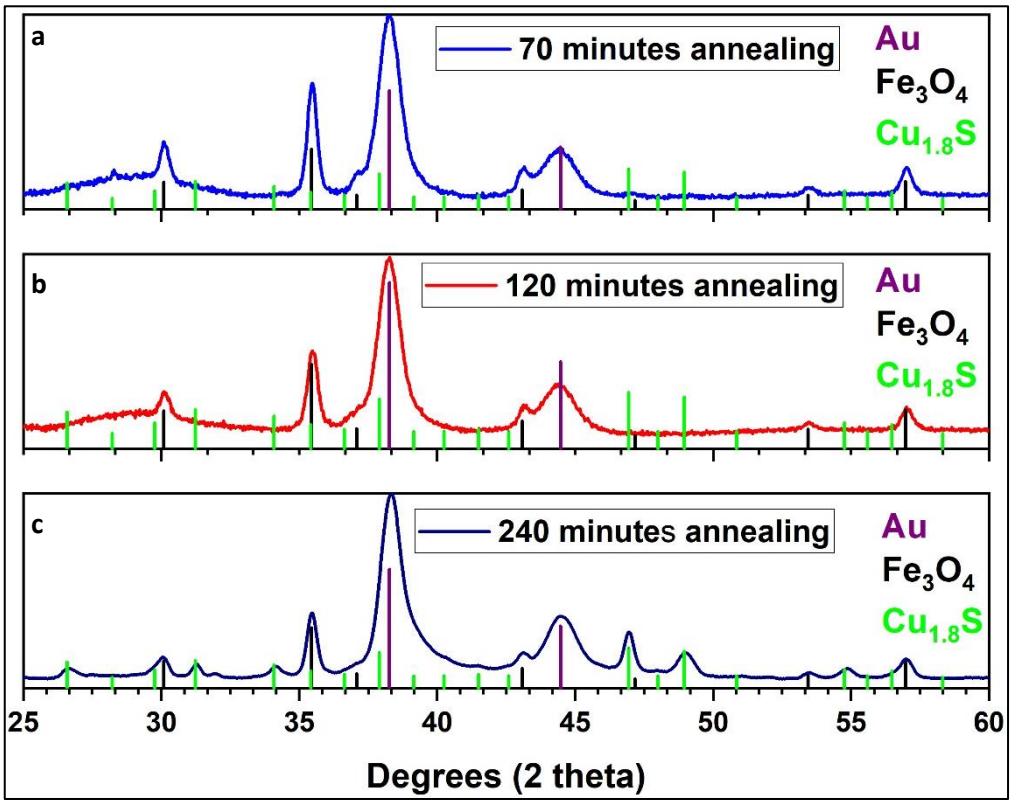

Figure 2.25: Experimental XRD diffraction patterns of trimers samples synthesized using an annealing at 160°C of (a) for 70 minutes (b) for 120 minutes and (c) for 240 minutes. All experimental patterns are compared with the expected reflections for gold (ICSD code 611625), iron oxide (ICSD code 247035) and roxbyite copper sulfide (ICSD code 185807).

While, in terms of XRD pattern, sample synthesized with 70 minutes of annealing and sample synthesized with 120 minutes of annealing are similar (Figure 2.25a and Figure 2.25b, respectively), the diffraction pattern of the sample synthesized using longer annealing (240 minutes, Figure 2.25c) clearly differs from the others, showing, apart from the expected reflections for Au and FeO_y particles (present in all the three diffractograms), also numerous Bragg peaks ascribed to the presence of a low-ordered copper sulfide phase. Noteworthy, the phase of the copper sulfide nanoparticles growing on the surface of Au NPs of Au@FeO_y dimers is not hexagonal as the one that was growing in Au@$Cu_{2-x}S$ dimers synthesis but has a much less symmetric triclinic roxbyite structure with $Cu_{29}S_{16}$ stoichiometry ($Cu_{1.81}S$). One of the possible explanations for this different phase could be the different temperature at which the $Cu_{2-x}S$ phase is grown. Indeed, lower temperature growth could give a less ordered crystal structure.

The stoichiometry of the copper-deficient copper sulfide crystals was also confirmed by inductively coupled atomic emission spectroscopy (ICP-OES), by which a Cu/S ratio equal to 1.80 was determined, in good accordance with the expected stoichiometry of the roxbyite phase.

Using the optimized parameters, that are 60 minutes of degassing step at 40°C, 240 minutes annealing at 160°C and an Au:Cu:S molar ratio of 1:13.3:266, it is possible to tune the size of the third domain ($Cu_{1.81}S$) by changing the concentrations of the precursors ($CuCl_2 \times 2H_2O$, FeO_y@Au seeds and TBDS) used in the reaction. The molar concentration of Cu in reaction batch was tuned from 0.05 M to 0.02 M with two intermediate steps (0.04 M and 0.03 M). TEM pictures and size dispersion graphs of the five different samples are shown in Figure 2.26. Since in all of these reaction the ratio between gold copper and sulfur coming from the three precursors was kept the same (Au:Cu:S molar ratio of 1:13.3:266) data are referred to copper concentration in reaction batch only.

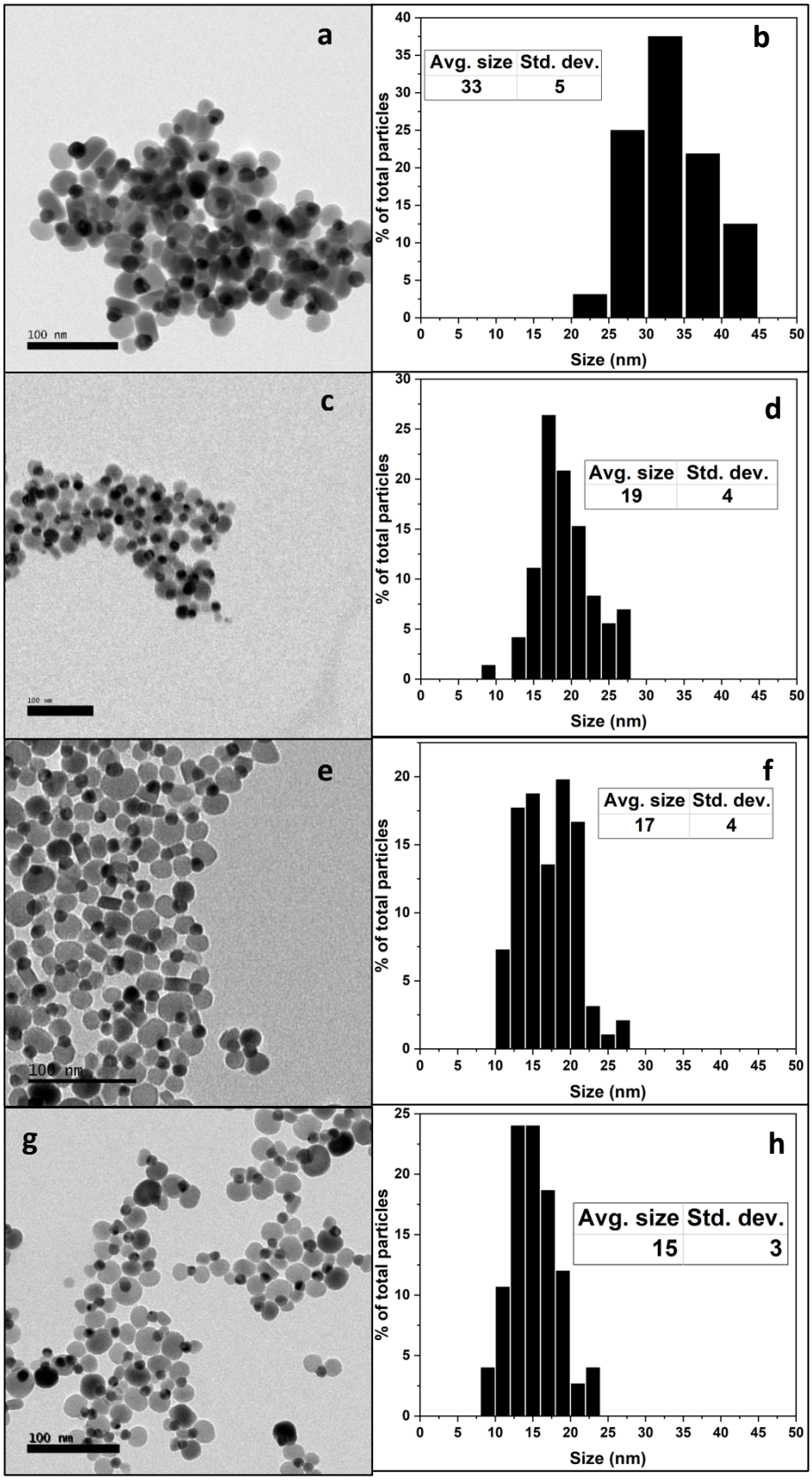

Figure 2.26: Representative TEM pictures and related size dispersion graph of the $Cu_{1.8}S$ domain of sample synthesized using a Cu molar concentration of (a-b) 0.05 M, (c-d) 0.04 M, (e-f) 0.03 M, (g-h) 0.02 M.

Although the clear distinction of the $Cu_{1.81}S$ domain from the FeO_y domain can be made only in the case of clearly platelet shape and, consequently, the number of particles measured is relatively low (≃100), there is a clear trend in size, as shown in Figure 2.26. When lowering the concentrations of the three precursors in the reaction batch, the size of the copper sulfide domain is reducing from 33 ± 5 nm, (0.05 M Cu concentration), to 15 ± 3 nm (0.02 M Cu concentration) with 19 ± 4 nm (0.04 M) and 17 ± 4 nm (0.03 M) as intermediate points. An additional trial was performed using a concentration of 0.01 M but in this case, no clear presence of $Cu_{1.81}S$ domain was found (see Figure 2.27) and only FeO_y@Au were composing the sample.

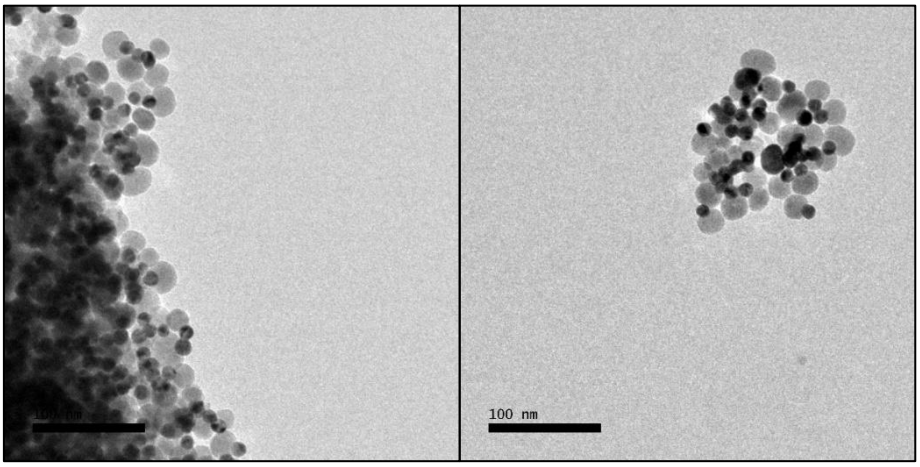

Figure 2.27: Representative TEM pictures of a sample synthesized using a molar concentration of copper of 0.01 M.

In order to acquire additional information on this trend in decreasing size, XRD analyses of the samples obtained with a copper concentration of 0.05 M, 0.03 M and 0.02 M are shown in Figure 2.28.

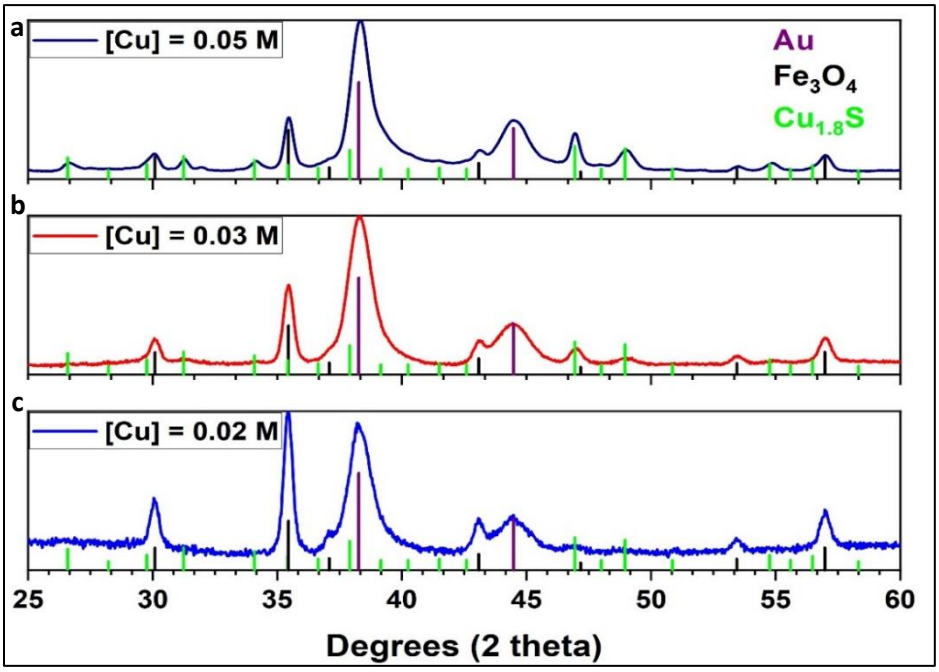

Figure 2.28: Experimental XRD patterns for three samples of trimers synthesized using a molar concentration of copper of (a) 0.05 M, (b) 0.03 M, (c) 0.02 M. All experimental patterns are compared with the expected reflections for gold (ICSD code 611625), iron oxide (ICSD code 247035) and roxbyite copper sulfide (ICSD code 185807).

Copper sulfide is clearly present in both the samples synthesized with copper molar concentration of 0.05 M (Figure 2.28a) and 0.03 M (Figure 2.28b). In third sample (Figure 2.28c), synthesized with a Cu molar concentration of 0.02 M, two main peaks of the roxbyite phase (2θ = 47° and 2θ = 49°) are present, however the absence of the other peaks (such as the ones at 2θ = 31° and 2θ = 34°) could indicate a low crystallinity or low amount of copper sulfide domains. Similarly to what was observed with annealing time, the precursors' concentration has a clear influence on the crystallinity of the newly formed $Cu_{2-x}S$ domains: when the concentration is low, copper sulfide domains are either not formed (0.01 M, Figure 2.27) or grown with poor crystallinity (0.02 M, Figure 2.26g-h and Figure 2.28c) while when high concentrations are used (0.05 M, Figure 2.26a-b and Figure 2.28a) copper sulfide domains are larger and with higher crystallinity.

In order to furtherly study the structural properties of the three phases, HR-TEM measurements of the three domains composing the particles of the sample synthesized using a copper concentration of 0.05 M were performed. Results are shown in Figure 2.29.

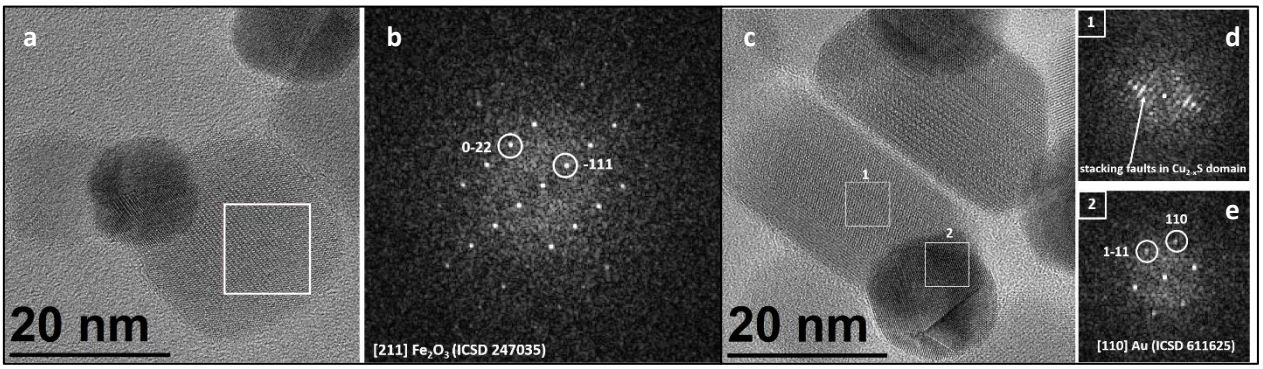

Figure 2.29: a) and c) Representative HR-TEM pictures of FeO_y@Au@$Cu_{1.81}S$ trimers, b) Fast Fourier Transform (FFT) of a selected area of picture a, d) Fast Fourier Transform (FFT) of area indicated with "1" in picture c, e) Fast Fourier Transform (FFT) of area indicated with "2" in picture c. For Au and FeO_y domains, the FFT images are respectively indexed with the reflections for cubic Au (ICSD code 611625) and for cubic γ-Fe_2O_3 (ICSD code 247035).

In the first picture (Figure 2.29a) the monocrystalline nature of the iron oxide domain is clearly observed. The crystal structure of those domains has been confirmed to be cubic. Also, in the case of gold NPs (HR TEM in Figure 2.29c and FTT in Figure 2.29e) the phase structure that was found through XRD analyses has been confirmed. As already reported in literature gold nanoparticles exhibit multiple twinning.[70] Noteworthy, the presence of twinning in metal nanoparticles (and especially in gold) has been reported to be a key parameter allowing the growth of highly anisotropic domain when these nanoparticles are used as seeds in seeded-growth procedures[71]. In $Cu_{1.8}S$ domains, the high density of structural defects (*e.g.* stacking faults, highlighted in Figure 2.29d) made difficult to find a single-crystal for zone-axis identification and consequently not possible to identify the crystal phase.

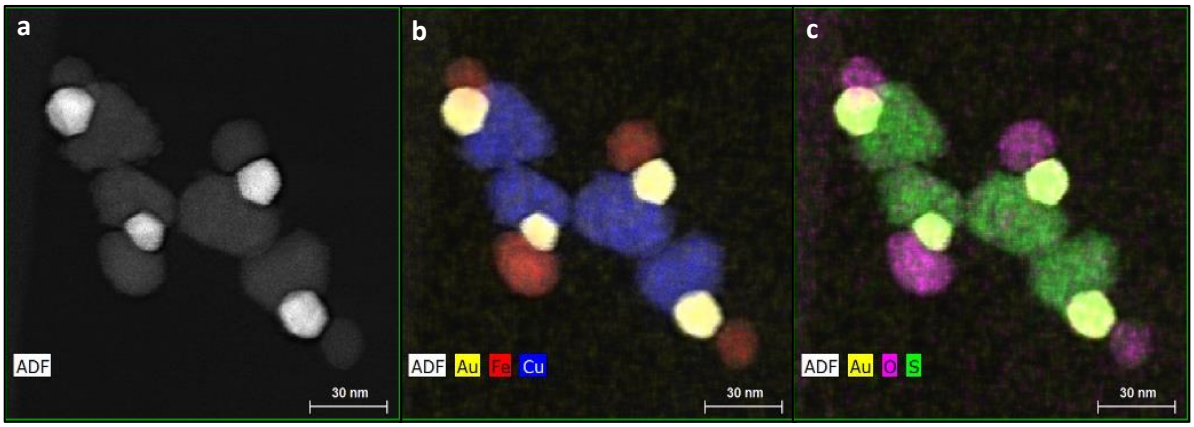

Figure 2.30: HAADF image (a) and EDS elemental analysis mappings for Au, Fe, Cu (b) and Au, O, S (c) of a sample of FeO_y@Au@$Cu_{2-x}S$ trimers.

EDS mapping (Figure 2.30) shows the composition of the three domains in the FeO_y@Au@$Cu_{2-x}S$ nano-heterostructures.

Energy Dispersive X-ray Spectroscopy quantitative analyses performed on the domains identified as made of copper and sulfur (see Figure 2.31), show a Cu/S ratio of 1.99 ± 0.4. Considering the error related to this technique, this value is matching the Cu/S ratio measured with ICP-OES (1.80) and the one expected for a roxbyite structure (1.81)

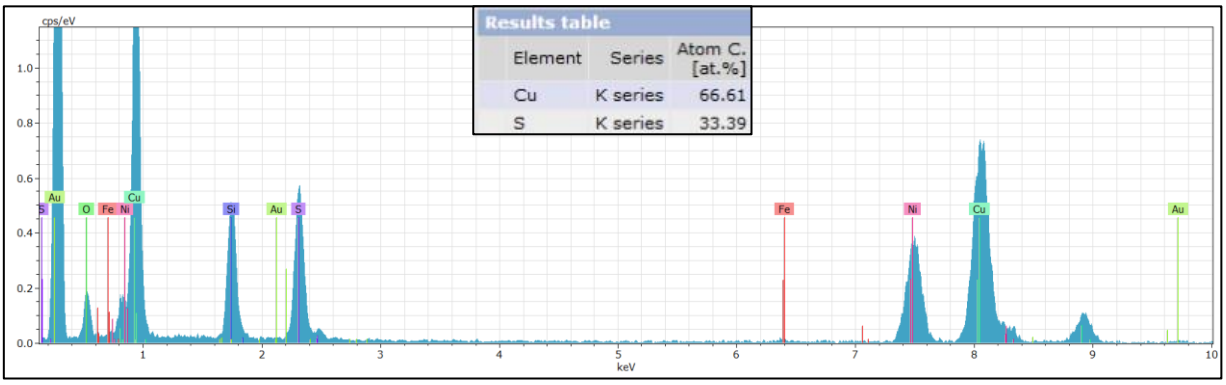

Figure 2.31: Spectrum obtained from quantitative Energy Dispersive X-ray Spectroscopy on multiple copper sulfide domains of a sample of trimers, insert: table with quantification related to copper and sulfur.

An interesting property of these three domains nano-heterostructures is the possibility to have two localized surface plasmon resonances (LSPR), displayed at different absorption wavelengths, in one single nanostructure. First LSPR should be coming from the metallic gold NPs, whose absorption band has been reported to be centered at approximatively 520 nm[72] for spherical 20-50 nm Au NPs, while a second absorption band should be arising from the presence of sub-stoichiometric copper(I) sulfide domains[73]. The absorption wavelength and the intensity of this second surface plasmon resonance has been reported to be strongly dependent on the stoichiometry of the copper sulfide phase ($Cu_{2-x}S$, $0< x <1$)[74].

During the formation of the FeO_y@Au@$Cu_{2-x}S$ trimers, absorption in the visible light wavelength range (500 nm – 800 nm) was checked through spectroscopy measurements. Measurements were performed after each synthesis step (after Au NPs nucleation, after FeO_y growth and after $Cu_{2-x}S$

formation) in order to monitor gold NPs plasmon absorption peak position. Results obtained from the measurements in chloroform are shown in Figure 2.32.

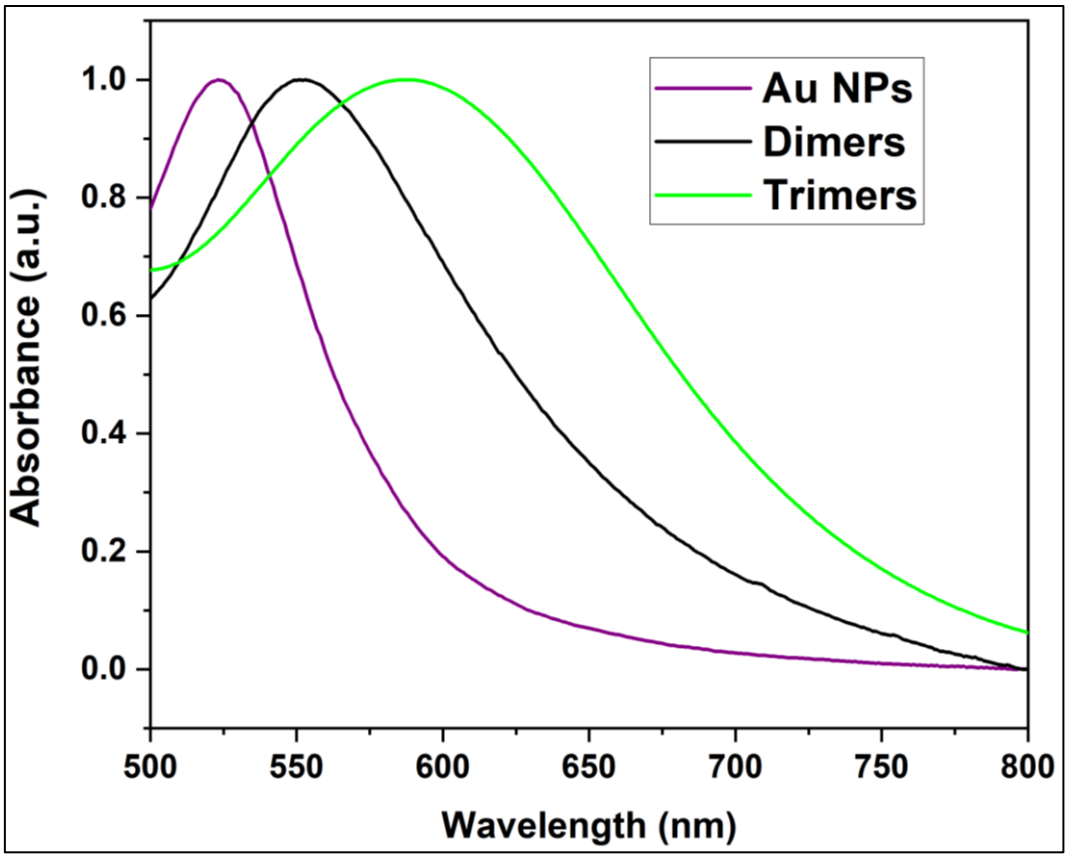

Figure 2.32: Visible (500-800 nm) spectra of gold NPs (purple line), Au@FeO_y dimers (black line) and FeO_y@Au@$Cu_{2-x}S$ trimers (green line), all particles were dispersed in chloroform. All curves are normalized on their maximum absorption in order to compare peaks positions and width.

Interestingly, with the growth of additional domains, the peak related to gold NPs LSPR is red-shifting. Indeed, while for gold NPs seeds the absorption is peaked at 524 nm (in good agreement with values reported in literature for small Au NPs), this peak is moved to 552 nm for Au@FeO_y dimers and 588 nm for FeO_y@Au@$Cu_{2-x}S$. This same behavior was found in all the sample of trimers synthesized, with small differences when varying the size of the three domains. Together with the red-shifting, also a broadening of the absorption band is taking place. The red-shift of the gold NPs plasmon in Au@FeO_y dumbbells is already reported in literature[46] and ascribed to the presence of the interface between Au and FeO_y, resulting in reduced electron population on Au. A red-shift in gold plasmon is also reported in the case of Au@$Cu_{2-x}S$ dimers[50], similarly to the case of Au@FeO_y, this shift can be ascribed to the growth of the $Cu_{2-x}S$ domain that is reducing electron density on the surface of the gold nanoparticle. This red-shift of the gold plasmon is of particular interest for biomedical application since after the growth of the additional iron oxide and copper sulfide domains, the tail of gold LSPR absorption band is entering the NIR biological window (NIR-I: 650–950 nm), and because of this can be used in photothermal therapy[75]. In order to also check the presence of the plasmon given by the copper-deficient copper sulfide domain, absorbance of trimers' sample was measured also in the Infrared Region with a long-range measurement (500-2000 nm). Spectrum resulting from the measurement of the absorbance of the chloroform dispersion of one trimers' sample is shown in Figure 2.33.

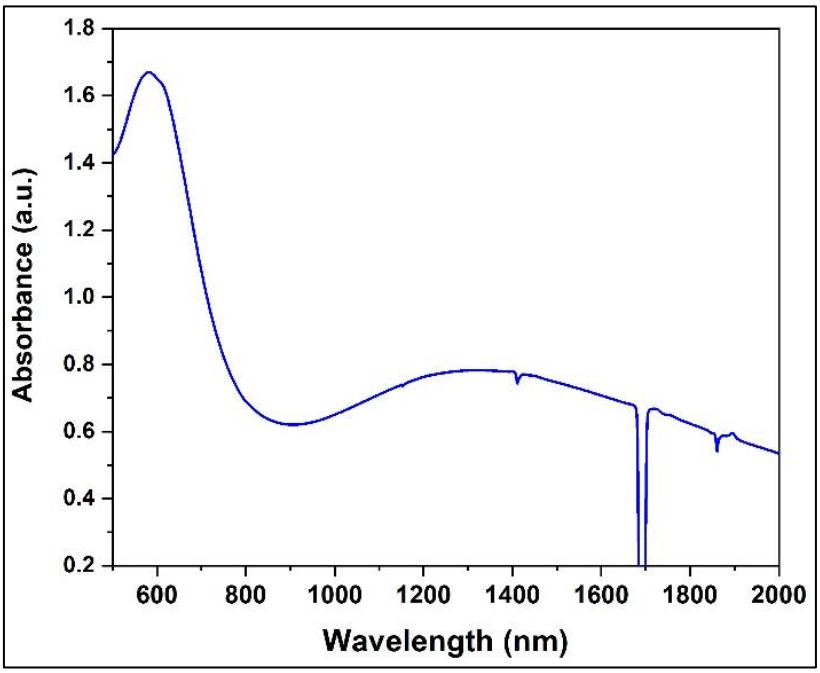

Figure 2.33: VIS-IR (500-2000 nm) spectrum of a sample of trimers, negative peak centered at 1700 nm and features around 1400 nm and 1850 nm are resulting from background ($CHCl_3$) signal subtraction.

Long-range spectrum reveals, together with gold plasmon, also a band centered around 1300 nm ascribable to copper-deficient copper sulfide. The band is broad and with low relative intensity, as expected when having a $Cu_{2-x}S$ domain with such a stoichiometry[76] and is centered in the second NIR biological window (1000 nm – 1350 nm)

Magnetic properties of FeO_y@Au@$Cu_{2-x}S$ were measured through SQUID magnetometry and compared with the ones of Au@FeO_y dimers used as seeds for that particular sample of trimers (see Figure 2.34).

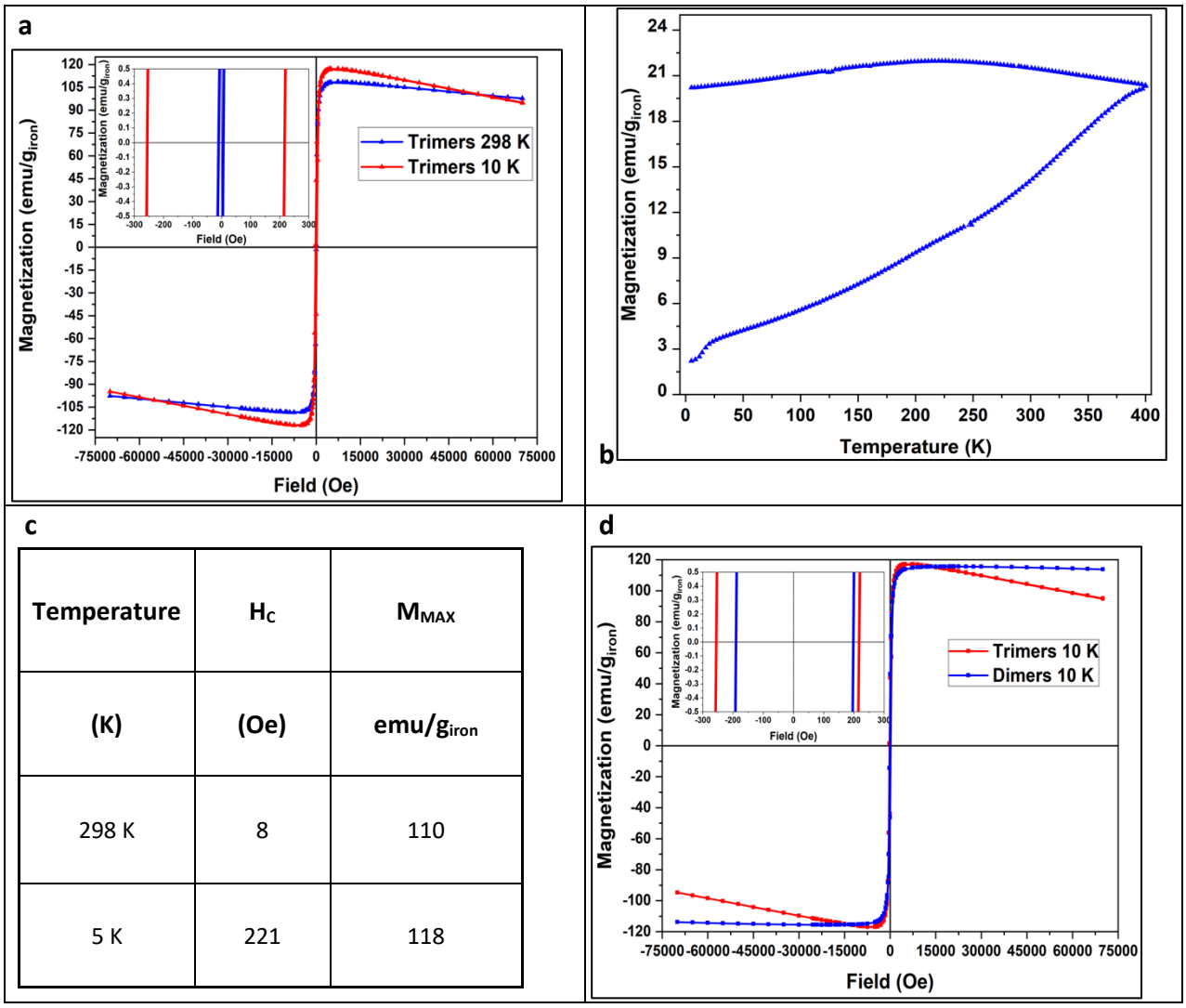

c

Temperature	H_C	M_{MAX}
(K)	(Oe)	emu/g_{iron}
298 K	8	110
5 K	221	118

Figure 2.34: Results obtained from magnetic measurements. a) Zero field cooled MH curves recorded in the range ± 70 kOe at 10 K (red line) and 298 K (blue line) on a sample of trimers having a 25 ± 4 nm iron oxide domain, insert: low field region of the MH curves at 10 K and 298 K; b) ZFC heating and FC cooling curves in the range 5 K – 400 K recorded using a 50 Oe field on a sample of trimers having a 25 ± 4 nm iron oxide domain; c) Parameters measured through SQUID measurement on a sample of FeO_y@Au@$Cu_{1.81}S$ with 25 ± 4 nm iron oxide domain. d) Comparison between zero field cooled MH curves recorded in the range ± 70 kOe at 10 K for a sample of trimers having a 25 ± 4 nm iron oxide domain (red line) and for a sample of dimers having a 25 ± 4 nm iron oxide domain (blue line)

Magnetic properties of the trimers are similar to what was found in the case of Au@FeO_y dimers (see paragraph 2.2.3), having the nanoparticles a high maximum magnetization (118 emu/g_{iron} at 10 K and 110 emu/ g_{iron} at 298 K). The small difference between these values and the ones obtained from Au@FeO_y with same iron oxide size (maximum magnetization of trimers is larger (+4%) at both temperatures), could be due to the error related to the measurement of iron content of each sample (ICP-OES measurements, 10 % error). Similarly to the case of dimers, trimers are blocked at RT (thus, trimer displays also a ferrimagnetic behavior at RT) and interacting as it can be clearly seen form ZFC-FC measurements results (Figure 2.34b). Interestingly, when comparing MH curves of dimers and trimers both at 298K and 10 K (see Figure 2.34d for curves comparison at 10 K), it is clear that trimers have a diamagnetic contribution at high fields that is not present in the hysteresis loop of dimers sample. This diamagnetic contribution was ascribed to the presence of $Cu_{2-x}S$ domains that, when *x* is between 0 and 0.2, are reported to be diamagnetic[77]. The similarity between the magnetic properties of trimers and the one of dimers make of FeO_y@Au@$Cu_{1.81}S$ trimers a possible candidate material to be used with good performances in magnetic hyperthermia cancer treatment.

2.3. Conclusions and outlook

Different trials were carried out in order to be able to merge in one single nano-heterostructure highly performing magnetic materials (iron oxide nanocubes and Au@FeO_y dimers developed in this research group) and a chalcogenide domain offering the possibility of incorporating ^{64}Cu (I) ions (demonstrated for $Cu_{2-x}S$ and for ZnS nanoparticles).

Trials to grow ZnS nanoparticles directly on the surface of Iron oxide nanocubes (IONCs) were unsuccessful, resulting in the growth of small ZnO particles surrounding IONCs with no clear formation of heterojunctions.

The possibility of using gold nanoparticles as "linkers" between the iron oxide and a chalcogenide domain was also tested. While it has been possible to grow Au@$Cu_{2-x}S$ dimers following a reported procedure, the modification of that procedure for the formation of Au@ZnS did not succeed. Indeed, the synthesis procedure resulted in either no nucleation of ZnS nanoparticles (with mild reaction parameters) or in the homonucleation of ZnS without the formation of any solid-solid interface (when more severe reaction conditions were used).

Adapting the synthesis of Au@$Cu_{2-x}S$ to the use of Au@FeO_y has brought to the successful synthesis of FeO_y@Au@$Cu_{2-x}S$ trimers. During the synthesis of these trimers, it is possible to vary the synthesis conditions (precursors' concentration) in order to tune the size of the novel $Cu_{2-x}S$ domain from 15 ± 3 nm to 33 ± 5 nm.

$Cu_{2-x}S$ domains are nucleated with low ordered roxbyite crystal structure, the crystals are highly defected and are growing on the surface of the twinned gold NPs. The nano-heterostructured trimers have two LSPRs: one due to the gold domain and centered at 588 nm, the second, due to the presence of the copper-deficient copper sulfide domain is centered at 1322 nm. Magnetic properties of the trimers are not significantly different from the ones of the dimers, apart from a diamagnetic contribution at high field caused by the presence of the copper sulfide domain.

The excellent magnetic properties (comparable with the one of the highly performing in hyperthermia IONCs and Au@FeO_y) of the trimers, together with two plasmonic absorption in the first and the second NIR biological windows, make of these heterostructures, once transferred to water, a candidate multifunctional material for the use in biomedical applications.

2.4. Experimental procedures

One-pot synthesis of γ-Fe_2O_3@ZnS heterostructures[28]

γ-Fe_2O_3 NCs were synthesized by thermal decomposition of iron pentacarbonyl ($Fe(CO)_5$) in the presence of capping molecules according to a previously reported procedure. After 11 mmol of oleic acid (OLAC) in 11 mL of octyl ether (OE) were vacuum-degassed at 100°C for at least 30 min, 1.5 mmol of $Fe(CO)_5$ were injected under N_2 atmosphere. The reaction mixture was refluxed at $T = 290$°C for 60 minutes. The γ-Fe_2O_3@ZnS heterostructures were synthesized by direct addition of sulfur and zinc reagent to the γ-Fe_2O_3 NCs reaction mixture. 0.25 mmol of sulfur powder were added to the flask containing crude γ-Fe_2O_3 NC reaction mixture at 100°C and stirred for 5 min. A solution of 0.25 mmol zinc acetate, and 1.034 mmol of tri octyl phosphine oxide (TOPO) in 1 mL of OE, which was vacuum-dried previously at 100°C, was then injected dropwise within one minute at 80°C. After 10 min of stirring at 80°C, temperature was raised to values ranging from 230°C to 280°C. The reaction mixture was allowed to anneal at high temperature for times ranging from 60 to 180 minutes and then cooled down to room temperature. Obtained nanoparticles were then purified from unreacted precursors and excess surfactants by dispersing them in chloroform and then precipitating with ethanol and centrifuging. After three centrifuging steps (2600 RCF, 5 minutes) using acetone as precipitant the particles were dispersed in chloroform to form a stable suspension.

Synthesis of iron oxide nanocubes (IONCs)[55]

The IONCs of edge length 16 ± 2 were prepared according to a procedure previously developed in this group[55]. Briefly, into a 100 mL three-neck flask, 15 mL of di benzyl ether (DBE), 10 mL squalane, 1 mmol iron (III) acetyl acetonate and 5.5 mmol of decanoic acid were dissolved. After degassing for 120 min at 65°C, the mixture was heated up to 200°C at a rate of 3°C/min and maintained at that temperature for 150 minutes. Later, the reaction temperature was increased to 310°C (with a rate of 7°C/min) and the reaction was carried on for sixty more minutes. After cooling down the solution to room temperature, acetone was added as precipitant and the mixture was centrifuged at 2600 RCF for 20 minutes. After repeating the centrifuging procedure twice, the obtained particles were dispersed in chloroform.

Seeded growth of ZnS particles on IONC seeds

In order to grow ZnS domains on IONCs, a chloroform solution of the nanocubes (≈ 0.15 mmol in iron) was mixed with 11 mL of OE and 11 mmol of OLAC and degassed under vacuum at 100°C for 60 minutes. After the degassing, 0.025 mmol of sulfur powder were added to the reaction mixture and the batch was annealed for 10 minutes. After cooling to 80°C a solution of 0.025 mmol zinc acetate, and 1.034 mmol of TOPO in 1 mL of octyl ether, that was previously degassed at 100 °C, was injected. After 10 min of stirring at 80 °C, temperature was raised to 280 °C and the reaction mixture was allowed to anneal by stirring at that temperature for 60 minutes and then cooled to room temperature. After three centrifuging steps (2600 RCF, 5 minutes) using acetone as precipitant the particles were dispersed in chloroform to form a stable suspension.

HR-TEM imaging, HAADF STEM imaging and EDS analyses

On some selected samples, crystal structure was analyzed by means of High Resolution Transition Electron Microscopy (HR-TEM) while chemical composition was evaluated exploiting energy-dispersive X-ray spectroscopy (EDS), performed in high angle annular dark field scanning TEM (HAADF-STEM) mode. HR-TEM imaging, HAADF-STEM imaging and EDS analyses were carried out using a JEOL JEM-2200FS microscope equipped with a Schottky emitter working at an accelerating voltage of 200 kV, a CEOS spherical aberration corrector for the objective lens, and a Bruker Quantax 400 system with a 60 mm^2 XFlash 5060 silicon drift detector (SDD). EDS analyses were performed drop-casting NCs suspensions (both in organic solvent and in water) on carbon coated nickel grids. The EDS spectra were quantified using the Cliff- Lorimer method on Zn K_α, Fe K_α, O K_α, S K_α, Au L_α and Cu K_α and the reported STEM-EDS maps were obtained by integrating the intensities over the same peaks.

Au@FeO_y dimers synthesis[19]

In a 100 ml three necked flask, equipped with a magnetic stirrer and connected to a standard Schlenk line set up, 0.1 mmol of $HAuCl_4 \times 3H_2O$ were dissolved in a solution containing 1 ml of Oleic Acid (OLAC), 3 ml of Oleyl amine (OA) and 20 ml of 1-octadecene (ODE). The mixture was heated to 95°C and degassed for 35 minutes. The flask was then switched to inert atmosphere (N_2 gas) and heated to 150°C. At this temperature, a solution of 0.6 mmol of $Fe(CO)_5$ in degassed ODE was injected into the reaction batch and the temperature increased to 200°C. The solution was then annealed for different amounts of time, ranging from thirty to ninety minutes. The reaction batch was then cooled to room temperature and the obtained product washed by means of centrifugation (2600 RCF 15 minutes) and redispersion using isopropanol as precipitant and chloroform as solvent. After supernatant removal, the washed particles were transferred using 40 ml of chloroform in a 40 ml glass vial. The Au-FeO_y dimers were then recollected to a 0.4 T magnet for 180 minutes. After supernatant removal, the particles were re-dispersed in 10 ml of chloroform in a 20 ml vial and sonicated at RT for 30 minutes. When Au@FeO_y dimers had to be used as seeds in other synthesis, they were dispersed in a 5% solution of OLAC in $CHCL_3$ (500 µl of Oleic Acid + 9.5 mL of chloroform) in order to improve stability.

SQUID magnetometer analyses

On some selected samples, the variation of the sample magnetization when changing external field (hysteresis loops or magnetization curves) or temperature (ZFC-FC curves) were measured using a super-conducting quantum interference device (SQUID) from Quantum Design (MPMS XL equipped with Evercool Dewar). Samples preparation was performed by drop casting chloroform solution of particles with known concentration onto 100 mg of Teflon film. The sample was allowed to dry overnight. Magnetization curves were measured from -70 to +70 kOe at 10 K and 298 K upon zero field cooling (ZFC). Zero field cooled (ZFC) and field cooled (FC) curves were recorded with a field of 50 Oe in the temperature range 5 K – 400 K (1.5 K/min in 2.99 K increments) to measure the thermal dependence of the magnetization. The background signal coming from 100 mg of Teflon tape and from the sample holder has been subtracted from the data obtained from all measurements.

Synthesis of gold nanoparticles[67]

Au NPs were obtained using a literature reported procedure.[66] In a 50 mL three necked flask, a solution of tetralin (10 mL), oleyl amine (OA, 10 mL), and 0.1 g (0.25 mmol) $HAuCl_4$ was prepared in air at room temperature (RT = 23 °C) and magnetically stirred under N_2 flow for 10 min. A reducing solution containing 43 mg (0.5 mmol) of Tert-butyl ammine-borane complex, tetralin (1 mL), and OA (1 mL) was mixed by sonication and injected into the precursor solution. The reduction was instantaneously initiated and the solution changed to a deep purple color within few seconds. The mixture was allowed to react at R.T. for 60 minutes before isopropanol was added to precipitate the Au NPs. The Au NPs were collected by centrifugation (6300 RCF, 5 minutes), washed again with isopropanol, dispersed in chloroform and then transferred, through evaporation and redispersion, in OA.

Seeded growth of Au@$Cu_{2-x}S$ nano-heterostructures[50]

In a typical preparation of Au-$Cu_{2-x}S$ NCs, 85.2 mg (0.5 mmol) of $CuCl_2 \cdot 2H_2O$, 7 mL of OA, and 3mL of an Au–OA (0.025 mmol Au) solution were successively introduced to a 25 mL four-neck flask connected to a Schlenk line. The mixture was fully flushed with nitrogen at room temperature and then heated to 180 °C. The nucleation and growth of $Cu_{2-x}S$ on the surface of the Au NCs was then initiated by the injection of 1 mL of di-tert-butyl disulfide (TBDS) (10 mmol). The reaction mixture was kept at 180 °C for 70 min to allow the NCs to grow. The flask was then rapidly cooled down to room temperature and the resulting NCs suspension was precipitated with isopropanol and centrifugation (2600 RCF, 5 minutes) and dispersed in chloroform for three cycles.

Seeded growth of Au@ZnS nano-heterostructures

In a typical synthesis, different amounts of $ZnCl_2$, 7 mL of OA, and 3mL of Au–OA solution (0.025 mmol of Au) were successively introduced to a 25 mL four-neck flask connected to a Schlenk line. The mixture was fully flushed with nitrogen at room temperature and then heated to annealing temperature. The nucleation and growth of ZnS nanoparticles was consequently started by the injection, of an amount of TBDS equal to twenty times the amount of zinc precursor. The reaction mixture was kept at the annealing temperature for 70 min. The flask was then rapidly cooled down to room temperature and the resulting NCs suspension was precipitated with isopropanol and centrifugation (2600 RCF, 5 minutes) and dispersed in chloroform for three cycles.

FeO_y@Au@$Cu_{2-x}S$ synthesis

8 mL of oleyl amine, chloroform solution of Au@FeO_y dimers (gold content equal to 1/13.3 of copper precursor used) and an amount of $CuCl_2 \times 2H_2O$ varying from 0.4 mmol to 0.1 mmol were degassed for 60 minutes at 40°C in order to remove $CHCl_3$. After the temperature was increased to 160°C, an amount of di-Tert-Butyl Disulfide (TBDS) with sulfur content equal to twenty times copper precursor used was injected and the reaction batch annealed at that temperature for 240 minutes. Reaction mixture was then transferred to three 50 mL falcon tubes and precipitated through the addition of isopropanol and centrifuging (2600 RCF, 7 minutes, 2 cycles). Resulting precipitate was dispersed in chloroform and precipitated again with isopropanol and centrifuging. After the washings, particles were dispersed in a 5% solution of oleic acid in chloroform and stored at room temperature.

UV−VIS−NIR spectroscopy

Absorption spectra of the samples were measured exploiting UV−VIS−NIR spectroscopy. Optical extinction spectra, of both chloroform and water stable sample, were acquired, both in the range 500-800 nm and in the range 500-2000 nm, on a Varian Cary 5000 UV−vis−NIR absorption spectrophotometer using a 3 mL quartz cuvette.

2.5. References

1. Walther, A. & Müller, A. H. E. Janus particles. *Soft Matter* **4**, 663–668 (2008).

2. de Gennes, P. G. Soft Matter. *Science (80-.).* **256**, 495–497 (1992).

3. Chun, H. J. *et al.* Water-soluble mercury ion sensing based on the thymine-Hg2+-thymine base pair using retroreflective Janus particle as an optical signaling probe. *Biosens. Bioelectron.* **104**, 138–144 (2018).

4. Ke, H., Ye, S., Carroll, R. L. & Showalter, K. Motion analysis of self-propelled Ptsilica particles in hydrogen peroxide solutions. *J. Phys. Chem. A* **114**, 5462–5467 (2010).

5. Mano, T., Delfau, J. B., Iwasawa, J. & Sano, M. Optimal run-And-Tumble-based transportation of a Janus particle with active steering. *Proc. Natl. Acad. Sci. U. S. A.* **114**, E2580–E2589 (2017).

6. Du, J. & O'Reilly, R. K. Anisotropic particles with patchy, multicompartment and Janus architectures: Preparation and application. *Chem. Soc. Rev.* **40**, 2402–2416 (2011).

7. Walther, A. & Müller, A. H. E. Janus particles: Synthesis, self-assembly, physical properties, and applications. *Chem. Rev.* **113**, 5194–5261 (2013).

8. Zhang, Y., Huang, K., Lin, J. & Huang, P. Janus nanoparticles in cancer diagnosis, therapy and theranostics. *Biomater. Sci.* **7**, 1262–1275 (2019).

9. Yang, T. *et al.* Dumbbell-Shaped Bi-component Mesoporous Janus Solid Nanoparticles for Biphasic Interface Catalysis. *Angew. Chemie - Int. Ed.* **56**, 8459–8463 (2017).

10. Najafishirtari, S. *et al.* Manipulating the morphology of the nano oxide domain in AuCu-iron oxide dumbbell-like nanocomposites as a tool to modify magnetic properties. *RSC Adv.* **8**, 22411–22421 (2018).

11. Alexeev, A., Uspal, W. E. & Balazs, A. C. Harnessing Janus nanoparticles to create controllable pores in membranes. *ACS Nano* **2**, 1117–1122 (2008).

12. Kherzi, B. & Pumera, M. Self-propelled autonomous nanomotors meet microfluidics. *Nanoscale* **8**, 17415–17421 (2016).

13. Ma, X. *et al.* Enzyme-Powered Hollow Mesoporous Janus Nanomotors. *Nano Lett.* **15**, 7043–7050 (2015).

14. Wang, H., Yang, S., Yin, S. N., Chen, L. & Chen, S. Janus suprabead displays derived from the modified photonic crystals toward temperature magnetism and optics multiple responses. *ACS Appl. Mater. Interfaces* **7**, 8827–8833 (2015).

15. Nisisako, T., Torii, T., Takahashi, T. & Takizawa, Y. Synthesis of monodisperse bicolored janus particles with electrical anisotropy using a microfluidic co-flow system. *Adv. Mater.* **18**, 1152–1156 (2006).

16. Yue, S. *et al.* SERS-Fluorescence Dual-Mode pH-Sensing Method Based on Janus

Microparticles. *ACS Appl. Mater. Interfaces* **9**, 39699–39707 (2017).

17. Lu, C. *et al.* Multifunctional Janus Hematite-Silica Nanoparticles: Mimicking Peroxidase-Like Activity and Sensitive Colorimetric Detection of Glucose. *ACS Appl. Mater. Interfaces* **7**, 15395–15402 (2015).

18. Rojas, D., Jurado-Sánchez, B. & Escarpa, A. 'Shoot and Sense' Janus Micromotors-Based Strategy for the Simultaneous Degradation and Detection of Persistent Organic Pollutants in Food and Biological Samples. *Anal. Chem.* **88**, 4153–4160 (2016).

19. Guardia, P. *et al.* Gold–iron oxide dimers for magnetic hyperthermia: the key role of chloride ions in the synthesis to boost the heating efficiency. *J. Mater. Chem. B* **5**, 4587–4594 (2017).

20. Iqbal, M. Z. *et al.* A facile fabrication route for binary transition metal oxide-based Janus nanoparticles for cancer theranostic applications. *Nano Res.* **11**, 5735–5750 (2018).

21. Park, S. S. *et al.* Functionalised mesoporous silica nanoparticles with excellent cytotoxicity against various cancer cells for pH-responsive and controlled drug delivery. *Mater. Des.* **184**, 108187 (2019).

22. Wang, C., Yin, H., Dai, S. & Sun, S. A general approach to noble metal-metal oxide dumbbell nanoparticles and their catalytic application for CO oxidation. *Chem. Mater.* **22**, 3277–3282 (2010).

23. Laursen, S. & Linic, S. Oxidation catalysis by oxide-supported Au nanostructures: The role of supports and the effect of external conditions. *Phys. Rev. Lett.* **97**, 1–4 (2006).

24. Hu, J., Zhou, S., Sun, Y., Fang, X. & Wu, L. Fabrication, properties and applications of Janus particles. *Chem. Soc. Rev.* **41**, 4356–4378 (2012).

25. Lattuada, M. & Hatton, T. A. Synthesis, properties and applications of Janus nanoparticles. *Nano Today* **6**, 286–308 (2011).

26. Jiang, S. *et al. Janus Particle Synthesis, Self-Assembly and Applications*. *Advanced Materials* **22**, (Royal Society of Chemistry, 2012).

27. Thanh, N. T. K., Maclean, N. & Mahiddine, S. Mechanisms of nucleation and growth of nanoparticles in solution. *Chem. Rev.* **114**, 7610–7630 (2014).

28. Kwon, K.-W. & Shim, M. γ-Fe 2 O 3 /II−VI Sulfide Nanocrystal Heterojunctions. *J. Am. Chem. Soc.* **127**, 10269–10275 (2005).

29. Wang, C., Wei, Y., Jiang, H. & Sun, S. Tug-of-war in nanoparticles: Competitive growth of Au on Au-Fe 3 O 4 nanoparticles. *Nano Lett.* **9**, 4544–4547 (2009).

30. Carbone, L. & Cozzoli, P. D. Colloidal heterostructured nanocrystals: Synthesis and growth mechanisms. *Nano Today* **5**, 449–493 (2010).

31. Shim, M. & McDaniel, H. Anisotropic nanocrystal heterostructures: Synthesis and lattice strain. *Curr. Opin. Solid State Mater. Sci.* **14**, 83–94 (2010).

32. Casavola, M., Buonsanti, R., Caputo, G. & Cozzoli, P. D. Colloidal strategies for preparing oxide-based hybrid nanocrystals. *Eur. J. Inorg. Chem.* 837–854 (2008). doi:10.1002/ejic.200701047

33. Gu, H., Zheng, R., Zhang, X. X. & Xu, B. Facile One-Pot Synthesis of Bifunctional Heterodimers of Nanoparticles: A Conjugate of Quantum Dot and Magnetic Nanoparticles. *J. Am. Chem. Soc.* **126**, 5664–5665 (2004).

34. McDaniel, H. & Shim, M. Size and growth rate dependent structural diversification of FeO/CdS anisotropic nanocrystal heterostructures. *ACS Nano* **3**, 434–440 (2009).

35. Kwon, K.-W., Lee, B. H. & Shim, M. Structural Evolution in Metal Oxide/Semiconductor Colloidal Nanocrystal Heterostructures. *Chem. Mater.* **18**, 6357–6363 (2006).

36. Mehdaoui, B. *et al.* Optimal size of nanoparticles for magnetic hyperthermia: A combined theoretical and experimental study. *Adv. Funct. Mater.* **21**, 4573–4581 (2011).

37. Liu, L. *et al.* Fabrication of fluorescent magnetic Fe3O4@ZnS nanocomposites. *J. Nanosci. Nanotechnol.* **14**, 5047–5053 (2014).

38. Zhan, F. & Zhang, C. Y. Bifunctional nanoparticles with superparamagnetic and luminescence properties. *J. Mater. Chem.* **21**, 4765–4767 (2011).

39. Lin, A. W. H. *et al.* Seed-mediated synthesis, properties and application of γ-Fe 2O3-CdSe magnetic quantum dots. *J. Solid State Chem.* **184**, 2150–2158 (2011).

40. Ang, C. Y. *et al.* Facile synthesis of Fe2O3 nanocrystals without Fe(CO)5 precursor and one-pot synthesis of highly fluorescent Fe 2O3-CdSe nanocomposites. *Adv. Mater.* **21**, 869–873 (2009).

41. Selvan, S. T., Patra, P. K., Ang, C. Y. & Ying, J. Y. Synthesis of silica-coated semiconductor and magnetic quantum dots and their use in the imaging of live cells. *Angew. Chemie - Int. Ed.* **46**, 2448–2452 (2007).

42. Zhou, H., Tao, K., Sui, Y. & Sun, K. Heterogeneous nucleation and growth of CdSe on magnetite seed nanocrystals: The influence of ligand and morphology. *Phys. E Low-Dimensional Syst. Nanostructures* **44**, 597–604 (2011).

43. Cho, M. *et al.* Characterization and optimization of the fluorescence of nanoscale iron oxide/quantum dot complexes. *J. Phys. Chem. C* **118**, 14606–14616 (2014).

44. Tian, Q. *et al.* Sub-10 nm Fe3O4@Cu2-xS core-shell nanoparticles for dual-modal imaging and photothermal therapy. *J. Am. Chem. Soc.* **135**, 8571–8577 (2013).

45. Shi, W. *et al.* A general approach to binary and ternary hybrid nanocrystals. *Nano Lett.* **6**, 875–881 (2006).

46. Yu, H. *et al.* Dumbbell-like Bifunctional Au−Fe 3 O 4 Nanoparticles. *Nano Lett.* **5**, 379–382 (2005).

47. Lin, F., Chen, W., Liao, Y.-H., Doong, R. & Li, Y. Effective approach for the synthesis of monodisperse magnetic nanocrystals and M-Fe3O4 (M = Ag, Au, Pt, Pd) heterostructures. *Nano Res.* **3**, 676–684 (2011).

48. Zhang, M., He, X., Chen, L. & Zhang, Y. Preparation of IDA-Cu functionalized core–satellite Fe3O4/polydopamine/Au magnetic nanocomposites and their application for depletion of abundant protein in bovine blood. *J. Mater. Chem.* **20**, 10696 (2010).

49. Kakwere, H. *et al.* Dually responsive gold-iron oxide heterodimers: Merging stimuli-responsive surface properties with intrinsic inorganic material features. *Nanoscale* **10**, 3930–3944 (2018).

50. Wang, H. *et al.* A simple strategy to achieve shape control of Au-Cu 2−x S colloidal heterostructured nanocrystals and their preliminary use in organic photovoltaics. *Nanoscale* **10**, 11745–11749 (2018).

51. Liu, M. & Zeng, H. C. General synthetic approach to heterostructured nanocrystals based on noble metals and I-VI, II-VI, and I-III-VI metal chalcogenides. *Langmuir* **30**, 9838–9849 (2014).

52. Sun, Z. *et al.* A general approach to the synthesis of gold-metal sulfide core-shell and heterostructures. *Angew. Chemie - Int. Ed.* **48**, 2881–2885 (2009).

53. Dutta, S. K., Mehetor, S. K. & Pradhan, N. Metal semiconductor heterostructures for photocatalytic conversion of light energy. *J. Phys. Chem. Lett.* **6**, 936–944 (2015).

54. Haldar, K. K., Sinha, G., Lahtinen, J. & Patra, A. Hybrid colloidal Au-CdSe pentapod heterostructures synthesis and their photocatalytic properties. *ACS Appl. Mater. Interfaces* **4**, 6266–6272 (2012).

55. Guardia, P. *et al.* One pot synthesis of monodisperse water soluble iron oxide nanocrystals with high values of the specific absorption rate. *J. Mater. Chem. B* **2**, 4426 (2014).

56. Guardia, P. *et al.* Water-Soluble Iron Oxide Nanocubes with High Values of Specific Absorption Rate for Cancer Cell Hyperthermia Treatment. *ACS Nano* **6**, 3080–3091 (2012).

57. Riedinger, A. *et al.* Post-Synthesis Incorporation of 64Cu in CuS Nanocrystals to Radiolabel Photothermal Probes: A Feasible Approach for Clinics. *J. Am. Chem. Soc.* **137**, 15145–15151 (2015).

58. Najafishirtari, S. *et al.* The effect of Au domain size on the CO oxidation catalytic activity of colloidal Au-FeOx dumbbell-like heterodimers. *J. Catal.* **338**, 115–123 (2016).

59. Xu, C. *et al.* Au–Fe3O4 Dumbbell Nanoparticles as Dual-Functional Probes. *Angew. Chemie Int. Ed.* **47**, 173–176 (2008).

60. Dreaden, E. C., Alkilany, A. M., Huang, X., Murphy, C. J. & El-Sayed, M. A. The golden age: gold nanoparticles for biomedicine. *Chem. Soc. Rev.* **41**, 2740–2779 (2012).

61. Popovtzer, R. *et al.* Targeted gold nanoparticles enable molecular CT imaging of cancer. *Nano Lett.* **8**, 4593–4596 (2008).

62. Riley, R. S. & Day, E. S. Gold nanoparticle-mediated photothermal therapy: applications and opportunities for multimodal cancer treatment. *Wiley Interdiscip. Rev. Nanomed. Nanobiotechnol.* **9**, e1449 (2017).

63. Hilger, I. & Kaiser, W. A. Iron oxide-based nanostructures for MRI and magnetic hyperthermia. *Nanomedicine* **7**, 1443–1459 (2012).

64. Muscas, G. *et al.* The interplay between single particle anisotropy and interparticle interactions in ensembles of magnetic nanoparticles. *Phys. Chem. Chem. Phys.* **20**, 28634–28643 (2018).

65. Mitra, A., Mohapatra, J., Meena, S. S., Tomy, C. V. & Aslam, M. Verwey transition in ultrasmall-sized octahedral Fe3O 4 nanoparticles. *J. Phys. Chem. C* **118**, 19356–19362 (2014).

66. Peng, S. *et al.* A facile synthesis of monodisperse Au nanoparticles and their catalysis of CO oxidation. *Nano Res.* **1**, 229–234 (2008).

67. Houk, L. R., Challa, S. R., Grayson, B., Fanson, P. & Datye, A. K. The Definition of "Critical Radius" for a Collection of Nanoparticles Undergoing Ostwald Ripening. *Langmuir* **25**, 11225–11227 (2009).

68. Holzwarth, U. & Gibson, N. The Scherrer equation versus the 'Debye-Scherrer equation'. *Nat. Nanotechnol.* **6**, 534 (2011).

69. Scherrer, P. & Debye, P. Werk Übergeordnetes Werk. *Nachr. Ges. Wiss. Göttingen, Math.-physik. Klasse* **2**, 101–120 (1918).

70. Portales, H. *et al.* Probing atomic ordering and multiple twinning in metal nanocrystals through their vibrations. *Proc. Natl. Acad. Sci. U. S. A.* **105**, 14784–14789 (2008).

71. Wang, Z. *et al.* Lattice-mismatch-induced twinning for seeded growth of anisotropic nanostructures. *ACS Nano* **9**, 3307–3313 (2015).

72. Amendola, V., Pilot, R., Frasconi, M., Maragò, O. M. & Iatì, M. A. Surface plasmon resonance in gold nanoparticles: A review. *J. Phys. Condens. Matter* **29**, 203002 (2017).

73. Zhao, Y. *et al.* Plasmonic Cu 2-xS nanocrystals: Optical and structural properties of copper-deficient copper(I) sulfides. *J. Am. Chem. Soc.* **131**, 4253–4261 (2009).

74. Kriegel, I. *et al.* Tuning the excitonic and plasmonic properties of copper chalcogenide nanocrystals. *J. Am. Chem. Soc.* **134**, 1583–1590 (2012).

75. Park, S. M., Aalipour, A., Vermesh, O., Yu, J. H. & Gambhir, S. S. Towards clinically translatable in vivo nanodiagnostics. *Nat. Rev. Mater.* **2**, (2017).

76. Xie, Y. *et al.* Copper Sulfide Nanocrystals with Tunable Composition by Reduction of Covellite Nanocrystals with Cu + Ions. *J. Am. Chem. Soc.* **135**, 17630–17637 (2013).

77. Kawai, S. Electrical conduction and phase transition of copper sulfides. *Jpn. J. Appl. Phys.* **12**, 1130–1138 (1973).

Chapter 3: FeO_y@Au@$Cu_{2-x}S$ nano-heterostructures as probes for magnetic hyperthermia, nuclear medicine and photothermal therapy.

3.1. Introduction

3.1.1. Treating cancer using heat with hyperthermia treatments

More than two thousand year ago, the father of medicine, Hippocrates (479 – 377 B.C.), was already aware of the potential of heat in the treatment of diseases.[1] Indeed, hyperthermia, the artificial temperature increase, of the body or of a tissue, above the normal temperature set by the thermoregulation system of an organism,[2] is nowadays a widely used cancer treatment.[3,4] This treatment can be used both as stand-alone therapy[5] or in combination with other treatments (e.g. chemotherapy, radiotherapy or surgery)[6–10] with the latter option being more effective.[11] Hyperthermia treatments are commonly differentiated based on the achieved temperature[12]: mild hyperthermia treatments are accomplished in a range of temperatures from 40 to 48°C while for higher temperatures the treatments are defined as coagulation[13] (>50°C), or thermal ablation[14] (60 to 90°C). Biological mechanism of cancer cells' death subjected to hyperthermia treatments are various and still objects of study.[15,16]

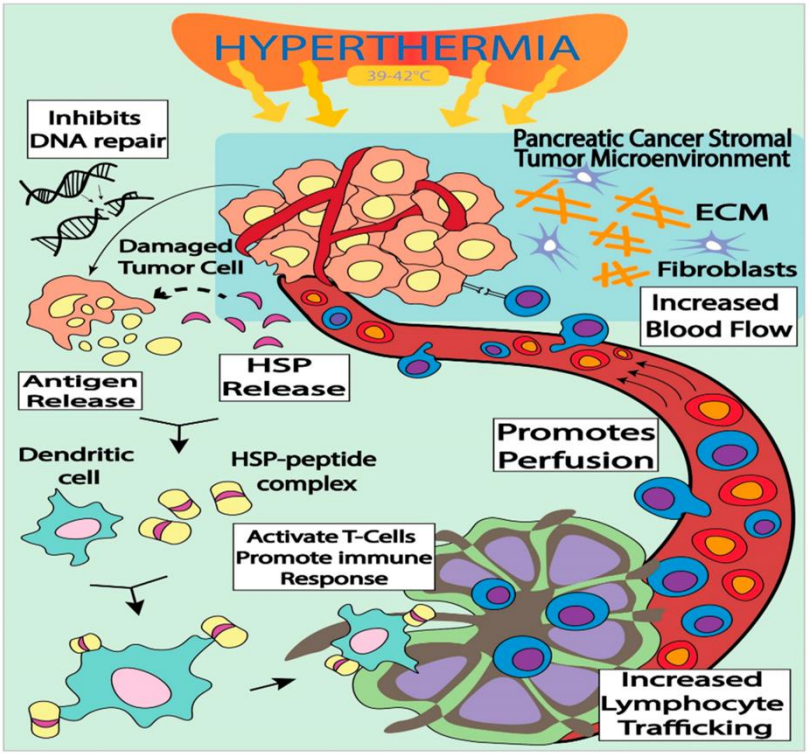

Figure 3.1: Impact of hyperthermia in activation of the immune response and inhibition of pancreatic cancer cell DNA repair. ECM: Extra Cellular Matrix; HSP: Heat Shock Protein. Reprinted with permission from reference 11.

Other than direct cell death, many other effects of hyperthermia treatments such as altered blood flow[17,18], inhibition of DNA repair pathways[19,20] and activation of immunological response[21,22] are reported (see Figure 3.1).

Hyperthermia can be administered to patients through three different methodologies: whole body hyperthermia, regional hyperthermia and local hyperthermia.[12] Whole-body hyperthermia (WBH) is usually performed on metastatic cancers[23] and applied through thermal chambers, hot water blankets or infrared radiation. The treatment is usually administered under general anesthesia and the temperature can be increased up to 42°C for 1 hour (extreme WBH) or kept in the range 39.5°C – 41°C for 3-4 hours (moderate WBH). Main advantage of these treatments is the homogeneous thermal distribution and the possibility to hit extended metastatic cancers, however, many complications such as cardiac disorders, changes in the coagulation system (thrombocytopenia and disseminated intravascular coagulation), and permeability of the capillary endothelia are reported.[10,24] Regional hyperthermia (also called part body hyperthermia) is employed to treat large parts of body (such as abdomen, pelvis or thighs) and is usually performed through external applicators producing microwaves[25] or radiofrequencies[26] or through perfusion[27]. Local (or targeted hyperthermia), on the other hand, is used to treat small areas (≤ 6 cm) either superficially located (skin) or accessible through body cavities (esophagus, rectum). Similarly to regional hyperthermia, lasers,[28] microwaves,[29] or ultrasounds[30] can be used to reach the aimed temperature in local hyperthermia treatments. In last decades,[31,32] many efforts were made in order to be able to exploit nanoparticles with different composition for local hyperthermia treatments. Main advantage of using nanoparticles for thermal treatments is the possibility to target a small area of tumoral tissue avoiding unspecific heating and overcoming the limitation of standard local hyperthermia treatments to superficial cancers. Another possibility related to the use of nanoparticles is, either exploiting their intrinsic properties or functionalizing their surface, to merge hyperthermia with other diagnosis or treatment applications, in order to exploit them as theragnostic agents.[33–35]

In order to be able to exploit nanoparticles for hyperthermia treatments, they have to be stable in aqueous media. Since as-synthesized particles are usually dispersed in organic solvents (hexane, chloroform or toluene), reproducible and high-yield water transfer procedures are needed. [36] In the group were this thesis was carried out, a broad portfolio of water transfer procedures for nanocrystals with different compositions has been developed. In particular, water transfer of metal oxide nanoparticles has been accomplished through a polymer coating (PC) procedure[37] (intercalating the ligand on the surface of the nanocrystal with an amphiphilic ligand) or through the exchange of the hydrophobic ligands on the surface of iron oxide particles with new amphiphilic ligands (ligand exchange procedure, LE) with catechol or carboxy groups anchoring nanocrystals' surface[38,39]. In the case of Au@FeO_y dimers, the phase transfer of the heterostructures in water was successfully accomplished[40] replacing the hydrophobic ligands with gallol-polyethylene glycol (GA-PEG), which covers both the iron oxide and the gold domain for their water stabilization. Copper-deficient copper sulfide nanocrystals covered with oleyl amine have been reported to be transferable in water using thiol-based amphiphilic polymers (*e.g.* methoxy-PEG2000-SH).[41] The water transfer of the newly synthesized trimers (see Chapter 2) has been accomplished through the use of these protocols with appropriate modifications.

3.1.2. Magnetic hyperthermia cancer treatments using magnetic nanoparticles

One possibility in order to perform thermal treatments using nanoparticles is given by the application of an alternating magnetic field (AMF) to a tissue where magnetic nanoparticles (MNPs) are dispersed. The use of magnetic nanoparticles as heating mediators in magnetic hyperthermia treatments (MHT) was already reported in 1957.[42] From that pioneering study the interest on this clinical methodology increased and today clinical phase II studies are led by MagForce company, in hospital Charité in Berlin.[43,44] When magnetic nanoparticles are stimulated through an alternating magnetic field, three different mechanisms can results in thermal energy production[45] (see Figure 3.2): Néel relaxation (rotation of the magnetic moment of the particle overcoming anisotropy energy barrier, Figure 3.2a), Brownian relaxation (mechanical rotation of the MNPs with friction against the surrounding medium, Figure 3.2b) and hysteresis losses (shifting of domains walls that takes place in multi-domain MNPs, Figure 3.2c).

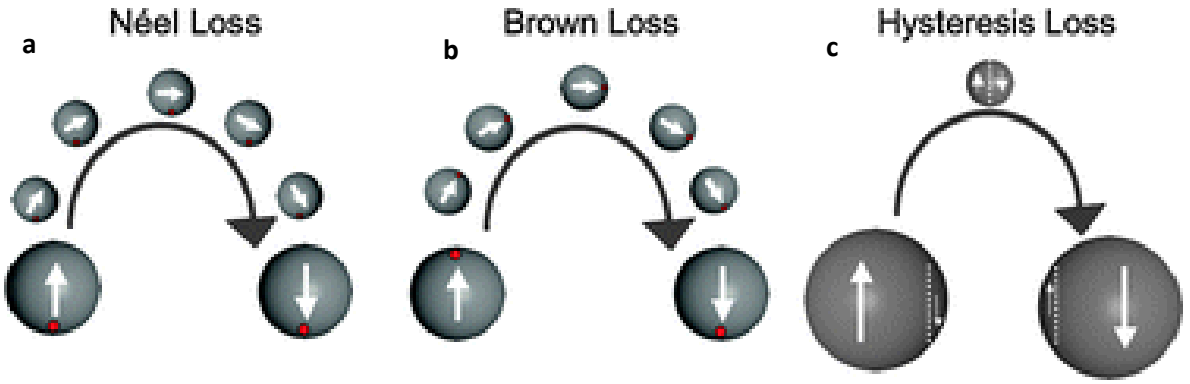

Figure 3.2: a) Rotation of the moment within the MNPs, overcoming their anisotropy energy barrier that leads to Néel Loss; b) mechanical rotation of the MNPs that results in friction with the environment and lead to Brown losses; c) movement of domain walls in multi-domain MNPs that leads to hysteresis loss. Reprinted with permission from reference 45.

Relative contribution of each of the three mechanisms is depending on many different parameters such as material composition, size, shape, magnetic anisotropy and grade of agglomeration of MNPs.[46–49] In particular, the size of the nanoparticles plays an important role on the heating mechanism. Indeed, under a certain value of diameter (called critical diameter, d_{cr}) the formation of domains wall is no more thermodynamically favored and each particle is formed by a single magnetic domain. The value of this critical diameter is changing from one magnetic material to another (see Figure 3.3).[50]

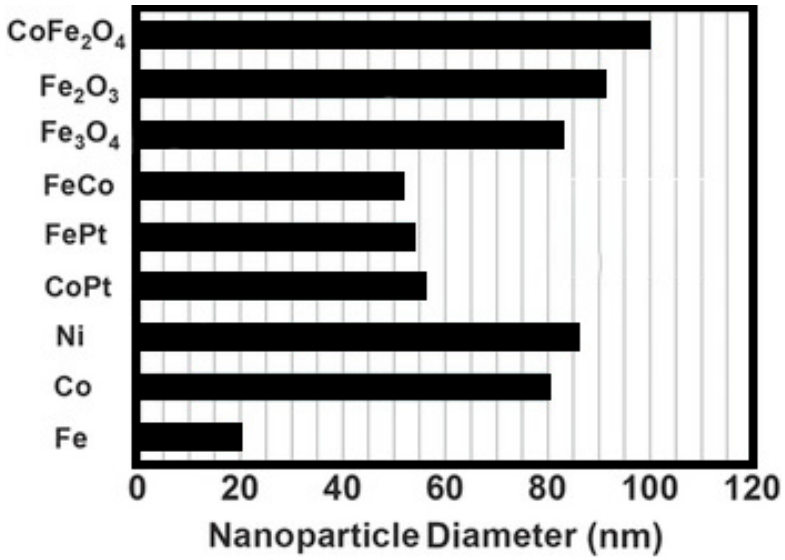

Figure 3.3: Single domain threshold diameter size for spherical nanoparticles of different materials. Calculated on the base of bulk materials parameters. Reprinted and adapted with permission from reference 50.

Below this critical diameter, hysteresis losses contribution is lost and the Néel and Brownian relaxations are the main heating mechanisms. Interplay between these two different mechanisms is given by particles' magnetic anisotropy, size, shape and solvent viscosity.[48,51,52] In general, smaller particles in high viscosity solvents tend to heat through Néel relaxation while larger particles in low viscosity solvents are usually undergoing Brownian relaxation. Combining all these parameters, many efforts have been made in order to be able to obtain magnetic nanoparticles with appropriate parameters for being used in high efficiency magnetic hyperthermia treatments.[53–55]

Heating performances of nanoparticles in magnetic fluid hyperthermia are usually evaluated through specific absorption rate (SAR o also SLP, specific loss power) values. SAR is defined as the power dissipated by MNPs per unit of mass. Two different methodologies (see Figure 3.4) are commonly used to assess hyperthermia efficiency of a MNPs sample[56]. The most common approach to determine SAR values is based on a calorimetric method (see Figure 3.4a). In this method, while MNPs' aqueous solutions are exposed to an AMF with given amplitude and frequency, the temperature increase is recorded through a fluoro-optic thermometer fiber probe over a period of time. AMF is applied through a magnetic induction heating system consisting of a water-cooled coil connected to a high power radio frequency generator. From the heating curve, SAR is calculated using the following formula:

$$SAR\left[\frac{W}{g}\right] = \frac{C}{m} \times \frac{dT}{dt}$$

Equation 3.1: Formula used to calculate SAR from calorimetric method

where *C* is the specific heat capacity of water per unit volume (4185 $J \times L^{-1} \times K^{-1}$), *m* is the concentration of magnetic material in solution ($g \times L^{-1}$ of Fe) and *dT/dt* is the slope of the measured heating curve. Although measurement chamber is isolated in order to reduce heat losses, these measurements are generally performed in non-adiabatic condition and, consequently, slope is measured from only the first seconds of measurements. The other methodology employed to evaluate efficiencies of

samples in magnetic hyperthermia experiments is the magnetometric method. In this method, dynamic magnetization M(t) of the sample is measured under an alternated magnetic field and integrated with respect to the applied field strength. SAR is then calculated following the formula:

$$SAR\left[\frac{W}{g}\right] = \frac{f}{c}\int m(t)dH$$

Equation 3.2: Formula to calculate SAR from magnetometric method

where f is the frequency of the applied field and c the magnetic material concentration.

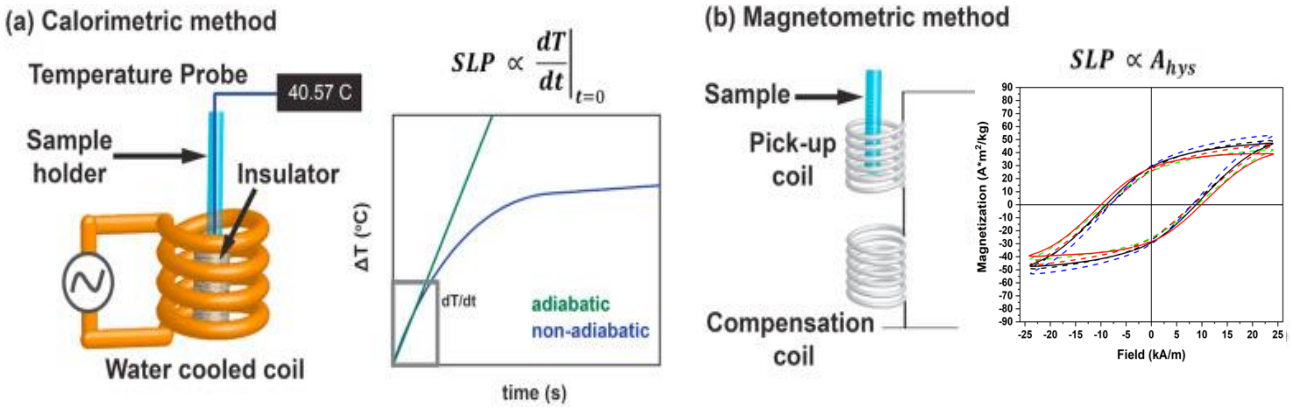

Figure 3.4: Diagrams of the different approaches used to evaluate the heating efficiency of magnetic nanoparticles: (a) calorimetric method: the changes in the temperature of the sample are recorded while it is exposed to an AMF and SLP is calculated from the initial slope of the sample's heating curve; and (b) magnetometric method, which involves the measurement of the AC hysteresis loop of the samples and wherein the SLP is proportional to the area of the hysteresis loop. Reproduced and adapted with permission from reference 56.

Both methodologies are commonly used in order to study dynamic magnetic properties of magnetic nanoparticles under the application of alternated magnetic fields.[38,48,57] In particular, although calorimetric method is the most commonly used technique in order to measure SAR values of magnetic nanoparticles,[37,58] the magnetometric method has currently been proven useful in order to investigate the influence of different parameters on the dynamic magnetic properties of nanoparticles.[39,48] In order to be able to compare the SAR values obtained for trimers with the ones obtained for the magnetic heterostructures used as seeds for their synthesis (Au@FeO_y dimers),[40] in this manuscript, SAR values have been measured through the calorimetric method. Hysteresis loops obtained by magnetometric method have been used in order to correlate the hyperthermia efficiencies of the different samples with their dynamic magnetic properties.

In last decades, many different nanomaterials suitable for magnetic hyperthermia treatments were developed. Among them, the most commonly used are FDA approved iron oxide nanoparticles[37,59–61] or mixed ferrite nanocrystals such as cobalt ferrite,[58,62,63] zinc ferrite[64,65] or manganese ferrite.[66,67] Currently, efforts of the researchers working in this field are oriented towards the development of nanomaterials with higher efficiencies (larger SAR values). Indeed, an increased SAR value would allow to scale down the amount of nanoparticles employed in each treatment and, consequently, to reduce the cytotoxicity of the nanomaterial.[68] In order to pursue this goal, also magnetic nano-heterostructures, such as Fe(0)@iron carbide[69] or soft core-hard shell[70] structures, were synthesized and found to have increased hyperthermia efficiencies if compared to the single material nanoparticles.

3.1.3. Photothermal therapy using nanoparticles

Another class of hyperthermia therapies in which nanomaterials are widely used are photothermal treatments (photothermal therapy, PTT). In these treatments, temperature increase is obtained through photothermal transducing agents (PTAs) that are harvesting energy from appropriate electromagnetic radiations and converting it into heat. Most commonly used nanoparticles as PTAs are the one exhibiting localized surface plasmon resonance (LSPR).[71,72] Localized surface plasmon resonance (see Figure 3.5) is the collective oscillation of the free electrons of a nanoparticle resulting from the interaction with an electromagnetic wave.[73–75]

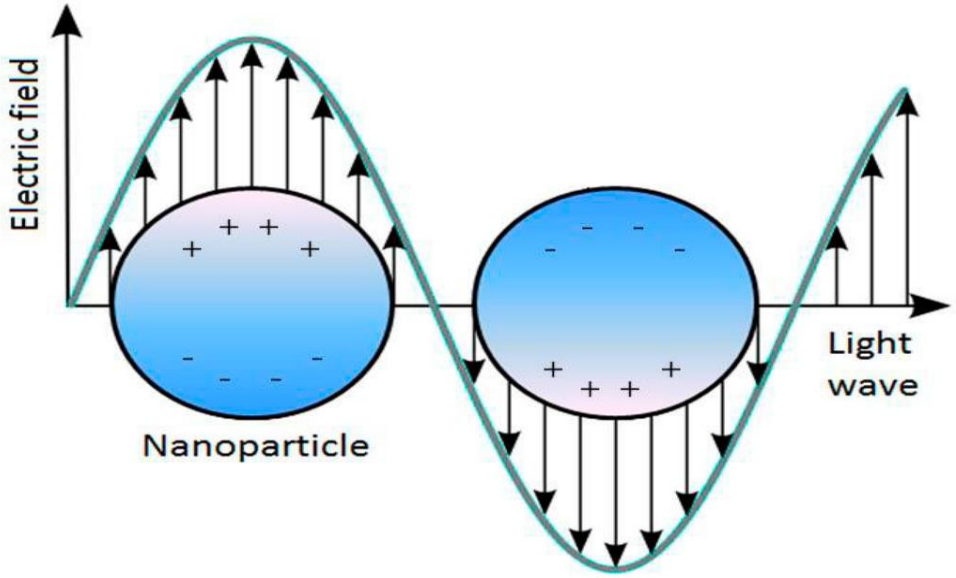

Figure 3.5: Schematic diagram showing localized surface plasmon resonance in nanoparticles, reproduced with permission from reference 72.

The intensity of the local electromagnetic field generated by this phenomenon on the surface of the nanoparticles can be orders of magnitude greater than those of the incident radiation.[76] This high intensity local fields are directly influencing the radiative and non-radiative properties of the plasmonic nanoparticles. Indeed, once exited, a plasmon can decay following two paths: non-radiatively, resulting in absorption of the exciting light; or radiatively, resulting in radiation scattering. Radiative decay of excited plasmonic nanoparticles is the base of their use as contrast agent in computer tomography (CT)[77,78] or in surface enhanced Raman spectroscopy (SERS)[79,80] imaging. On the other hand, non-radiative decay through electron–electron collisions and electron–lattice phonon coupling is the phenomenon on which photothermal therapy is based on. The predominant decay mechanism of excited nanoparticles is influenced by many different factors such as shape and size (as an example, 20 nm spherical nanoparticles are almost completely decaying by non-radiative processes),[81] consequently the properties of the nanoparticles have to be carefully tuned based on the aimed application.

M. A. El-Sayed group[82–84] thoroughly studied, through ultrafast dynamics, the mechanism behind heat production in photothermal heating by plasmonic nanostructures (see Figure 3.6).

Briefly, photoexcitation of the free electrons gas, resulting in rapid non-equilibrium heating, is followed by relaxation through electron–electron scattering. This results in rapid increase in the surface temperature of the metal, followed by cooling to equilibrium by energy transfer through

electrons and lattice phonons coupling. Finally, the lattice cools via phonon–phonon coupling and resulting heat is dissipated through the nanoparticle's surrounding media.

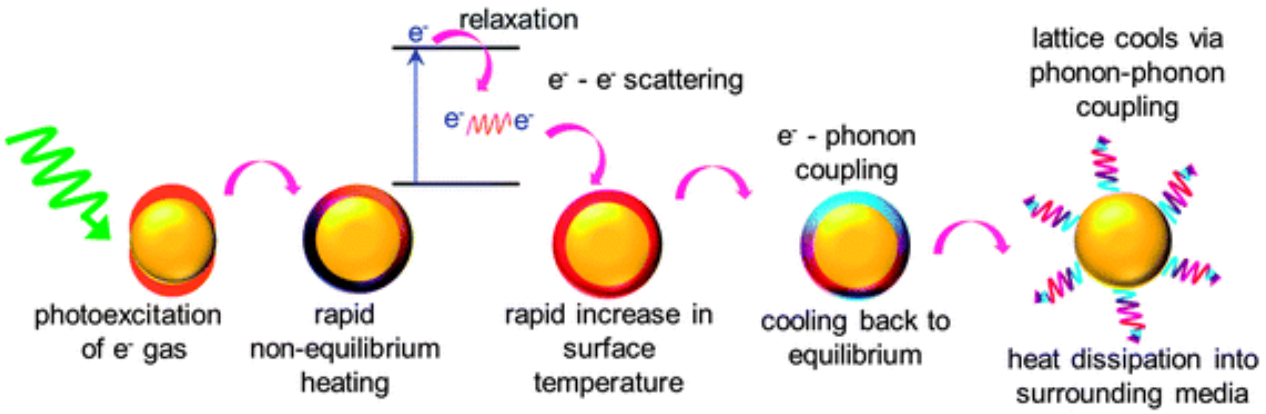

Figure 3.6: Schematic diagram representing the conversion of light into heat by plasmonic nanostructures Reprinted with permission from reference 75.

A key parameter, when designing plasmonic nanoparticles to be used as PTAs, is the wavelength absorption corresponding to the plasmon resonance. Indeed, the laser radiation used to excite plasmonic nanoparticles has to be able to reach nanoparticle without being absorbed from the surrounding tissues since this would reduce the energy of the incoming radiation and would damage healthy tissues. Typically, for this purpose, laser radiations with wavelengths in the near infrared region (NIR) are used.[85] Indeed, the scattering and absorption of NIR radiation by human tissues is lower if compared to the one obtained with visible light or UV light lasers.[86] In particular, tissues' absorption and scattering of laser radiation is negligible (radiation can travel through tissues with 2 – 3 cm path length) in the three so-called NIR biological windows (see Figure 3.7).

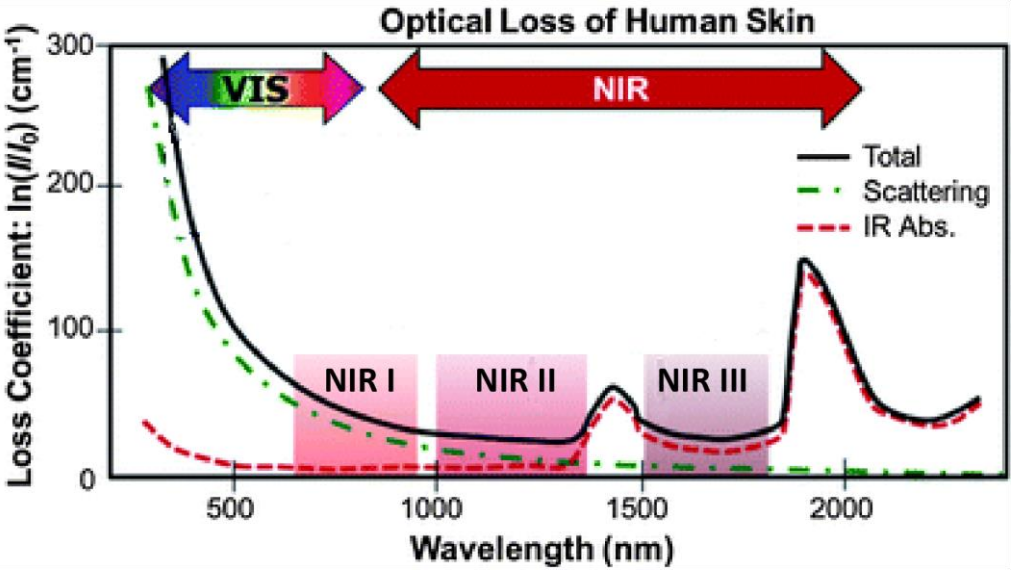

Figure 3.7: Absorption spectrum of human skin showing the first, second and third NIR windows. Reprinted and adapted with permission from reference 85.

First NIR window is ranging from 650 nm to 950 nm, while the second and the third ones are between 1000 nm and 1350 nm and between 1500 nm and 1800 nm, respectively.

Among all the nanoparticles investigated for the application in photothermal therapy, gold nanoparticles of different sizes and shapes are the most studied and promising.[87–89] Absorption of

Au nanospheres is usually centered in the range between 500 nm and 600 nm with larger particles having higher absorption wavelength. These spherical nanoparticles are usually exploited with laser having wavelengths in the 1st NIR biological window[90] targeting the absorption tail of the gold NPs plasmonic peak. Another class of gold nanomaterial widely exploited for photothermal treatments are gold Nanorods (NRs)[91,92]. The peculiarity of the Au NRs is to have, due to their shape anisotropy, two plasmon resonances: transverse plasmon resonance, usually centered between 500 and 550 nm, and longitudinal resonance between 650 nm and 850 nm. This second absorption wavelength can be tuned to higher values by increasing NRs' aspect ratio.[93] Photothermal treatments exploiting other gold nanostructures such as nanoshells (GNSs),[94,95] or nanostars (GNSTs)[96,97] have also been reported. Together with gold, also other noble metals nanocrystals, such as Pt or Pd[98,99] have been demonstrated to be effective when used as PTAs in PTT.

In 2010, Chen and coworkers indicated copper deficient copper sulfide nanocrystals as candidate material to be used as PTAs in photothermal therapy using a 808 nm laser.[100] Although in this pioneering study the power density used (> 24 W/cm^2) was more than 70 times higher than the safe value for biological applications (0.33 W/cm^2),[101] its publication leaded the way to many further studies on this class of materials. Indeed, in last two decades, many studies were carried out in which performances of copper-deficient copper sulfide nanoparticles were increased by changing either shape or stoichiometry of the material.[41,102–105]

In this chapter, after illustrating the development of a quantitative and reproducible water transfer procedure for FeO_y@Au@$Cu_{2-x}S$, are shown and discussed the results obtained by photothermal and magnetic hyperthermia characterization of FeO_y@Au@$Cu_{2-x}S$ trimers. In addition, also the results obtained from radiolabeling experiments performed in collaboration with Dr. Nisarg Rohitbhai Soni with ^{64}Cu on aqueous stable samples of trimers are presented.

3.2. Results and discussion

3.2.1. Water transfer of FeO_y@Au@$Cu_{2-x}S$ heterostructures

First step in order to check the possibility to use the newly synthesized FeO_y@Au@$Cu_{2-x}S$ in biomedical applications was to find a reliable and reproducible procedure to transfer those particles in aqueous media. The phase transfer of FeO_y@Au@$Cu_{2-x}S$ trimers in aqueous media is a challenging task being these heterostructures composed of three different domains with different surface chemistry and with different ligands stabilizing them in organic solvent. Considering the synthetic route developed for the formation of the trimers (see Chapter 2), oleic acid is expected to cover iron oxide surface whereas oleyl amine is expected to cover both gold and copper sulfide domains. Consequently, in ligand exchange procedures used for the water transfer of trimers, ligands having catechol groups were used for the replacement of oleic acid on iron oxide domains whereas thiol terminated ligands were employed to stabilize in water Au and $Cu_{2-x}S$ moieties. Consequently, different trials were carried on using both commercial polymers (poly(maleic anhydride-alt-1-octadecene), PMAO and CH_3O-PEG2000-SH) or molecules synthesized in our lab (α-nitrodopamine-ω-carboxy-poly(ethylene glycol), ND-PEG1500-COOH[106] and poly-catechol-PEG900).

First water transfer trials were carried out using ND-PEG1500-COOH (Figure 3.8a) synthesized by Dr. Helena Gavilan Rubio as amphiphilic ligands for the iron oxide domain (using 70 equivalent of tri ethyl amine for each ND-PEG1500-COOH molecule in order to deprotonate its carboxy an catechol groups) and CH_3O-PEG2000-SH (Figure 3.8b) to substitute oleyl amine molecules covering gold and copper sulfide domains.

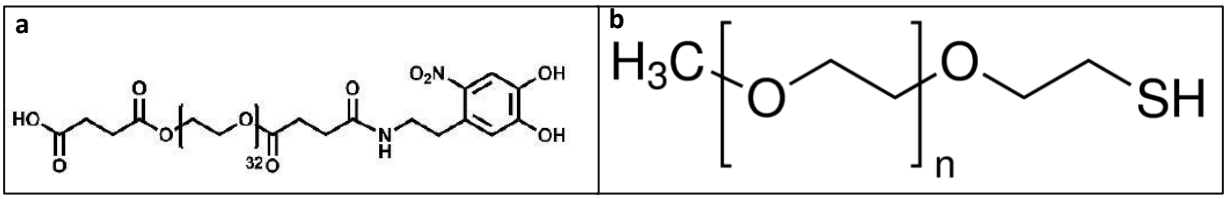

Figure 3.8: Formulas of a) synthesized ND-PEG1500-COOH and b) commercially available CH_3O -PEG2000-SH

In these first attempts, both the amphiphilic polymers were mixed together (one-step approach) with the chloroform solution of the sample and let under vigorous shaking overnight. After the shaking, sample was extracted with a toluene/water mixture in a separating funnel and the resulting aqueous phases dialyzed (using a cellulose membrane with MWCO = 50 kDa) in order to remove excess polymer.

Figure 3.9 shows a representative TEM picture and DLS size distribution (by intensity) of a water stable sample obtained following this procedure.

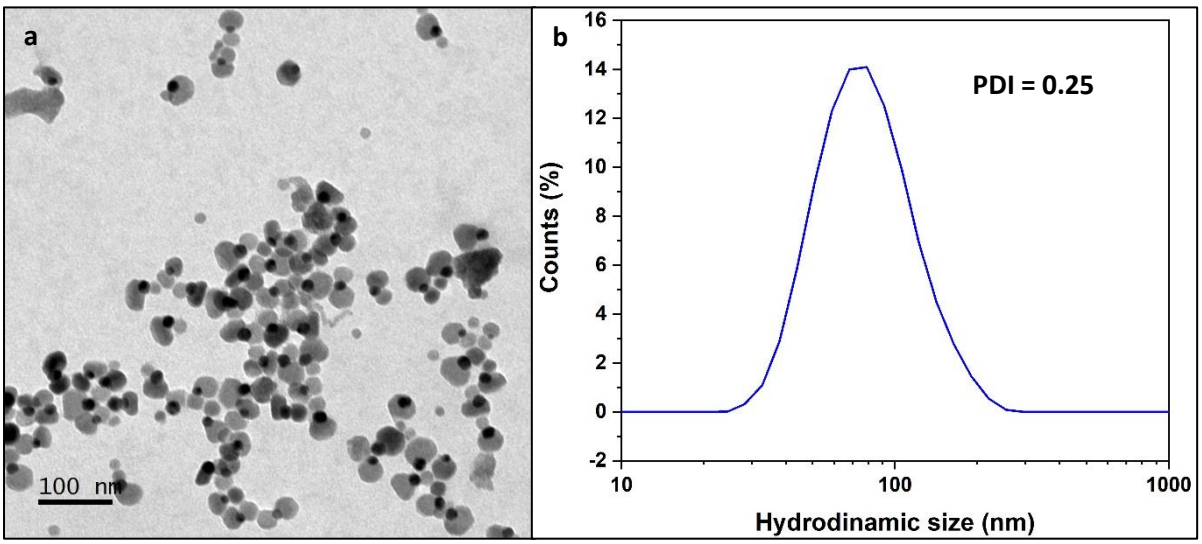

Figure 3.9: a) Representative TEM picture of a water stable sample of trimers water transferred using a one-step approach with ND-PEG1500-COOH and CH_3O-PEG2000-SH and b) related DLS hydrodynamic size distribution graph by intensity.

Using this procedure, trimers can be transferred in water with good stability (see DLS results in Figure 3.9b). However, as it is clearly shown by TEM analyses of the sample (see Figure 3.9a), together with the water transferred trimers, also traces of organic dirt and partially decomposed domains are present. In addition, many isolated domains (if compared with as-synthesized sample, see chapter 2) are surrounding water stable trimers, this indicating that a domain (presumably $Cu_{2-x}S$) is detaching from the heterostructures during the water transfer procedure. Water transfer procedure yield, measured by ICP-OES, was of only ≈ 25 %. Since the results obtained from this first procedure where unsatisfactory, a new two-step procedure was set up. Amounts of reactants, extraction and purification procedures remained the same as in previous trial. However, in this case, first chloroform solution of CH_3O-PEG2000-SH was added to the sample, and the reaction mixture let under vigorous shaking overnight. Afterwards, the chloroform solution of ND-PEG1500-COOH and the corresponding TEA base were added and an additional step of overnight shaking was added before extraction and purification.

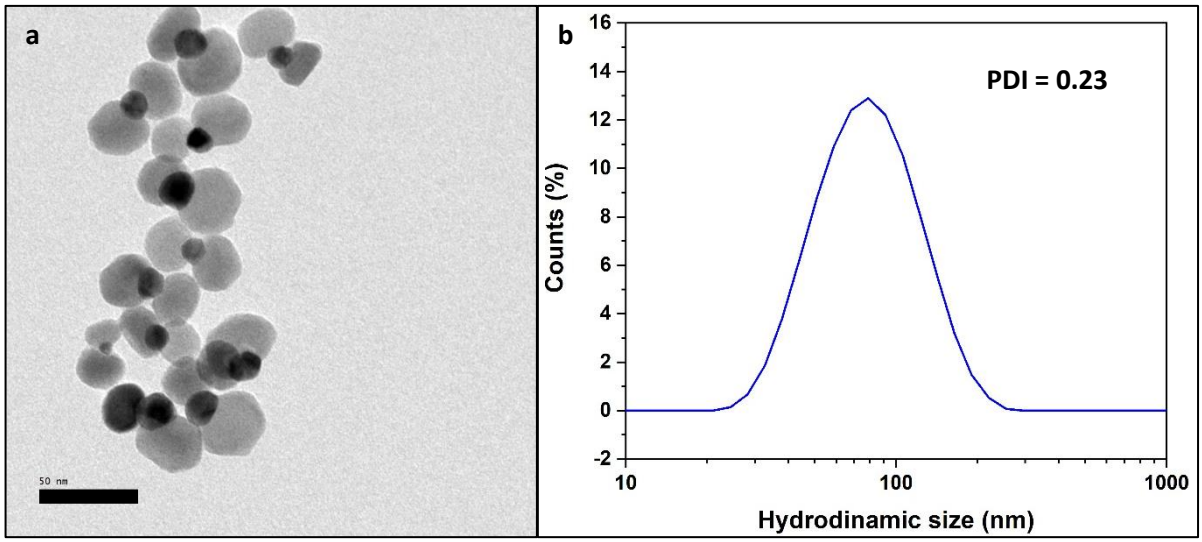

Figure 3.10: a) Representative TEM picture of a water stable sample of trimers water transferred using a two-step approach with ND-PEG1500-COOH and CH_3O-PEG2000-SH and b) related DLS hydrodynamic size distribution graph by intensity.

Results, shown in Figure 3.10, clearly indicate a better quality of the sample obtained through water transfer procedure if compared to the ones obtained with the one-step methodology. While DLS results (Figure 3.10b) are similar to the ones obtained in previous case, TEM analyses (see Figure 3.10a) are showing no organic dirt nor decomposed domains. Moreover, in this case the yield for the water transfer procedure was increased up to ≈ 40%. These results clearly indicate that the two-step procedure is more convenient for the water transfer of these kind of heterostructures, having three domains with completely different surface chemistry.

In order to further improve the efficiency of the water transfer procedure (in particular in terms of procedure's yield), additional trials were carried out using a multi-dentate poly-catechol-PEG900 ligand (see formula in Figure 3.11) developed and synthesized by Dr. Than Binh Mai, instead of the previously used mono-dentate ND-PEG1500-COOH ligand.

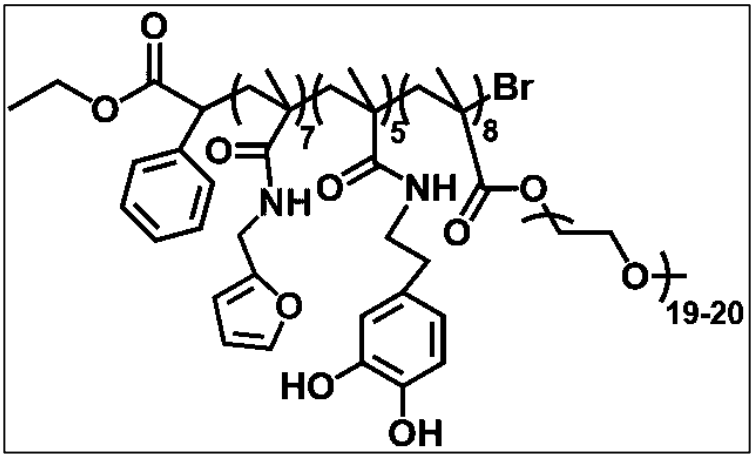

Figure 3.11: Formula of poly-catechol-PEG900 used as ligand stabilizing iron oxide domains in water.

The idea leading to the use of this polymer was to increase stability of the trimers using a multi dentate molecule (each polymer molecule has five catechol units). Indeed, has been previously reported that multi-dentate polymers provides an higher long-term stability of water transferred nanoparticles if compared to their mono-dentate counterparts[107]. The procedure used was again a two-step ligands addition followed by overnight shaking. Instead of doing an extraction, the water stable particles were separated from organic phase through addition of hexane, mild centrifugation and redispersion in water of the precipitated particles. Excess polymer in this case was not removed trough dialysis but through Amicon (100 kDa MWCO) washings. TEM and DLS results obtained using this new procedure are shown in Figure 3.12.

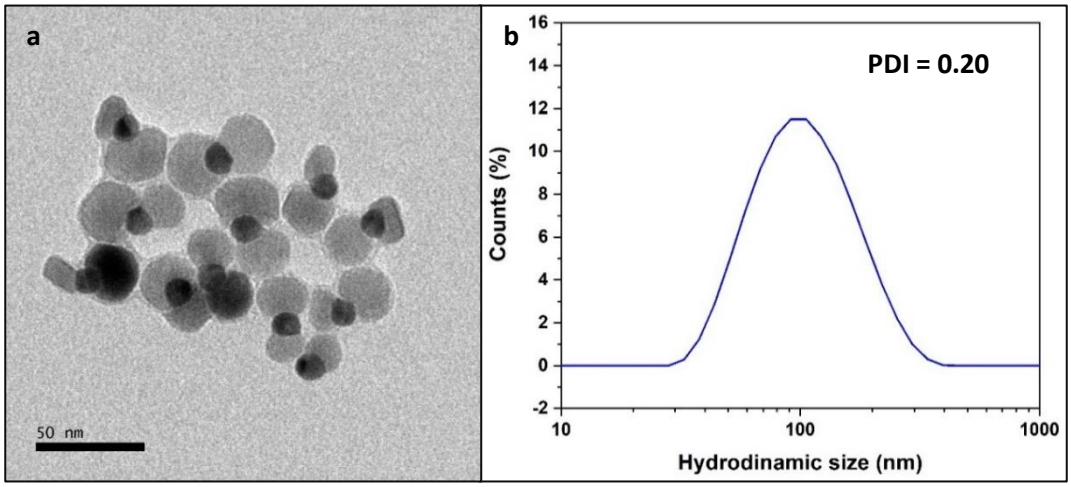

Figure 3.12:a) Representative TEM picture of a sample of trimers water-trasferred using a two-step approach with poly-catechol-PEG900 and CH_3O-PEG2000-SH b) related DLS hydrodynamic size distribution graph by intensity.

Results obtained by both TEM and DLS analyses are similar to the ones obtained in the two-step procedure performed using ND-PEG-COOH. However, in this case, the yield calculated for the water transfer procedure is higher (> 80 %). This increased efficiency of the water transfer procedure demonstrates that multi-dentate ligands are effectively increasing the stability of the water stable particles and leading to diminished nanoparticles' loss during the procedure

After obtaining excellent results with the two-step procedure employing CH_3O-PEG2000-SH and poly-catechol-PEG900, the possibility to water transfer FeO_y@Au@$Cu_{2-x}S$ trimers using only commercially available polymers was also tested. To fulfill this aim, a polymer coating procedure using poly-(maleic anhydride)-alt-1-octadecene (PMAO) was set-up and results obtained were compared with the best ones obtained with ligand exchange procedures. The polymer coating procedure developed in our group[108] relies on the intercalation of an amphiphilic polymeric shell on the hydrophobic surface of the nanoparticle. The shell is formed due to the favorable interactions between the alkyl chains of the surfactants coating the organic solvent-stable nanoparticles and the hydrophobic regions of the used polymer. This process is different from the ligand exchange procedure where the surface chemistry of the as-synthesized nanoparticles is a key parameter for the choice of the amphiphilic polymer. Indeed, in polymer coating, the formation of the polymeric shell around the particles is less influenced by the type of surfactant covering the nanoparticles and by the specific inorganic material that forms the nanocrystal cores. For these reasons, using this procedure, it has been reported the water transfer of different types of hydrophobic nanoparticles.[109] This advantage of the polymer coating procedure is of key importance for particles

such as the newly synthesized FeO_y@Au@$Cu_{2-x}S$ trimers, in which the different composition of the three domains in the heterostructure does not allow the use of one single amphiphilic ligand, as conventionally used for ligand exchange procedures of homostructures. Another advantage of this procedure is that the used polymer is commercially available and cost-effective. For the water transfer of the trimers through polymer coating, the standard procedure[108] has been adapted with some modifications. The procedure starts with the mixing of sample solution with PMAO in a large amount of chloroform (50 mL, in order to guarantee trimers' stability in a diluted solution) with a ligands/nm^2 ratio of 500 (considering total trimers' surface). After stabilization through mild sonication, the chloroform is evaporated using rotavapor. Since the intercalation between ligands and PMAO is taking place during the removal of the solvent, the optimization of the chloroform evaporation step is a key task when performing polymer coating. Having the trimers a large size (sum of the three domain-lengths is generally above 50 nm), the parameters were set up in order to have a solvent evaporation as gentle as possible, in order to guarantee a proper coating of the particles. Using a bath temperature of the rotavapor of 50°C and a rotation speed of 140 rpm, chloroform was evaporated through three pressure steps. Pressure was first set to 800 mbar for 30 minutes and to 700 mbar for 30 minutes more. Solvent was then evaporated at 650 mbar for 1 hour and finally the pressure was reduced to 600 mbar until complete drying of the product (usually 2 more hours). The dried black precipitate was then brought back to solution using 20 mL borate buffer and sonication at high temperature (65°C was set as starting temperature of the sonication batch) for at least 2 hours. After, the sample's volume was reduced (to about 3 mL) through Amicon tube filters (100 kDa MWCO) centrifugation. The sample was finally loaded on top of a sucrose gradient (from top to bottom: 2 mL of 20 m/v %, 3 mL of 40 m/v % and 3 mL of 60 m/v % in an ultra-centrifugal tube) for ultracentrifugation. Ultracentrifugation in sucrose gradient is used to separate the coated particles from the unreacted free polymer that, being lighter, is not migrating through the gradient during the procedure. However, high centrifugation speed could cause precipitation and aggregation of larger particles. In order to optimize ultracentrifugation parameters, the migration of the sample inside sucrose gradient was monitored after 30, 45, 60 and 75 minutes of centrifugation at 10000 rpm (see Figure 3.13).

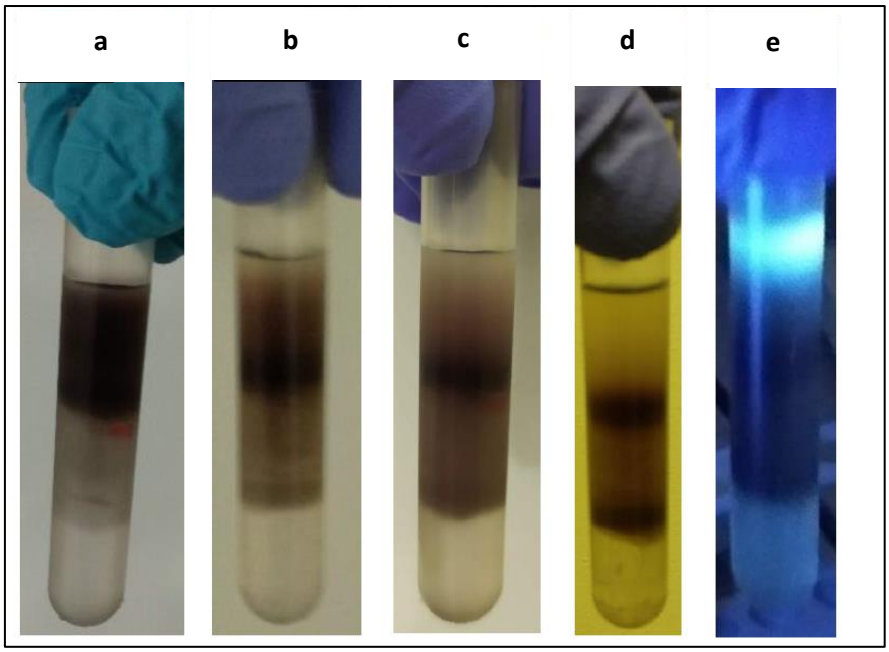

Figure 3.13:Digital photograph of a sample of trimers after polymer coating and after a) 30 minutes of ultracentrifugation at 13700 RCF; b) 45 minutes of ultracentrifugation at 13700 RCF; c) 60 minutes of ultracentrifugation at 13700 RCF; d) 75 minutes of ultracentrifugation at 13700 RCF; d) digital photograph of sample shown in d) under UV-light irradiation.

After 30 minutes of ultracentrifugation (Figure 3.13a), based on the color, most of the sample was still in fraction one (20 m/v %) of the sucrose gradient. In order to have most of the particles lying in the second fraction (40 % sucrose m/v %), for a proper separation from free polymer, the sample had to be centrifuged for 75 minutes. At this point (see Figure 3.13d) most of the particles are localize in two bands, corresponding to the interfaces between 1st and 2nd fraction and the one between 2nd and 3rd fraction with a small amount in the second fraction. This is indicating a size distribution in the polymer coated nanoparticles that, consequently, are not moving coherently inside the gradient. Likewise, many particles are also found in the bottom of the ultracentrifuge tube, indicating that larger particles are aggregating and that the ultracentrifugation should be stopped. As clearly indicated by Figure 3.13e, excess polymer is only localized in first fraction of the gradient. After removal of the polymer, fraction 2 and 3 of the gradient were recovered. Part of the sample was stuck onto the bottom of the ultracentrifuge tubes and was not possible to recover. Recovered fractions were then washed from the sucrose through Amicon washings. After concentration, the sample was characterized and compared with results obtained for FeO_y@Au@$Cu_{2-x}S$ trimers water transferred using ligand exchange procedure with CH_3O-PEG2000-SH and poly-catechol-PEG900.

In Figure 3.14, TEM, DLS, and gel electrophoresis characterizations for a sample of polymer-coated trimers are shown and compared with the results obtained performing water transfer through a ligand exchange procedure on the same starting trimers' sample.

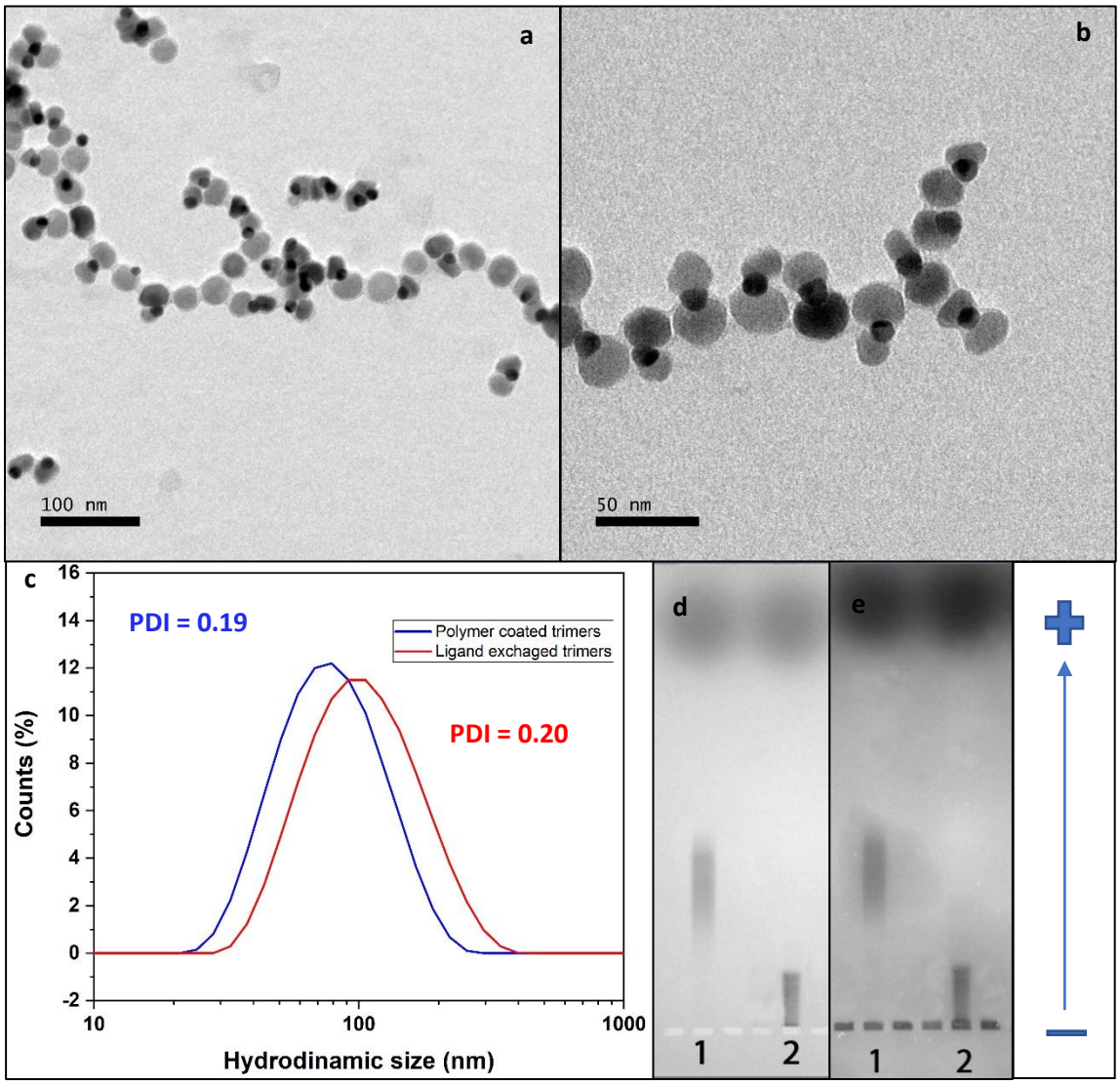

Figure 3.14: Comparisons of the properties of a trimers' sample when water transferred with polymer coating or ligand exchange procedure. a) representative TEM picture of trimers water transferred through polymer coating; b) representative TEM picture of trimers water transferred through ligand exchange; c) comparison of DLS hydrodynamic size distribution graph (by intensity) for polymer coated trimers (blue line) and ligand exchanged trimers (red line); d) image acquired under visible light of gel electrophoresis run (45 min, 100 V, 1% agarose gel) of polymer coated trimers (1) and ligand exchanged trimers (2); e) image acquired under ultraviolet light of the same gel electrophoresis run of polymer coated trimers (1) and ligand exchanged trimers (2)

From DLS size distribution (shown in Figure 3.14c) is clear that, as was happening for the trimers when transferred with ligand exchange procedure employing CH_3O-PEG2000-SH and poly-catechol-PEG900, the polymer coating is transferring particles in water without producing any aggregate. In addition, from TEM pictures (see Figure 3.14a), no trace of aggregates formation was found. Interestingly, although the starting sample on which the two water transfer procedures were carried on was the same (with average diameters of 20 ± 3 nm for $Cu_{2-x}S$ domains, 21 ± 5 nm for iron oxide domains and 12 ± 1 nm for gold NPs), in the case of the sample water transferred through polymer coating, the hydrodynamic size distribution peak is centered around 80 nm while for the ligand-exchanged sample the peak is at 100 nm. This difference between the DLS analyses outcome of the two water transfer procedures could suggest that the larger or the more interacting among the trimers are lost during the ultracentrifugation of polymer-coated sample (fraction found on the bottom of the ultracentrifuge tube). This loss is largely reflected in the calculated procedure yield for polymer coating. Indeed, while ligand exchange procedure was able to quantitatively (≥ 80%)

transfer to water the trimers, with polymer coating procedure the process' yield drops to only 15 %. In Figure 3.14d and 3.14e, are shown digital photographs of gel electrophoresis runs for the two water-transferred samples, acquired under both visible (Figure 3.14d) and UV (Figure 3.14e) light. The difference in the results obtained with the two samples should be ascribed both to the different size distribution and to the different zeta potential of the water-transferred particles (measured z potential was -34 mV for polymer-coated trimers and -19 mV for ligand-exchanged trimers). Most importantly, pictures acquired under ultraviolet light (Figure 3.14e) show that there are no traces of free polymers (both PMAO and poly-cathecol-PEG900) in the two samples, thus indicating that the cleaning protocols were successful.

In order to be able to select the best water transfer procedure for trimers, polymer coated and ligand exchanged (procedure employing CH_3O-PEG2000-SH and poly-catechol-PEG900) heterostructures were also compared based on their heating efficiency when used in magnetic hyperthermia treatments. First, hyperthermia efficiencies of the two sample were evaluated and compared through calorimetric Specific Absorption Rate (SAR) measurements using alternating magnetic fields (AMF) with frequencies between 105 and 300 kHz and amplitudes between 12 kA/m and 32 kA/m. SAR was calculated according to the formula and the procedure explained in experimental section. Results obtained are shown in Figure 3.15.

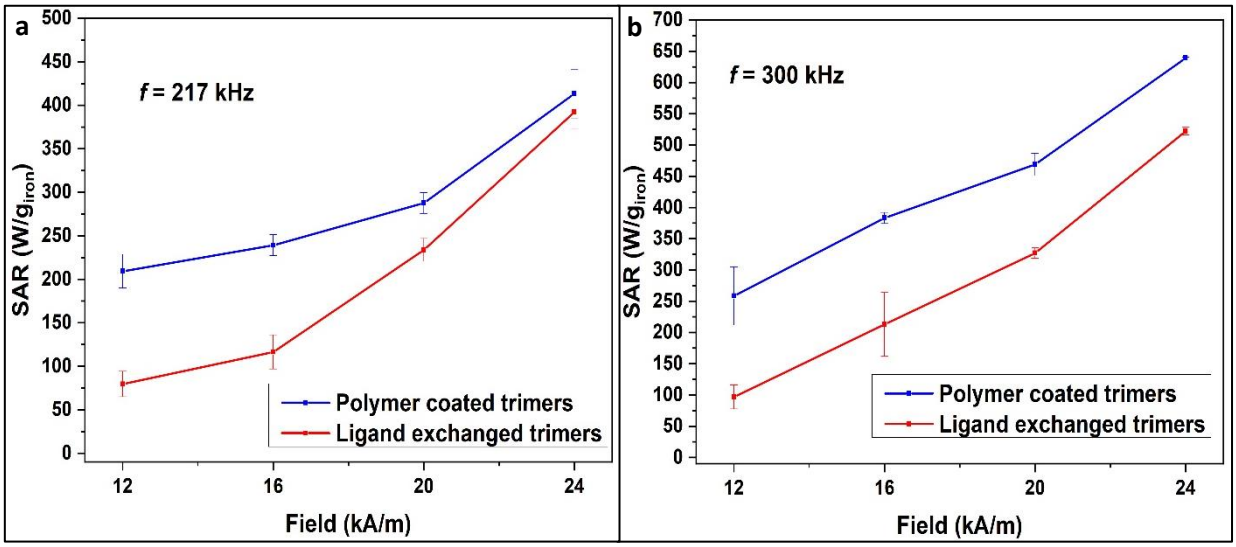

Figure 3.15: Comparison of SAR vs field amplitude data obtained from the same sample of trimers water transferred with polymer coating (blue lines) and with ligand exchange (red lines); a) data obtained using a field frequency of 217 kHz; a) data obtained using a field frequency of 300 kHz. Lines are a guide to the eye.

Both the samples show good heating efficiencies, with the one of the polymer-coated sample being higher than the one of the trimers water transferred through ligand exchange (566 ± 6 W/g for the ligand-exchanged sample and 688 ± 1 W/g for the polymer-coated sample at 300 kHz, 24 kA/m). This difference could be explained by the aforementioned quality and size selection, taking place during ultracentrifugation step of the polymer coating procedure. In order to further deepen the understanding of this behavior, AC hysteresis loops of the two differently water transferred samples were measured using the same field parameters. Results obtained on the two samples, using fields with frequencies of 200 kHz and 300 kHz and amplitudes of 12 kA/m and 24 kA/m are shown, in Figure 3.16.

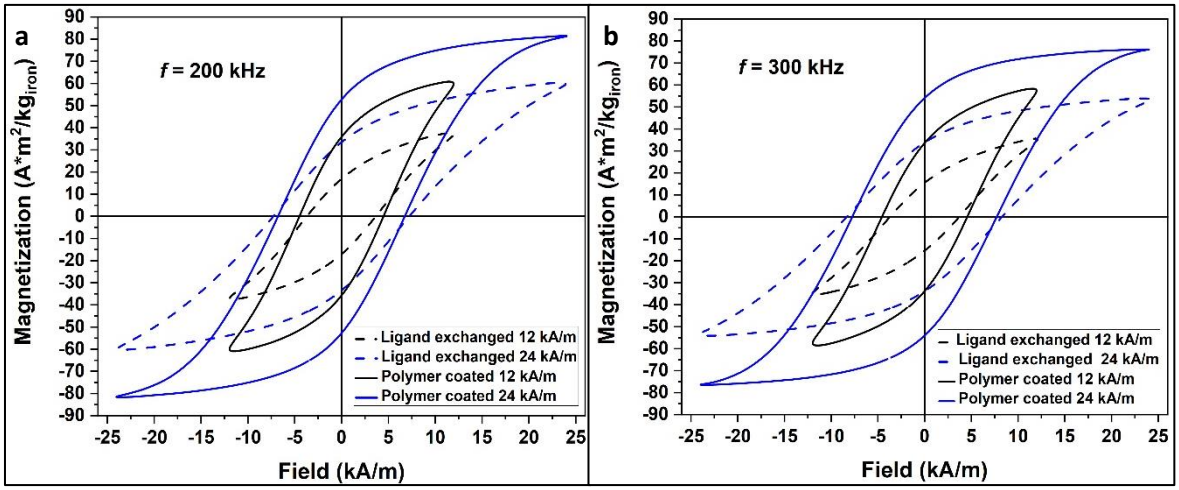

Figure 3.16: AC hysteresis loops obtained from a sample of trimers water transferred through polymer coating (continuous lines) or ligand exchange (dashed lines) measured using a) alternated fields with frequency of 200 kHz and amplitudes of 12 kA/m (black lines) and 24 kA/m (blue lines); b) alternated fields with frequency of 300 kHz and amplitudes of 12 kA/m (black lines) and 24 kA/m (blue lines).

While the coercivity of the loops of the two samples is similar, the value of the maximum magnetization achieved is higher in the case of polymer-coated nanoparticles (76 Am^2/kg *vs* 53 Am^2/kg when a field with frequency of 300 kHz and an amplitude of 24 kA/m was used). The different shape of the loops directly reflects on the measured values for loops' area (2748 mJ/kg *vs* 2064 mJ/kg when a field with frequency of 300 kHz and an amplitude of 24 kA/m was used) this resulting in the difference in SAR measured through calorimetric measurements. The fact that polymer-coated trimers can achieve a higher value of maximum magnetization under same field conditions, strengthen the hypothesis of the polymer coating operating a quality selection of the transferred particles. Larger, or more interacting, particles are lost during the ultracentrifuge step of water transfer procedure and only best performing particles are remaining in the water stable sample.

Despite this difference in the hyperthermia performances favors polymer coating, ligand exchange procedure was selected as the candidate procedure for the water transfer of trimers given the higher yield (≥ 80 % *vs* 15 %) and the straightforwardness and reproducibility of the procedure in which less parameters have to be tuned and monitored. Consequently, on the sample transferred with this latter procedure, also UV-VIS-IR and XRD analyses were performed in order to check whether plasmonic absorption or crystalline phase of the sample were modified or not. Results are shown in Figure 3.17.

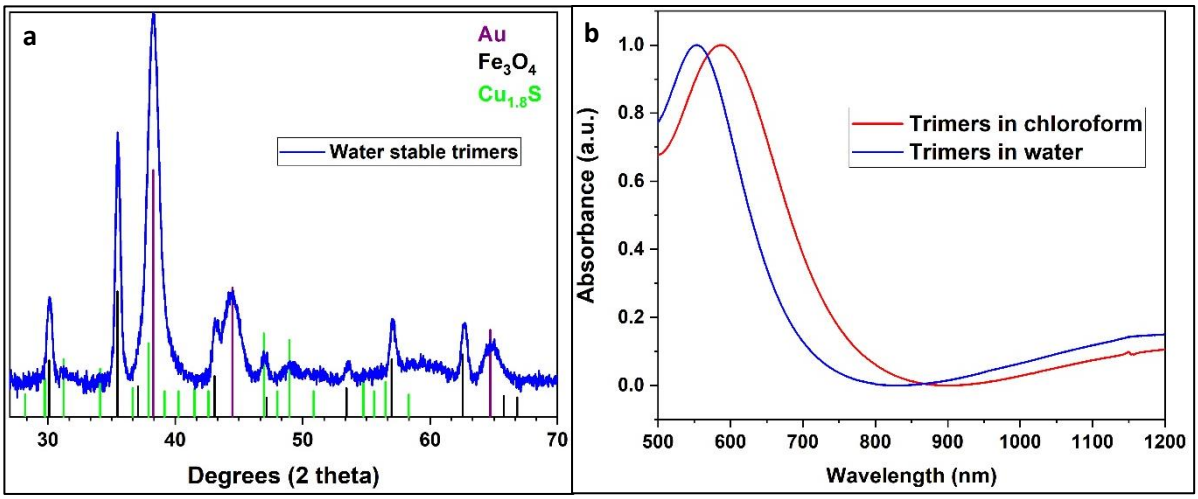

Figure 3.17: a) Experimental XRD pattern of a sample of water transferred trimers compared with expected reflections for Au (ICSD code 611625), iron oxide (ICSD code 247035) and $Cu_{29}S_{16}$ (ICSD code 185807); b) VIS-NIR (500-1200 nm) spectrum of a sample of trimers in chloroform (red line) and of the same sample after water transfer (blue line), spectra are normalized on the absorption intensity of gold plasmon.

The XRD pattern of the water-transferred trimers (see Figure 3.17a) is comparable with the one obtained for the trimers in chloroform (see Figure 2.25c), all the expected reflections for cubic gold, cubic iron oxide and triclinic roxbyite copper sulfide are present. In both the VIS-NIR (500 – 1200 nm) spectra (shown in Figure 3.17b) Au and $Cu_{2-x}S$ plasmon absorption are clearly recognizable. Both the absorption peaks are blue-shifted in case of the water-transferred sample. This shifting of the plasmonic absorption bands has to be ascribed to the change of dispersing solvent and to the chemistry of the amphiphilic ligand stabilizing the surface of the FeO_y@Au@$Cu_{2-x}S$.[110]

3.2.2. Magnetic hyperthermia performances of FeO_y@Au@$Cu_{2-x}S$ heterostructures

In order to be able to compare the hyperthermia efficiency of the FeO_y@Au@$Cu_{2-x}S$ trimers with the one of the dimers, which were used as starting seeds for the synthesis of these novel heterostructures, a sample of dimers (Au@ FeO_y) was transferred to water using the same ligand exchange procedure adopted for trimers. Noteworthy, the sample of dimers transferred and measured is the same used as seeds in the synthesis for that particular sample of trimers. This was planned in order to be able to evaluate the contribution due to the third domain growth only, out ruling any influence on the heating performances coming from the differences in either the gold (15 ± 3 nm in both samples) or iron oxide domain (26 ± 4 nm in both samples). TEM pictures of the water-transferred dimers and trimers are compared in Figure 3.18.

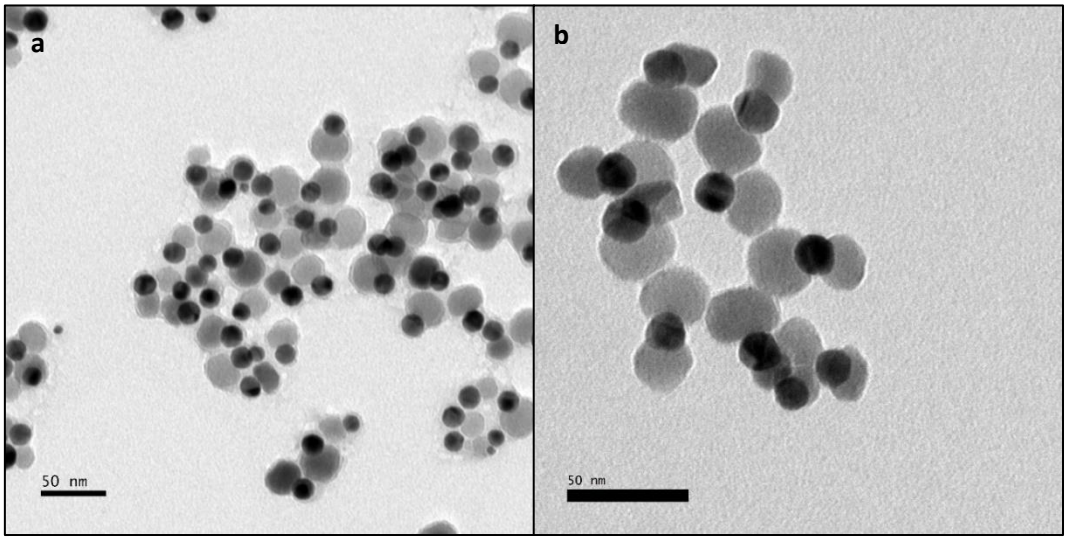

Figure 3.18: a) representative TEM picture of a sample of dimers water transferred through ligand exchange procedure using poly-cathechol-PEG900 and CH_3O-PEG2000-SH; b) representative TEM picture of a sample of trimers water transferred through ligand exchange procedure using poly-cathechol-PEG900 and CH_3O-PEG2000-SH.

TEM pictures of water transferred dimers (Figure 3.18a) and trimers (Figure 3.18b) show the good quality of both the samples. DLS and UV-VIS-NIR characterization for the water transferred dimers and trimers whose hyperthermia efficiencies are compared in Figure 3.19.

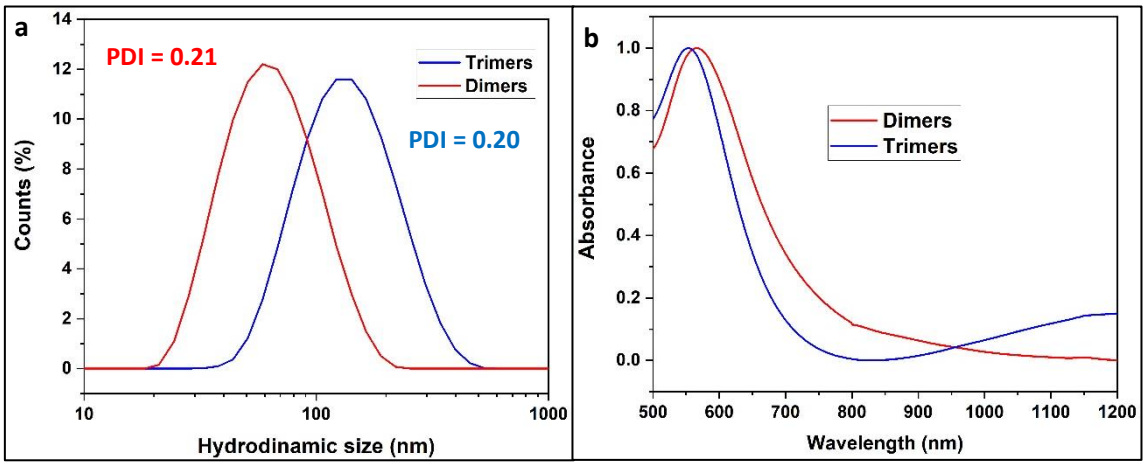

Figure 3.19: a) comparison of DLS size distribution graph (by intensity) for dimers (red line) and trimers (blue line); b) comparison of VIS-NIR (500-1200 nm) spectra of water dispersed dimers (red line) and trimers (blue line).

No traces of aggregates were found, the hydrodynamic diameter of trimers is obviously bigger than the one of dimers, due to the presence of the additional copper sulfide domain. These results demonstrate how the water transfer procedure developed for FeO_y@Au@$Cu_{2-x}S$ can be used with excellent results also for the water transfer of FeO_y@Au dimers, in substitution of the already reported ligand exchange procedure employing gallol-poly(ethylene glycol) (GA-PEG).[40] Comparing the UV-VIS-NIR (500 nm – 1200 nm) spectra, it is clear that, whilst the small differences in the position of the absorption peak related to the presence of the gold plasmon, the plasmonic absorption at high wavelengths (starting at about 850 nm) is completely absent in the dimers' sample. Given the good results obtained for the water transfer or the dimers, magnetic hyperthermia performances of the two heterostructures were measured and compared (see Figure 3.20).

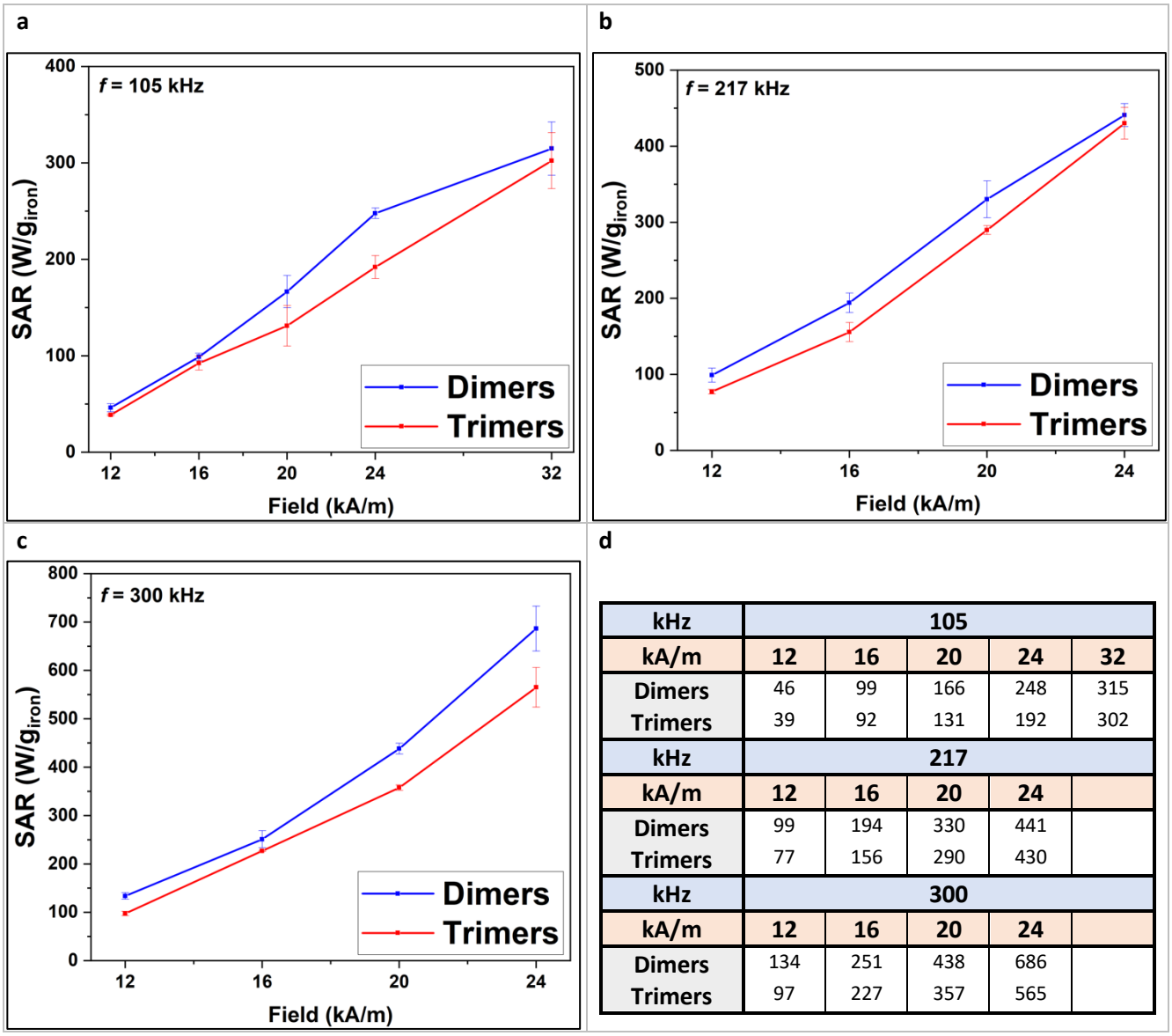

d

kHz	105				
kA/m	12	16	20	24	32
Dimers	46	99	166	248	315
Trimers	39	92	131	192	302
kHz	217				
kA/m	12	16	20	24	
Dimers	99	194	330	441	
Trimers	77	156	290	430	
kHz	300				
kA/m	12	16	20	24	
Dimers	134	251	438	686	
Trimers	97	227	357	565	

Figure 3.20: a-c) SAR vs field amplitude graphs for Au@FeO_y dimers (blue lines) and FeO_y@Au@$Cu_{2-x}S$ trimers (red lines) using a field frequency of a) 105 kHz; b) 217 kHz; c) 300 kHz. For all frequencies, field amplitudes of 12 kA/m, 16 kA/m, 20 kA/m and 24 kA/m were used. For 105 kHz frequency, data obtained using a field amplitude of 32 kA/m are also shown; d) table with SAR performances of dimers and trimers samples when different field amplitudes and frequencies are applied. Both the measured samples had an iron oxide domain with 26 ± 4 nm average size.

In all cases, heating performances of the trimers are slightly worse than the ones of the dimers. This difference could be due to the increased size of the trimers, hindering particles rotation. However, when using frequencies and fields below the H×*f* limit value of 5×10^{-9} A/(m×s) (commonly considered the maximum value of the field×frequency product that is safe for human tissues)[111], that are, among the measurements performed, the ones at 105 kHz (12 kA/m, 16 kA/m, 20 kA/m, 24 kA/m and 32 kA/m) 217 kHz (12 kA/m, 16 kA/m, 20 kA/m) and 300 kHz (12 kA/m, 16 kA/m), the SAR values obtained using FeO_y@Au@$Cu_{2-x}S$ trimers, are in line with the ones obtained for other magnetic heterostructures reported for hyperthermia applications.[112] Dynamic magnetic properties of the trimers were also studied and compared with the ones of dimers through the measurement

of AC hysteresis loops. Results obtained using alternated magnetic fields with frequencies of 200 kHz and 300 kHz and amplitudes of 12 kA/m and 24 kA/m are shown in Figure 3.21.

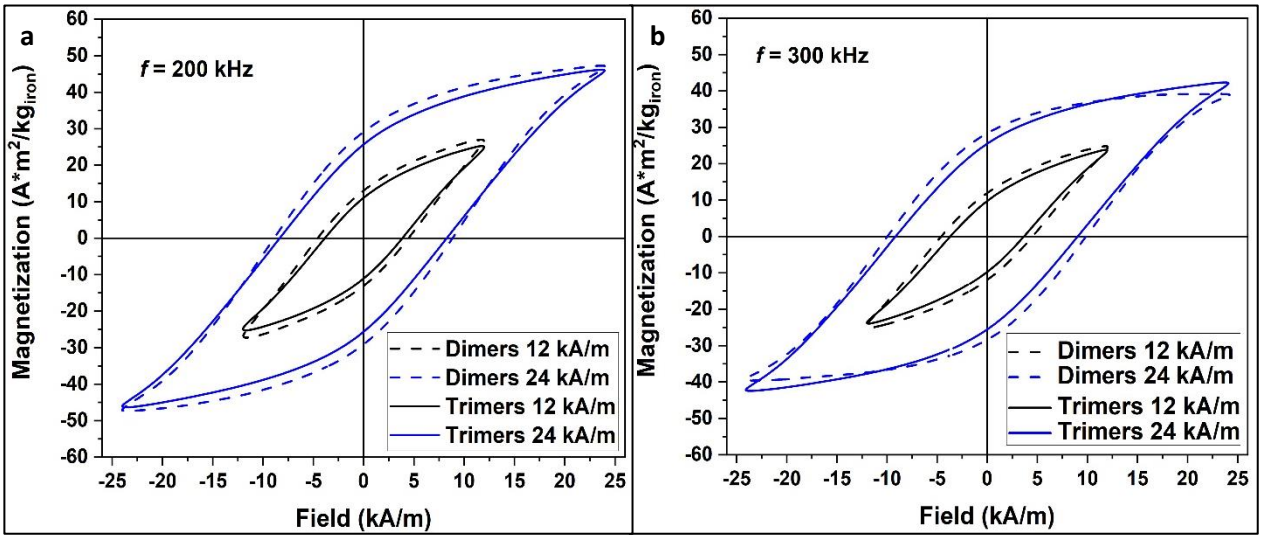

Figure 3.21: AC hysteresis loops of a sample of trimers (continuous lines) and dimers (dashed lines) having a 26 ± 4 nm iron oxide domain. a) Measurements performed using fields with frequency of 200 kHz and fields of 12 kA/m (black lines) and 24 kA/m (blue lines); b) measurements performed using fields with frequency of 300 kHz and fields of 12 kA/m (black lines) and 24 kA/m (blue lines).

From the AC hysteresis loops is clear that, as already expected from SAR values, there is only small difference between the dynamic loop of dimers and trimers, this resulting in similar heating performances when used in magnetic hyperthermia. These results demonstrated how, fulfilling the first task of this work, a chalcogenide domain can be grown on Au@FeO_y dimers without compromising their excellent performances for magnetic fluid hyperthermia.

3.2.3. Radiolabeling with ^{64}Cu of FeO_y@Au@$Cu_{2-x}S$ heterostructures

Once confirmed that the performances of Au@FeO_y dimers as heating probes under the application of an alternating magnetic field are preserved after the growth of the copper sulfide domain, radiolabeling reactions, following the protocol used for ZnS nanoparticles in Chapter 1, were carried out. The final goal of these nano-heterostructures is to be used as multifunctional probes feasible to be exploited both in radiotherapy and hyperthermia, the latter requiring a relatively high iron concentration in order to be effective. Being the typical molar ratio between iron and copper in water stable trimers' samples between 1.4 and 2, the amount of nanocrystals used had to be tuned accordingly in order to have iron concentration similar to the ones used in hyperthermia experiments (1-3 g/L). The percentage ratio between radioactive ^{64}Cu used and the copper present in FeO_y@Au@$Cu_{2-x}S$ nanocrystals was defined as ^{64}Cu feed percentage ratio ($^{64}Cu \times 100/Cu_{NCs}$). Different trials, using varied ^{64}Cu feed percentage ratios where performed, in order to check the related radiochemical yields. Similarly to what has been done for ZnS nanoparticles, all the experiments were performed using an amount of $^{64}CuCl_2$ (2.03×10^{-12} moles) corresponding to an activity of 18.5 MBq (500 µCi), consequently $^{64}Cu/Cu_{NCs}$ has been reduced by increasing the amount of trimers nanocrystals used.

Radiolabeling reactions and subsequent purification were carried out following the same procedure (see Figure 3.22) used for ZnS NPs, using ascorbic acid as biocompatible mild reducing agent for the reduction of the introduced ^{64}Cu (II) ions to ^{64}Cu(I).

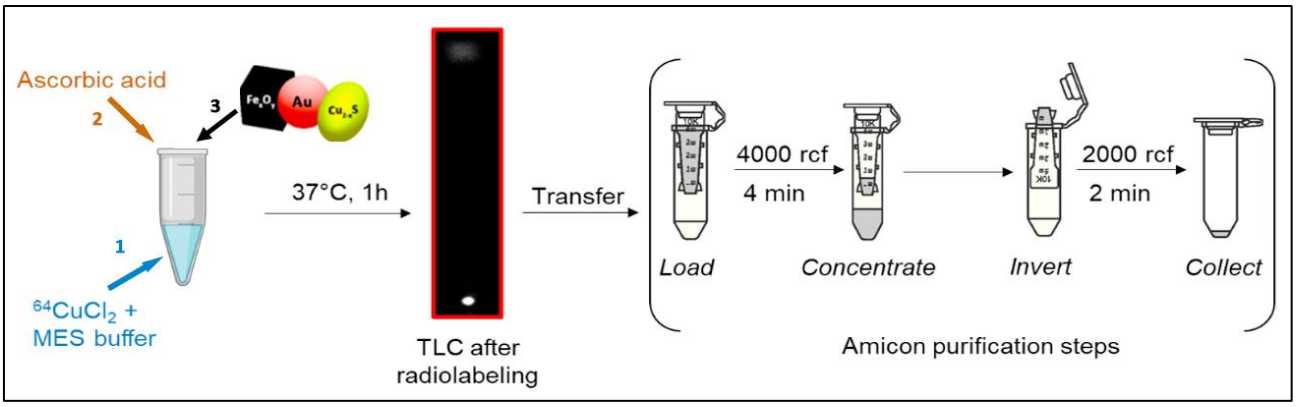

Figure 3.22: Scheme of the radiolabeling procedure and of the subsequent purification steps.

Three sets of radiolabeling reaction were set up in order to evaluate the radiochemical yields of the radiolabeling procedures when using different $^{64}Cu/Cu_{NCs}$ percentage ratios. Results are shown in Figure 3.23.

a

^{64}Cu feed	Cu_{NCS}	^{64}Cu	RCY
(%)	(moles)	(moles)	(%)
1%	2.03×10^{-10}	2.03×10^{-12}	9.5
0.1%	2.03×10^{-9}	2.03×10^{-12}	31.5
0.01%	2.03×10^{-8}	2.03×10^{-12}	97

b

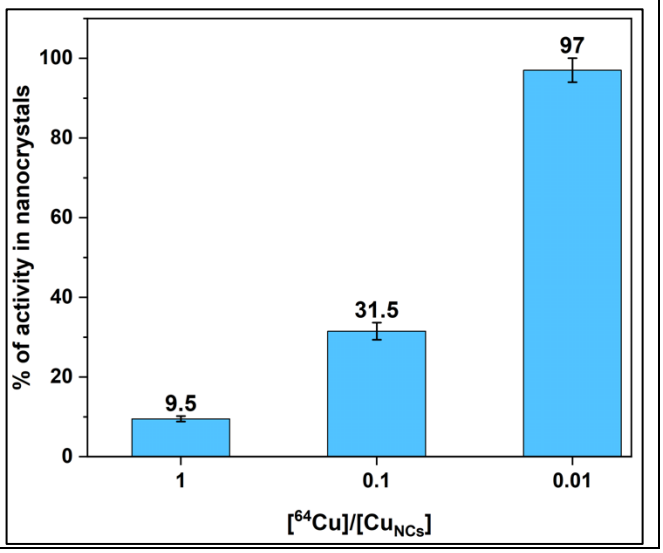

Figure 3.23: a) table with parameters used in different trials of radiolabeling reactions; b) radiochemical yield obtained for three sets of reaction carried out using [^{64}Cu]/[Cu_{NCs}] percentage ratios of 1 %, 0.1 % and 0.01 %.

While in the case of 1% and 0.1% ^{64}Cu feed percentage ratios the radiochemical yield of the reaction is below 50%, in the case where a 0.01 % $^{64}Cu/Cu_{NCs}$ percentage ratio was used, the average radiochemical yield obtained was of 97 %, meaning that the used ^{64}Cu is almost quantitatively incorporated inside the FeO_Y@Au@$Cu_{2-x}S$ nanocrystals. This value is almost two times the one reported before for radiolabeling of water stable copper sulfide nanocrystals (49%)[113] and similar to the one reported for ^{64}Cu:CuS nanocrystals synthesized using a mixture of $CuCl_2$ and $^{64}CuCl_2$.[114] Although with such high radiochemical yield the purification of the nanocrystals solution from free radioactive copper is not needed, during our experiments radiolabeled particles were cleaned using one Amicon purification step (see Figure 3.22), in order to get rid of excess ascorbic acid and to concentrate the sample.

To evaluate the stability of the particles during this washing step, similarly to what was done for ZnS nanoparticles, activity of all the washing fractions were measured through a dose calibrator and compared with the starting activity measured from the reaction batch after the incubation of 1 hour at 37°C. Three trials were carried out adding different amounts of a 0.0049 M CYS-PIMA-PEG2000 solution. CYS-PIMA-PEG2000 is a multi-dentate ligand that has been previously used (see chapter 1) for the stabilization in water of chalcogenides nanocrystals. Results obtained using 0, 20 µL and 50 µL of 0.0049 M CYS-PIMA-PEG2000 solution are compared, based on radiochemical yield and on the yield of the purification process, in Figure 3.24.

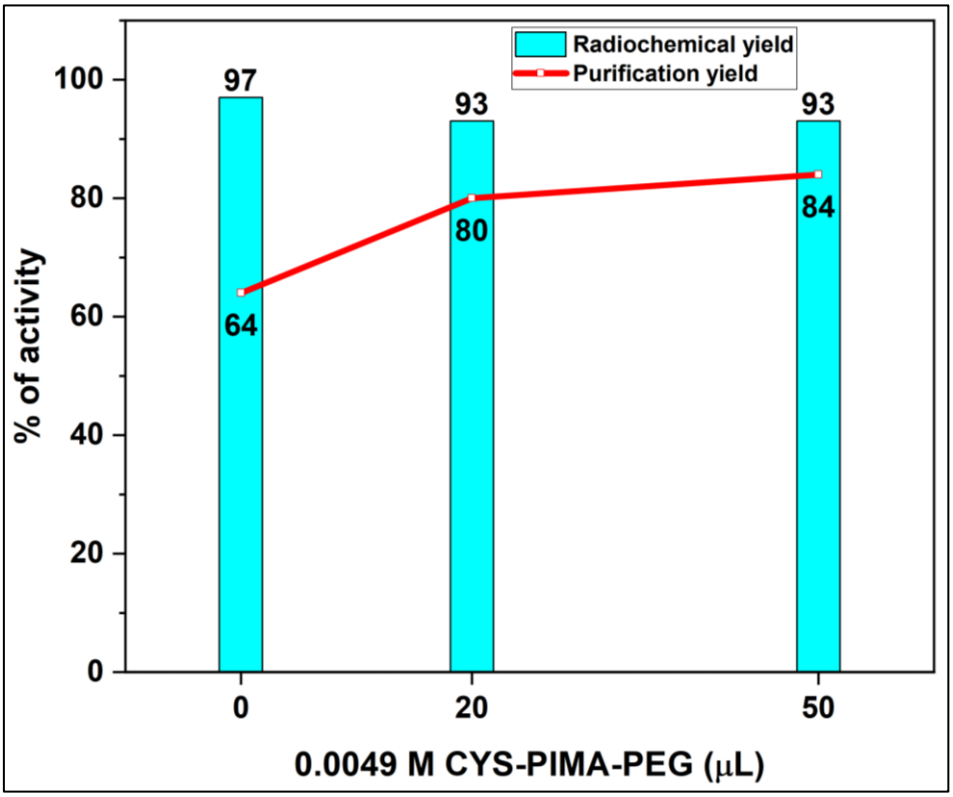

Figure 3.24: Radiochemical yield (bars) and purification yield (red line) obtained for radiolabeling reactions performed adding increasing amount of 0.0049 M CYS-PIMA-PEG2000 solution.

First important result is that RCY, although being reduced from 97 % in the case no stabilizing agent was used to 93 % when increasing amounts of CYS-PIMA-PEG2000 were added, is over 90 % in any case. This indicates that the addition of a thiol-terminated agent, potentially able to chelate free ^{64}Cu ions, is not significantly affecting the amount of activity successfully incorporated in the nanocrystals. On the other hand, while increasing the amount of CYS-PIMA-PEG2000 added, the yield of the purification process is drastically improved from 64 % (when no CYS-PIMA-PEG2000 was added) to 84 % (when 50 µL of CYS-PIMA-PEG2000 solution were added). In order to further study the fate of ^{64}Cu (I) during the purification process in the three cases, activity data obtained from the different fractions of the washings are compared in table 3.1.

Table 3.1: Percentage of starting activity measured during purification steps of three radiolabeling reaction performed (1) without adding any stabilizing agent (2) adding 20 µL (3) adding 50 µL of a 0.0049 M solution of CYS-PIMA-PEG. Vial: activity remained in the reaction vial after the transfer of the solution in Amicon filter; Washing: percentage of activity recovered in the bottom of the Eppendorf vial after centrifugation; Filter: percentage of activity stuck in the Amicon filter cartridge after nanocrystals solution recovery; Recovered: percentage of activity of the final nanocrystals solution; Lost: percentage corresponding to the difference between the initial activity and the activities measured during purification steps.

Reaction N°	CYS-PIMA-PEG (µL)	RCY (%)	Vial (%)	Washing (%)	Filter (%)	Recovered (%)	Lost (%)
1	0	97	16	0	17	64	3
2	20	93	4	0	12	80	4
3	50	93	3	0	7	84	6

From the results obtained is clear that the addition of even small amounts of a stabilizing agent is increasing the stability of the radiolabeled nanocrystals both during the radiolabeling reaction and during the centrifuging step. The loss of stability during the radiolabeling reaction can be evaluated by the amount of activity that is remaining stuck in the reaction vial. When no stabilizing agent is added, 16 % of the activity is found in the reaction vial while this amount is reduced to 4 % and 3 % when 20 µL and 50 µL of 0.0049 M CYS-PIMA-PEG2000 are respectively added. This demonstrates that CYS-PIMA-PEG2000 addition helps improving the stability of the nanocrystals during the 1 hour incubation, consequently reducing the amount of ^{64}Cu that is loss in the reaction vial. Stability of the crystals during the centrifuging step can be evaluated through the amount of activity found in the cartridge of the Amicon filter used for crystals purification and concentration. This amount is decreased when the amount of CYS-PIMA-PEG2000 added to the radiolabeling reaction is increased. Indeed, while in reaction n°1 17 % of the activity was found in the filter, with 50 µL of 0.0049 M CYS-PIMA-PEG2000 this value was reduced to 7 %. The column indicated as "lost" in table 3.1 reports the difference between the starting activity value and the ones measured during purifications step, considering other losses that were not measured during these experiments. These losses, whose values are in any case low, could be due to nanocrystals remaining inside micropipette tips used for sample transfer to Amicon or to natural decay of ^{64}Cu (0.66 % during 10 minutes of purification). The obtained results demonstrated that, if a purification and washing procedure is needed to clean the sample from unreacted reagents and to reduce radiolabeled nanocrystals' solution volume, few microliters (20 – 50 µL) of a 0.0049 M CYS-PIMA-PEG2000 solution can be added in order to guarantee perfect stability and quantitative activity recovery.

In order to further study the process, a scaled-up reaction employing "cold" (non-radioactive) $CuCl_2$ was performed reproducing the conditions of the radiolabeling reactions that were previously carried out. In order to have a reliable picture of the radiolabeling reaction, the reaction was set up considering not only radioactive copper corresponding to the 18.5 MBq activity used (2.03×10^{-12} moles of Cu), but the total ("hot" plus "cold") amount of copper used in the radio labeling experiments. This value is 1.32×10^{-10} moles of Cu at production time and it is increasing over time with radioactive copper decay. Consequently, the ratio between non-radioactive $CuCl_2$ and Cu_{NCs} used was calculated accordingly. All the other parameters where kept the same as in radiolabeling reactions, included the addition of 0.0049 M CYS-PIMA-PEG as stabilizer agent. After the reaction, sample was cleaned using the Amicon filter washing procedure already used in the case of radiolabeled crystals. Results obtained by TEM, VIS-NIR and DLS analyses on this trimers' sample are shown in Figure 3.25. Also, DLS hydrodynamic size distribution graph and VIS-NIR spectra of the sample before reaction with $CuCl_2$ are reported for comparison.

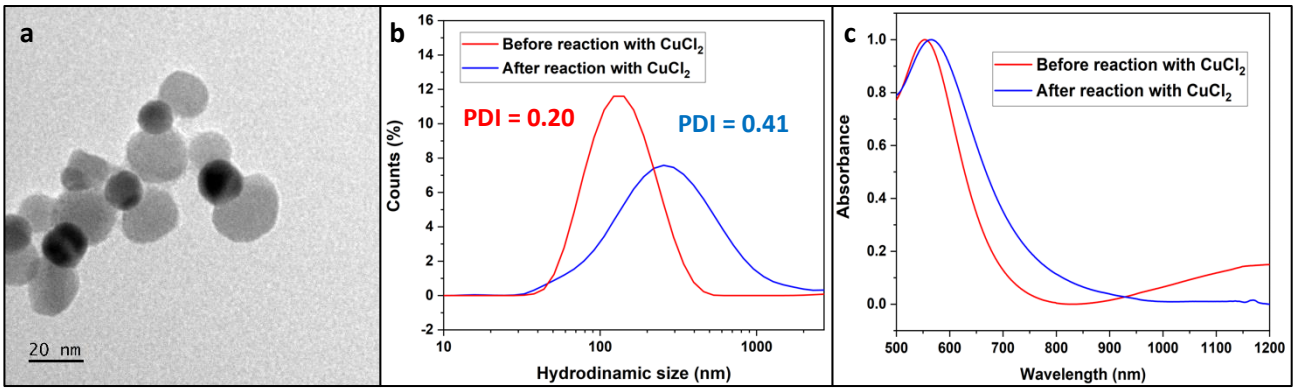

Figure 3.25: a) Representative TEM picture of a sample of FeO_y@Au@$Cu_{2-x}S$ trimers after "cold" reaction with $CuCl_2$ and Amicon filter purification; b) DLS size distribution graph (by intensity) of a sample of FeO_y@Au@$Cu_{2-x}S$ trimers after "cold" reaction with $CuCl_2$ and Amicon filter purification (blue line) compared with DLS size distribution graph (by intensity) of the same sample before the reaction; c) UV-VIS-NIR (500 nm -1200 nm) spectrum of a sample of FeO_y@Au@$Cu_{2-x}S$ trimers after "cold" reaction with $CuCl_2$ and Amicon filter purification (blue line) compared with UV-VIS-NIR (500 nm -1200 nm) spectrum of the same sample before the reaction.

TEM picture in Figure 3.25a shows how the FeO_y@Au@$Cu_{2-x}S$ trimers are not changing shape or size (compare with TEM picture in Figure 3.12a) during the reaction with $CuCl_2$. As DLS size distribution graphs reported in Figure 3.25b show, trimers are losing part of their stability during the reaction and purification step. Indeed, hydrodynamic size distribution of the trimers after the reaction with "cold" $CuCl_2$ is broader and shifted to higher values if compared to the one of the starting sample. Although the amount of copper used in the reaction is reduced (copper coming from $CuCl_2$ was 0.65 % of the copper already present in the nanocrystals), from Figure 3.25c it can be seen that in the sample measured after the reaction, while the absorption peak related to gold LSPR is preserved, the absorption peak ascribed to the presence of copper-deficient copper sulfide domains completely disappeared. This situation is typical of $Cu_{2-x}S$ domains with x = 0[115] and could be explained with the incorporated Cu (I) ions filling the holes in nanocrystal lattice.

In order to further study the radiolabeling process on trimers, the same procedure was performed on Au@FeO_y dimers. In particular, this study was set up in order to understand if the radiolabeling was specifically taking place on the copper sulfide and to be able to out rule the possibility of nonspecific radiolabeling. Being copper element absent in dimers' chemical composition, the amount of Au@FeO_y used in the reactions was tuned in order to have the same iron content used in radiolabeling of FeO_y@Au@$Cu_{2-x}S$ heterostructures (when a 0.01 % $^{64}Cu/Cu_{NCs}$ percentage ratio was used). Reactions were performed without the addition of CYS-PIMA-PEG2000 in order to avoid introducing another potential source of activity withdrawal. Results are shown in Figure 3.26.

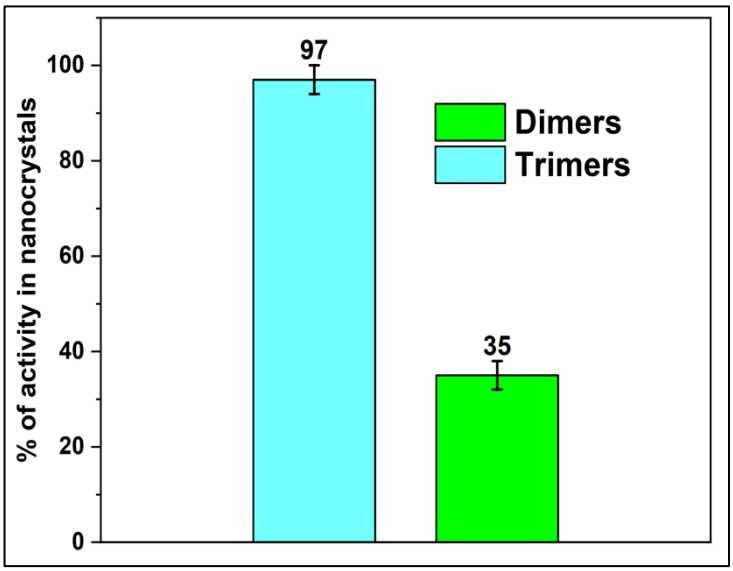

Figure 3.26: Radiochemical yields obtained for radiolabeling reactions, performed using same reaction parameters, on dimers (green bar) and trimers (light blue bar).

Surprisingly, also the radiolabeling of the dimers resulted in ^{64}Cu incorporation in nanocrystals. This incorporation of 35 % of ^{64}Cu used could be ascribed either to the chelation of some ^{64}Cu ions by thiol groups of CH_3O-PEG2000-SH molecules stabilizing gold and copper sulfide domains or to unspecific labeling from Au or FeO_y domains. In order to further study these radiolabeling reactions, EDTA challenge for the radiolabeled dimers and trimers was performed by adding to the reaction batch, after the incubation with $^{64}Cu:CuCl_2$, 150 µL of 0.5 M EDTA and checking the percentage of activity in the crystal fraction (RCY) through iTLC every 60 minutes for 3 hours. Results obtained are shown in Figure 3.27.

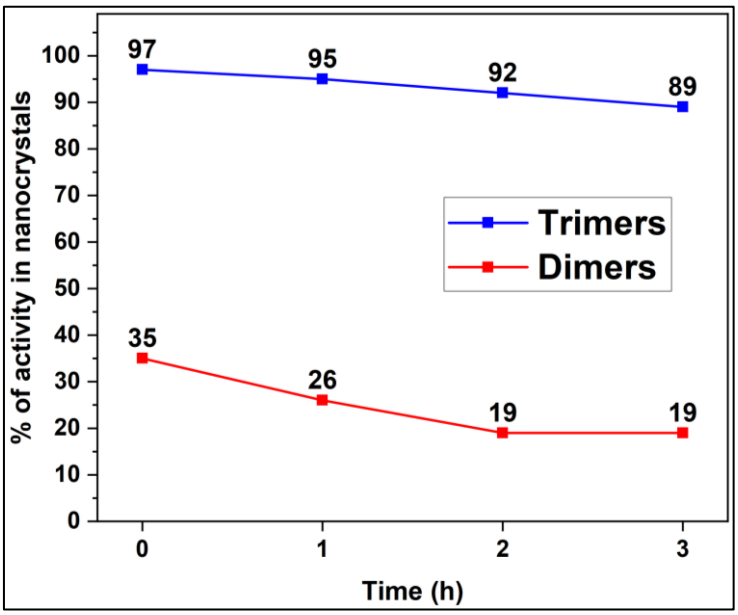

Figure 3.27: Percentage of activity in the nanocrystals fraction (RCY) measured during EDTA challenge on radiolabeled dimers (red line) and trimers (blue line) every 60 minutes for 3 hours.

Interestingly, while the activity incorporated in trimers' sample is reduced of only 8% after 3 hours of EDTA challenge, already after 2 hours dimers lost 16 % of their bounded ^{64}Cu, reducing the ^{64}Cu present in nanocrystals fraction of the TLC to 19 %. This indicates that ^{64}Cu affinity for the trimers is higher if compared to the one of the dimers, candidating the former as a better material for the aimed use as radioisotope ions carriers.

3.2.4. Photothermal performances of FeO_y@Au@$Cu_{2-x}S$ heterostructures

Another interesting property of the FeO_y@Au@ $Cu_{2-x}S$ trimers that can be used in biomedical applications is the presence of two LSPRs: the one of the gold nanoparticles acting as bridge between FeO_y and $Cu_{2-x}S$ domains and the one related to the presence of copper-deficient copper sulfide domains. The localized surface plasmon resonance absorbance peaks of Au and $Cu_{2-x}S$ domains are (see Figure 3.17b) respectively centered, in the water transferred samples, at 554 nm and around 1200 nm. The band of gold NPs' absorption is partially inside first NIR biological window (650 nm – 950 nm) while the absorption of $Cu_{2-x}S$ domains is centered inside the second NIR biological window (1000 nm – 1350 nm). Indeed, both Au[116] and $Cu_{2-x}S$[102] nanoparticles have been reported to be used in photothermal therapy. In order to combine together measurements of photothermal heating with measurements of magnetic hyperthermia heating (DUAL experiments), a special set-up had to be designed. Indeed, the capillary containing trimers' water stable sample had to be centered both with the coil of the hyperthermia set-up used (DM3 Series, NanoScale Biomagnetics) and with the laser beam. To achieve this aim, a custom sample holder was 3D-printed in polylactic acid (see Figure 3.28).

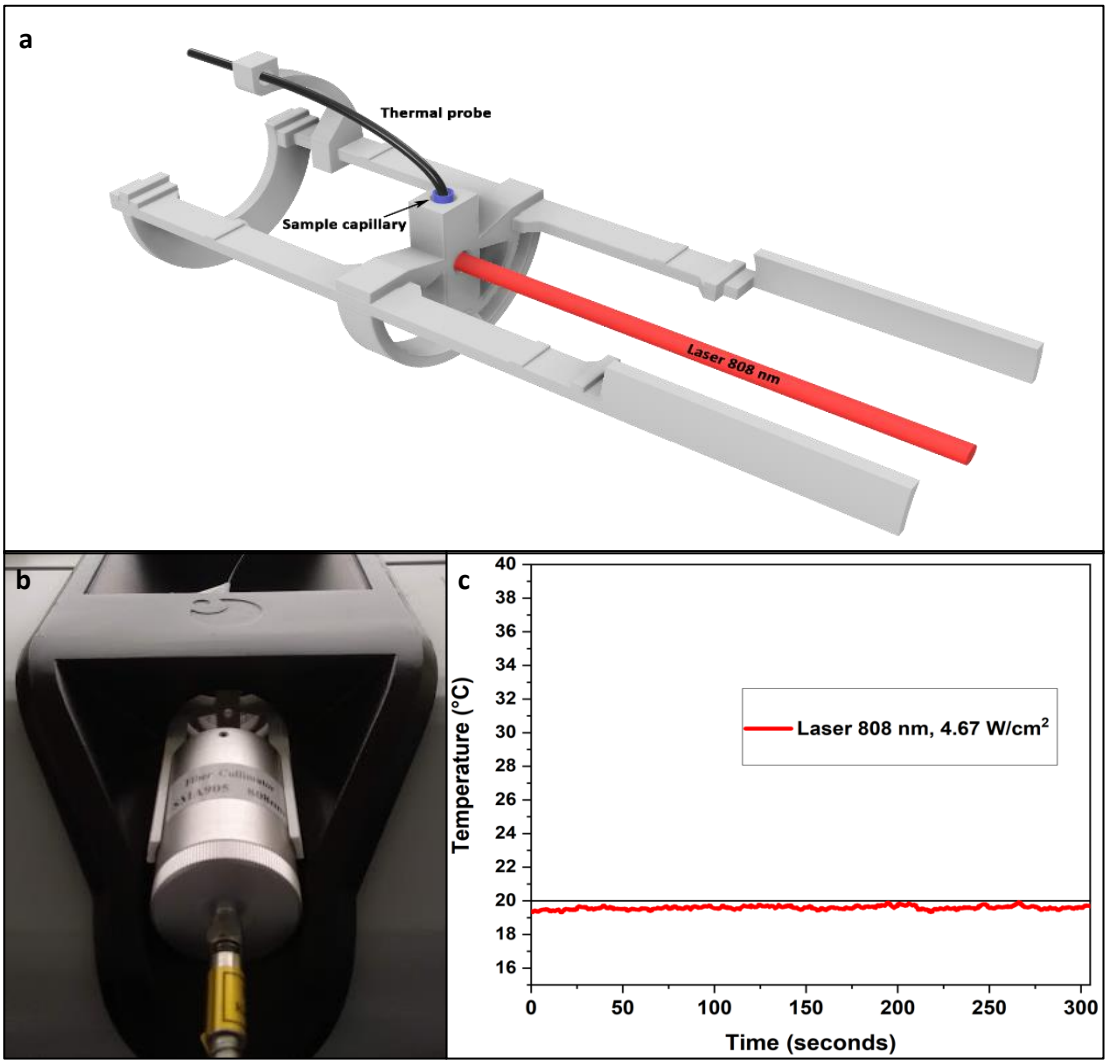

Figure 3.28: a) Graphical representation of the custom 3D-printed sample holder used for photothermal measurements and for DUAL (laser + magnetic hyperthermia) measurements; b) custom sample holder inserted in DM3 series hyperthermia set up and coupled with 808 nm laser; c) Heating curve of the empty capillary under 808 nm laser light with 4.67 W/cm² power density.

Sample holder was designed in order to properly shine the laser in the middle of the capillary while it is standing in the center of the hyperthermia set up solenoid. Moreover, the holder is designed in order to avoid the laser to directly hit the thermal probe, producing unspecific heating. The distance between laser optic and sample's capillary was set to be 4 cm: at this distance the laser beam has a diameter corresponding to the width of the capillary (3 mm diameter, 0.07065 cm^2 surface). The capillary holder has a window of 4 mm, through which the samples is exposed to the laser. The absence of unspecific heating given by the laser was confirmed by measuring the heating curve of the empty capillary (see Figure 3.28c). Results obtained irradiating trimers' sample (50 µL, [Fe] = 2.8 g/L, [Cu] = 1.6 g/L [Au] = 4.0 g/L) for 5 minutes using a 808 nm laser with power density of 4.67 W/cm^2 are shown and compared with the ones obtained on MilliQ water in Figure 3.29a. The reproducibility of the photothermal heating was tested through cycles of seven minutes laser irradiation (see Figure 3.29b).

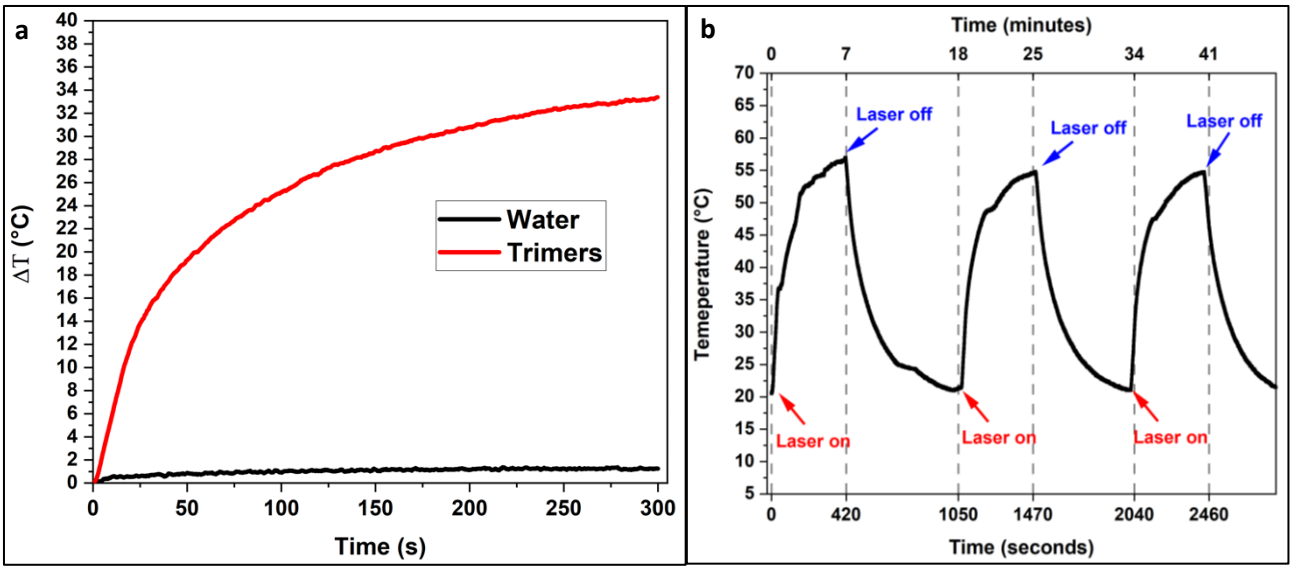

Figure 3.29: a) Heating curves (5 minutes) obtained by water (black line) and by trimers' sample (red line) irradiation using a 808 nm laser with power density of 4.67 W/cm²; b) test of laser heating reproducibility with seven minute cycles using same laser parameters.

While after 5 minutes of laser irradiation the temperature of water is substantially unchanged (ΔT = 1.3 °C), the temperature of trimers' sample after the same time was increased by 33°C.This temperature increase is in line with the one reported for photothermal experiments performed on Fe_3O_4@CuS heterostructures under similar conditions.[117] As shown in Figure 3.29b, FeO_y@Au@$Cu_{2-x}S$ trimers can be used for multiple cycles of laser heating since photothermal performances are not significantly reduced after the first heating ramp. Dual (laser irradiation + alternating magnetic field) heating curve was measured using same laser parameters and applying AMF with amplitude of 24 kA/m and frequency of 120 kHz. Results are shown in Figure 3.30.

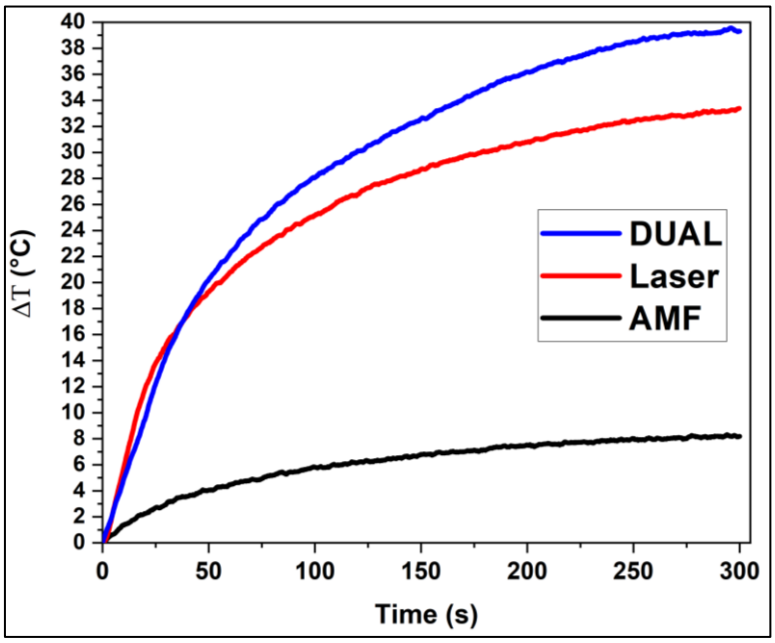

Figure 3.30: Heating curves (5 minutes) obtained from FeO_y@Au@$Cu_{2-x}S$ trimers under AMF (24 kA/m, 120 kHz, black line), 808 nm laser irradiation (4.67 W/cm², red line) and DUAL treatment (blue line).

When merging 808 nm laser irradiation with AMF application, the temperature increase of sample's solution is 39.6°C, this demonstrating the possibility to combine the two different heating modalities in order to obtain higher treatment efficiency (maximum temperature increase reached for hyperthermia treatment only is 8°C). Heating efficiency of the FeO_y@Au@$Cu_{2-x}S$ trimers was also tested using lower laser power density (2 W/cm^2). Indeed, for a bio-safe application, the limit value in order to avoid skin damage is reported to be of 0.33 W/cm^2.[101] Results are shown in Figure 3.31.

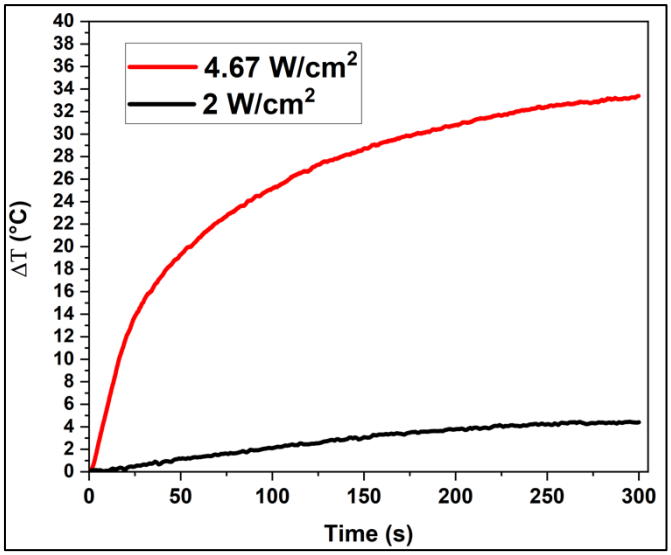

Figure 3.31: Heating curves (5 minutes) of FeO_y@Au@$Cu_{2-x}S$ trimers obtained under irradiation with 808 nm laser using a power density of 4.67 W/cm^2 (red line) and 2 W/cm^2 (black line).

Heating curves obtained by trimers under laser irradiation are strongly dependent on the power density used. Indeed, when the power density is reduced to 2 W/cm^2 the increase in temperature is of only 4.5°C. This is probably related to the low absorption of the water-transferred trimers at the used wavelength of 808 nm (see Figure 3.17b). One possibility to increase heating output with low laser power density could be to use lasers with smaller wavelength (remaining in NIR first biological window), a zone of FeO_y@Au@$Cu_{2-x}S$ spectrum where gold LSPR absorbance is more intense. Also, it could be possible, by changing synthesis parameters, to tune copper sulfide LSPR in order to have higher absorption intensity at lower wavelengths, exploiting lasers in the second NIR biological window (1000 nm – 1350 nm) One last possibility could be to try to design heterostructures using, instead of spherical gold nanoparticles as linkers between magnetic and chalcogenide domains, gold nanorods having one of their two LSPRs centered around 800 nm.

3.3. Conclusions and outlook

Different procedure and polymers (both commercially available and synthesized by researchers of our group) were used in order to phase transfer to water the newly synthesized FeO_y@Au@$Cu_{2-x}S$ trimers. Best results were obtained employing: i) a ligand exchange procedure with poly-catechol-PEG900 and CH_3O-PEG2000-SH; or ii) a polymer coating procedure with Poly-(Maleic Anhydride-alt-1-Octadecene). Both water transfer procedures preserved the morphology of the nano-heterostructures, while providing them excellent stability in aqueous media. Trimers transferred through polymer coating show slightly better hyperthermia performances, probably due to an inherent quality-sorting process. However, the simplicity of the ligand exchange procedure and its quantitative yield (> 80 % versus a yield of 15 % for polymer coating procedure), made this procedure the candidate for the experiments further performed.

Hyperthermia performances of ligand exchanged FeO_y@Au@$Cu_{2-x}S$ trimers were measured both through calorimetry and AC hysteresis loops measurements and compared with the one obtained for Au@FeO_y dimers with same iron oxide size and transferred to water with same procedure. SAR values obtained for trimers are similar to the one obtained for the excellently performing dimers and, when using Hf factors below the limit for safe clinical application (Hf ≤ 5×10^{-9} A/(m×s)), their properties (302 W/g when a field with frequency of 105 kHz and an amplitude of 32 kA/m were used) are in line with the values obtained with other magnetic heterostructures reported for hyperthermia applications.

Trimers were employed for aqueous phase radiolabeling reactions using $^{64}CuCl_2$. Using an activity of 18.5 MBq and a percentage ratio between added ^{64}Cu and copper in nanocrystals (Cu_{NCs}) of 0.01 %, it has been possible to incorporate 97 ± 3 % of the activity in the nanocrystals. Particles have been demonstrated to be stable during radiolabeling and subsequent purification procedure upon the addition of a small volume of 0.0049 M CYS-PIMA-PEG2000 solution. These experiments candidate FeO_y@Au@$Cu_{2-x}S$ nano-heterostructures as an efficient carrier for ^{64}Cu ions (and, eventually, ^{67}Cu ions). To the best of our knowledge, this is the first nano-heterostructure having a magnetic domain with excellent magnetic hyperthermia performances joint with another domain able to incorporate quantitatively ^{64}Cu ions.

FeO_y@Au@$Cu_{2-x}S$ nano-heterostructures were also tested in photothermal experiments both as stand-alone technique or in combination with magnetic hyperthermia (DUAL treatments). In order to perform DUAL measurements a custom 3D-printed sample holder was designed and used. While using an AMF with frequency of 120 kHz and amplitude of 32 kA/m, a temperature increase of 8 °C degrees was achieved in the sample's solution after 5 minutes, this value raised to 39.6 °C degrees in the case of DUAL treatment, which was performed by irradiating the sample with a 808 nm laser with 4.67 W/cm^2 power density. The heating performances under 808 nm laser irradiation of the trimers are strongly correlated to the power density. Indeed, while the temperature increase is of 33°C degrees after 5 minutes irradiation with a power density of 4.67 W/cm^2, this value drops to only 4°C in case of a power density of 2 W/cm^2. These preliminary results obtained for photothermal heating of FeO_y@Au@$Cu_{2-x}S$ trimers could be consistently improved by tuning wavelength absorption of both the gold and the copper-deficient copper sulfide domains by changing either their composition or their shape.

3.4. Experimental procedures

FeO_y@Au@$Cu_{2-x}S$ water transfer though ligand exchange using ND-PEG1500-COOH and CH_3O-PEG2000-SH: one-step procedure

1 mL of particles solution was mixed in a 40 mL glass vial with a 2mg/mL chloroform solution of CH_3O-PEG2000-SH in order to have a ligands/nm^2 ratio of 300 (based on gold and copper sulfide domains' surface) and with a 0.05 M solution of ND-PEG1500-COOH in order to have a ligands/nm^2 ratio of 300 (based on iron oxide domains' surface). Tri ethyl amine in amount equal to 70 equivalents of the ND-PEG1500-COOH was also added to the solution. Mixture was left under vigorous shaking at room temperature overnight. The sample was then recovered with toluene and extracted with MilliQ water two times. Resulting aqueous phases were recollected and bubbled with N_2 gas for at least two hours in order to remove traces of organic solvents. After the bubbling, aqueous phases were sonicated for 1 hour at 65°C and concentrated to a volume smaller than 10 mL using a 100 kDa MWCO Amicon filter. Resulting solution was then transferred in spectrum labs dialysis membrane (MWCO = 50 kDa) and dialyzed against water for two days. Water transfer was then completed by centrifuge concentration (400 RCF, 10 minutes) through 100 kDa MWCO Amicon filter up to a volume equal or smaller the one of the starting organic solvent-stable sample (1 mL).

FeO_y@Au@$Cu_{2-x}S$ water transfer though ligand exchange using ND-PEG1500-COOH and CH_3O-PEG2000-SH: two-steps procedure

1 mL of particles solution was mixed in a 40 mL glass vial with a 2 mg/mL chloroform solution of CH_3O-PEG2000-SH in order to have a ligands/nm^2 ratio of 300 (based on gold and copper sulfide domains' surface). After overnight shaking at room temperature, a 0.05 M solution of ND-PEG1500-COOH in order to have a ligands/nm^2 ratio of 300 (based on iron oxide domains' surface) and tri ethyl amine in amount equal to 70 equivalents of the ND-PEG1500-COOH were added to the solution and the mixture was shaken for one more night at room temperature. The sample was then recovered with toluene and extracted with MilliQ water two times. Resulting aqueous phases were recollected and bubbled with N_2 gas for at least two hours in order to remove traces of organic solvents. After the bubbling, aqueous phases were sonicated for 1 hour at 65°C and concentrated to a volume smaller than 10 mL using a 100 kDa MWCO Amicon filter. Resulting solution was then transferred in spectrum labs dialysis membrane (MWCO = 50 kDa) and dialyzed against water for two days. Water transfer was then completed by centrifuge concentration (400 RCF, 10 minutes) through 100 kDa MWCO Amicon filter up to a volume equal or smaller the one of the starting organic solvent stable sample (1 mL).

FeO_y@Au@$Cu_{2-x}S$ water transfer though ligand exchange using poly-catechol-PEG900 and CH_3O-PEG2000-SH

1 mL of particles solution was mixed in a 40 mL glass vial with a 2mg/mL chloroform solution of CH_3O-PEG2000-SH in order to have a ligands/nm^2 ratio of 300. For this ratio, only the surface of the Au NPs and $Cu_{2-x}S$ domains was taken into account. After overnight shaking at room temperature (RT = 25°C), a chloroform solution of multi-dentate (five catechol groups per molecule) poly-catechol-PEG900 was added to the sample and CH_3O-PEG2000-SH mixture. The amount of poly

catechol solution added was calculated in order to have a ligands/nm^2 ratio of 300, considering only FeO_y domains' surface. Tri ethyl amine (in [TEA] : [Catechol] molar ratio of 10:1) was further added to the mixture that was then let under shaking for another night. Afterwards, chloroform was evaporated from the vial through bubbling, 2 mL of THF were added to dissolve the IONCs and an excess amount of hexane (10 folds of volume) was added to induce the precipitation of ligand-exchanged particles. After 15 minutes of centrifugation at 300 RCF, the supernatant was then discarded and the process repeated one more time. After the second washing, particles were dispersed in water and, after 5 minutes sonication at RT, excess ligands were removed by means of centrifugal filtration. A 15 mL Amicon filter with molecular weight cut off (MWCO) of 100 kDa was used and 5 cycles of centrifuge washings (400 RCF, 10 minutes) were used in order to get rid of the free ligands.

FeO_y@Au@$Cu_{2-x}S$ water transfer through polymer coating with poly-(maleic anhydride-alt-1-octadecene)

As synthesized hydrophobic trimers were transferred to water by means of poly(maleic anhydride-alt-1-octadecene) (PMAO) using a protocol developed by our group with minor modifications.[108,109] 1 mL of the starting trimers samples is mixed with PMAO (with a ligands/nm^2 ratio of 500) in 50 mL of chloroform. Sample is then stabilized through sonication at 65°C. Chloroform is then evaporated using rotavapor with a batch temperature of 50°C and a rotation speed of 140 rpm. After 30 minutes rotavapor evaporation with 800 mbar pressure, followed by 30 minutes at 700 mbar, solvent was then evaporated at 650 mbar for 1 hour. As last step, the pressure was reduced to 600 mbar until complete drying of the product (usually 2 hours more). The dried black precipitate was then solubilized using 20 mL borate buffer and sonication at high temperature (65°C set as starting temperature of the sonication batch) for at least 2 hours. After, the sample's volume was reduced (to about 3 mL) through Amicon tube filters (100 k Da MWCO) centrifugation. The sample was finally loaded on top of a sucrose gradient (from top to bottom: 2 mL of 20%, 3 mL of 40% and 3 mL of 60% in an ultra-centrifugal tube) for ultracentrifugation in order to separate the coated particles from the unreacted polymer. 75 minutes of ultracentrifugation at 13700 RCF followed. Excess of polymer is then removed by means of a syringe and particles are cleaned from the sucrose and concentrated to 300 µL through centrifuge washings using 15 mL 100 kDa MWCO Amicon filter.

Gel electrophoresis

Gel electrophoresis was employed to evaluate water transferred trimers migration in a solid agarose matrix (1 % m/V agarose gel, 50 mg agarose in 50 mL TBE buffer). Samples were loaded on the matrix together with orange G visualizing dye and electrophoresis run was performed in tris-borate-EDTA (TBE) buffer applying a voltage of 100 V for 45 minutes.

Calorimetric measurements of Specific Absorption Rate

A commercially available set-up (DM1 Series, NanoScale Biomagnetics) was used to assess hyperthermia performance of gold–iron oxide dimers and of iron oxide-gold-copper sulfide trimers. 50 µL of an aqueous solution of nanoparticles' sample (with concentration ranging from 1 to 3 g_{iron}/L) were placed in a sample holder and introduced in the instrument. The device can apply fields up to 24 kA/m (for 217 kHz and 300 kHz) and 32 kA/m (in the case of used frequency of 105 kHz).

During alternated magnetic field application, temperature was measured through a fluoro-optic thermometer fiber probe (Luxtron Corp.) every 0.25 s. Reported SAR values and error bars were calculated respectively from average value and standard deviation of at least three experimental measurements according to the following equation:

$$SAR\left(\frac{W}{g}\right) = \frac{C}{m} \times \frac{dT}{dt}$$

where *C* is the specific heat capacity of water (4185 $J \times L^{-1} \times K^{-1}$), *m* is the concentration ($g \times L^{-1}$ of Fe) of magnetic material in solution and *dT/dt* the slope of the measured heating curve. In the used system, measurements were carried out under non-adiabatic conditions. For this reason, when measuring the slope of the curve *dT/dt* only the first few seconds of the temperature vs. time curve were taken into account.

AC hysteresis loops measurements

AC hysteresis loops were measured using a custom-made device for AC magnetic measurements (IMDEA). Hysteresis loops were recorded using different field's amplitudes (12 – 16 - 20 - 24 kA/m) and frequencies (100-200-300 kHz). Experiments were performed on both dimers and trimers, using 40 µL of sample with iron concentrations in the range $1 g_{iron}/L$ – $3 g_{iron}/L$.

Radiolabeling of FeO_y@Au@$Cu_{2-x}S$ trimers

Into an Eppendorf tube, a quantity of $^{64}CuCl_2$ corresponding to an activity of 18.5 MBq and 150 µL of 0.3 M MES buffer (pH 5.6) were added. The pH of the solution was then brought to a value around 6 by 2 M NaOH addition, in amounts depending on the specific activity and on the pH of the received $^{64}CuCl_2$ solution (typically, 6 µL of 2 M NaOH were used in order to adjust the pH of 35 µL of starting solution). Once the solution was brought to desired pH, 10 µL of ascorbic acid (0.1 M) as a reducing agent and NPs solution, (containing 10000 times the equivalent of ^{64}Cu (II) used for 0.01 % $^{64}Cu/Cu_{NCS}$ percentage ratio), were added. In order to stabilize the nanocrystals during the radiolabeling, 50 µL of a 0.0049 M aqueous solution of CYS-PIMA-PEG were added. After the addition of the stabilizing agent, the reaction mixture was incubated at 37°C for 60 minutes. Then, 1 µL of the reaction mixture was spotted on iTLC-SG chromatography paper (Agilent technology) and the iTLC was developed in 0.1 M EDTA (pH = 7.5) as mobile phase. The dried ITLC plates were exposed on an Imaging Plate for 30 seconds and the results were analyzed on an appropriate imaging system (FLA-9000, Perking Elmer).

Concentration and purification of the solution of radiolabeled nanocrystals

The washing and concentration of the nanocrystals after the radiolabeling procedure has been performed using 0.5 mL 100 kDa MWCO Amicon centrifugal filters (Merck). After the radiolabeling, the reaction mixture (approximatively 300 µL) was transferred to an Amicon filter inserted in an Eppendorf vial and MilliQ water added up to 500 µL. After 4 minutes of centrifugation at 4000 RCF, the filter containing radiolabeled nanocrystals was removed and inserted upside down in a new Eppendorf vial and centrifuged for 2 minutes at 2000 RCF. Through a dose calibrator (VDC-603, Comecer) the activity of the final nanocrystals' solution was checked and the percentage of activity recovered was compared with the radiochemical yield.

EDTA challenge on radiolabeled FeO_y@Au@$Cu_{2-x}S$ trimers and Au@ FeO_y dimers

In order to perform EDTA challenge, 150 µL of EDTA 0.5 M were mixed to the radiolabeling batch of dimers and trimers and incubated for 3 hours at 37°C. Through iTLC the percentage of radioactive ^{64}Cu incorporated in the nanocrystals has been checked after 60, 120 and 180 minutes.

Measurements of photothermal and DUAL modality heating performances of FeO_y@Au@$Cu_{2-x}S$ trimers

50 µL of trimers' sample with the same concentration used for a typical magnetic hyperthermia experiment ([Fe] = 2.8 g/L, [Cu] = 1.6 g/L [Au] = 4.0 g/L) are inserted in a glass capillary, placed in a custom-made 3D-printed sample holder. 808 nm laser with different power densities (4.67 W/cm^2 or 2 W/cm^2) is irradiated on the sample. Distance between laser optic and sample is 4 cm, laser spot size on the capillary is 0.07065 cm^2. For the DUAL treatment, the sample holder was positioned in the middle of the coil of a commercially available set-up (DM3 Series, NanoScale Biomagnetics) for hyperthermia measurements. Alternating magnetic field used for the DUAL measurements had a frequency of 120 kHz and amplitude of 24 kA/m. Temperature of the samples' solution was measured through a fluoro-optic thermometer fiber probe (Luxtron Corp.) every 0.25 s.

3.5. References

1. Dewhirst, M. W., Vujaskovic, Z., Jones, E. & Thrall, D. Re-setting the biologic rationale for thermal therapy. *Int. J. Hyperth.* **21**, 779–790 (2005).

2. Peng, L. *Hyperthermia in oncology*. (CRC Press, 2015).

3. DeNardo, G. L. & DeNardo, S. J. Turning the heat on cancer. *Cancer Biother. Radiopharm.* **23**, 671–679 (2008).

4. Chang, D. *et al.* Biologically targeted magnetic hyperthermia: Potential and limitations. *Front. Pharmacol.* **9**, (2018).

5. Servadio, C., Leib, Z. & Lev, A. Diseases of prostate treated by local microwave hyperthermia. *Urology* **30**, 97–99 (1987).

6. Franckena, M. *et al.* Long-Term Improvement in Treatment Outcome After Radiotherapy and Hyperthermia in Locoregionally Advanced Cervix Cancer: An Update of the Dutch Deep Hyperthermia Trial. *Int. J. Radiat. Oncol.* **70**, 1176–1182 (2008).

7. Van Driel, W. J. *et al.* Hyperthermic intraperitoneal chemotherapy in ovarian cancer. *N. Engl. J. Med.* **378**, 230–240 (2018).

8. Verwaal, V. J., Bruin, S., Boot, H., Van Slooten, G. & Van Tinteren, H. 8-Year follow-up of randomized trial: Cytoreduction and hyperthermic intraperitoneal chemotherapy versus systemic chemotherapy in patients with peritoneal carcinomatosis of colorectal cancer. *Ann. Surg. Oncol.* **15**, 2426–2432 (2008).

9. Van Leeuwen, C. M. *et al.* A short time interval between radiotherapy and hyperthermia reduces in-field recurrence and mortality in women with advanced cervical cancer. *Radiat. Oncol.* **12**, 75 (2017).

10. Wust, P. *et al.* Hyperthermia in combined treatment of cancer. *Lancet Oncol.* **3**, 487–497 (2002).

11. Mahmood, J. *et al.* Immunotherapy, radiotherapy, and hyperthermia: A combined therapeutic approach in pancreatic cancer treatment. *Cancers (Basel).* **10**, 469 (2018).

12. Chicheł, A., Skowronek, J., Kubaszewska, M. & Kanikowski, M. Hyperthermia – description of a method and a review of clinical applications. *Reports Pract. Oncol. Radiother.* **12**, 267–275 (2007).

13. Matsukawa, T. *et al.* Percutaneous microwave coagulation therapy in liver tumors: A 3-year experience. *Acta radiol.* **38**, 410–415 (1997).

14. Goldberg, S. N., Gazelle, G. S. & Mueller, P. R. Thermal ablation therapy for focal malignancy: A unified approach to underlying principles, techniques, and diagnostic imaging guidance. *Am. J. Roentgenol.* **174**, 323–331 (2000).

15. Roti, J. L. Cellular responses to hyperthermia (40-46°C): Cell killing and molecular events. *Int.*

J. Hyperth. **24**, 3–15 (2008).

16. Hildebrandt, B. *et al.* The cellular and molecular basis of hyperthermia. *Crit. Rev. Oncol. Hematol.* **43**, 33–56 (2002).

17. Song, C. W. Effect of local hyperthermia on blood flow and microenvironment: A review. *Cancer Res.* **44**, (1984).

18. Song, C. W., Park, H. J., Lee, C. K. & Griffin, R. Implications of increased tumor blood flow and oxygenation caused by mild temperature hyperthermia in tumor treatment. *Int. J. Hyperth.* **21**, 761–767 (2005).

19. Oei, A. L., Vriend, L. E. M., Crezee, J., Franken, N. A. P. & Krawczyk, P. M. Effects of hyperthermia on DNA repair pathways: One treatment to inhibit them all. *Radiat. Oncol.* **10**, 1–13 (2015).

20. Eppink, B., Krawczyk, P. M., Stap, J. & Kanaar, R. Hyperthermia-induced DNA repair deficiency suggests novel therapeutic anti-cancer strategies. *Int. J. Hyperth.* **28**, 509–517 (2012).

21. Burd, R. *et al.* Tumor cell apoptosis, lymphocyte recruitment and tumor vascular changes are induced by low temperature, long duration (fever-like) whole body hyperthermia. *J. Cell. Physiol.* **177**, 137–147 (1998).

22. Frey, B. *et al.* Old and new facts about hyperthermia-induced modulations of the immune system. *Int. J. Hyperth.* **28**, 528–542 (2012).

23. Oda, M., Koga, S. & Maeta, M. Effects of Total-Body Hyperthermia on Metastases from Experimental Mouse Tumors. *Cancer Res.* **45**, 1532–1535 (1985).

24. Westermann, A. M. *et al.* A Systemic Hyperthermia Oncologic Working Group Trial. *Oncology* **64**, 312–321 (2003).

25. Amichetti, M., Valdagni, R., Graiff, C. & Valentini, A. Local-regional recurrences of breast cancer: Treatment with radiation therapy and local microwave hyperthermia. *Am. J. Clin. Oncol. Cancer Clin. Trials* **14**, 60–65 (1991).

26. Hiraoka, M. *et al.* Radiofrequency capacitive hyperthermia for deep-seated tumors. I. Studies on thermometry. *Cancer* **60**, 121–127 (1987).

27. Stehlin, J. S., Giovanella, B. C., de Ipolyi, P. D., Muenz, L. R. & Anderson, R. F. Results of hyperthermic perfusion for melanoma of the extremities. *Surg. Gynecol. Obstet.* **140**, 339–48 (1975).

28. Masters, A. & Bown, S. G. Interstitial laser hyperthermia. *Semin. Surg. Oncol.* **8**, 242–249 (1992).

29. Mendecki, J., Friedenthal, E., Botstein, C., Paglione, R. & Sterzer, F. Microwave applicators for localized hyperthermia treatment of cancer of the prostate. *Int. J. Radiat. Oncol. Biol. Phys.* **6**, 1583–1588 (1980).

30. Marmor, J. B., Pounds, D., Postic, T. B. & Hahn, G. M. Treatment of superficial human neoplasms by local hyperthermia induced by ultrasound. *Cancer* **43**, 188–197 (1979).

31. Cherukuri, P., Glazer, E. S. & Curley, S. A. Targeted hyperthermia using metal nanoparticles. *Adv. Drug Deliv. Rev.* **62**, 339–345 (2010).

32. Chatterjee, D. K., Diagaradjane, P. & Krishnan, S. Nanoparticle-mediated hyperthermia in cancer therapy. *Ther. Deliv.* **2**, 1001–1014 (2011).

33. Cole, A. J., Yang, V. C. & David, A. E. Cancer theranostics: The rise of targeted magnetic nanoparticles. *Trends in Biotechnology* **29**, 323–332 (2011).

34. Sharma, H., Mishra, P. K., Talegaonkar, S. & Vaidya, B. Metal nanoparticles: A theranostic nanotool against cancer. *Drug Discovery Today* **20**, 1143–1151 (2015).

35. Hayashi, K. *et al.* Superparamagnetic nanoparticle clusters for cancer theranostics combining magnetic resonance imaging and hyperthermia treatment. *Theranostics* **3**, 366–376 (2013).

36. Branca, M., Ibrahim, M., Ciuculescu, D., Philippot, K. & Amiens, C. Water transfer of hydrophobic nanoparticles: Principles and methods. in *Handbook of Nanoparticles* 1279–1311 (Springer International Publishing, 2015). doi:10.1007/978-3-319-15338-4_29

37. Guardia, P. *et al.* Water-Soluble Iron Oxide Nanocubes with High Values of Specific Absorption Rate for Cancer Cell Hyperthermia Treatment. *ACS Nano* **6**, 3080–3091 (2012).

38. Guardia, P. *et al.* One pot synthesis of monodisperse water soluble iron oxide nanocrystals with high values of the specific absorption rate. *J. Mater. Chem. B* **2**, 4426 (2014).

39. Lak, A. *et al.* Fe2+ Deficiencies, FeO Subdomains, and Structural Defects Favor Magnetic Hyperthermia Performance of Iron Oxide Nanocubes into Intracellular Environment. *Nano Lett.* **18**, 6856–6866 (2018).

40. Guardia, P. *et al.* Gold–iron oxide dimers for magnetic hyperthermia: the key role of chloride ions in the synthesis to boost the heating efficiency. *J. Mater. Chem. B* **5**, 4587–4594 (2017).

41. Wang, S. *et al.* Plasmonic copper sulfide nanocrystals exhibiting near-infrared photothermal and photodynamic therapeutic effects. *ACS Nano* **9**, 1788–1800 (2015).

42. GILCHRIST, R. K. *et al.* Selective inductive heating of lymph nodes. *Ann. Surg.* **146**, 596–606 (1957).

43. MagForce. Available at: https://www.magforce.com/home/.

44. Mahmoudi, K., Bouras, A., Bozec, D., Ivkov, R. & Hadjipanayis, C. Magnetic hyperthermia therapy for the treatment of glioblastoma: a review of the therapy's history, efficacy and application in humans. *Int. J. Hyperth.* **34**, 1316–1328 (2018).

45. Colombo, M. *et al.* Biological applications of magnetic nanoparticles. *Chem. Soc. Rev.* **41**, 4306 (2012).

46. Lévy, M. *et al.* Magnetically induced hyperthermia: Size-dependent heating power of γ-Fe2O3

nanoparticles. *J. Phys. Condens. Matter* **20**, (2008).

47. Ma, M. *et al.* Size dependence of specific power absorption of Fe 3 O 4 particles in AC magnetic field. *J. Magn. Magn. Mater.* **268**, 33–39 (2004).

48. Cabrera, D. *et al.* Unraveling viscosity effects on the hysteresis losses of magnetic nanocubes. *Nanoscale* **9**, 5094–5101 (2017).

49. Cabrera, D., Camarero, J., Ortega, D. & Teran, F. J. Influence of the aggregation, concentration, and viscosity on the nanomagnetism of iron oxide nanoparticle colloids for magnetic hyperthermia. *J. Nanoparticle Res.* **17**, (2015).

50. Majetich, S. A., Wen, T. & Mefford, O. T. Magnetic nanoparticles. *MRS Bull.* **38**, 899–903 (2013).

51. Nemati, Z. *et al.* Improving the Heating Efficiency of Iron Oxide Nanoparticles by Tuning Their Shape and Size. *J. Phys. Chem. C* **122**, 2367–2381 (2018).

52. Nemati, Z. *et al.* Enhanced Magnetic Hyperthermia in Iron Oxide Nano-Octopods: Size and Anisotropy Effects. *J. Phys. Chem. C* **120**, 8370–8379 (2016).

53. Hergt, R. & Dutz, S. Magnetic particle hyperthermia-biophysical limitations of a visionary tumour therapy. *J. Magn. Magn. Mater.* **311**, 187–192 (2007).

54. Gazeau, F., Lévy, M. & Wilhelm, C. Optimizing magnetic nanoparticle design for nanothermotherapy. *Nanomedicine* **3**, 831–844 (2008).

55. Deatsch, A. E. & Evans, B. A. Heating efficiency in magnetic nanoparticle hyperthermia. *Journal of Magnetism and Magnetic Materials* **354**, 163–172 (2014).

56. Abenojar, E. C., Wickramasinghe, S., Bas-Concepcion, J. & Samia, A. C. S. Structural effects on the magnetic hyperthermia properties of iron oxide nanoparticles. *Prog. Nat. Sci. Mater. Int.* **26**, 440–448 (2016).

57. Périgo, E. A. *et al.* Fundamentals and advances in magnetic hyperthermia. *Appl. Phys. Rev.* **2**, (2015).

58. Sathya, A. *et al.* Co x Fe 3– x O 4 Nanocubes for Theranostic Applications: Effect of Cobalt Content and Particle Size. *Chem. Mater.* **28**, 1769–1780 (2016).

59. Martinez-Boubeta, C. *et al.* Learning from nature to improve the heat generation of iron-oxide nanoparticles for magnetic hyperthermia applications. *Sci. Rep.* (2013). doi:10.1038/srep01652

60. Bauer, L. M., Situ, S. F., Griswold, M. A. & Samia, A. C. S. High-performance iron oxide nanoparticles for magnetic particle imaging – guided hyperthermia (hMPI). *Nanoscale* **8**, 12162–12169 (2016).

61. Unni, M. *et al.* Thermal Decomposition Synthesis of Iron Oxide Nanoparticles with Diminished Magnetic Dead Layer by Controlled Addition of Oxygen. *ACS Nano* acsnano.7b00609 (2017).

doi:10.1021/acsnano.7b00609

62. Habib, A. H., Ondeck, C. L., Chaudhary, P., Bockstaller, M. R. & McHenry, M. E. Evaluation of iron-cobalt/ferrite core-shell nanoparticles for cancer thermotherapy. *J. Appl. Phys.* **103**, (2008).

63. Amiri, S. & Shokrollahi, H. The role of cobalt ferrite magnetic nanoparticles in medical science. *Materials Science and Engineering C* **33**, 1–8 (2013).

64. Hanini, A. *et al.* Zinc substituted ferrite nanoparticles with Zn0.9Fe2.1O4 formula used as heating agents for in vitro hyperthermia assay on glioma cells. *J. Magn. Magn. Mater.* **416**, 315–320 (2016).

65. Esmaeili, A. & Alizadeh Hadad, N. Preparation of ZnFe<inf>2</inf>O<inf>4</inf>-chitosan-doxorubicin hydrochloride nanoparticles and investigation of their hyperthermic heat-generating characteristics. *Ceram. Int.* **41**, 7529–7535 (2015).

66. Pradhan, P., Giri, J., Banerjee, R., Bellare, J. & Bahadur, D. Preparation and characterization of manganese ferrite-based magnetic liposomes for hyperthermia treatment of cancer. *J. Magn. Magn. Mater.* **311**, 208–215 (2007).

67. Doaga, A. *et al.* Synthesis and characterizations of manganese ferrites for hyperthermia applications. *Mater. Chem. Phys.* **143**, 305–310 (2013).

68. Singh, N., Jenkins, G. J. S., Asadi, R. & Doak, S. H. Potential toxicity of superparamagnetic iron oxide nanoparticles (SPION). *Nano Rev.* **1**, 5358 (2010).

69. Mehdaoui, B. *et al.* Magnetic anisotropy determination and magnetic hyperthermia properties of small Fe nanoparticles in the superparamagnetic regime. *J. Appl. Phys.* **107**, 09A324 (2010).

70. Lee, J. H. *et al.* Exchange-coupled magnetic nanoparticles for efficient heat induction. *Nat. Nanotechnol.* **6**, 418–422 (2011).

71. Lim, W. Q. & Gao, Z. Plasmonic nanoparticles in biomedicine. *Nano Today* **11**, 168–188 (2016).

72. Khlebtsov, N. G. & Dykman, L. A. Optical properties and biomedical applications of plasmonic nanoparticles. *J. Quant. Spectrosc. Radiat. Transf.* **111**, 1–35 (2010).

73. Hammond, J., Bhalla, N., Rafiee, S. & Estrela, P. Localized Surface Plasmon Resonance as a Biosensing Platform for Developing Countries. *Biosensors* **4**, 172–188 (2014).

74. Mayer, K. M. & Hafner, J. H. Localized surface plasmon resonance sensors. *Chem. Rev.* **111**, 3828–3857 (2011).

75. Unser, S., Bruzas, I., He, J. & Sagle, L. Localized Surface Plasmon Resonance Biosensing: Current Challenges and Approaches. *Sensors* **15**, 15684–15716 (2015).

76. Webb, J. A. & Bardhan, R. Emerging advances in nanomedicine with engineered gold nanostructures. *Nanoscale* **6**, 2502–2530 (2014).

77. Hainfeld, J. F., Slatkin, D. N., Focella, T. M. & Smilowitz, H. M. Gold nanoparticles: a new X-ray contrast agent. *Br. J. Radiol.* **79**, 248–253 (2006).

78. Popovtzer, R. *et al.* Targeted gold nanoparticles enable molecular CT imaging of cancer. *Nano Lett.* **8**, 4593–4596 (2008).

79. Qian, X. M. & Nie, S. M. Single-molecule and single-nanoparticle SERS: From fundamental mechanisms to biomedical applications. *Chem. Soc. Rev.* **37**, 912–920 (2008).

80. Dasary, S. S. R., Singh, A. K., Senapati, D., Yu, H. & Ray, P. C. Gold nanoparticle based label-free SERS probe for ultrasensitive and selective detection of trinitrotoluene. *J. Am. Chem. Soc.* **131**, 13806–13812 (2009).

81. Jain, P. K., Lee, K. S., El-Sayed, I. H. & El-Sayed, M. A. Calculated Absorption and Scattering Properties of Gold Nanoparticles of Different Size, Shape, and Composition: Applications in Biological Imaging and Biomedicine. *J. Phys. Chem. B* **110**, 7238–7248 (2006).

82. Link, S., Burda, C., Nikoobakht, B. & El-Sayed, M. A. Laser-induced shape changes of colloidal gold nanorods using femtosecond and nanosecond laser pulses. *J. Phys. Chem. B* **104**, 6152–6163 (2000).

83. Link, S., Burda, C., Mohamed, M. B., Nikoobakht, B. & El-Sayed, M. A. Laser Photothermal Melting and Fragmentation of Gold Nanorods: Energy and Laser Pulse-Width Dependence. *Journal of Physical Chemistry A* **103**, 1165–1170 (1999).

84. Link, S. & El-Sayed, M. A. Size and temperature dependence of the plasmon absorption of colloidal gold nanoparticles. *J. Phys. Chem. B* **103**, 4212–4217 (1999).

85. Doughty, A. C. V. *et al.* Nanomaterial applications in photothermal therapy for cancer. *Materials (Basel).* **12**, (2019).

86. Hemmer, E. *et al.* Upconverting and NIR emitting rare earth based nanostructures for NIR-bioimaging. *Nanoscale* **5**, 11339 (2013).

87. Jing-Liang Li & Min Gu. Gold-Nanoparticle-Enhanced Cancer Photothermal Therapy. *IEEE J. Sel. Top. Quantum Electron.* **16**, 989–996 (2010).

88. Hwang, S. *et al.* Gold nanoparticle-mediated photothermal therapy: current status and future perspective. *Nanomedicine* **9**, 2003–2022 (2014).

89. Riley, R. S. & Day, E. S. Gold nanoparticle-mediated photothermal therapy: applications and opportunities for multimodal cancer treatment. *Wiley Interdiscip. Rev. Nanomed. Nanobiotechnol.* **9**, e1449 (2017).

90. Huang, X., Qian, W., El-Sayed, I. H. & El-Sayed, M. A. The potential use of the enhanced nonlinear properties of gold nanospheres in photothermal cancer therapy. *Lasers Surg. Med.* **39**, 747–753 (2007).

91. Dickerson, E. B. *et al.* Gold nanorod assisted near-infrared plasmonic photothermal therapy (PPTT) of squamous cell carcinoma in mice. *Cancer Lett.* **269**, 57–66 (2008).

92. Choi, W. Il *et al.* Tumor regression in vivo by photothermal therapy based on gold-nanorod-loaded, functional nanocarriers. *ACS Nano* **5**, 1995–2003 (2011).

93. Huang, X., El-Sayed, I. H., Qian, W. & El-Sayed, M. A. Cancer Cell Imaging and Photothermal Therapy in the Near-Infrared Region by Using Gold Nanorods. *J. Am. Chem. Soc.* **128**, 2115–2120 (2006).

94. Liu, H. *et al.* Multifunctional gold nanoshells on silica nanorattles: A platform for the combination of photothermal therapy and chemotherapy with low systemic toxicity. *Angew. Chemie - Int. Ed.* **50**, 891–895 (2011).

95. Melancon, M. P. *et al.* In vitro and in vivo targeting of hollow gold nanoshells directed at epidermal growth factor receptor for photothermal ablation therapy. *Mol. Cancer Ther.* **7**, 1730–1739 (2008).

96. Chen, H. *et al.* Multifunctional gold nanostar conjugates for tumor imaging and combined photothermal and chemo-therapy. *Theranostics* **3**, 633–649 (2013).

97. Liu, Y. *et al.* A plasmonic gold nanostar theranostic probe for in vivo tumor imaging and photothermal therapy. *Theranostics* **5**, 946–960 (2015).

98. Zhou, Z., Wang, Y., Yan, Y., Zhang, Q. & Cheng, Y. Dendrimer-Templated Ultrasmall and Multifunctional Photothermal Agents for Efficient Tumor Ablation. *ACS Nano* **10**, 4863–4872 (2016).

99. Tang, S., Chen, M. & Zheng, N. Sub-10-nm Pd nanosheets with renal clearance for efficient near-infrared photothermal cancer therapy. *Small* **10**, 3139–3144 (2014).

100. Li, Y., Lu, W., Huang, Q., Li, C. & Chen, W. Copper sulfide nanoparticles for photothermal ablation of tumor cells. *Nanomedicine* **5**, 1161–1171 (2010).

101. Laser Institute of America. *American National Standard for Safe Use of Lasers*. (2007).

102. Tian, Q. *et al.* Hydrophilic Cu 9 S 5 Nanocrystals: A Photothermal Agent with a 25.7% Heat Conversion Efficiency for Photothermal Ablation of Cancer Cells in Vivo. *ACS Nano* **5**, 9761–9771 (2011).

103. Tian, Q. *et al.* Sub-10 nm Fe3O4@Cu2-xS core-shell nanoparticles for dual-modal imaging and photothermal therapy. *J. Am. Chem. Soc.* **135**, 8571–8577 (2013).

104. Tian, Q. *et al.* Hydrophilic flower-like cus superstructures as an efficient 980 nm laser-driven photothermal agent for ablation of cancer cells. *Adv. Mater.* **23**, 3542–3547 (2011).

105. Liu, Y., Bhattarai, P., Dai, Z. & Chen, X. Photothermal therapy and photoacoustic imaging: Via nanotheranostics in fighting cancer. *Chem. Soc. Rev.* **48**, 2053–2108 (2019).

106. Gomes, J., Grunau, A., Lawrence, A. K., Eberl, L. & Gademann, K. Bioinspired, releasable quorum sensing modulators. *Chem. Commun.* **49**, 155–157 (2013).

107. Na, H. Bin *et al.* Multidentate catechol-based polyethylene glycol oligomers provide

enhanced stability and biocompatibility to iron oxide nanoparticles. *ACS Nano* **6**, 389–399 (2012).

108. Pellegrino, T. *et al.* Hydrophobic nanocrystals coated with an amphiphilic polymer shell: A general route to water soluble nanocrystals. *Nano Lett.* **4**, 703–707 (2004).

109. Di Corato, R. *et al.* Water solubilization of hydrophobic nanocrystals by means of poly(maleic anhydride-alt-1-octadecene). *J. Mater. Chem.* **18**, 1991–1996 (2008).

110. Ghosh, S. K., Nath, S., Kundu, S., Esumi, K. & Pal, T. Solvent and ligand effects on the localized surface plasmon resonance (LSPR) of gold colloids. *J. Phys. Chem. B* **108**, 13963–13971 (2004).

111. Hergt, R., Dutz, S., Müller, R. & Zeisberger, M. Magnetic particle hyperthermia: Nanoparticle magnetism and materials development for cancer therapy. *J. Phys. Condens. Matter* **18**, (2006).

112. Espinosa, A. *et al.* Can magneto-plasmonic nanohybrids efficiently combine photothermia with magnetic hyperthermia? *Nanoscale* **7**, 18872–18877 (2015).

113. Riedinger, A. *et al.* Post-Synthesis Incorporation of 64Cu in CuS Nanocrystals to Radiolabel Photothermal Probes: A Feasible Approach for Clinics. *J. Am. Chem. Soc.* **137**, 15145–15151 (2015).

114. Zhou, M. *et al.* A chelator-free multifunctional [64Cu]CuS nanoparticle platform for simultaneous micro-PET/CT imaging and photothermal ablation therapy. *J. Am. Chem. Soc.* **132**, 15351–15358 (2010).

115. Kriegel, I. *et al.* Tuning the excitonic and plasmonic properties of copper chalcogenide nanocrystals. *J. Am. Chem. Soc.* **134**, 1583–1590 (2012).

116. Huang, X., Jain, P. K., El-Sayed, I. H. & El-Sayed, M. A. Plasmonic photothermal therapy (PPTT) using gold nanoparticles. *Lasers Med. Sci.* **23**, 217–228 (2008).

117. Wu, Z. C., Li, W. P., Luo, C. H., Su, C. H. & Yeh, C. S. Rattle-Type Fe3O4@CuS Developed to Conduct Magnetically Guided Photoinduced Hyperthermia at First and Second NIR Biological Windows. *Adv. Funct. Mater.* **25**, 6527–6537 (2015).

Appendix

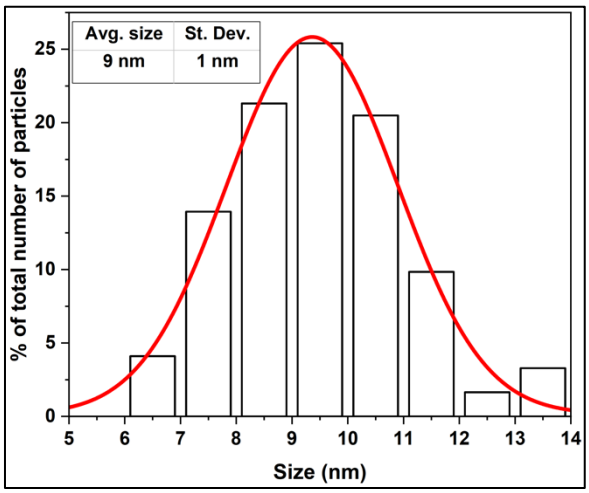

Figure A1: Size dispersion graph of water-transferred ZnS nanoparticles shown in Figure 1.7a.

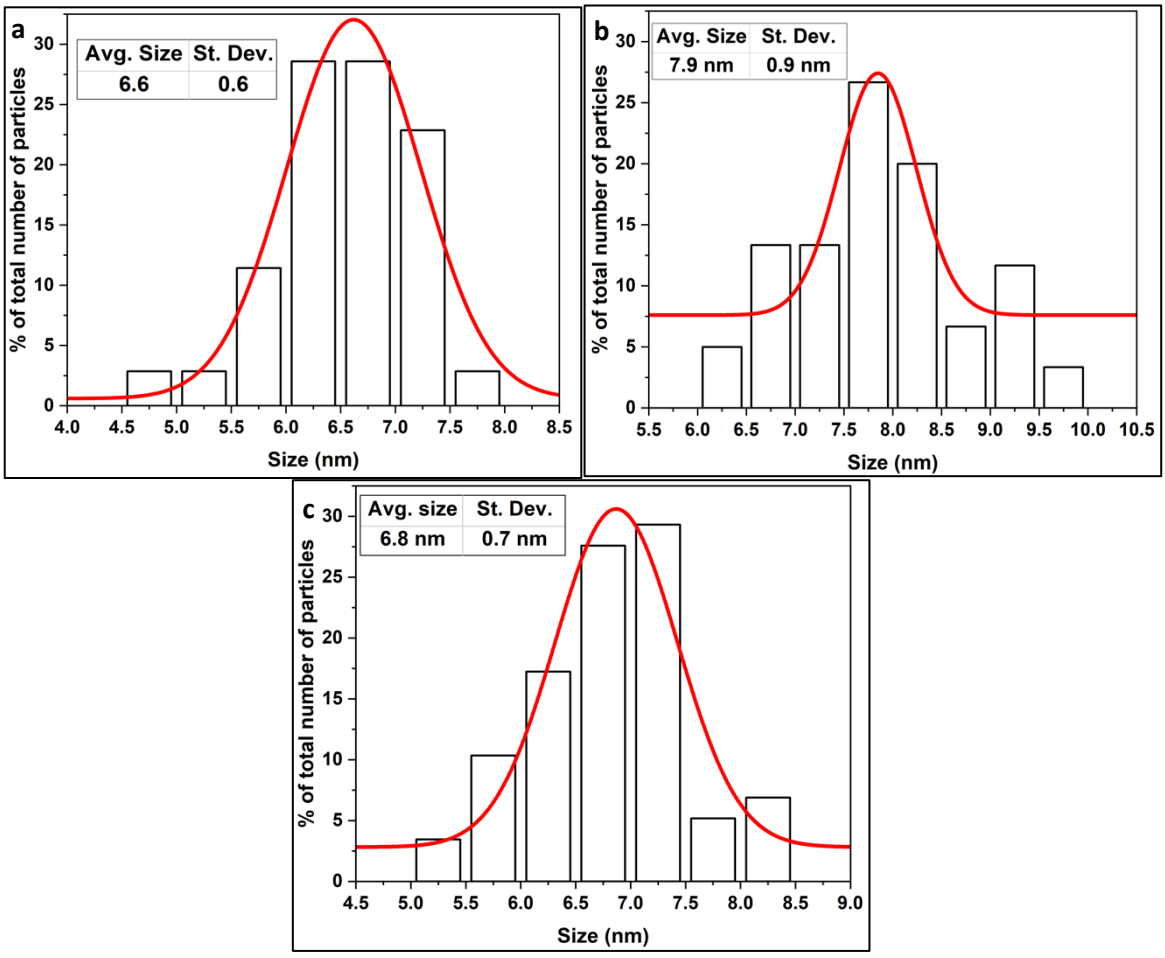

Figure A2: Size dispersion graphs of γ-Fe_2O_3 domains shown in a) Figure 2.2a; b) Figure 2.2b; c) Figure 2.2c.

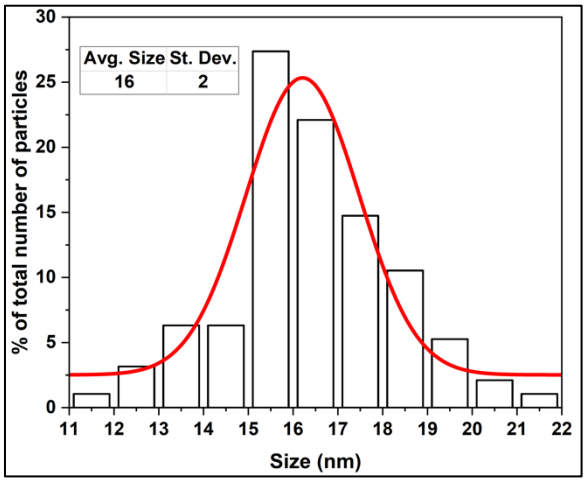

Figure A 3: Size dispersion graph of IONCs sample shown in Figure 2.4a.

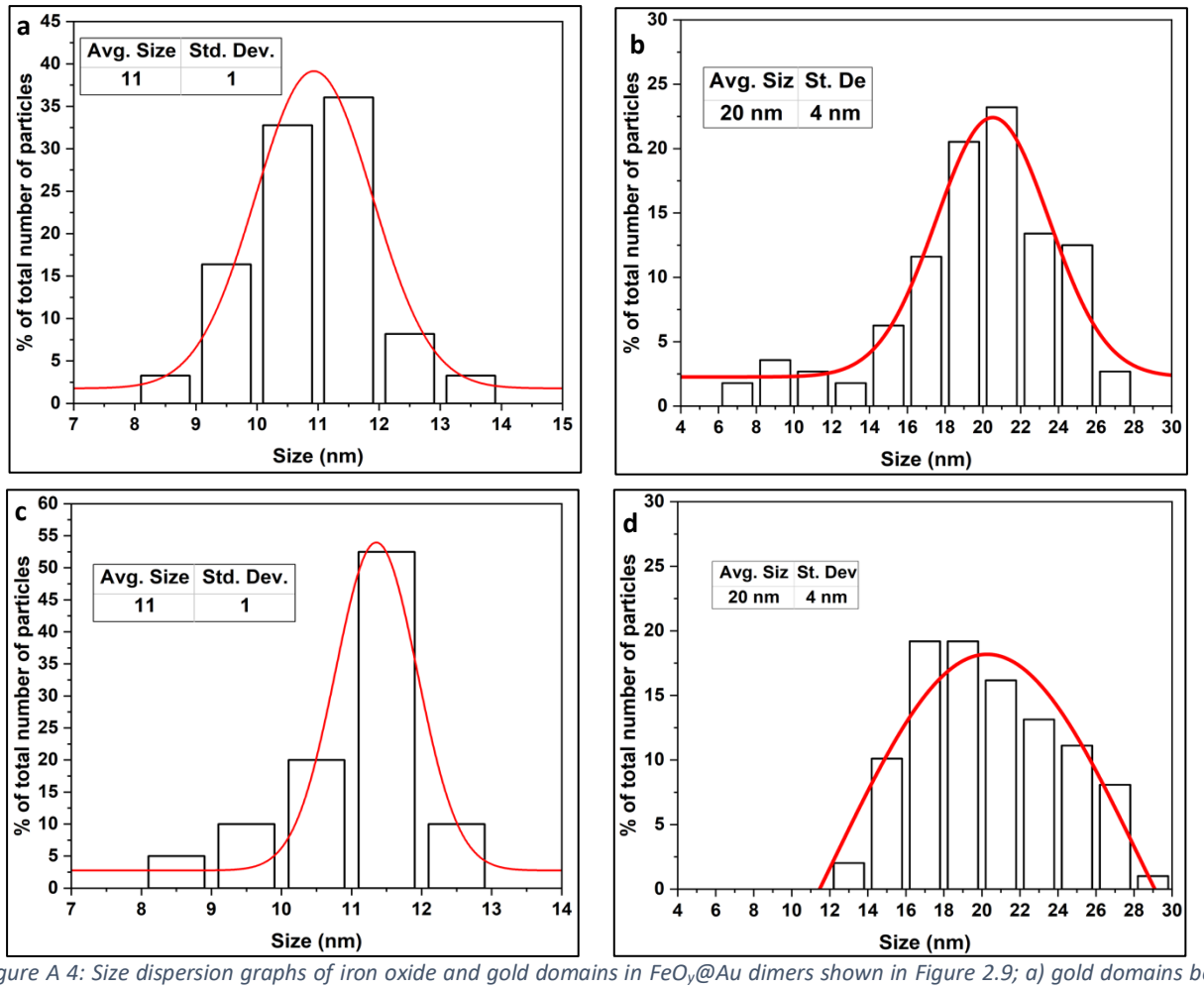

Figure A 4: Size dispersion graphs of iron oxide and gold domains in FeO_y@Au dimers shown in Figure 2.9; a) gold domains before magnetic separation; b) iron oxide domains before magnetic separation; c) gold domains after magnetic separation; d) iron oxide domains after magnetic separation

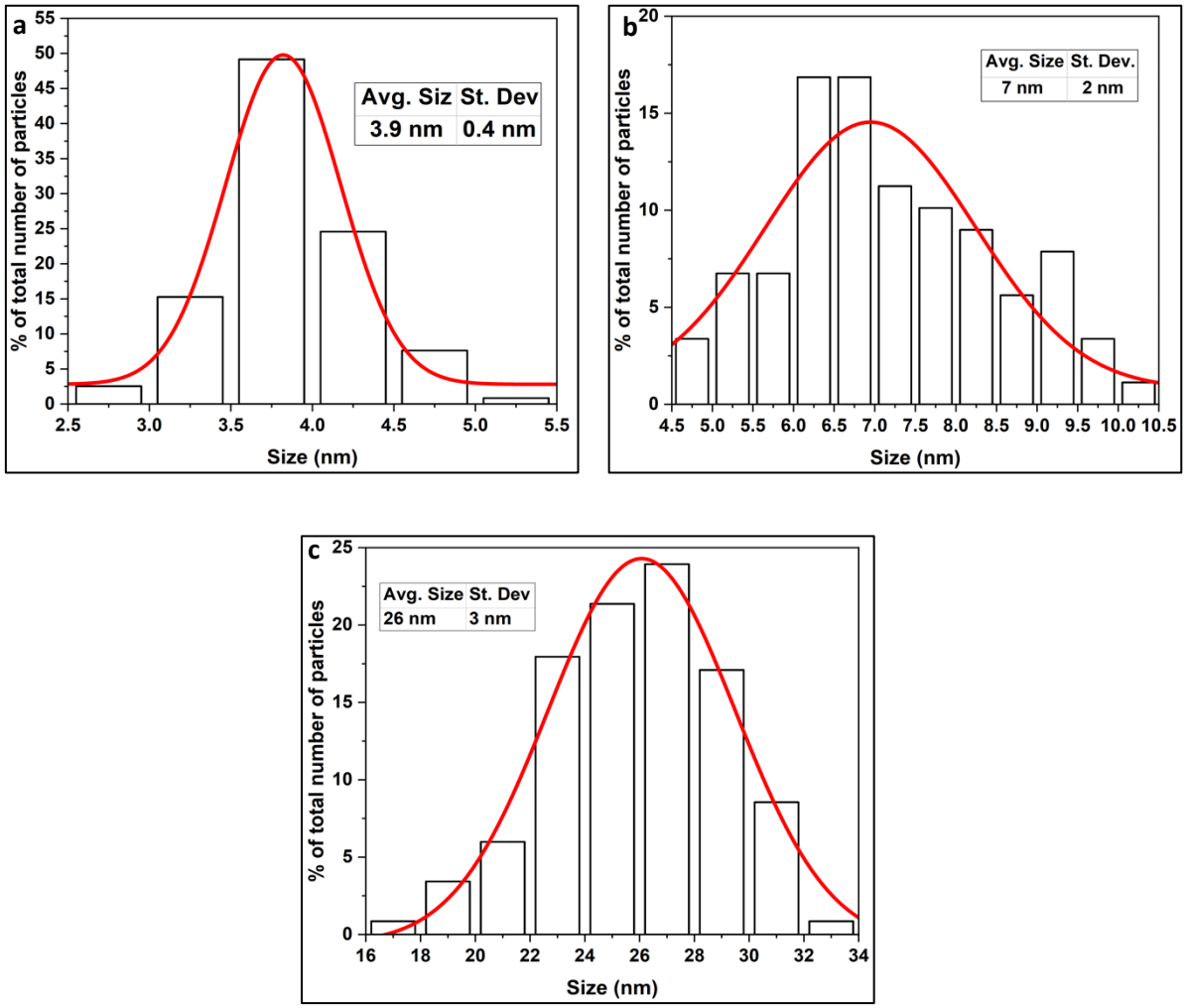

Figure A 5: Size dispersion graphs of a) gold NPs seeds shown in Figure 2.12a; b) gold domains shown in Figure 2.12b; c) $Cu_{2-x}S$ domains shown in Figure 2.12b.

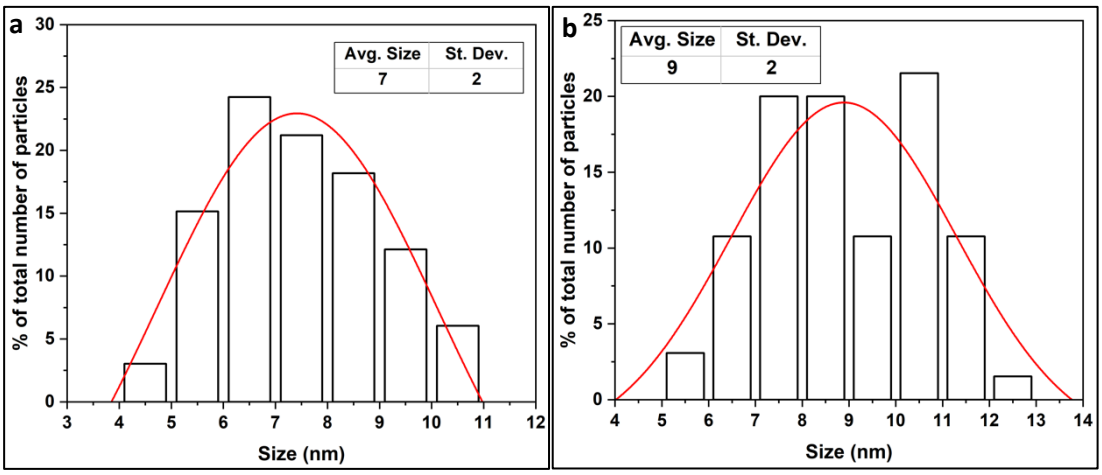

Figure A 6: Size dispersion graphs of gold nanoparticles shown in a) Figure 2.14a; b) Figure 2.14b.

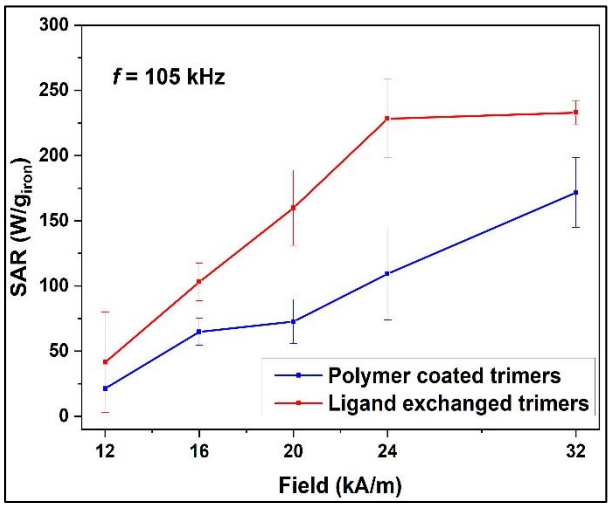

Figure A 7: Comparison of SAR data for the same sample of trimers water transferred with polymer coating (blue lines) and with ligands exchange (red lines), data obtained using a field frequency of 105 kHz and amplitudes of 12 kA/m, 16 kA/m, 20 kA/m, 24 kA/m and 32 kA/m. Lines are a guide to the eye.

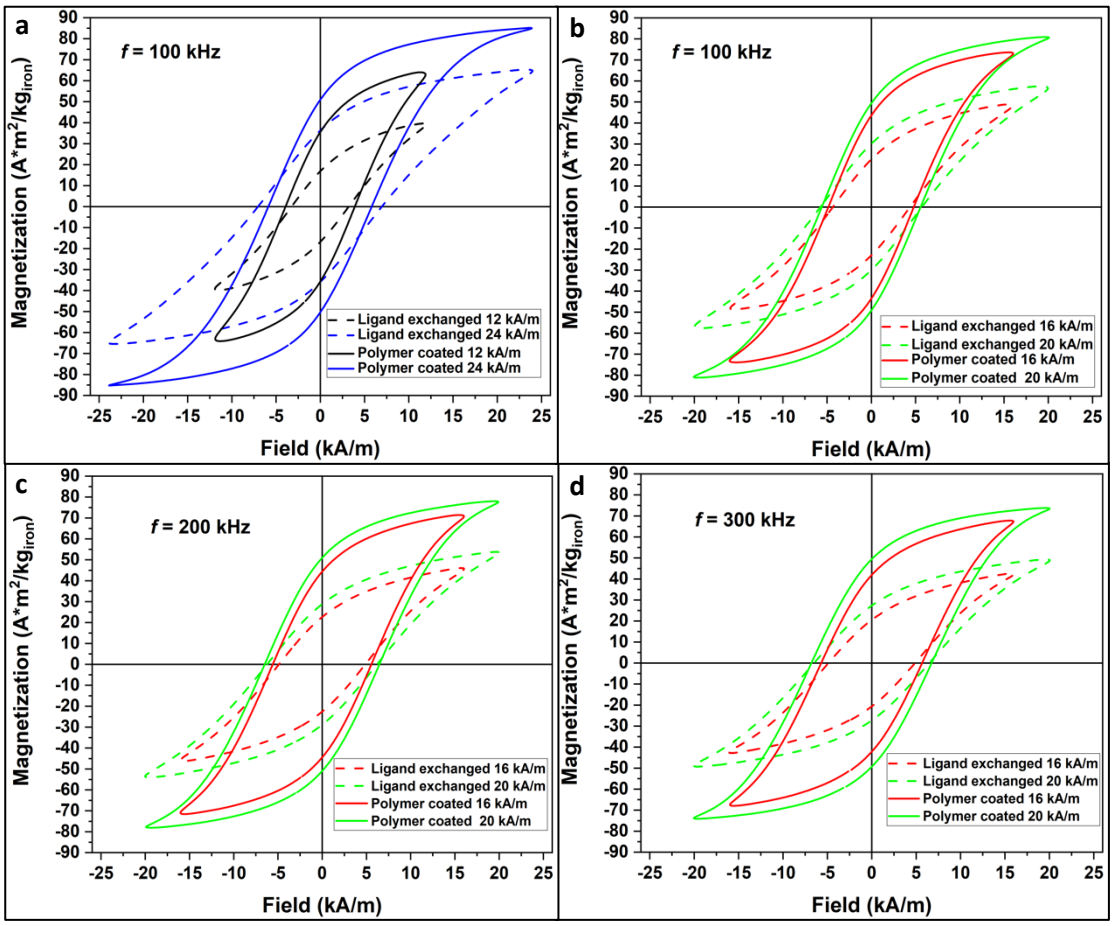

Figure A 8: AC hysteresis loops of samples of trimers water transferred through polymer coating (continuous lines) or ligand exchange (dashed lines) measured using a) alternated fields with frequency of 100 kHz and amplitudes of 12 kA/m (black lines) and 24 kA/m (blue lines); b) alternated fields with frequency of 100 kHz and amplitudes of 16 kA/m (red lines) and 20 kA/m (green lines); c) alternated fields with frequency of 200 kHz and amplitudes of 16 kA/m (red lines) and 20 kA/m (green lines); d) alternated fields with frequency of 300 kHz and amplitudes of 16 kA/m (red lines) and 20 kA/m (green lines).

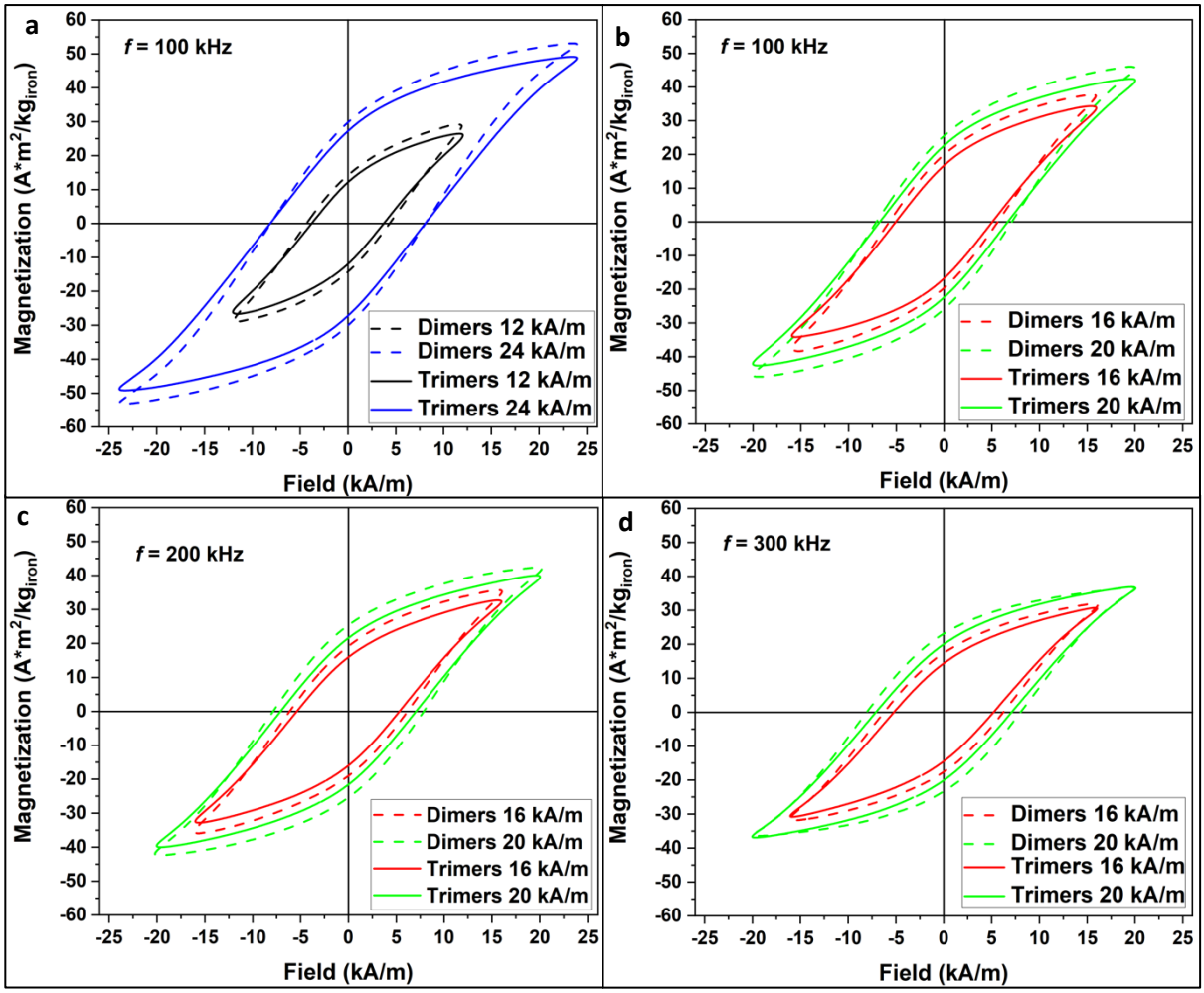

Figure A 9: AC hysteresis loops of a sample of trimers (continuous lines) and dimers (dashed lines) having a 26 ± 4 nm iron oxide domain measured using a) alternated fields with frequency of 100 kHz and amplitudes of 12kA/m (black lines) and 24 kA/m (blue lines); b) alternated fields with frequency of 100 kHz and amplitudes of 16 kA/m (red lines) and 20 kA/m (green lines); c) alternated fields with frequency of 200 kHz and amplitudes of 16 kA/m (red lines) and 20 kA/m (green lines); d) alternated fields with frequency of 300 kHz and amplitudes of 16 kA/m (red lines) and 20 kA/m (green lines).

List of abbreviations

AA: **A**scorbic **A**cid

AC: **A**lternating **C**urrent

AMF: **A**lternating **M**agnetic **F**ield

CE: **C**ation **E**xchange

CYS: **CYS**teamine

CT: **C**omputer **T**omography

DBE: **D**i**B**enzyl **E**ther

DLS: **D**ynamic **L**ight **S**cattering

DMSO: **D**i **M**ethyl **S**ulf**O**xide

EDS: **E**nergy **D**ispersive X-ray **S**pectroscopy

EDTA: **E**thylene**D**iamine**T**etraacetic **A**cid

FC: **F**ield **C**ooled

FDA: **F**ood and **D**rug **A**dministration

FFT: **F**ast **F**ourier **T**ransform

GNPs: **G**old **N**ano**P**article**s**

GNSs: **G**old **N**ano**S**hell**s**

GNSTs: **G**old **N**ano**ST**ar**s**

HAADF: **H**igh **A**ngle **A**nnular **D**ark **F**ield

HR-TEM: **H**igh **R**esolution **T**ransmission **E**lectron **M**icroscopy

IONPs: **I**ron **O**xide **N**ano Particles

IONCs: **I**ron **O**xide **N**ano **C**ube**s**

JNPs: **J**anus **N**ano**P**article**s**

LE**: L**igands **E**xchange

LET: **L**inear **E**nergy **T**ransfer

LSPR: **L**ocalized **S**urface **P**lasmon **R**esonance

MDR: **M**ulti**D**rug **R**esistance

MES: 2-(N-**M**orpholino) **E**thane **S**ulfonic acid

MH curves: **M**agnetization *vs* Field (**H**) curves

MHT: **M**agnetic **H**yperthermia **T**reatment

MNPs: **M**agnetic **N**ano**P**article**s**

MPI: **M**agnetic **P**articles **I**maging

MRI: **M**agnetic **R**esonance **I**maging

MWCO: **M**olecular **W**eight **C**ut **O**ff

NHs: **N**ano **H**eterostructure**s**

NIR: **N**ear **I**nfrared **R**egion

NPs: **N**ano**P**article**s**

NRs: **N**ano**R**od**s**

ODE: 1-**O**cta**D**ecen**E**

OE: **O**ctyl **E**ther

OLA: **OL**eyl **A**mine

OLAC: **OL**eic **AC**id

PC: **P**olymer **C**oating

PEG: **P**oly-(**E**thylene-**G**lycol)

PET: **P**ositron **E**mission **T**omography

PIMA: **P**oly-(**I**sobutylene-alt-**M**aleic-**A**nhydride)

PMAO: **P**oly-(**M**aleic **A**nhydride-alt-1-**O**ctadecene)

PTA: **P**hotothermal **T**ransduction **A**gent

PTT: **P**hotho**T**hermal **T**herapy

RCY: **R**adio **C**hemical **Y**ield

RCF: **R**elative **C**entrifugal **F**orce

ROS: **R**eactive **O**xygen **S**pecies

RT: **R**oom **T**emperature

SAR: **S**pecific **A**bsorption **R**ate

SDD: **S**ilicon **D**rift **D**etector

SERS: **S**urface **E**nhanced **R**aman **S**pectroscopy

SLP: **S**pecific **L**oss **P**ower

SPR: **S**urface **P**lasmon **R**esonance

SQUID: **S**uperconducting **Q**uantum **I**nterference **D**evice

STEM: **S**canning **T**ransition **E**lectron **M**icroscopy

TEM: **T**ransmission **E**lectron **M**icroscopy

TBDS: di-**T**ert-**B**utyl **D**i**S**ulfide

TBE: **T**ris **B**orate **E**DTA buffer

TOPO: **T**ri**o**ctyl **P**hosphine **O**xide

TRT: **T**argeted **R**adionuclide **T**herapy

UV: **U**ltra **V**iolet

VIS: **VIS**ible

WBH: **W**hole **B**ody **H**yperthermia

XRD: **X**-**R**ay **D**iffraction

ZFC: **Z**ero **F**ield **C**ooled

List of contributions

Results obtained from ZnS nanoparticles synthesis, water transfer and radiolabeling experiments (Chapter 1) will be included in a manuscript, currently under submission, by Dr. Tommaso Avellini.

A cation exchange protocol to radiolabel with ^{64}Cu aqueous stabilized ZnS, ZnSe and $CuFeS_2$ nanocrystals: accumulating a large radio dose on a nanomolar NC amount for combined radio and photothermal therapy. Avellini, T.; Soni, S.; Silvestri, N.; Cassani, M.; **Fiorito, S**.; De Donato, F.; Ghosh, S.; Manna, L.; Holger, S.; Pellegrino, T.

Results obtained on the synthesis and characterization of FeO_Y@Au@$Cu_{2-x}S$ trimers (Chapter 2) and by their radiolabeling, magnetic hyperthermia and photothermal therapy applications (Chapter 3) will be the content of a manuscript with the PhD candidate as first author.

The PhD candidate also collaborated on the magnetic characterization of nanoparticles with different composition, which resulted in the publishing of two manuscripts.

Manipulating the Morphology of the Nano Oxide Domain in AuCu-Iron Oxide Dumbbell-like Nanocomposites as a Tool to Modify Magnetic Properties. Najafishirtari, S.; Lak, A.; Guglieri, C.; Marras, S.; Brescia, R.; **Fiorito, S**.; Sadrollahi, E.; Litterst, F. J.; Pellegrino, T.; Manna, L.; et al. RSC Adv. **2018**, 8, 22411–22421.

Fe^{2+} Deficiencies, FeO Subdomains, and Structural Defects Favor Magnetic Hyperthermia Performance of Iron Oxide Nanocubes into Intracellular Environment. Lak, A.; Cassani, M.; Mai, B. T.; Winckelmans, N.; Cabrera, D.; Sadrollahi, E.; Marras, S.; Remmer, H.; **Fiorito, S**.; Cremades-Jimeno, L.; et al. Nano Lett. **2018**, 18, 6856–6866.

Curriculum Vitae of the candidate

SERGIO FIORITO

Genova, GE, Italy| +393402619877 | s.fiorito@icloud.com

RESEARCH EXPERIENCE:

From 11/2019 to present	**Institution:** Istituto Italiano di Tecnologia (IIT), Genova, Italy, Website **Position:** Ph.D. student Fellow **Project:** FeO_y@Au@$Cu_{2-x}S$ trimers as multifunctional probes for DUAL modality hyperthermia treatments **Tasks**: Development of a measurement setup for DUAL (photothermal plus magnetic) hyperthermia experiments and measurements on multifunctional heterostructures
From 12/2019 to 02/2020	**Institution:** Lawrence Berkeley National Laboratory, Berkeley, California (US), Website **Position:** Affiliate Researcher **Project:** High-throughput synthesis of magnetic nano-heterostructures **Tasks:** Development of reproducible procedures for robot-assisted high-throughput synthesis and characterization of magnetic nano-heterostructures
From 11/2016 to 10/2019	**Institution:** Istituto Italiano di Tecnologia (IIT), Genova, Italy, Website **Position:** Ph.D. candidate in Nanochemistry **Project**: Synthesis of multidomain nanoparticles for combination of magnetic and photothermal hyperthermia, radiotherapy and positron emission tomography, in the framework of the ERC-founded project ICARO (ERC starting grant n° 678109, Principal Investigator: Teresa Pellegrino) **Tasks:** Nano-heterostructures synthesis and characterization, phase transfer of nanoparticles in water, SAR measurements, radiolabeling of nanocrystals, SQUID magnetometer supervisor
From 4/2016 to 05/2016	**Institution:** Dipartimento di Chimica e Chimica Industriale (DCCI), Genova, Italy, Website **Position:** Post-graduate Fellow **Project**: Synthesis through polyol reduction and characterization of cobalt carbides NPs with different magnetic properties **Tasks**: Nanoparticles synthesis, magnetic characterization, thermal characterization

EDUCATION:

From 11/2016 to 03/2020 (expected)	**Institution:** Università degli studi di Genova, Dipartimento di chimica e chimica industriale **Degree** Ph.D. school in Science and Technology of Chemistry and materials Curriculum: Nanochemistry **Subjects:** Nanoparticles synthesis and post synthesis modifications, characterization techniques (electron microscopy, spectroscopy, NMR, XRD diffraction)
From 1/2014 to 03/2016	**Institution:** Università degli studi di Genova, Dipartimento di chimica e chimica industriale **Degree** Master of Science in Solid State Chemistry (LM54) **Final mark:** 110/110 with honors **Subjects:** Solid State Chemistry, Crystallography, Physics, Magnetism
From 9/2009 to 01/2014	**Institution:** Università degli studi di Genova, Dipartimento di chimica e chimica industriale **Degree** Bachelor of Science in Chemistry (LT27) **Final mark:** 110/110 **Subjects:** Analytical Chemistry, Physical Chemistry, Inorganic Chemistry, Organic Chemistry, Math

SCIENTIFIC PUBBLICATIONS:

Fe^{2+} Deficiencies, FeO Subdomains, and Structural Defects Favor Magnetic Hyperthermia Performance of Iron Oxide Nanocubes into Intracellular Environment. Lak, A.; Cassani, M.; Mai, B. T.; Winckelmans, N.; Cabrera, D.; Sadrollahi, E.; Marras, S.; Remmer, H.; **Fiorito, S**.; Cremades-Jimeno, L.; et al. Nano Lett. **2018**, 18, 6856–6866.

Manipulating the Morphology of the Nano Oxide Domain in AuCu-Iron Oxide Dumbbell-like Nanocomposites as a Tool to Modify Magnetic Properties. Najafishirtari, S.; Lak, A.; Guglieri, C.; Marras, S.; Brescia, R.; **Fiorito, S**.; Sadrollahi, E.; Litterst, F. J.; Pellegrino, T.; Manna, L.; et al. RSC Adv. **2018**, 8, 22411–22421.

CONFERENCES PRESENTATIONS:

Poster presentation: **RADIOMAG COST ACTION FINAL MEETING,** Florence, Italy, October 16-18, 2018
Magnetic Nano-systems with High Heat Performance: Fe_3O_4 Assemblies and Au-Fe_xO_y Heterostructures; H. Gavilan, **S. Fiorito**, D. Niculaes, P. Guardia, T. Pellegrino

Poster presentation: **NanotechITALY2015,** Bologna, Italy, November 25-27 November, 2015
Magnetic Nanoparticles for Biosensors, Catalysts and High-Density Permanent Magnets; S. Villa, P. Riani**, S. Fiorito**, F. Canepa; **2015**;

Poster presentation: **CALPHAD XLIV**, *Loano, Italy, May 31 – June 5, 2015*
Structural and magnetic characterization of Co-Carbides particles
S. Villa, **S. Fiorito**, P. Riani, F. Canepa; **2015**;

REFERENCES:

Dr. Teresa Pellegrino
Istituto Italiano di Tecnologia (IIT) Via Morego 30, 16163 Genova, Italy. teresa.pellegrino@iit.it

Prof. Liberato Manna
Istituto Italiano di Tecnologia (IIT) Via Morego 30, 16163 Genova, Italy. liberato.manna@iit.it

Summary

The present dissertation is resulting from the work performed during the Ph.D. research activity carried out at the Italian Institute of Technology (IIT) under the supervision of Dr. Teresa Pellegrino (Nanomaterials for biomedical research line) and of the University of Genova. The thesis has been conducted in the framework of the ERC-founded project ICARO (ERC starting grant n° 678109, Principal Investigator: Dr. Teresa Pellegrino), whose main purpose is the development of novel inorganic nanostructures for radiotherapy and chemotherapy of cancer. Thus, this thesis aims to progress the field of nanomedicine. In particular, the first goal of this work is to synthesize innovative water stable chalcogenide nanoparticles, with the purpose of achieving nano-sized platforms capable of incorporating radioactive ^{64}Cu ions, which would make such systems suitable for the use in radiotherapy and for positron emission tomography. The second goal is to explore the coupling of such chalcogenide nanocrystals with magnetic nanoparticles, which are already part of the nanoparticles' portfolio available in the research group where this thesis was carried out. These nanoparticles have shown great potential for magnetic hyperthermia treatment of cancer and, in combination with radiotherapy, could result in a synergic and more effective cancer treatment. Thus, this thesis provides new ground in the rational design of multifunctional nano-heterostructures for cancer diagnosis and therapy.

Introduction:

Cancer is one of the leading causes of death worldwide accounting for 9.6 million of deaths (almost 17 % of all deaths globally, 20 % of all deaths in Europe) in 2018[1]. Most commonly used therapies, other than surgery, are chemotherapy and radiotherapy. However, together with the large heterogeneity of cancers, many factors, such as, for example, multidrug resistance (MDR) in the case of chemotherapy and, for what regards radiotherapy treatments, the low sensitivity of hypoxic cancers to the ionizing radiations, can reduce the effectiveness of these treatments.[2] This called for the development of new innovative cancer treatments, with higher specificity and causing less damage to surroundings healthy tissues. Among the different strategies investigated, the use of nanoparticles as remote probes for cancer diagnosis and treatment (nanomedicine) has widely attracted the attention of the research community in last two decades.[3,4] Among the different classes of nanoparticles studied, inorganic nanoparticles are of particular importance due to their peculiar and tunable chemical and physical properties that can be used to add additional cancer treatment and diagnosis features to the nano-pharmaceutical.[5] Among the wide number of inorganic nanoparticles with different composition studied for biomedical applications, three classes have been of particular interest for their chemical and physical properties: noble metal nanoparticles,[6] semiconductors nanoparticles.[7] and magnetic nanoparticles.[8] Some of the nanoparticles reported for biomedical applications have intrinsic multimodal diagnosis and therapy features.[9] Some examples are gold nanorods, that have been reported to be exploitable both in cancer cell imaging and photothermal therapy[10], or copper sulfide nanocrystals that have been exploited for dual PDT and PTT treatment[11] or for photoacoustic imaging-guided photothermal therapy.[12] Iron oxide nanoparticles are also commonly studied for theragnostic, exploiting MRI (or MPI) as imaging technique and MHT for therapy[13] and have recently been reported to be exploitable in dual MHT and PTT treatments.[14] The possibility to obtain through one single nano-object multiple

treatment and diagnosis modalities is of key interest for the future development of nanomedicine. Indeed, the development of multimodal treatment and diagnosis nano-platform, would permit to increase the efficiency of the treatments, this scaling down the amount, and related cytotoxicity,[15] of the nanoparticles used.[16] In order to further enhance this possibility, researchers working on nanoparticles for biomedical applications started working on the development of nano-heterostructures (NHs) composed of different nano-domains with different properties. This work was focused on the study of nano-heterostructures having different domains joint through a solid interface, this allowing to obtain multifunctional nano-objects with reduced size and to tune properties arising from the formation of the solid heterojunction.[17] Moreover, particular interest was directed towards nano-heterostructures developed in order to combine multiple therapeutic modality overcoming the intrinsic limitations of each single therapy, with a special focus on the ones having a magnetic domain.

Chapter 1:

In the medical practice, radioisotopes can be used for two main applications: nuclear imaging and targeted radionuclide therapy (TRT). In both cases, an appropriate radioisotope is bound to a carrier that has the role to specifically bring the radioisotope to the tissue selected as target of the treatment or as area of interest for diagnosis. These pharmaceutical radiolabeled drugs are commonly referred to as radiopharmaceuticals. One of the most common nuclear imaging techniques is positron emission tomography (PET)[18]. Positron emission tomography is performed using radioisotopes that are decaying through the emission of positrons (i.e. positive electrons, β^+). Targeted radionuclide therapy[19–22] is a radiation therapy treatment performed using radiopharmaceuticals to deliver therapeutic radiation to targets inside the body. Main important advantage of targeted radionuclide therapy, when compared to standardly used external beam therapy, is its selectivity, allowing to ideally affect mainly cancer cells, reducing the unspecific damage to healthy tissues.[23] Among all the radiometals used in PET imaging and TRT, of particular interest is ^{64}Cu for its desirable relatively long half-life (12.7 h) and for the possibility to be used in theragnostic applications. Indeed, together with positron emission (17 % 0.655 MeV) suitable for PET imaging, ^{64}Cu is decaying also through β^- emission (39 %, 0.573 MeV) and electron capture (44 %) that can be exploited in targeted radionuclide therapy. Another important advantage of ^{64}Cu is that it is currently produced in many cyclotron facilities on a routine basis,[24–26] making it an ideal candidate for the production of radio-therapeutic agents.[27–29] Recently great interest was shown[30–32] towards the use of functionalized nanoparticles as radionuclide carriers. Most used strategy in order to radiolabel with ^{64}Cu different nanocrystals is the use of suitable metal chelators anchored to the surface of the nanoparticles. Following this path, metal[33], quantum dots[34] and magnetic nanoparticles[35] were successfully radiolabelled with ^{64}Cu. Recently, new approaches for the incorporation of radioactive ions in nanocrystals were reported. Zhou et al[36] in 2010 reported the synthesis of ^{64}CuS nanocrystals using a mixture of “hot” (radioactive) and “cold” (non-radioactive) $CuCl_2$ while Sun et al[37] in 2014 reported the feasibility of a cation exchange reaction performed at 60°C in organic solvent in order to introduce radioactive ^{64}Cu in pre-synthesized CdSe/ZnS quantum dots. Main limitation of these procedures is the fact that the radioactive nuclide is introduced at an early stage of the material preparation pathway. The possibility of radiolabelling nanocrystals with ^{64}Cu as last step of the material production and functionalization pipeline with simple and fast water

phase intercalation reaction was investigated by researchers from the group in which this research activity was carried out.[38] By means of intercalation reactions in aqueous solution it has been possible to successfully radiolabel CuS covelite nanocrystals with excellent results.

The first chapter of this thesis deals with the synthesis, water transfer and radiolabeling of ZnS nanoparticles. A non-hydrolytic thermal decomposition synthesis route[39] was exploited in order to obtain quasi-spherical nanoparticles with average diameter's size of 9 ± 1 nm. As synthesized particles have a sphalerite cubic structure (ICSD card n° 77082) and are perfectly stable in hexane. In order to phase transfer to water the organic solvent-stable NPs, a ligand exchange procedure employing a multi-dentate amphiphilic polymer (cysteamine-poly-(isobutylene-*alt*-maleic anhydride)-polyethylene glycol, CYS-PIMA-PEG) was used in order to improve stability. This procedure allowed to obtain nanoparticles with perfect aqueous phase stability. Also, no appreciable change in crystalline structure or nanoparticles shape was found. On the water stable nanoparticles, cation exchange reactions with both radioactive and non-radioactive copper were carried out. Cation exchange with non-radioactive $CuCl_2$, using a ratio between added Cu^{2+} and Zn^{2+} present in nanocrystals of 1.8:1 and ascorbic acid as mild reducing agent, were performed. Resulting nanocrystals, characterized by ICP-OES and XRD shown completely replacement of Zn (II) ions with Cu(I) ions. Exploiting an analogous procedure but using as copper source radioactive $^{64}Cu:CuCl_2$ radiolabeling reactions were performed on the water stable ZnS nanocrystals. Radiolabeling reaction resulted in high values of radiochemical yield (93%). Moreover, the excellent stability of the particles allowed to recover quantitatively (purification yield = 87%) the nanocrystals after radiolabeling reaction and subsequent purification process. The results obtained indicate ZnS nanoparticles as an efficient nano-platform for the use in radiotherapy and positron emission tomography, given the fast, reproducible and easily clinical-translatable radiolabeling procedure resulting in quantitative incorporation of ^{64}Cu ions.

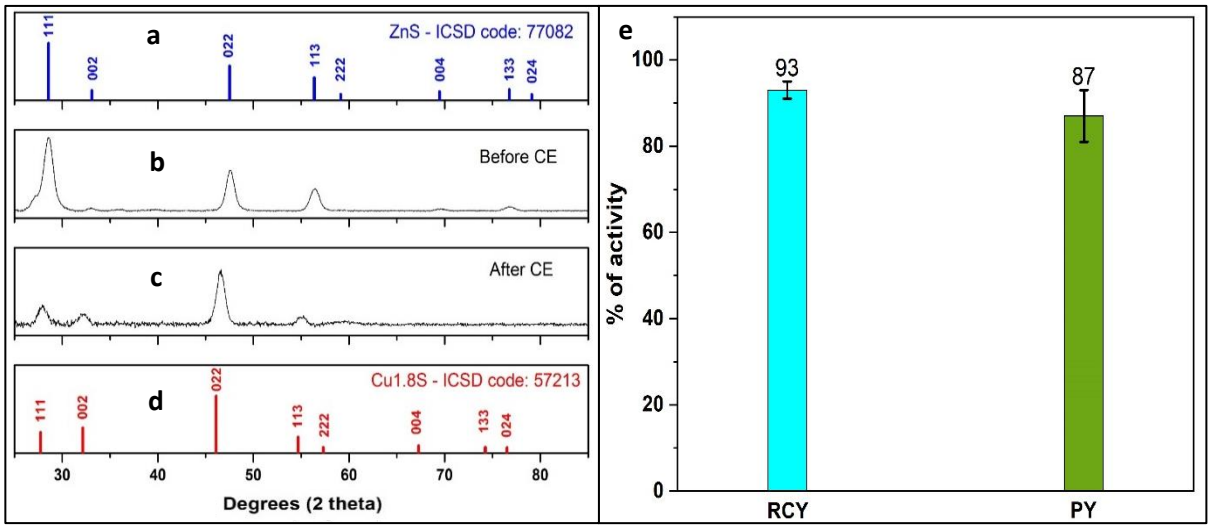

Figure 1: Experimental XRD pattern of a sample of ZnS nanoparticles before (b) and after (c) cation exchange reaction with non-radioactive Cu (Cu_{used} : S_{NCs} = 1.8), in comparison with expected reflections for cubic ZnS (a, ICSD code: 77082) and cubic $Cu_{1.8}S$ (d, ICSD code 57213); e) radiochemical yield (RCY) and purification yield (PY) of radiolabeling experiments performed on ZnS NPs with $^{64}Cu:CuCl_2$ (^{64}Cu (II) ions added in amount equivalent to 0.2 % of S atoms in nanocrystals).

Chapter 2:

Janus nanoparticles (JNPs), named after the double-faced Roman god, are compartmentalized particles with two sides having different chemical properties or polarity[40]. The great importance of such materials in merging different physical and chemical properties in one single nanostructure was already realized by Nobel laureate P. G. de Gennes in 1991.[41] From that year on, the synthesis of inorganic Janus NPs was further developed and optimized, increasing exponentially the number of reported procedures to obtain this kind of nanomaterial. [42–47]. Depending on the shape and on the composition of the different heterostructures' domains, these materials have been demonstrated to be useful in many different applications, including catalysis[48,49], micromotors[50–52],displays[53,54] and biosensors[55–57]. Recently, the possibility to merge domains with completely different properties in one single nano-heterostructure and the opportunity to tune these properties have attracted the interest of researchers working in the development of nanomaterials for biomedical applications, who, in the last decade, have thoroughly studied the processes happening at the domains' interfaces and worked in the development of nanoparticles for cancer theragnostic[58–60]. Of particular interest for the scientific community is that these multiple-domain nano-heterostructures maintain the properties of each single domain and, in addition, new properties can also arise from the presence of an interface between the different materials. In last two decades, many efforts have been made in order to develop colloidal synthesis procedures for inorganic Janus nano-heterostructures, formed by two (or more) distinct domains permanently joint through chemical bonding interfaces (i.e., without any molecular bridges)[61]. Most of those procedures rely on the growth of a second domain on the surface of a preformed nanoparticle. This mechanism is commonly referred to as "seeded growth" (or "seed mediated growth") being the starting preformed nanoparticles defined as "seeds". In order to obtain those two (or more) domains heterostructures[62], it is critical to favor the heteronucleation of the second material on seeding NPs (against the homonucleation that is the formation of separate second material NPs surrounding the seeds). Among the wide amount of literature on JNPs, only few heterostructures composed by an iron oxide and a semiconductor domain are reported. [63–72]

In the second chapter of this thesis are described the results obtained by the different trials performed in order to couple in a single nano-heterostructure the developed ZnS nanoparticles or copper-deficient copper sulfide nanoparticles (previously reported to be exploitable as radioisotopes carriers) with highly performing magnetic nanoparticles (iron oxide nanocubes, IONCs)[73] or nano-heterostructures (gold-iron oxide dimers, Au@FeO_y)[58]. Initially, a reported synthesis procedure[63] for the growth of ZnS domains on the surface of small γ-Fe_2O_3 nanoparticles has been adapted in order to grow ZnS domains on IONCs but these trials were not successful. Then, the possibility to grow chalcogenide domains on the surface of gold nanoparticles was investigated. While the growth of ZnS nanoparticles did not result in the formation of heterostructures, but only in homonucleation of ZnS domain around gold NPs used as seeds, following a reported procedure[74] it has been possible to successfully couple in a single heterodimer a gold NPs with a copper deficient copper sulfide domain. Subsequently, using the Au@FeO_y dimers, developed in this group and having high magnetic hyperthermia efficiency, as seed for the growth of $Cu_{2-x}S$ domains, FeO_y@Au@$Cu_{2-x}S$ were synthesized. The developed synthesis procedure allows, through the variation of precursors' concentration, the tuning of the newly grown $Cu_{2-x}S$ domain's size from 15

± 3 nm to 33 ± 5 nm. These FeO_y@Au@$Cu_{2-x}S$ trimers were thoroughly characterized by TEM, XRD, SQUID magnetometry and UV-VIS-NIR spectroscopy. XRD analyses identified the crystal phase of the $Cu_{2-x}S$ as low ordered triclinic roxbyite. Trimers were found to have magnetic properties similar to the ones of the Au@FeO_y dimers used as seeds a part from a diamagnetic contribution at high fields coming from copper sulfide domain. FeO_y@Au@$Cu_{2-x}S$ also show two LSPR absorption bands, related to the presence of gold and copper sulfide domains. Both of them are exploitable for the application in photothermal therapy with laser having wavelength in the NIR biological windows.

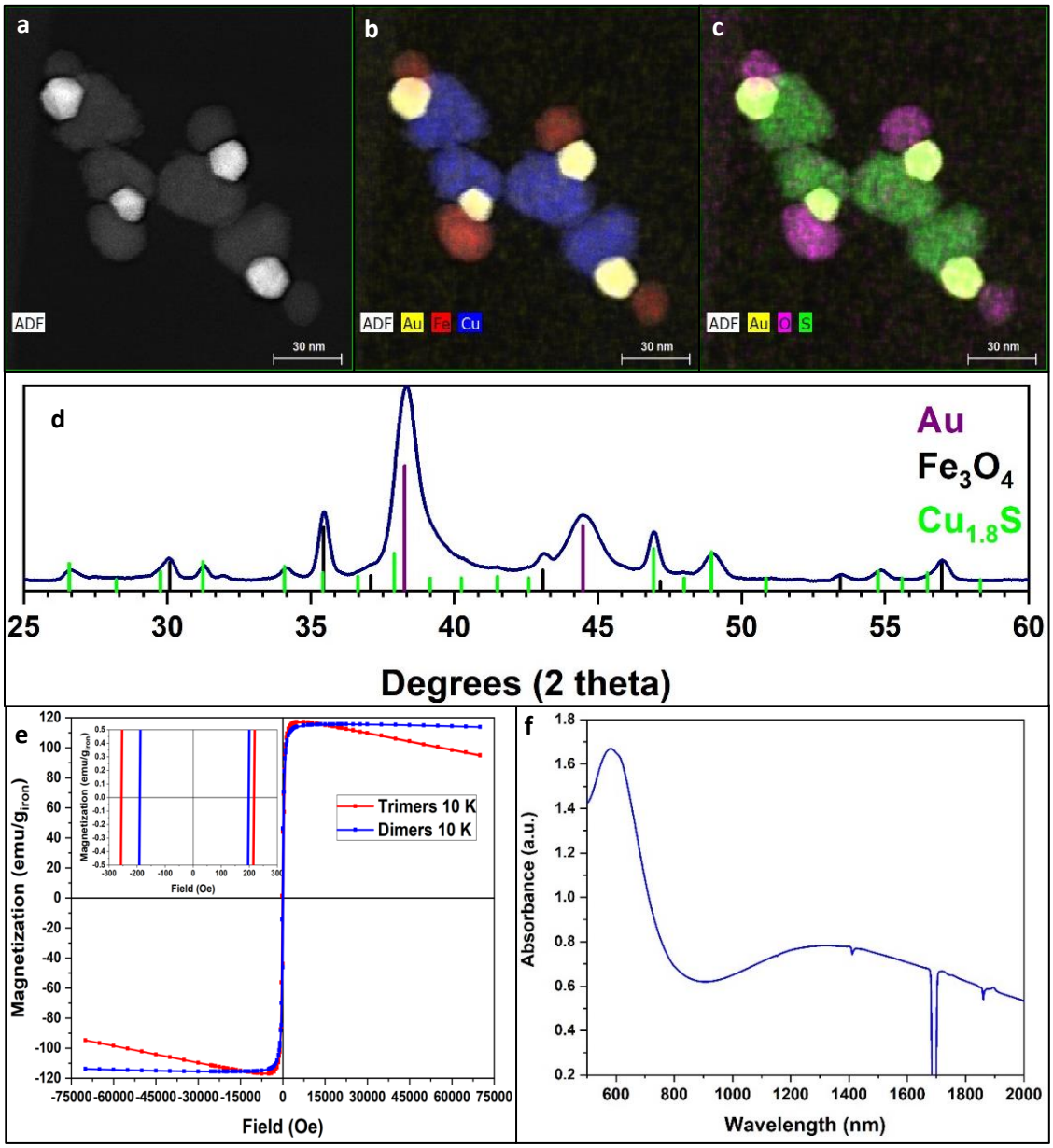

Figure 2: Characterization for a sample of FeO_y@Au@$Cu_{2-x}S$ trimers. HAADF image (a) and EDS elemental analysis mappings for Au, Fe, Cu (b) and Au, O, S (c); d) experimental XRD patterns compared with the expected reflections for gold (ICSD code 611625), iron oxide (ICSD code 247035) and roxbyite copper sulfide (ICSD code 185807); e) comparison between zero field cooled MH curves recorded in the range ± 70 kOe at 10 K, for a sample of trimers (red line) and for a sample of dimers (blue line) having iron oxide domains with same average size (25 ± 4 nm), f) VIS-IR (500-2000 nm) spectrum.

Chapter 3:

Hyperthermia, the artificial temperature increase of the body or of a tissue above the normal temperature set by the thermoregulation system of an organism,[75] is nowadays a widely used cancer treatment.[76,77] This treatments can be used both as stand-alone therapy[78] or in combination with other treatments (e.g. chemotherapy, radiotherapy or surgery)[79–83] with the latter option being more effective.[84] Hyperthermia can be administered to patients through three different methodologies: whole body hyperthermia, regional hyperthermia and local hyperthermia.[85] In last decades,[86,87] many efforts were made in order to be able to exploit nanoparticles with different composition for local hyperthermia treatments. Main advantage of using nanoparticles for thermal treatment is the possibility to target a small area of tumoral tissue avoiding unspecific heating and overcoming the limitation of standard local hyperthermia treatments to superficial cancers. Another possibility related to the use of nanoparticles is, either exploiting their intrinsic properties or functionalizing their surface, to merge hyperthermia with other diagnosis or treatment applications, in order to exploit them as theragnostic agents.[88–90] One possibility in order to perform thermal treatments using nanoparticles is given by the application of an alternating magnetic field (AMF) to a tissue where magnetic nanoparticles (MNPs) are dispersed. The use of magnetic nanoparticles as heating mediators in magnetic hyperthermia treatments (MHT) was already reported in 1957[91]. From that pioneering study the interest on this clinical methodology increased and today clinical phase II studies are led by MagForce company, in hospital Charité in Berlin.[92,93] When magnetic nanoparticles are stimulated through an alternating magnetic field, three different mechanisms can results in thermal energy production[94]: Néel relaxation (rotation of the magnetic moment of the particle overcoming anisotropy energy barrier), Brownian relaxation (mechanical rotation of the MNPs with friction against the surrounding medium) and hysteresis losses (shifting of domains walls that takes place in multi-domain MNPs). Relative contribution of each of the three mechanisms is depending on many different parameters such as material composition, size, shape, magnetic anisotropy and grade of agglomeration of MNPs. Heating performances of nanoparticles in magnetic fluid hyperthermia are usually evaluated through specific absorption rate (SAR o also SLP, specific loss power) values. SAR is defined as the power dissipated by MNPs per unit of mass. In last decades, many different nanomaterials suitable for magnetic hyperthermia treatments were developed. Among them, the most commonly used are FDA approved iron oxide nanoparticles[73,95–97] or mixed ferrite nanocrystals such as cobalt ferrite[98–100], zinc ferrite[101,102] or manganese ferrite[103,104]. Currently, efforts of the researched working in this field are oriented towards the development of nanomaterials with higher efficiencies (larger SAR values). Indeed, an increased SAR value would allow to scale down the amount of nanoparticles employed in each treatment and, consequently, to reduce the cytotoxicity of the nanomaterial.[105] In order to pursue this goal, also magnetic nano-heterostructures, such as Fe(0)@iron carbide[106] or soft core-hard shell[107] structures, were synthesized and found to have increased hyperthermia efficiencies if compared to the single material nanoparticles. Another class of hyperthermia therapies in which nanomaterials are widely used are photothermal treatments (photothermal therapy, PTT). In these treatments, temperature increase is obtained through photothermal transducing agents (PTAs) that are harvesting energy from appropriate electromagnetic radiations and converting it into heat. Most commonly used nanoparticles as PTAs are the one exhibiting localized surface plasmon resonance (LSPR).[108,109] A key parameter, when designing plasmonic nanoparticles to be used as PTAs, is the wavelength

absorption corresponding to the plasmon resonance. Indeed, the laser radiation used to excite plasmonic nanoparticles has to be able to reach nanoparticle without being absorbed from the surrounding tissues since this would reduce the energy of the incoming radiation and damage healthy tissues. Typically, for this purpose, laser radiations with wavelengths in the near infrared region (NIR) are used[110]. Indeed, the scattering and absorption of NIR radiation by human tissues is lower if compared to the one obtained with visible light or UV light lasers.[111] In particular, tissues' absorption and scattering of laser radiation is negligible (radiation can travel through tissues with 2 – 3 cm path length) in the three so-called NIR biological windows . Among all the nanoparticles investigated for the application in photothermal therapy, gold nanoparticles of different sizes and shapes are the most studied and promising.[112–114] Absorption of Au nanospheres is usually centered in the range between 500 nm and 600 nm with larger particles having higher absorption wavelength. These spherical nanoparticles are usually exploited with laser having wavelengths in the 1st NIR biological window[115] targeting the absorption tail of the gold NPs plasmonic peak. Another class of gold nanomaterial widely exploited for photothermal treatments are gold Nanorods (NRs)[116,117]. The peculiarity of the Au NRs is to have, due to their shape anisotropy, two plasmon resonances: transverse plasmon resonance, usually centered between 500 and 550 nm, and longitudinal resonance between 650 nm and 850 nm. This second absorption wavelength can be tuned to higher values by increasing NRs' aspect ratio.[10] Photothermal treatments exploiting other gold nanostructures such as nanoshells (GNSs),[118,119] or nanostars (GNSTs)[120,121] have also been reported. Together with gold, also other noble metals nanocrystals, such as Pt or Pd[122,123] have been demonstrated to be effective when used as PTAs in PTT. In 2010, Chen and coworkers indicated copper deficient copper sulfide nanocrystals as candidate material to be used as PTAs in photothermal therapy using a 808 nm laser.[124] Although in this pioneering study the power density used (> 24 W/cm^2) was more than 70 times higher than the safe value for biological applications (0.33 W/cm^2),[125] its publication leaded the way to many further studies on this class of materials. Indeed, in last two decades, many studies were carried out in which performances of copper-deficient copper sulfide nanoparticles were increased by changing either shape or stoichiometry of the material.[71,126–129]

In the third chapter, the newly synthesized trimers were transferred to water phase and tested for the aimed applications. Different strategies were explored in order to develop a reproducible and high-yield water transfer procedure. Among them, a two-step ligands exchange procedure employing CH_3O-PEG2000-SH and poly-catechol-PEG900 as amphiphilic ligands resulted in aqueous phase stable trimers with high water transfer procedure yield (> 80 %). FeO_y@Au@$Cu_{2-x}S$ trimers were also successfully transferred to water, although with lower yields if compared to previous procedure, using a polymer coating procedure and employing commercially available and cost-effective poly-(Maleic Anhydride-alt-1-Octadecene). Lastly, the developed nano-platform showed great relevance in the field of nanomedicine. Indeed, when employed in magnetic hyperthermia, trimers resulted in high SAR values (302 W/g when a field with frequency of 105 kHz and an amplitude of 32 kA/m were used), preserving the excellent hyperthermia performances of the Au@FeO_y used as seeds for their synthesis and thus in line with the best magnetic nano-heterostructures reported so far. Radiolabeling reactions were performed on trimers, resulting in a radiochemical yield of 97 %, higher than any value reported so far for ^{64}Cu incorporation in nanocrystals. Furthermore, the stability of the trimers during the radiolabeling and subsequent purification procedures was likewise ensured by the use of CYS-PIMA-PEG as stabilizing agent

allowing to quantitatively recover the nanocrystals and the associated radioactivity. The performances of FeO_y@Au@$Cu_{2-x}S$ trimers when used in photothermal heating were also tested under the exposure to 808 nm laser irradiation. Although the performances obtained with lower laser's power density were limited, the possibility to tune the absorption wavelengths by means of changing gold and copper sulfide domain's properties, gives space to further improvements for these multifunctional nano-heterostructures. To the best of our knowledge, the here described FeO_y@Au@$Cu_{2-x}S$ trimers are the first ever reported nano-heterostructures able to combine in one single nano-object the possibility to perform magnetic hyperthermia, photothermal therapy and radiotherapy/positron emission tomography, thus allowing the possible development of more efficient cancer treatments.

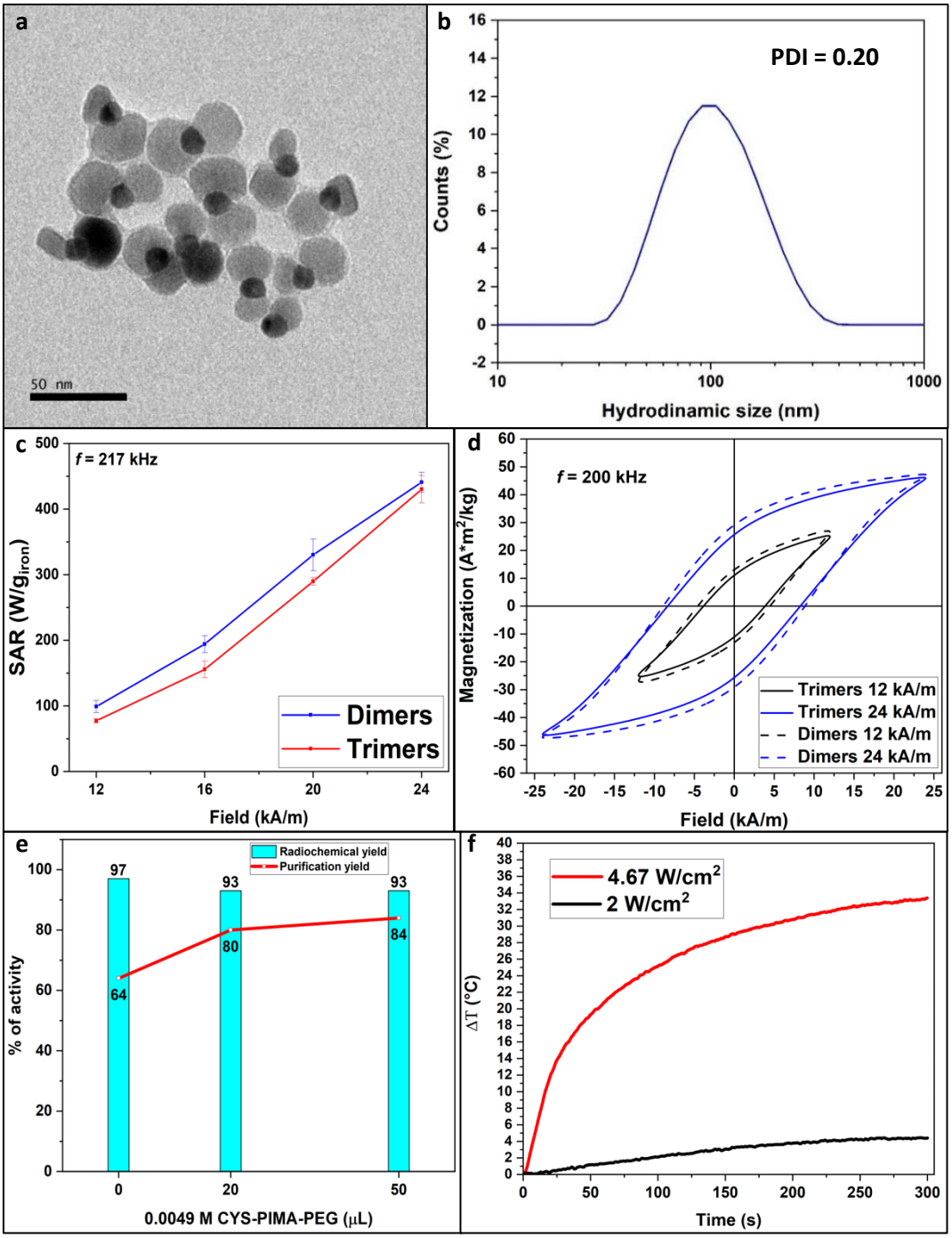

Figure 3: a) Representative TEM picture of a sample of trimers water transferred using a ligand exchange procedure employing poly-catechol-PEG900 and CH3O-PEG2000-SH; b) related DLS hydrodynamic size distribution graph by intensity; c) SAR vs field amplitude graphs for Au@FeO_y dimers (blue line) and FeO_y@Au@$Cu_{2-x}S$ trimers (red line) having a 26 ± 4 nm iron oxide domain measured using a field frequency of 217 kHz; d) AC hysteresis loops of a sample of trimers (continuous lines) and dimers (dashed lines) having a 26 ± 4 nm iron oxide domain performed using fields with frequency of 200 kHz and fields of 12 kA/m (black lines) and 24 kA/m (blue lines); e) radiochemical yield (bars) and purification yield (red line) obtained for radiolabeling reactions performed adding increasing amount of 0.0049 M CYS-PIMA-PEG2000 solution. f) heating curves (5 minutes) of FeO_y@Au@$Cu_{2-x}S$ trimers obtained under irradiation with 808 nm laser using a power density of 4.67 W/cm² (red line) and 2 W/cm² (black line).

References

1. World Health Organization (WHO). Available at: https://www.who.int/news-room/fact-sheets/detail/cancer.

2. Fan, W., Yung, B., Huang, P. & Chen, X. Nanotechnology for Multimodal Synergistic Cancer Therapy. *Chem. Rev.* **117**, 13566–13638 (2017).

3. Mi, Y., Shao, Z., Vang, J., Kaidar-Person, O. & Wang, A. Z. Application of nanotechnology to cancer radiotherapy. *Cancer Nanotechnol.* **7**, (2016).

4. Zhao, C. Y., Cheng, R., Yang, Z. & Tian, Z. M. Nanotechnology for cancer therapy based on chemotherapy. *Molecules* **23**, (2018).

5. Anselmo, A. C. & Mitragotri, S. A Review of Clinical Translation of Inorganic Nanoparticles. *AAPS J.* **17**, 1041–54 (2015).

6. Jain, P. K., Huang, X., El-Sayed, I. H. & El-Sayed, M. A. Noble metals on the nanoscale: Optical and photothermal properties and some applications in imaging, sensing, biology, and medicine. *Acc. Chem. Res.* **41**, 1578–1586 (2008).

7. Abbasi, E. *et al.* Biomedical and biological applications of quantum dots. *Artif. Cells, Nanomedicine Biotechnol.* **44**, 885–891 (2016).

8. Reddy, L. H., Arias, J. L., Nicolas, J. & Couvreur, P. Magnetic nanoparticles: Design and characterization, toxicity and biocompatibility, pharmaceutical and biomedical applications. *Chem. Rev.* **112**, 5818–5878 (2012).

9. Lee, D. E. *et al.* Multifunctional nanoparticles for multimodal imaging and theragnosis. *Chem. Soc. Rev.* **41**, 2656–2672 (2012).

10. Huang, X., El-Sayed, I. H., Qian, W. & El-Sayed, M. A. Cancer Cell Imaging and Photothermal Therapy in the Near-Infrared Region by Using Gold Nanorods. *J. Am. Chem. Soc.* **128**, 2115–2120 (2006).

11. Li, L. *et al.* CuS nanoagents for photodynamic and photothermal therapies: Phenomena and possible mechanisms. *Photodiagnosis Photodyn. Ther.* **19**, 5–14 (2017).

12. Mou, J. *et al.* Ultrasmall Cu2-xS nanodots for highly efficient photoacoustic imaging-guided photothermal therapy. *Small* **11**, 2275–2283 (2015).

13. Ereath Beeran, A., Fernandez, F. B. & Varma, P. R. H. Self-Controlled Hyperthermia & MRI Contrast Enhancement via Iron Oxide Embedded Hydroxyapatite Superparamagnetic particles for Theranostic Application. *ACS Biomater. Sci. Eng.* **5**, 106–113 (2019).

14. Espinosa, A. *et al.* Duality of Iron Oxide Nanoparticles in Cancer Therapy: Amplification of Heating Efficiency by Magnetic Hyperthermia and Photothermal Bimodal Treatment. *ACS Nano* **10**, 2436–2446 (2016).

15. Lewinski, N., Colvin, V. & Drezek, R. Cytotoxicity of nanopartides. *Small* **4**, 26–49 (2008).

16. Mura, S. & Couvreur, P. Nanotheranostics for personalized medicine. *Advanced Drug Delivery Reviews* **64**, 1394–1416 (2012).

17. Wang, C., Yin, H., Dai, S. & Sun, S. A general approach to noble metal-metal oxide dumbbell

nanoparticles and their catalytic application for CO oxidation. *Chem. Mater.* **22**, 3277–3282 (2010).

18. Jones, T. The role of positron emission tomography within the spectrum of medical imaging. *Eur. J. Nucl. Med.* **23**, 207–211 (1996).

19. Jhanwar, Y. S. & Divgi, C. Current status of therapy of solid tumors. *J. Nucl. Med.* **46**, 141–151 (2005).

20. Müller, C. *et al.* Terbium-161 for PSMA-targeted radionuclide therapy of prostate cancer. *Eur. J. Nucl. Med. Mol. Imaging* **46**, 1919–1930 (2019).

21. Kratochwil, C. *et al.* PSMA-targeted radionuclide therapy of metastatic castration-resistant prostate cancer with 177Lu-Labeled PSMA-617. *J. Nucl. Med.* **57**, 1170–1176 (2016).

22. Welsh, J. S., Kennedy, A. S. & Thomadsen, B. Selective internal radiation therapy (SIRT) for liver metastases secondary to colorectal adenocarcinoma. *Int. J. Radiat. Oncol. Biol. Phys.* **66**, 62–73 (2006).

23. Paes, F. M. Radionuclide Therapy. in *Cancer Metastasis - Biology and Treatment* **21**, 197–215 (2014).

24. McCarthy, D. W. *et al.* Efficient production of high specific activity 64Cu using a biomedical cyclotron. *Nucl. Med. Biol.* **24**, 35–43 (1997).

25. Monica, S. & Anderson, C. J. Molecular imaging of cancer with copper-64 radiopharmaceuticals and positron emission tomography (PET). *Acc. Chem. Res.* **42**, 832–841 (2009).

26. Matarrese, M. *et al.* Automated production of copper radioisotopes and preparation of high specific activity [64Cu]Cu-ATSM for PET studies. *Appl. Radiat. Isot.* **68**, 5–13 (2010).

27. Obata, A. *et al.* Basic characterization of 64Cu-ATSM as a radiotherapy agent. *Nucl. Med. Biol.* **32**, 21–28 (2005).

28. Yoshii, Y. *et al.* 64Cu-ATSM therapy targets regions with activated DNA repair and enrichment of CD133+ cells in an HT-29 tumor model: Sensitization with a nucleic acid antimetabolite. *Cancer Lett.* **376**, 74–82 (2016).

29. Yoshii, Y. *et al.* Multiple Administrations of 64Cu-ATSM as a Novel Therapeutic Option for Glioblastoma: a Translational Study Using Mice with Xenografts. *Transl. Oncol.* **11**, 24–30 (2018).

30. Cho, Y. W. *et al.* In vivo tumor targeting and radionuclide imaging with self-assembled nanoparticles: Mechanisms, key factors, and their implications. *Biomaterials* **28**, 1236–1247 (2007).

31. Cao, J. *et al.* Preparation and radiolabeling of surface-modified magnetic nanoparticles with rhenium-188 for magnetic targeted radiotherapy. *J. Magn. Magn. Mater.* **277**, 165–174 (2004).

32. Ting, G., Chang, C.-H., Wang, H.-E. & Lee, T.-W. Nanotargeted Radionuclides for Cancer Nuclear Imaging and Internal Radiotherapy. *J. Biomed. Biotechnol.* **2010**, 1–17 (2010).

33. Zhao, Y. *et al.* Copper-64-alloyed gold nanoparticles for cancer imaging: Improved radiolabel

stability and diagnostic accuracy. *Angew. Chemie - Int. Ed.* **53**, 156–159 (2014).

34. Schipper, M. L. *et al.* MicroPET-based biodistribution of quantum dots in living mice. *J. Nucl. Med.* **48**, 1511–1518 (2007).

35. Glaus, C., Rossin, R., Welch, M. J. & Bao, G. In vivo evaluation of 64Cu-labeled magnetic nanoparticles as a dual-modality PET/MR imaging agent. *Bioconjug. Chem.* **21**, 715–722 (2010).

36. Zhou, M. *et al.* A chelator-free multifunctional [64Cu]CuS nanoparticle platform for simultaneous micro-PET/CT imaging and photothermal ablation therapy. *J. Am. Chem. Soc.* **132**, 15351–15358 (2010).

37. Sun, X. *et al.* Self-illuminating 64Cu-Doped CdSe/ZnS nanocrystals for in vivo tumor imaging. *J. Am. Chem. Soc.* **136**, 1706–1709 (2014).

38. Riedinger, A. *et al.* Post-Synthesis Incorporation of 64Cu in CuS Nanocrystals to Radiolabel Photothermal Probes: A Feasible Approach for Clinics. *J. Am. Chem. Soc.* **137**, 15145–15151 (2015).

39. Joo, J. *et al.* Generalized and Facile Synthesis of Semiconducting Metal Sulfide Nanocrystals. *J. Am. Chem. Soc.* **125**, 11100–11105 (2003).

40. Walther, A. & Müller, A. H. E. Janus particles. *Soft Matter* **4**, 663–668 (2008).

41. de Gennes, P. G. Soft Matter. *Science (80-.).* **256**, 495–497 (1992).

42. Chun, H. J. *et al.* Water-soluble mercury ion sensing based on the thymine-Hg2+-thymine base pair using retroreflective Janus particle as an optical signaling probe. *Biosens. Bioelectron.* **104**, 138–144 (2018).

43. Ke, H., Ye, S., Carroll, R. L. & Showalter, K. Motion analysis of self-propelled Ptsilica particles in hydrogen peroxide solutions. *J. Phys. Chem. A* **114**, 5462–5467 (2010).

44. Mano, T., Delfau, J. B., Iwasawa, J. & Sano, M. Optimal run-And-Tumble-based transportation of a Janus particle with active steering. *Proc. Natl. Acad. Sci. U. S. A.* **114**, E2580–E2589 (2017).

45. Du, J. & O'Reilly, R. K. Anisotropic particles with patchy, multicompartment and Janus architectures: Preparation and application. *Chem. Soc. Rev.* **40**, 2402–2416 (2011).

46. Walther, A. & Müller, A. H. E. Janus particles: Synthesis, self-assembly, physical properties, and applications. *Chem. Rev.* **113**, 5194–5261 (2013).

47. Zhang, Y., Huang, K., Lin, J. & Huang, P. Janus nanoparticles in cancer diagnosis, therapy and theranostics. *Biomater. Sci.* **7**, 1262–1275 (2019).

48. Yang, T. *et al.* Dumbbell-Shaped Bi-component Mesoporous Janus Solid Nanoparticles for Biphasic Interface Catalysis. *Angew. Chemie - Int. Ed.* **56**, 8459–8463 (2017).

49. Najafishirtari, S. *et al.* Manipulating the morphology of the nano oxide domain in AuCu-iron oxide dumbbell-like nanocomposites as a tool to modify magnetic properties. *RSC Adv.* **8**, 22411–22421 (2018).

50. Alexeev, A., Uspal, W. E. & Balazs, A. C. Harnessing Janus nanoparticles to create controllable pores in membranes. *ACS Nano* **2**, 1117–1122 (2008).

51. Kherzi, B. & Pumera, M. Self-propelled autonomous nanomotors meet microfluidics. *Nanoscale* **8**, 17415–17421 (2016).

52. Ma, X. *et al.* Enzyme-Powered Hollow Mesoporous Janus Nanomotors. *Nano Lett.* **15**, 7043–7050 (2015).

53. Wang, H., Yang, S., Yin, S. N., Chen, L. & Chen, S. Janus suprabead displays derived from the modified photonic crystals toward temperature magnetism and optics multiple responses. *ACS Appl. Mater. Interfaces* **7**, 8827–8833 (2015).

54. Nisisako, T., Torii, T., Takahashi, T. & Takizawa, Y. Synthesis of monodisperse bicolored janus particles with electrical anisotropy using a microfluidic co-flow system. *Adv. Mater.* **18**, 1152–1156 (2006).

55. Yue, S. *et al.* SERS-Fluorescence Dual-Mode pH-Sensing Method Based on Janus Microparticles. *ACS Appl. Mater. Interfaces* **9**, 39699–39707 (2017).

56. Lu, C. *et al.* Multifunctional Janus Hematite-Silica Nanoparticles: Mimicking Peroxidase-Like Activity and Sensitive Colorimetric Detection of Glucose. *ACS Appl. Mater. Interfaces* **7**, 15395–15402 (2015).

57. Rojas, D., Jurado-Sánchez, B. & Escarpa, A. 'Shoot and Sense' Janus Micromotors-Based Strategy for the Simultaneous Degradation and Detection of Persistent Organic Pollutants in Food and Biological Samples. *Anal. Chem.* **88**, 4153–4160 (2016).

58. Guardia, P. *et al.* Gold–iron oxide dimers for magnetic hyperthermia: the key role of chloride ions in the synthesis to boost the heating efficiency. *J. Mater. Chem. B* **5**, 4587–4594 (2017).

59. Iqbal, M. Z. *et al.* A facile fabrication route for binary transition metal oxide-based Janus nanoparticles for cancer theranostic applications. *Nano Res.* **11**, 5735–5750 (2018).

60. Park, S. S. *et al.* Functionalised mesoporous silica nanoparticles with excellent cytotoxicity against various cancer cells for pH-responsive and controlled drug delivery. *Mater. Des.* **184**, 108187 (2019).

61. Lattuada, M. & Hatton, T. A. Synthesis, properties and applications of Janus nanoparticles. *Nano Today* **6**, 286–308 (2011).

62. Jiang, S. *et al. Janus Particle Synthesis, Self-Assembly and Applications*. *Advanced Materials* **22**, (Royal Society of Chemistry, 2012).

63. Kwon, K.-W. & Shim, M. γ-Fe 2 O 3 /II−VI Sulfide Nanocrystal Heterojunctions. *J. Am. Chem. Soc.* **127**, 10269–10275 (2005).

64. McDaniel, H. & Shim, M. Size and growth rate dependent structural diversification of FeO/CdS anisotropic nanocrystal heterostructures. *ACS Nano* **3**, 434–440 (2009).

65. Mehdaoui, B. *et al.* Optimal size of nanoparticles for magnetic hyperthermia: A combined theoretical and experimental study. *Adv. Funct. Mater.* **21**, 4573–4581 (2011).

66. Lin, A. W. H. *et al.* Seed-mediated synthesis, properties and application of γ-Fe 2O3-CdSe magnetic quantum dots. *J. Solid State Chem.* **184**, 2150–2158 (2011).

67. Ang, C. Y. *et al.* Facile synthesis of Fe2O3 nanocrystals without Fe(CO)5 precursor and one-pot synthesis of highly fluorescent Fe 2O3-CdSe nanocomposites. *Adv. Mater.* **21**, 869–873

(2009).

68. Selvan, S. T., Patra, P. K., Ang, C. Y. & Ying, J. Y. Synthesis of silica-coated semiconductor and magnetic quantum dots and their use in the imaging of live cells. *Angew. Chemie - Int. Ed.* **46**, 2448–2452 (2007).

69. Zhou, H., Tao, K., Sui, Y. & Sun, K. Heterogeneous nucleation and growth of CdSe on magnetite seed nanocrystals: The influence of ligand and morphology. *Phys. E Low-Dimensional Syst. Nanostructures* **44**, 597–604 (2011).

70. Cho, M. *et al.* Characterization and optimization of the fluorescence of nanoscale iron oxide/quantum dot complexes. *J. Phys. Chem. C* **118**, 14606–14616 (2014).

71. Tian, Q. *et al.* Sub-10 nm Fe3O4@Cu2-xS core-shell nanoparticles for dual-modal imaging and photothermal therapy. *J. Am. Chem. Soc.* **135**, 8571–8577 (2013).

72. Shi, W. *et al.* A general approach to binary and ternary hybrid nanocrystals. *Nano Lett.* **6**, 875–881 (2006).

73. Guardia, P. *et al.* Water-Soluble Iron Oxide Nanocubes with High Values of Specific Absorption Rate for Cancer Cell Hyperthermia Treatment. *ACS Nano* **6**, 3080–3091 (2012).

74. Wang, H. *et al.* A simple strategy to achieve shape control of Au-Cu 2−x S colloidal heterostructured nanocrystals and their preliminary use in organic photovoltaics. *Nanoscale* **10**, 11745–11749 (2018).

75. Peng, L. *Hyperthermia in oncology*. (CRC Press, 2015).

76. DeNardo, G. L. & DeNardo, S. J. Turning the heat on cancer. *Cancer Biother. Radiopharm.* **23**, 671–679 (2008).

77. Chang, D. *et al.* Biologically targeted magnetic hyperthermia: Potential and limitations. *Front. Pharmacol.* **9**, (2018).

78. Servadio, C., Leib, Z. & Lev, A. Diseases of prostate treated by local microwave hyperthermia. *Urology* **30**, 97–99 (1987).

79. Franckena, M. *et al.* Long-Term Improvement in Treatment Outcome After Radiotherapy and Hyperthermia in Locoregionally Advanced Cervix Cancer: An Update of the Dutch Deep Hyperthermia Trial. *Int. J. Radiat. Oncol.* **70**, 1176–1182 (2008).

80. Van Driel, W. J. *et al.* Hyperthermic intraperitoneal chemotherapy in ovarian cancer. *N. Engl. J. Med.* **378**, 230–240 (2018).

81. Verwaal, V. J., Bruin, S., Boot, H., Van Slooten, G. & Van Tinteren, H. 8-Year follow-up of randomized trial: Cytoreduction and hyperthermic intraperitoneal chemotherapy versus systemic chemotherapy in patients with peritoneal carcinomatosis of colorectal cancer. *Ann. Surg. Oncol.* **15**, 2426–2432 (2008).

82. Van Leeuwen, C. M. *et al.* A short time interval between radiotherapy and hyperthermia reduces in-field recurrence and mortality in women with advanced cervical cancer. *Radiat. Oncol.* **12**, 75 (2017).

83. Wust, P. *et al.* Hyperthermia in combined treatment of cancer. *Lancet Oncol.* **3**, 487–497 (2002).

84. Mahmood, J. *et al.* Immunotherapy, radiotherapy, and hyperthermia: A combined therapeutic approach in pancreatic cancer treatment. *Cancers (Basel).* **10**, 469 (2018).

85. Chicheł, A., Skowronek, J., Kubaszewska, M. & Kanikowski, M. Hyperthermia – description of a method and a review of clinical applications. *Reports Pract. Oncol. Radiother.* **12**, 267–275 (2007).

86. Cherukuri, P., Glazer, E. S. & Curley, S. A. Targeted hyperthermia using metal nanoparticles. *Adv. Drug Deliv. Rev.* **62**, 339–345 (2010).

87. Chatterjee, D. K., Diagaradjane, P. & Krishnan, S. Nanoparticle-mediated hyperthermia in cancer therapy. *Ther. Deliv.* **2**, 1001–1014 (2011).

88. Cole, A. J., Yang, V. C. & David, A. E. Cancer theranostics: The rise of targeted magnetic nanoparticles. *Trends in Biotechnology* **29**, 323–332 (2011).

89. Sharma, H., Mishra, P. K., Talegaonkar, S. & Vaidya, B. Metal nanoparticles: A theranostic nanotool against cancer. *Drug Discovery Today* **20**, 1143–1151 (2015).

90. Hayashi, K. *et al.* Superparamagnetic nanoparticle clusters for cancer theranostics combining magnetic resonance imaging and hyperthermia treatment. *Theranostics* **3**, 366–376 (2013).

91. GILCHRIST, R. K. *et al.* Selective inductive heating of lymph nodes. *Ann. Surg.* **146**, 596–606 (1957).

92. MagForce. Available at: https://www.magforce.com/home/.

93. Mahmoudi, K., Bouras, A., Bozec, D., Ivkov, R. & Hadjipanayis, C. Magnetic hyperthermia therapy for the treatment of glioblastoma: a review of the therapy's history, efficacy and application in humans. *Int. J. Hyperth.* **34**, 1316–1328 (2018).

94. Colombo, M. *et al.* Biological applications of magnetic nanoparticles. *Chem. Soc. Rev.* **41**, 4306 (2012).

95. Martinez-Boubeta, C. *et al.* Learning from nature to improve the heat generation of iron-oxide nanoparticles for magnetic hyperthermia applications. *Sci. Rep.* (2013). doi:10.1038/srep01652

96. Bauer, L. M., Situ, S. F., Griswold, M. A. & Samia, A. C. S. High-performance iron oxide nanoparticles for magnetic particle imaging – guided hyperthermia (hMPI). *Nanoscale* **8**, 12162–12169 (2016).

97. Unni, M. *et al.* Thermal Decomposition Synthesis of Iron Oxide Nanoparticles with Diminished Magnetic Dead Layer by Controlled Addition of Oxygen. *ACS Nano* acsnano.7b00609 (2017). doi:10.1021/acsnano.7b00609

98. Sathya, A. *et al.* Co x Fe 3– x O 4 Nanocubes for Theranostic Applications: Effect of Cobalt Content and Particle Size. *Chem. Mater.* **28**, 1769–1780 (2016).

99. Habib, A. H., Ondeck, C. L., Chaudhary, P., Bockstaller, M. R. & McHenry, M. E. Evaluation of iron-cobalt/ferrite core-shell nanoparticles for cancer thermotherapy. *J. Appl. Phys.* **103**, (2008).

100. Amiri, S. & Shokrollahi, H. The role of cobalt ferrite magnetic nanoparticles in medical science. *Materials Science and Engineering C* **33**, 1–8 (2013).

101. Hanini, A. *et al.* Zinc substituted ferrite nanoparticles with Zn0.9Fe2.1O4 formula used as heating agents for in vitro hyperthermia assay on glioma cells. *J. Magn. Magn. Mater.* **416**, 315–320 (2016).

102. Esmaeili, A. & Alizadeh Hadad, N. Preparation of ZnFe<inf>2</inf>O<inf>4</inf>-chitosan-doxorubicin hydrochloride nanoparticles and investigation of their hyperthermic heat-generating characteristics. *Ceram. Int.* **41**, 7529–7535 (2015).

103. Pradhan, P., Giri, J., Banerjee, R., Bellare, J. & Bahadur, D. Preparation and characterization of manganese ferrite-based magnetic liposomes for hyperthermia treatment of cancer. *J. Magn. Magn. Mater.* **311**, 208–215 (2007).

104. Doaga, A. *et al.* Synthesis and characterizations of manganese ferrites for hyperthermia applications. *Mater. Chem. Phys.* **143**, 305–310 (2013).

105. Singh, N., Jenkins, G. J. S., Asadi, R. & Doak, S. H. Potential toxicity of superparamagnetic iron oxide nanoparticles (SPION). *Nano Rev.* **1**, 5358 (2010).

106. Mehdaoui, B. *et al.* Magnetic anisotropy determination and magnetic hyperthermia properties of small Fe nanoparticles in the superparamagnetic regime. *J. Appl. Phys.* **107**, 09A324 (2010).

107. Lee, J. H. *et al.* Exchange-coupled magnetic nanoparticles for efficient heat induction. *Nat. Nanotechnol.* **6**, 418–422 (2011).

108. Lim, W. Q. & Gao, Z. Plasmonic nanoparticles in biomedicine. *Nano Today* **11**, 168–188 (2016).

109. Khlebtsov, N. G. & Dykman, L. A. Optical properties and biomedical applications of plasmonic nanoparticles. *J. Quant. Spectrosc. Radiat. Transf.* **111**, 1–35 (2010).

110. Doughty, A. C. V. *et al.* Nanomaterial applications in photothermal therapy for cancer. *Materials (Basel).* **12**, (2019).

111. Hemmer, E. *et al.* Upconverting and NIR emitting rare earth based nanostructures for NIR-bioimaging. *Nanoscale* **5**, 11339 (2013).

112. Jing-Liang Li & Min Gu. Gold-Nanoparticle-Enhanced Cancer Photothermal Therapy. *IEEE J. Sel. Top. Quantum Electron.* **16**, 989–996 (2010).

113. Hwang, S. *et al.* Gold nanoparticle-mediated photothermal therapy: current status and future perspective. *Nanomedicine* **9**, 2003–2022 (2014).

114. Riley, R. S. & Day, E. S. Gold nanoparticle-mediated photothermal therapy: applications and opportunities for multimodal cancer treatment. *Wiley Interdiscip. Rev. Nanomed. Nanobiotechnol.* **9**, e1449 (2017).

115. Huang, X., Qian, W., El-Sayed, I. H. & El-Sayed, M. A. The potential use of the enhanced nonlinear properties of gold nanospheres in photothermal cancer therapy. *Lasers Surg. Med.* **39**, 747–753 (2007).

116. Dickerson, E. B. *et al.* Gold nanorod assisted near-infrared plasmonic photothermal therapy (PPTT) of squamous cell carcinoma in mice. *Cancer Lett.* **269**, 57–66 (2008).

117. Choi, W. Il *et al.* Tumor regression in vivo by photothermal therapy based on gold-nanorod-loaded, functional nanocarriers. *ACS Nano* **5**, 1995–2003 (2011).

118. Liu, H. *et al.* Multifunctional gold nanoshells on silica nanorattles: A platform for the combination of photothermal therapy and chemotherapy with low systemic toxicity. *Angew. Chemie - Int. Ed.* **50**, 891–895 (2011).

119. Melancon, M. P. *et al.* In vitro and in vivo targeting of hollow gold nanoshells directed at epidermal growth factor receptor for photothermal ablation therapy. *Mol. Cancer Ther.* **7**, 1730–1739 (2008).

120. Chen, H. *et al.* Multifunctional gold nanostar conjugates for tumor imaging and combined photothermal and chemo-therapy. *Theranostics* **3**, 633–649 (2013).

121. Liu, Y. *et al.* A plasmonic gold nanostar theranostic probe for in vivo tumor imaging and photothermal therapy. *Theranostics* **5**, 946–960 (2015).

122. Zhou, Z., Wang, Y., Yan, Y., Zhang, Q. & Cheng, Y. Dendrimer-Templated Ultrasmall and Multifunctional Photothermal Agents for Efficient Tumor Ablation. *ACS Nano* **10**, 4863–4872 (2016).

123. Tang, S., Chen, M. & Zheng, N. Sub-10-nm Pd nanosheets with renal clearance for efficient near-infrared photothermal cancer therapy. *Small* **10**, 3139–3144 (2014).

124. Li, Y., Lu, W., Huang, Q., Li, C. & Chen, W. Copper sulfide nanoparticles for photothermal ablation of tumor cells. *Nanomedicine* **5**, 1161–1171 (2010).

125. Laser Institute of America. *American National Standard for Safe Use of Lasers*. (2007).

126. Tian, Q. *et al.* Hydrophilic Cu 9 S 5 Nanocrystals: A Photothermal Agent with a 25.7% Heat Conversion Efficiency for Photothermal Ablation of Cancer Cells in Vivo. *ACS Nano* **5**, 9761–9771 (2011).

127. Tian, Q. *et al.* Hydrophilic flower-like cus superstructures as an efficient 980 nm laser-driven photothermal agent for ablation of cancer cells. *Adv. Mater.* **23**, 3542–3547 (2011).

128. Liu, Y., Bhattarai, P., Dai, Z. & Chen, X. Photothermal therapy and photoacoustic imaging: Via nanotheranostics in fighting cancer. *Chem. Soc. Rev.* **48**, 2053–2108 (2019).

129. Wang, S. *et al.* Plasmonic copper sulfide nanocrystals exhibiting near-infrared photothermal and photodynamic therapeutic effects. *ACS Nano* **9**, 1788–1800 (2015).

Acknowledgments

After 3 years, 160 pages and more than 50000 words I would like to thank anyone that gave a contribution to this work.

First, I would like to show my gratitude to my Ph.D. supervisor, Dr. Teresa Pellegrino, for giving me the opportunity to work on this project and for her guidance during these three years.

For proofreading this thesis and for the many useful suggestions that helped improve the quality of the document, I am deeply grateful to Dr. Helena Gavilan Rubio and Dr. Nisarg Rohitbhai Soni.

For the synthesis of the water stable polymers, I thank Dr. Helena Gavilan Rubio and Dr. Than Binh Mai. For teaching me how to perform radiolabeling experiments and for helping me with all the experiments with ^{64}Cu, I am thankful to Dr. Tommaso Avellini and Dr. Nisarg Rohitbhai Soni. I am grateful to Dr. Aidin Lak for teaching me how to perform SQUID measurements. For the HR-TEM and STEM-EDS analyses, I thank Dr. Luca Leoncino and Dr. Rosaria Brescia. I thank Dr. Niccolò Silvestri for the help in designing the set-up for DUAL hyperthermia measurements and Stefano Toso for 3D printing it.

To the NACH lab technicians (Simone Nitti, Filippo Drago, Gabriele La Rosa, Giammarino Pugliese and Francesco De Donato) goes a special thank, if everything is working in our lab is mainly because of you.

Many people are or have been part of NABM research group in these three years, all of them helped me being a better researcher and a better person. They are not only colleagues but also good friends and we had a lot of fun together, in and outside the lab.

A special thanks goes to Ciccio Dream Team players and supporters, IIT football tournament will never be the same after last year.

To Guido, Ilaria, Carlo, Fang Fang, Liliana, Marco and Angela, thanks for being always next to me, even when we are scattered around Italy and the world.

I would like to thank my parents for believing in me and for always giving me their support.

To my girlfriend, Laura, goes my deep love and gratitude, everything good I did in these last nine years, it was because of us.